Lawrence Berkeley National Laboratory
Recent Work

Title
KINETICS AND TRANSPORT PROCESSES IN AQUEOUS POLYSULFIDE ELECTRODE REACTIONS

Permalink
https://escholarship.org/uc/item/46g96124

Authors
Lessner, P.M.
McLarnon, F.R.
Cairns, E.J.

Publication Date
1986-09-01

eScholarship.org Powered by the California Digital Library
University of California

UC-94cc
LBL-22399
c.1

Lawrence Berkeley Laboratory
UNIVERSITY OF CALIFORNIA

APPLIED SCIENCE DIVISION

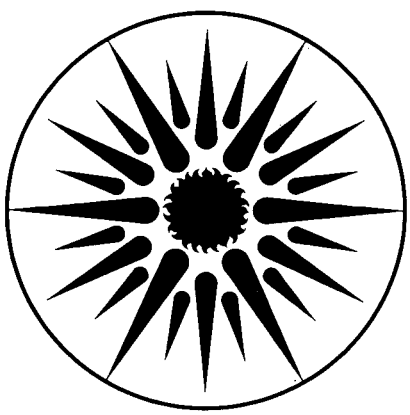
RECEIVED
LAWRENCE
BERKELEY LABORATORY
MAR 2 1987
LIBRARY AND
DOCUMENTS SECTION

KINETICS AND TRANSPORT PROCESSES
IN AQUEOUS POLYSULFIDE ELECTRODE REACTIONS

P.M. Lessner*, F.R. McLarnon and E.J. Cairns
(*Ph.D. Thesis)

For Reference
Not to be taken from this room

September 1986



APPLIED SCIENCE DIVISION

Prepared for the U.S. Department of Energy under Contract DE-AC03-76SF00098

LBL-22399
c.1

DISCLAIMER

This document was prepared as an account of work sponsored by the United States Government. While this document is believed to contain correct information, neither the United States Government nor any agency thereof, nor the Regents of the University of California, nor any of their employees, makes any warranty, express or implied, or assumes any legal responsibility for the accuracy, completeness, or usefulness of any information, apparatus, product, or process disclosed, or represents that its use would not infringe privately owned rights. Reference herein to any specific commercial product, process, or service by its trade name, trademark, manufacturer, or otherwise, does not necessarily constitute or imply its endorsement, recommendation, or favoring by the United States Government or any agency thereof, or the Regents of the University of California. The views and opinions of authors expressed herein do not necessarily state or reflect those of the United States Government or any agency thereof or the Regents of the University of California.

LBL-22399

KINETICS AND TRANSPORT PROCESSES IN AQUEOUS POLYSULFIDE ELECTRODE REACTIONS

by

Philip M. Lessner, Frank R. McLarnon and Elton J. Cairns

September 1986

Applied Science Division
Lawrence Berkeley Laboratory
University of California
Berkeley, California 94720

This work was supported by the Assistant Secretary for Conservation and Renewable Energy, Office of Energy Storage and Distribution of the U.S. Department of Energy under Contract No. DE-AC03-76SF00098.

Kinetics and Transport Processes in Aqueous Polysulfide Electrode Reactions

Philip Michael Lessner

Abstract

Fundamental and applied research on the aqueous sulfide/polysulfide redox couple has been carried out, motivated by its possible use in photoelectrochemical cells (PECs) and redox batteries. Recent work on PECs has concentrated on the reactions at photoelectrodes. Much less attention has been given to the development of efficient redox electrodes which can be used as a counterelectrode in a PEC or as an electrode in a redox cell. The objectives of the present work are to obtain information on the electrochemical and chemical reactions of the aqueous sulfide/polysulfide redox couple and to use that information to design a stable and efficient redox electrode.

Previous chemical and spectroscopic investigations have shown that, when an alkali metal sulfide and sulfur are dissolved in water, monosulfides (H_2S, HS^-, and S^{2-}), polysulfides (S_x^{2-}, x=2 to 5), and sulfur radicals (S_2^-) are present in equilibrium with one another. At equilibrium, the alkaline polysulfide electrochemical reactions can be represented by:

$$\frac{1}{3}S_4^{2-} + \frac{4}{3}H_2O + 2e^- \rightleftarrows \frac{4}{3}HS^- + \frac{4}{3}OH^- \qquad (1)$$

We have shown that the electrochemical measurements performed by other investigators correlate well with Reaction 1 and an equilibrium model that is based on chemical and spectroscopic analyses.

The kinetics of the aqueous polysulfide redox couple were investigated using a transient potential step technique in a solution 1 M in S^0 and 1.3 M in total S^{2-}, at pH 12. This pH was selected in order to minimize the disproportionation of polysulfides to thiosulfate and sulfide. The low-overpotential region (-25 to +25 mV) was investigated for cobalt and platinum

electrodes from 25 to 80 °C. The active species concentration was found to be several orders of magnitude lower than those of any of the major (poly)sulfide ions, and its temperature dependence corresponded to an E_a of about 10 kcal/mole. These results are consistent with the idea that the electrochemically active species is S_2^-. Deviations were found between experimental data for temperatures above 45 °C and the simple analytical form of the current response for an electrode reaction with one rate-determining step. The results agree with a new model proposed here that considers two rate-determining steps, one of which is the homogeneous chemical reaction:

$$S_4^{2-} \rightleftharpoons 2S_2^- \tag{2}$$

The rate constants for this reaction determined using this new model agree with those measured for similar reactions. Exchange current densities (i_o/ν) were on the order of 1 mA/cm^2 at 60 °C.

The steady-state current density-overpotential relationships for cobalt and platinum rotating disk electrodes were determined for a range of temperatures. A model was developed to take into account the rate of Reaction 2 as well as a finite heterogeneous reaction rate. The parameters determined by the potential step method could be used with this model to explain the current density-overpotential behavior in the low-overpotential cathodic region. At higher overpotentials in the cathodic region a second cathodic reaction was evident. This second cathodic reaction was less prominent when the current densities were lower (as on Pt electrodes) or when the S_2^- concentrations were higher (as temperature increased).

The addition of 13 mole-% DMF to the aqueous polysulfide solution was found to increase significantly the current density, at a given temperature and overpotential, by increasing the equilibrium concentration of the electrochemically active sulfur radical anion. In the range of overpotentials studied, the first cathodic reaction wave becomes much more prominent. Although independent quantitative data are lacking for the DMF-water mixtures, the use of reasonable values for k_f and i_o/ν allows the quantitative prediction of the observed cathodic behavior in the temperature range of 25 to 77 °C.

The results of the rotating disk work indicate that porous electrodes are required for the counterelectrode in a PEC utilizing the aqueous sulfide/polysulfide redox couple in order to meet a design goal of supporting 10-20 mA/cm^2 at less than 50 mV overpotential. A flow cell for testing flow-through porous electrodes was constructed and operated. The effect of electrode material, temperature, flow rate, and the addition of DMF on electrode performance were studied. Ni electrodes showed some evidence of initial corrosion. Co (plated on Ni screens) and MoS_2 (grown by reaction of S vapor with Mo on expanded-metal mesh) electrodes gave similar performances which were more than adequate to meet the design goals. Flow rate variation between 0.1 liter/min and 1.6 liter/min had only a small effect on the current density-overpotential curves. Raising the temperature and/or the addition of DMF had much larger effects. These observations are in accord with the steady-state results obtained on the rotating disk electrodes.

The design of aqueous polysulfide-based PECs is discussed from the standpoint of electrolyte composition, heat transfer, and absorption of light by the electrolyte. Important aspects of polysulfide chemistry in its relation to redox battery cycling are also discussed.

Acknowledgements

I would like to express my gratitude to Professor Elton Cairns who has guided me throughout my stay at Berkeley and during the preparation of this thesis. Frank McLarnon and Jack Winnick provided many valuable suggestions during the experimental portion of the work and during the writing of this thesis. I would like to thank Ms. Susan Lauer for her help in the preparation of the manuscript and figures.

This work was supported by the Assistant Secretary for Conservation and Renewable Energy, Office of Energy Storage and Distribution of the U.S. Department of Energy under Contract No. DE-AC03-76SF00098.

Table of Contents

Chapter 1 Introduction 1

1.1 Applications of the Aqueous Polysulfide Electrolyte 1

1.2 Organization of This Thesis 4

Chapter 2 Previous Work on the Aqueous Polysulfide System 6

2.1 Aqueous Polysulfide Chemistry 6

2.2 Aqueous Polysulfide Electrochemistry 12

2.3 Aqueous Polysulfide Photoelectrochemistry 18

2.4 Summary 25

Chapter 3 Kinetics and Mechanism of the Aqueous Sulfide/Polysulfide Electrode Reaction by the Potential-Step Method 27

3.1 Introduction 27

3.2 Background 28

3.3 Experimental Procedure 32

3.4 Results 40

3.5 Discussion 53

3.6 Summary 58

Chapter 4 Investigation of the Polysulfide Electrode Reaction by the Rotating Disk Method 59

4.1 Introduction 59

4.2 Experimental Procedure 60

4.3 Results 63

4.4 Discussion 73

4.5 Discussion of Results with the Addition of DMF 82

4.6 Summary 86

Chapter 5 Performance of Aqueous Polysulfide Flow-Through Electrodes 87

5.1 Introduction 87

5.2 Experimental Procedure 88

5.3 Results and Discussion 100

5.4 Summary 109

Chapter 6 Conclusions and Recommendations 111

6.1 Introduction 111

6.2 Photoelectrochemical Cell Optimization 111

6.3 Redox Batteries 125

6.4 Recommendations 131

6.5 Summary 132

Nomenclature 134

References 140

Appendix A Computer Programs for Ionic Equilibrium Calculations 153

A.1 Introduction 153

A.2 Programs for Calculating Quatities of Chemicals Required 154

A.2 Programs for Electrochemical Equilibria 157

A.3 Sample Output 166

Appendix B Non-Linear Least Squares Analysis of Potential-Step Data 167

B.1 Introduction 167

B.2 Computer Implementation 169

B.3 Program Listings 171

B.4 Sample Output 176

Appendix C Coupled Electrochemical and Chemical Reactions: Response to a Potential Step 177

C.1. Introduction 177

C.2 Method of Solution 180

C.3 Results and Discussion 182

C.4. Proof of Symmetrical Response for Linear Homogeneous Kinetics 193

C.5 Summary 194

C.7 Computer Programs 196

C.8 Sample Output 214

Appendix D Coupled Electrochemical and Chemical Reactions at the RDE 216

D.1 Introduction 216

D.2 Computer Implementation 216

D.3 Computer Programs 220

D.4 Sample Output 228

Appendix E Heat Transfer Analysis 231

E.1 Estimation of the Physical Properties of Air 231

E.2 Computer Programs 232

E.3 Sample Output 235

List of Figures

1-1 The fraction of the solar energy which can be utilized in electron-hole pair generation as a function of semiconductor band gap 3

2-1 Time for 1% disproportionation of polysulfide to thiosulfate versus 1/T 12

2-2 Aqueous polysulfide electrode rest potential at 25, 70 and 90 °C. 15

2-3 Aqueous polysulfide electrode rest potential at 80 °C. 16

2-4 The Photoelectrochemical Cell 19

2-5 Voltage correlations in the depletion region of an n-type semiconductor in contact with an electrolyte. 21

2-6 Relation of decomposition potential to semiconductor stability 23

3-1 Apparatus Block Diagram 34

3-2 Cell used for potential step experiments 37

3-3 Transient current response for a 0.32 cm^2 Pt electrode in 1 mM $K_3Fe(CN)_6/K_4Fe(CN)_6$-1 M KCl electrolyte 41

3-4 Transient current response to a potential step for a 0.2 cm^2 Co electrode in 1.3 M S^{2-}, 1 M S^0, pH=12 at 26 °C 42

3-5 Transient current response to a potential step for a 0.2 cm^2 Co electrode in 1.3 M S^{2-}, 1 M S^0, pH=12 at 35 °C 43

3-6 Transient current response to a potential step for a 0.2 cm^2 Co electrode in 1.3 M S^{2-}, 1 M S^0, pH=12 at 48 °C 44

3-7 Transient current response to a potential step for a 0.2 cm^2 Co electrode in 1.3 M S^{2-}, 1 M S^0, pH=12 at 63 °C 45

3-8 Transient current response to a potential step for a 0.2 cm^2 Co electrode in 1.3 M

S^{2-}, 1 M S^0, pH=12 at 80 °C 46

3-9 Transient current response to a potential step on a Co electrode at 63 °C. Comparision of computer model and experimental data 48

3-10 Transient current response to a potential step on a Co electrode at 80 °C. Comparision of computer model and experimental data 49

3-11 Active species concentration versus 1/T 51

3-12 Voltage sweep and current step on a 0.2 cm^2 MoS_2^- electrode at 57 °C 52

4-1 Schematic diagram of the glass cell used in the rotating disk electrode experiments 61

4-2 Current density-overpotential behavior for a Pt rde in 1.3 M S^{2-}, 1 M S^0, pH=12 at 25 and 40 °C and a rotation rate of 1000 rpm. Comparison of computer model and experimental data 64

4-3 Current density-overpotential behavior for at Pt rde in 1.3 M S^{2-}, 1 M S^0, pH=12 at 60 and 77 °C and a rotation rate of 1000 rpm. Comparision of computer model and experimental data 65

4-4 Current density-overpotential behavior for a Co rde in 1.3 M S^{2-}, 1 M S^0, pH=12 at 25 and 41 °C and a rotation rate of 400 rpm 66

4-5 Current density-overpotential behavior for a Co rde in 1.3 M S^{2-}, 1 M S^0, pH=12 at 60 and 77 °C and a rotation rate of 1000 rpm. Comparision of computer model and experimental data 67

4-6 log(i) versus overpotential in anodic branch for Co and Pt at 25 °C 69

4-7 Current density-overpotential behavior for Co an Pt rde in an aqueous 1.3 M S^{2-}, 1 M S^0 electrolyte containing 13 mole-% DMF as a cosolvent at 25 and 40 °C and a rotation rate of 1000 rpm. Comparision of computer model and experimental data 71

4-8 Current density-overpotential behavior for Co an Pt rde in an aqueous 1.3 M S^{2-}, 1 M S^0 electrolyte containing 13 mole-% DMF as a cosolvent at 60 and 77 °C and a rotation rate of 1000 rpm. Comparision of computer model and experimental data 72

4-9 log(κT) versus 1/T for aqueous 1.3 M S^{2-}, 1 M S^0 electrolyte with and without the addition of 13 mole-% DMF 73

4-10 Coordinate system for the rotating disk electrode 75

4-11 log (i_o/ν) and log(k_f) versus 1/T 85

5-1 Cross-Section of the flow cell 89

5-2 Diagram of the flow system 92

5-3 Photograph of the flow system 93

5-4 Cobalt electrodeposit on a 40 mesh nickel screen 97

5-5 Quartz ampoule for preparation of metal sulfides 98

5-6 Current density vs. overpotential on a 80 mesh Pt-10% Rh screen in 10 mM $K_3Fe(CN)_6/K_4Fe(CN)_6$/1 M KCl at various flow rates 101

5-7 Current density versus overpotential on 2 Mo/MoS_2 expanded-metal screens at 23-47 °C, with and without the addition of 13 mole-% DMF 103

5-8 Current density versus overpotential on 2 Mo/MoS_2 expanded-metal screens at 64-80 °C and with and without the addition of 13 mole-% DMF 104

5-9 Comparison of the effect of an increase in flow rate with an addition of 13 mole-% DMF on 2 Mo/MoS_2 expanded-metal screens at 64 °C 105

5-10 Change in the current density versus overpotential response of 5, 100-mesh Ni screens with repeated potential scans 107

5-11 Current density versus overpotential on 2 Co electroplated 100-mesh Ni screens 108

6-1 Optimum X_s versus pH 113

6-2 u_3 versus X_s 114

6-3 Solubility of Na_2S and K_2S 115

6-4 Spectral Distribution of Sunlight 117

6-5 Photoelectrochemical Cell Configurations 120

6-6 Effect of Wind Velocity on Cell Temperature 124

6-7 Maximum value of X_s as a function of pH. 127

6-8a Hydroxide and bisulfide concentrations versus State of Charge 129

6-8b Distribution of Polysulfide Species versus State of Charge 129

6-9a Redox Potential versus State of Charge 130

6-9b Rate of Disproportionation versus State of Charge 130

C-1 Error in using least squares fit to Equation 3-2 when slow homogeneous reactions are coupled to a heterogeneous electrode reaction 184

C-2 Case I kinetics. Effect of variation of k_b/λ^2 at $C_{ob}/C_{rb}=0$ 187

C-3 Case I kinetics. Effect of variation of k_b/λ^2 at $C_{ob}/C_{rb}=1$ 188

C-4 Case II kinetics. Effect of variation of k_bC_{ob}/λ^2 at $C_{ob}/C_{rb}=0$ 189

C-5 Error in determination of intercept 193

List of Tables

1-1 Photoelectrochemical Cells Employing Aqueous Polysulfides 1

1-2 Comparison of Redox Electrolytes 4

2-1 Equilibria in Aqueous Polysulfide Solutions 7

2-2 Species Distribution in 1.33 M S^{2-}, 1 M S at pH=12 8

2-3 Summary of Thermodynamic Results 17

3-1 Selection of Electrocatalyst 35

3-2 Summary of Rate Constants for Cobalt Electrodes 56

4-1 Possible Values of the Transfer Coefficients 78

4-2 Values of Parameters 79

4-3 Mechanistic Possibilities 80

5-1 Properties of Screens and Expanded Metal 95

5-2 Cobalt Plating Bath and Conditions 96

5-3 Performance of Co and MoS_2 Electrodes: Current Density (mA/cm^2) at -50 mV Overpotential 109

6-1 Relative Rate of Disproportionation 116

6-2 Wavelength of Maximum Absorption 118

C-1 Reaction Schemes 177

C-2 Material Balances 178

C-3 Dimensionless Variables 179

C-4 Dimensionless Equations 180

C-5 Parameters for Figure C-1 185

C-6 Sensitivity of Current to Change in Kinetics 191

D-1 Definitions 217

D-2 Dimensionless Equations 218

Chapter 1

Introduction

1.1. Applications of the Aqueous Polysulfide Electrolyte

Due to the uncertainty in world petroleum prices and availability, there has been a renewed interest in alternative sources of energy (1), along with a substantial effort to develop new energy storage technologies (2). Electrochemical energy storage and generation can be used for load leveling in electric utility networks (3), electric vehicle propulsion (4), and to store energy from advanced energy conversion systems which produce power intermittently (5) (such as solar and wind energy conversion). The aqueous polysulfide redox couple has shown promise for use in both energy conversion (photoelectrochemical cells (PECs)) and energy storage (redox batteries). This thesis reports on some aspects of the electrochemistry of the aqueous polysulfide redox couple and the development of efficient redox electrodes for use in PECs or redox batteries.

PECs are possible alternatives to solid-state photovoltaic cells. The maximum theoretical conversion efficiency of any single solar cell is a function of the bandgap of the semiconductor. Figure 1-1 illustrates this point. Table 1-1 shows that aqueous polysulfide electrolytes are useful in stabilizing several semiconductor photoelectrodes with bandgaps near the maximum shown in Figure 1-1.

Recently, aqueous polysulfide based PECs have been produced with efficiencies greater than 12% (8). Such efficient cells have been produced by a combination of semiconductor and redox

Table 1-1: Photoelectrochemical Cells Employing Aqueous Polysulfides

Semiconductor	Bandgap (ev)	Electrolyte	η_{eff}	Comments	Ref.
n-CdSe	1.7	1 M Na_2S, 1 M S, 1 M NaOH	8.4%	Single Crystal	(6)
n-CdSe	1.7	2.5 M Na_2S, 1 M S, 1 M NaOH	5%	Film	(7)
n-$CdSe_{0.65}Te_{0.35}$	1.47	1.8 M Cs_2S, 3 M S, 0.5 mM $CuSO_4$	12.7%	Single Crystal	(8)
n-$CuInS_2$	1.4	3 M Na_2S, 3 M S, 4 M KOH	4.95%	Measured at 69 °C	(9)
n-$CuInSe_2$	1.0	3 M Na_2S, 3 M S, 4 M KOH	7.47%	Measured at 73 °C	(9)

electrolyte modifications. Differences in preparation techniques (10) and modification of the semiconductor surface (11) have both led to improvements in efficiency and stability. Changing the polysulfide solution composition has also led to improved photoelectrochemical cells (8,12-14).

A photoelectrochemical cell requires an efficient counterelectrode in addition to a photoelectrode. If the overpotential at the counterelectrode is high, then cell efficiency will be reduced (15). Previous work on the polysulfide redox system has shown that several transition metals and transition metal sulfides are good electrocatalysts (15-17). However, more work is needed to gather fundamental kinetic information and develop procedures for making and testing these electrodes in a form that can be used in practical cells.

Redox batteries are a class of energy storage systems that have been proposed for load leveling in power plants and storage of solar-generated electricity. In a redox cell both forms of the redox couple are soluble. Energy is stored or removed by converting from one soluble form to another on an electrocatalytic porous electrode. An example of a system that has undergone significant development is the NASA iron-chromium system (18,19). Advantages of redox batteries include versatility in sizing, long cycle life, and relatively low temperature of operation.

To be practical, a redox electrolyte must have high solubility, be low in cost, and have good kinetics on a low-cost redox electrode. Table 1-2 compares the aqueous polysulfide electrolyte with other proposed redox electrolytes. From the cost and storage capacity standpoint, it offers improvements over other proposed electrolytes. The redox electrode would need to have electrocatalytic properties similar to those of the counterelectrode for a PEC.

PECs could also be used in an *in situ* storage arrangement. This would be a three-electrode cell with a photoelectrode, redox electrode, and storage electrode. A membrane would separate the storage electrode from the photoelectrode and redox electrode. Aqueous polysulfide PECs have been tested using this scheme. Both Sn/SnS (22) and $Zn/Zn(OH)_4^{2-}$ (23) have been used as storage electrodes.

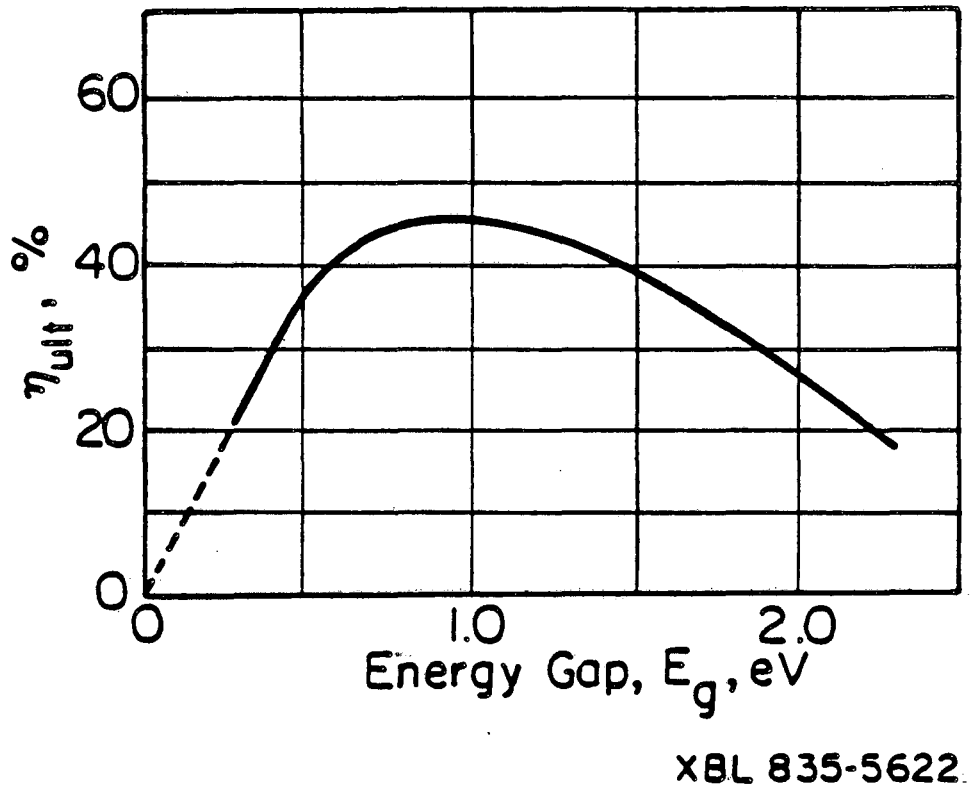


Figure 1-1: The fraction of the solar energy which can be utilized in electron-hole pair generation as a function of semiconductor band gap.

Table 1-2: Comparison of Redox Electrolytes

Electrochemical Couple	Storage Capacity (A-hr/liter)	Cost (Dollars/kA-hr)	Comments	Ref.
Fe^{3+}/Fe^{2+}	27	4.50	Chromium/Iron Redox Battery, $V_{oc} = 1.2$ V	(19)
Cr^{3+}/Cr^{2+}	24	4.50	See above	(19)
$Fe(CN)_6^{3-/4-}$	32	12.00	Zinc/Ferricyanide Battery, $V_{oc} = 1.74$ V	(20)
Br^-/Br_2	41	15.00	Zinc/Bromine Battery, $V_{oc} = 1.7$ V	(21)
S^{2-}/S	80	2.25	———	———

1.2. Organization of This Thesis

This thesis is organized into six chapters and five appendices. Chapter 2 discusses previous work on the chemistry, electrochemistry, and photoelectrochemistry of aqueous polysulfides. Several detailed studies on the distribution of (poly)sulfide ions in aqueous solution were reported in the late 1960's and early 1970's. Some of the previous electrochemical thermodynamic work is reexamined in light of these studies.

Chapter 3 discusses the use of transient experiments to elucidate aqueous polysulfide electrochemistry. The use of the potential step method is the focus of this chapter, but linear sweep voltammetry and the current steps are also discussed. The experimental results did not adequately fit the existing theory for a single rate-determining step redox reaction. A new theory that accounts for processes in the aqueous polysulfide electrolyte is presented. Appendix C discusses the application of this theory to other systems and the computer implementation in more detail.

Chapter 4 presents the results of rotating disk experiments. These experiments were performed in order to obtain steady state design data and determine the current-overpotential relationship outside the linear overpotential region. A model was written to account for processes occurring in solution and at the electrode-electrolyte interface. The agreement between the parameters for this model and those used in the model for the transient experiments is discussed, and areas where the model disagrees with experiment are noted. Data on the effect of the

addition of dimethylformamide (DMF) to the aqueous polysulfide solution are compared with data on the electrode response in pure aqueous solution.

Chapter 5 discusses the results of porous electrode experiments. A cell for flow-through porous electrode experiments was designed, built and operated. The preparation of the electrocatalysts and their performance are discussed.

Chapter 6 uses the experimental information in this thesis to give preliminary design information for aqueous polysulfide-based PECs and redox batteries. The effect of temperature, redox electrode structure, and redox electrode configuration are examined.

Chapter 2

Previous Work on the Aqueous Polysulfide System

2.1. Aqueous Polysulfide Chemistry

A major feature of sulfur chemistry is the ability of sulfur to form homonuclear chains or rings. One form of solid sulfur is an S_8 ring. In the gaseous state sulfur forms chains with lengths of 2-8 atoms. In some non-polar solvents, such as CS_2, sulfur dissolves in the form of chains or rings. Molecular sulfur is sparingly soluble or insoluble in polar solvents. If the sulfide ion is present, sulfur atoms can link to the sulfide ion forming polysulfide species (S_x^{2-}, where x ranges from 2 to a maximum that depends on the nature of the solvent). Polysulfide ions have been found in melts of alkali metal sulfides and sulfur (24,25), in molten solvents (24,25), in organic solvents (26), and in aqueous solution (27,28).

Several sulfur-bearing species are present in aqueous solution depending on the temperature, the pH and the sulfur to sulfide ratio (X_s), where X_s is defined as the ratio of total zero-valent sulfur to total sulfide:

$$X_s = \frac{\sum nC_{S_nS^{2-}}}{C_{H_2S}+C_{HS^-}+C_{S^{2-}}+\sum C_{S_nS^{2-}}} \qquad (2\text{-}1)$$

$\sum nC_{S_nS^{2-}}$ will be abbreviated as $C_{S(0)}$. It is to be emphasised, however, that there is no molecular sulfur in aqueous solution; $C_{S(0)}$ is just an convenient shorthand. Solution composition could affect interfacial kinetics if the different sulfur species have different kinetic activities. Mass transport processes would be important if an active sulfur species was present in low concentration. Table 2-1 lists the species that can be present and some measured equilibrium constants. Teder (33) found that, for a factor of eight change in X_s, several minutes were required to establish equilibrium among the polysulfides in Reactions 2-4 through 2-6. The rates of Reaction 2-7 and similar disproportionation reactions are slow; this is discussed in more detail below. The

Table 2-1: Equilibria in Aqueous Polysulfide Solutions†

$$\log K = \frac{A}{T} + BT + C + D\sqrt{I}$$

Equation	K_i	Reaction	A	B	C	D	Range, (°C)	Ref.
2-2	K_{a1}	$H_2S \rightleftarrows H^+ + HS^-$	-1158		-3.10		15-35	(29)
2-3	K_{a2}	$HS^- \rightleftarrows H^+ + S^{2-}$	-1,426		-12.0		15-270	(30)
2-4	$K_{1/2}$	$S_3^{2-} + HS^- + OH^- \rightleftarrows 2S_2^{2-} + H_2O$			-4.2	0.35	20-140	(27)
2-5	$K_{2/3}$	$2S_4^{2-} + HS^- + OH^- \rightleftarrows 3S_3^{2-} + H_2O$			-1.75	0.35	20-140	(27)
2-6	$K_{3/4}$	$3S_5^{2-} + HS^- + OH^- \rightleftarrows 4S_4^{2-} + H_2O$			5.6	0.35	20-140	(27)
2-7	$K_{t/3}$	$4S_4^{2-} + 8OH^- + H_2O \rightleftarrows 3S_2O_3^{2-} + 10HS^-$	-48,168	-0.28551	261.2	0.90	150-210	(31)
2-8	K_d	$S_4^{2-} \rightleftarrows 2S_2^-$	-4,533		6.42		100-250	(32)

†Most of the equilibrium constants in this table were calculated from observations on dilute (less than 0.1 M) solutions of polysulfides. The equilibrium constants are not corrected for the (unknown) activities of the polysulfide ions. In the more concentrated solutions employed here some deviation between the calculated species concentrations and actual species concentration might be expected.

---

rate of Reaction 2-8 was measured in the experiments of Chapters 3 and 4.

Polysulfide ions, monosulfide ions, and sulfur radicals (such as S_2^-, supersulfide) can coexist in aqueous solution. Table 2-2 shows the distribution of species in a solution which is 1.3 M in total S^{2-}, 1 M in S^0, and at a pH of 12 (the reasons for choosing these conditions will be explained below). The computer programs used to calculate the species distributions in Table 2-2 using the equilibrium constants of Table 2-1 are listed in Appendix A. S_x^{2-} with x = 2 to 5 are formed in aqueous solution. Early work based on electrochemical measurements (34-36)

Table 2-2: Species Concentrations in 1.33 M S^{2-}, 1 M S at pH=12

Temperature	25 °C		63 °C		80 °C	
Ion	Conc.	% of S^0	Conc.	% of S^0	Conc.	% of S^0
HS^-	0.991 M	———	0.991 M	———	0.991 M	———
S^{2-}	7.9 μM	———	27 μM	———	43 μM	———
S_2^{2-}	0.22 mM	0.02	0.22 mM	0.02	0.22 mM	0.02
S_3^{2-}	0.025 M	5.04	0.025 M	5.04	0.025 M	5.04
S_4^{2-}	0.33 M	89.87	0.33 M	89.85	0.33 M	89.82
S_5^{2-}	0.013 M	5.07	0.013 M	5.07	0.013 M	5.07
S_2^-	22 μM	0.004	0.16 mM	0.024	0.36 mM	0.054

suggested that polysulfides with x=2 to 6 were formed in significant amounts in the pH range of 10 to 13. More recent chemical (28,37) and spectroscopic (27,38-40) investigations that have shown that S_4^{2-} is the major polysulfide species over the range of compositions of interest in photoelectrochemical work (although there is some variation in the equilibrium constants obtained). The major monosulfide species is HS^- (bisulfide). Recent work using ultraviolet (30) and raman (41) spectroscopy has shown that S^{2-} is a very strong base (Reaction 2-3), and it will be present in appreciable quantities only in highly alkaline solution. The concentrations of the polysulfide ions do not depend appreciably on temperature (31), whereas the concentration of the supersulfide radical anion is strongly dependent on temperature (32).

Sulfur oxyanions such as $S_2O_3^{2-}$ (thiosulfate) and SO_4^{2-} (sulfate) can also be present. Polysulfide ions can be converted into sulfur oxyanions by three principal methods: exposure to oxygen, electrochemical oxidation, and homogeneous disproportionation. Chen and Morris (42) investigated the oxidation of aqueous sulfide by O_2. To avoid this degradation mechanism, aqueous polysulfide solutions should be stored and handled under an inert atmosphere. As will be discussed in Section 2.2, no appreciable electrochemical oxidation to sulfur oxyanions can take place at anodic overpotentials less than 200 mV. Aqueous polysulfide ions undergo disproportionation to thiosulfate (31,43,44) in alkaline solutions, and they decompose to sulfur and H_2S in acid solutions (43). Photoelectrochemical cells use aqueous polysulfide solutions in the alkaline pH range, and therefore acid decomposition is unimportant in this work. The equilibrium amount of thiosulfate is dependent on temperature, pH, and X_s (see Equation 2-7 in Table 2-1).

It increases as temperature and X_s increase. At lower pH, where S_5^{2-} and S_4^{2-} are the major species, the equilibrium thiosulfate concentration increases with increasing pH. At very high pH, the concentration of thiosulfate decreases because the kinetically stable lower polysulfide ions S_3^{2-} and S_2^{2-} are the dominant species.

Fortunately the rate of disproportionation can be made sufficiently slow so that aqueous polysulfide solutions can exist metastably. Giggenbach (44) has identified S_5^{2-} as the polysulfide ion most active for disproportionation. The disproportionation reaction can be represented as:

$$S_5^{2-} + 3OH^- \rightleftharpoons S_2O_3^{2-} + 3HS^- \tag{2-9}$$

with a rate expression given by (44):

$$-\frac{dC_{S_5^{2-}}}{dt} = \frac{k_f C_{S_5^{2-}} C_{OH^-}}{C_{HS^-}^2} - \frac{k_r C_{S_2O_3^{2-}} C_{HS^-}}{C_{OH^-}^2} \tag{2-10}$$

The rate constants depend on temperature in the following manner (44):

$$\log k_f = \frac{-5600}{T} + 10.9 \tag{2-11(a)}$$

$$\log k_r = \frac{-9800}{T} + 10.5 \tag{2-11(b)}$$

Aqueous polysulfide solutions used in photoelectrochemical cells must have both sulfur (present as polysulfide) and sulfide (present as bisulfide or polysulfide) in quantities that will support current densities in excess of 10 mA/cm^2. It has been found empirically that concentrations on the order of 1 mole/liter are needed for both sulfur and sulfide. An optimum solution composition would have a high electrochemical kinetic activity and would only undergo disproportionation to thiosulfate slowly.

Equations 2-10 and 2-11 show there are several ways to decrease the rate of disproportionation. A decrease in pH or an increase in C_{HS^-} will decrease the forward rate of reaction. The dependence on C_{HS^-} is stronger. Two ways to increase the bisulfide concentration would be to:

1. Lower the sulfur concentration at a constant sulfide concentration
2. Increase the sulfide concentration at a constant sulfur concentration

The first option would decrease the total amount of sulfur in solution and shift the equilibria

toward lower polysulfide ions. This might have an adverse effect on electrode kinetics (see the discussion in Section 2.2 and Chapters 3 and 4). The utility of the second option is limited by the solubility of sodium sulfide, which is about 2.5 M at room temperature. However, the recent discovery that potassium sulfide is more soluble than sodium sulfide (45,46) might make this option viable in the future.

The pH of the solution can be varied more readily than the bisulfide concentration. Three methods of pH control may be possible:

1. Addition of H_2S to the polysulfide solution
2. Addition of another acid (such as sulfuric acid)
3. Use of a buffer solution

Both options 1 and 2 have been used in previous work (17,44) and in this work. Option 1 has the advantage that no foreign anions (that might be adsorbed) are introduced. Option 3 was tried by Gustaffsson and Teder (43) with a carbonate/bicarbonate buffer. They found that bicarbonate accelerated the rate of disproportionation, so this method was not used here. At the molar concentrations of polysulfide used in the present work, the buffer would have to be very soluble, and it is unlikely that a suitable buffer could be found for these concentrated solutions.

An estimate is needed of the amount of disproportionation as a function of time in order to find a range of acceptably stable solution compositions. For small amounts of disproportionation and relatively high pH, the reverse reaction term in Equation 2-10 can be neglected. Equation 2-10 can then be written in terms of the concentration of sulfur and the fraction of sulfur that is present as pentasulfide (u_4) (27,44). The value of u_4 can be calculated from the equilibrium constants in Table 2-1 (see Appendix A). The rate expression is:

$$-\frac{dC_{S(0)}}{dt} = \frac{k_f u_4 C_{S(0)} C_{OH^-}}{C_{HS^-}^2} \qquad (2\text{-}12)$$

At small conversions or where the concentrations of the species do not change appreciably, Equation 2-12 can be integrated to give:

$$t = \ln\left[\frac{C_{S(0)_i}}{C_{S(0)_f}}\right]\cdot\frac{C_{HS^-}^2}{k_f u_4 C_{OH^-}} \qquad (2\text{-}13)$$

Figure 2-1 shows, at pH=12, that the time to 1% disproportionation is several days near 80 °C and several years at low temperatures. This pH was chosen, for some of the work reported in this thesis (see Table 2-2), as a compromise between the higher disproportionation rates at higher pH and the decreasing sulfur solubility (37) and possible OH^- mass transfer limitations at lower pH.

2.2. Aqueous Polysulfide Electrochemistry

Stoichiometry

Investigations into sulfide and polysulfide electrochemistry go back to the turn of the century (47). Fetzer (48) was the first to determine quantitatively the reaction products during the bulk electrolysis of sodium sulfide. He developed methods of chemical analysis for aqueous polysulfide solutions that allowed sulfide, sulfur, thiosulfate, and sulfate to be determined. During galvanostatic electrolysis on Pt electrodes, only polysulfide was formed at low current densities. As current increased, sulfur precipitated, and at higher currents, sulfur oxyanions were formed. Gerischer (49,50) performed experiments similar to those of Fetzer, but they were carried out potentiostatically. At anodic overpotentials of less than about 200 mV, sulfide was oxidized exclusively to polysulfide. At higher overpotentials, varying amounts of thiosulfate and sulfate were produced. Allen and Hickling (51) studied solutions containing substantial amounts of sulfur (X_s up to 3.5). Using Fetzer's method of chemical analysis, they found that polysulfides were the exclusive reactants and products in the overpotential range of 50 to 150 mV.

Thermodynamics

Fetzer and Gerischer carried out bulk electrolysis in solutions containing little zerovalent sulfur. In a redox battery or PEC, a substantial concentration of polysulfide will be present. Various attempts have been made to correlate solution composition with equilibrium potential.

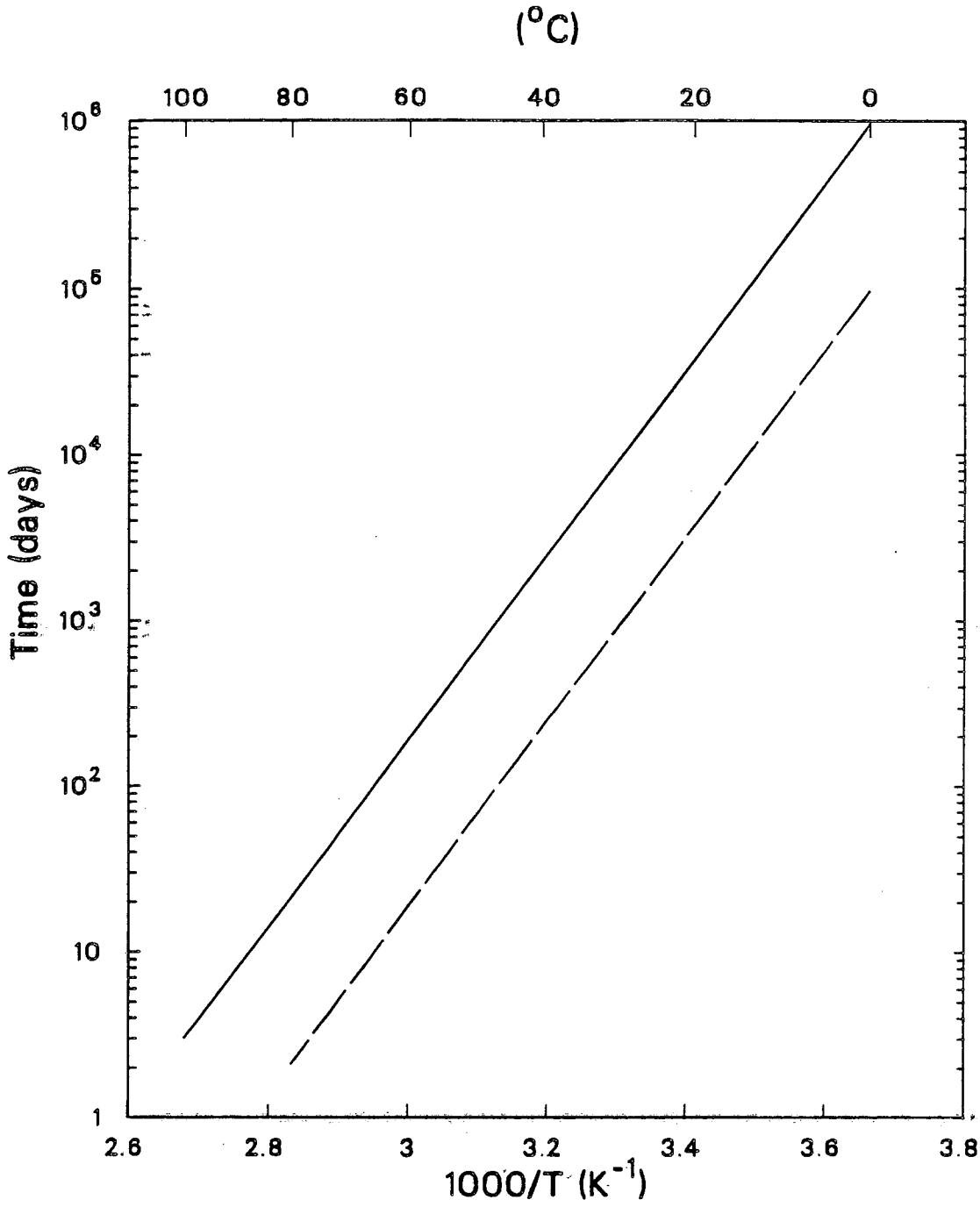


Figure 2-1: Time for 1% disproportionation of polysulfide to thiosulfate:
————————, pH 12;
— — — — — —, pH 13.

Most of this work has not taken into account the actual concentrations of polysulfide ions in solution either because the work was done before a model to calculate these concentrations was developed or the conditions of the experiments were too ill-defined to allow such a model to be used.

Allen and Hickling (51) studied polysulfide solutions that were similar in concentration to electrolytes used in PECs. Rest potentials (on Pt) were determined versus the SCE. As sulfur was added to sodium sulfide (in 1M NaOH), a plot of potential versus log(S)-log(Na_2S) was linear until about 2.5 g-mol/liter of sulfur was added. Allen and Hickling did not account for any pH variations. They recognized that the concentrations of the various polysulfide ions might vary as X_s changed and presented equations to show how this variation might affect the calculated potential. They lacked the necessary equilibrium constants to allow them to make quantitative use of these equations.

In the 1960's, there was an interest in modifying the kraft process for paper pulping by adding sulfur to kraft liquor (which contains sodium sulfide). The modified liquor (before adding wood chips) was of a composition similar to the electrolyte used in polysulfide-based PECs. In addition to the engineering studies on polysulfide pulping (52), several fundamental studies on aqueous polysulfide chemistry and electrochemistry were carried out (53). Teder (54) measured the electrode potential of the sulfide/polysulfide couple under well-defined conditions of pH, X_s, and $C_{S(0)}$. He was the first to recognize the influence of pH on electrode potential. Teder proposed that the electrode equilibrium could be represented in the form:

$$S_nS^{2-} + (n+1)H_2O + 2ne^- \rightleftarrows (n+1)HS^- + (n+1)OH^- \qquad (2\text{-}14)$$

This work was completed before data were available to calculate individual polysulfide ion concentrations. Teder attempted a correlation in terms of an average polysulfide ion, S_nS^{2-}. He was able to obtain a correlation relating potential to pH, X_s, and $C_{S(0)}$. There was a fair amount of scatter of the data, and no theoretical meaning could be attached to the regression coefficients or the intercept.

Bogomolova *et al.* (55) determined polysulfide redox potentials over a restricted range of pH, X_s, and temperature ($0.16<X_s<1.5$, pH about 13 to 14, and 25 °C). The data agreed well when correlated by equations of the form of Equation 2-14 with species concentrations calculated by use of the equilibrium model presented above. We can now reanalyze the more extensive data of Teder ($0.1<X_s<3.0$, $10.6<pH<13.8$ at 25, 70, 80, and 90 °C) using the equilibrium constants of Table 2-1 to calculate the species concentrations. We can write Equation 2-14 in the form:

$$S_4^{2-} + 4H_2O + 6e^- \rightleftarrows 4HS^- + 4OH^- \tag{2-15}$$

and the dependence of electrode potential on the activities of the ions is then:

$$E=E^\circ-\frac{RT}{6F}\ln\left(\frac{a_{HS^-}^4 a_{OH^-}^4}{a_{S_4^{2-}}}\right) \tag{2-16}$$

We could have chosen to write Equation 2-16 in a number of equivalent ways. S_4^{2-} was chosen because it is the polysulfide ion in highest concentration over the range of compositions studied.

Since the activity coefficient corrections are not known, it will be convenient to write Equation 2-16 as:

$$E=E^\circ-\frac{RT}{6F}\ln\left(\frac{C_{HS^-}^4 C_{OH^-}^4}{C_{S_4^{2-}}}\right)-\frac{RT}{6F}\ln\left(\frac{\gamma_{HS^-}^4 \gamma_{OH^-}^4}{\gamma_{S_4^{2-}}}\right) \tag{2-17}$$

The concentration term was calculated for each electrode potential-solution composition point. The details of these calculations are given in Appendix A. Plots for the four temperatures investigated by Teder are presented in Figures 2-2 and 2-3. Table 2-3 summarizes the slope and intercept obtained from each plot.

Except for the points for $X_s=3$ at 80 °C, the regression lines represent the electrode potentials at each temperature to within 2%. Several possible explanations can be offered for the deviation of the $X_s=3$ points. The equilibrium model may break down under these conditions because there could be species present in solution that are not listed in Table 2-1. The neglect of the activity coefficients in Equation 2-17 may be important under these conditions. Disproportionation of polysulfides to thiosulfate would be expected to be most favored at high X_s and

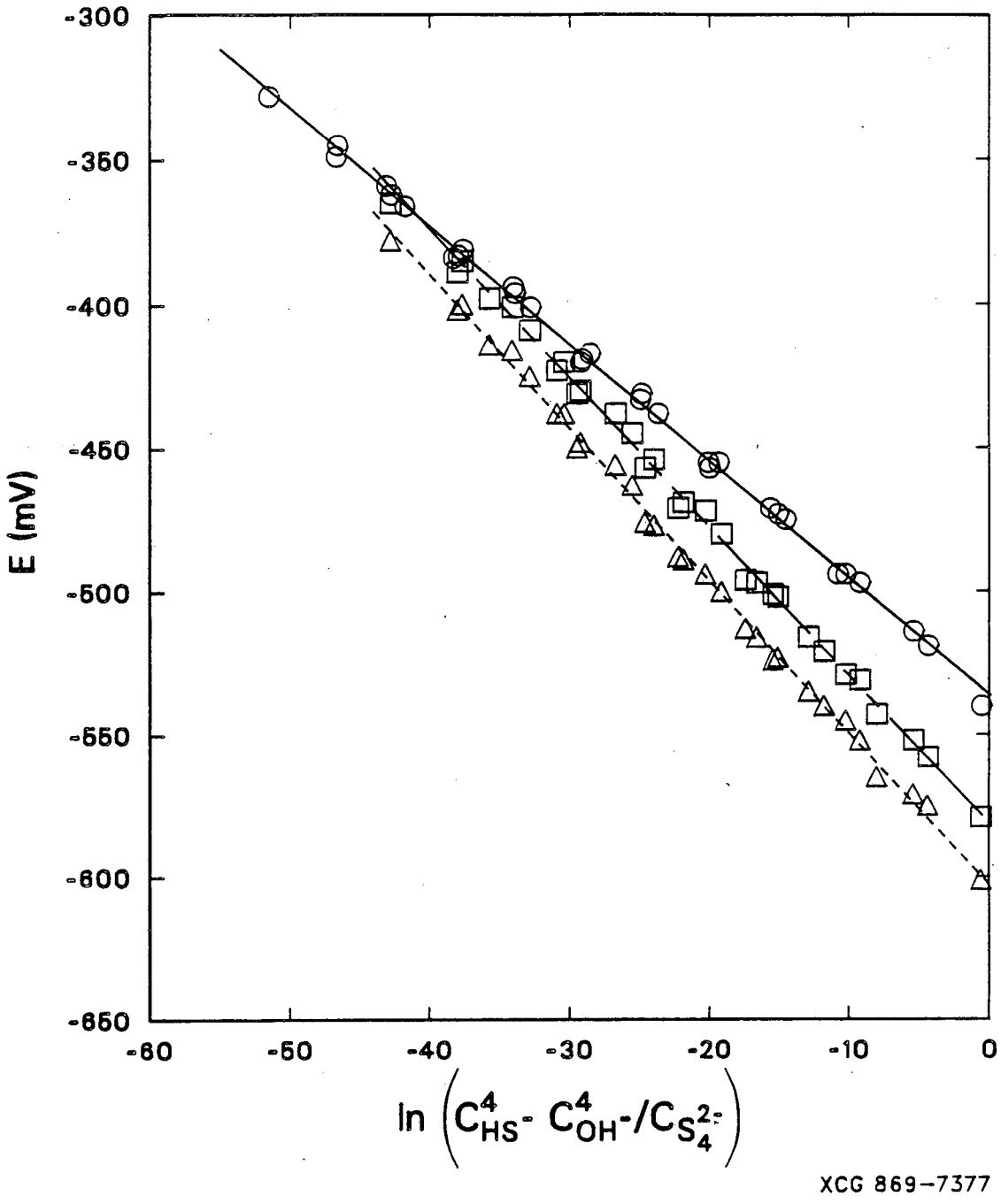


Figure 2-2: Aqueous Polysulfide Electrode Rest Potential versus $\ln\left(C^4_{HS^-}C^4_{OH^-}/C_{S_4^{2-}}\right)$

Experimental Data from (54):
○, 25 °C, ————————, least squares fit;
□, 70 °C, —— — — ——, least squares fit;
△, 90 °C, ————————, least squares fit.

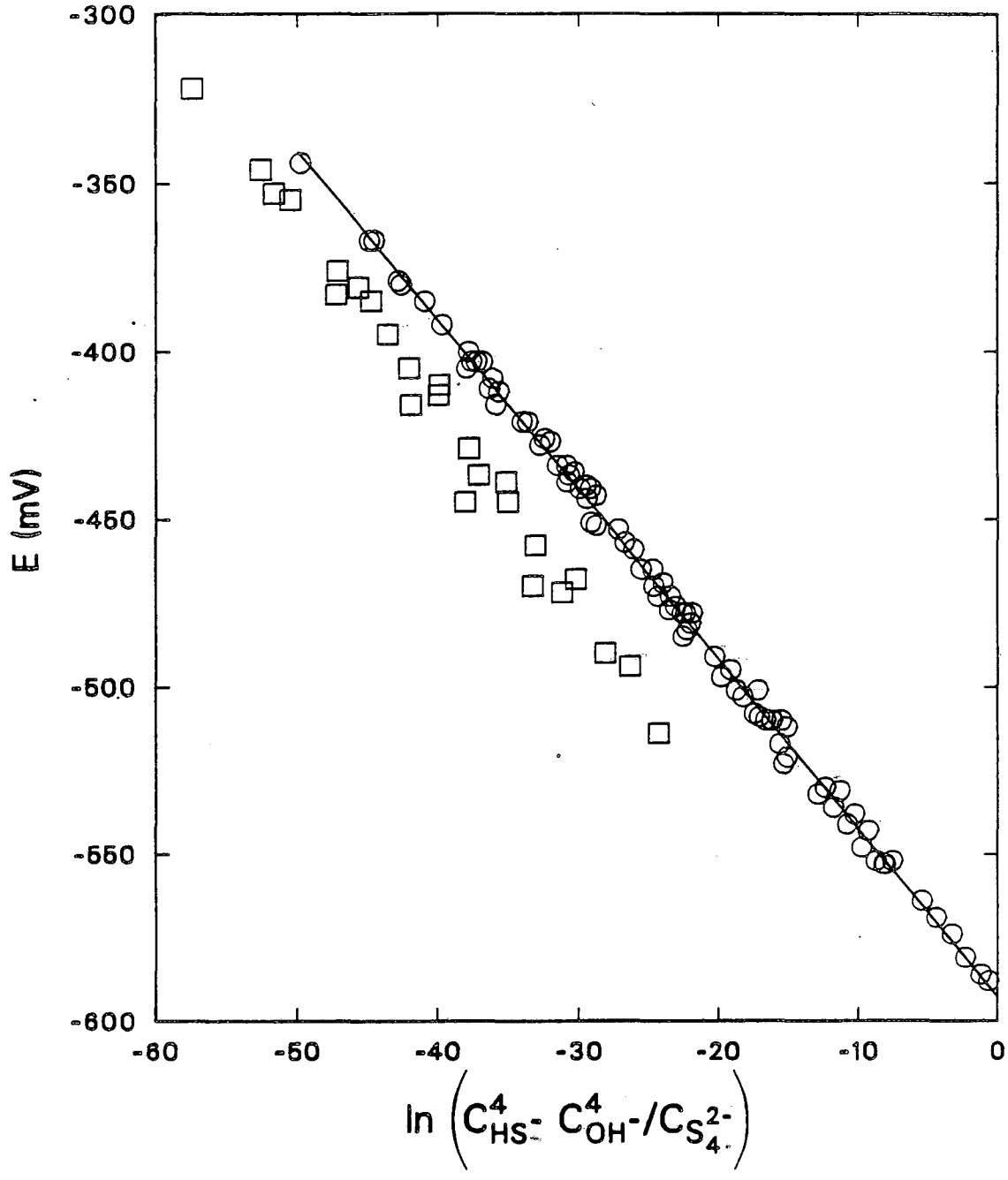


Figure 2-3: Aqueous Polysulfide Electrode Rest Potential versus $\ln\left(C^4_{HS^-}C^4_{OH^-}/C_{S_4^{2-}}\right)$ at 80 °C
Experimental Data from (54):
○, X_s=0.2→2, _____, least squares fit;
□, X_s=3.0.

Table 2-3: Summary of Thermodynamic Results

Temperature (°C)	E° (mV)	Slope (mV)	Theoretical Slope (mV)
25	-536	-4.08	-4.28
70	-581	-5.18	-4.93
80†	-593	-5.05	-5.07
90	-603	-5.33	-5.21

†Not including data at X_s=3

elevated temperatures, which would decrease the total sulfur and increase the total sulfide, so the compositions calculated based on the initial amounts added would be erroneous.

Electrode Kinetics

Allen and Hickling (51) also performed overpotential versus current measurements in the anodic overpotential range from 50 to 150 mV. They determined exchange current densities and Tafel slopes, but their results were not corrected for mass transfer or solution ohmic resistance. Even so, they reported some valuable semiquantitative results. Platinum, platinized Pt, Au, W, and Ni all assumed the polysulfide redox potential. Nickel and platinized Pt were the best electrocatalysts. The exchange current density on Pt had a temperature dependence of 10.8 kcal/mole. They also found that the kinetics become more facile as the concentration of sulfur (at constant sulfide concentration) was increased. The effect of these additions would be to shift the distribution toward larger polysulfide ions (see Section 2.1 and Appendix A). This suggests different kinetic activities for different polysulfide ions.

Because of the possible use of aqueous polysulfide electrolytes in PEC and redox batteries, there has been some more recent work on dark electrochemistry in order to develop an efficient redox electrode. Most of this work has been of a semiquantitative nature. Hodes *et al.* (15,16) tested several metals and metal sulfides for their electrocatalytic activity toward polysulfide oxidation and reduction. CoS and copper sulfide/brass were found to be the best electrocatalysts.

Since the aqueous polysulfide electrolyte is very aggressive toward copper or brass, the brass electrodes do not give good long-term performance. Higher currents were found in the anodic direction than in the cathodic direction at the same overpotential. Since the results were not corrected for resistive effects and the actual microscopic area of the electrodes is not known, it is difficult to say anything else of a quantitative nature. Remick and Camara (17) tested Ni, Co, Mo, and their sulfides for their electrocatalytic activity. All were active toward the polysulfide redox couple except for unsulfided Mo, which formed a corrosion layer. They also tested a NiS_x electrode in a redox cell with a polyhalogen as the other couple (56,57). Open-circuit voltages were close to 1 volt, and a higher overpotential was found in the cathodic reduction of polysulfide than in the anodic oxidation.

2.3. Aqueous Polysulfide Photoelectrochemistry

There has been an effort to investigate the photoelectrochemistry of the aqueous polysulfide couple in addition to the dark electrochemistry. This thesis does not deal directly with photoelectrochemistry; photoelectrochemical terms will be referred to later, and one needs an appreciation of the basic operation of PECs to understand the development of a counterelectrode for a PEC.

The basic parts of a PEC are shown in Figure 2-4. In some ways a PEC is analogous to a Schottky-barrier solar cell, but there are significant differences. We will consider the case where the semiconductor has n-type doping, which is the case for most semiconductors that use the aqueous polysulfide electrolyte. If the semiconductor is p-type, the principles of operation are similar. If only one type of redox couple is present in solution, the cell is termed "regenerative" because electricity is produced with no net change in the solution composition. Another possibility is to have two redox couples in solution; for example H_2/H_2O and O_2/H_2O. In the later case electrolysis takes place, and energy is stored as a pair of reactants. Aqueous polysulfide cells are regenerative because only one redox couple is present.

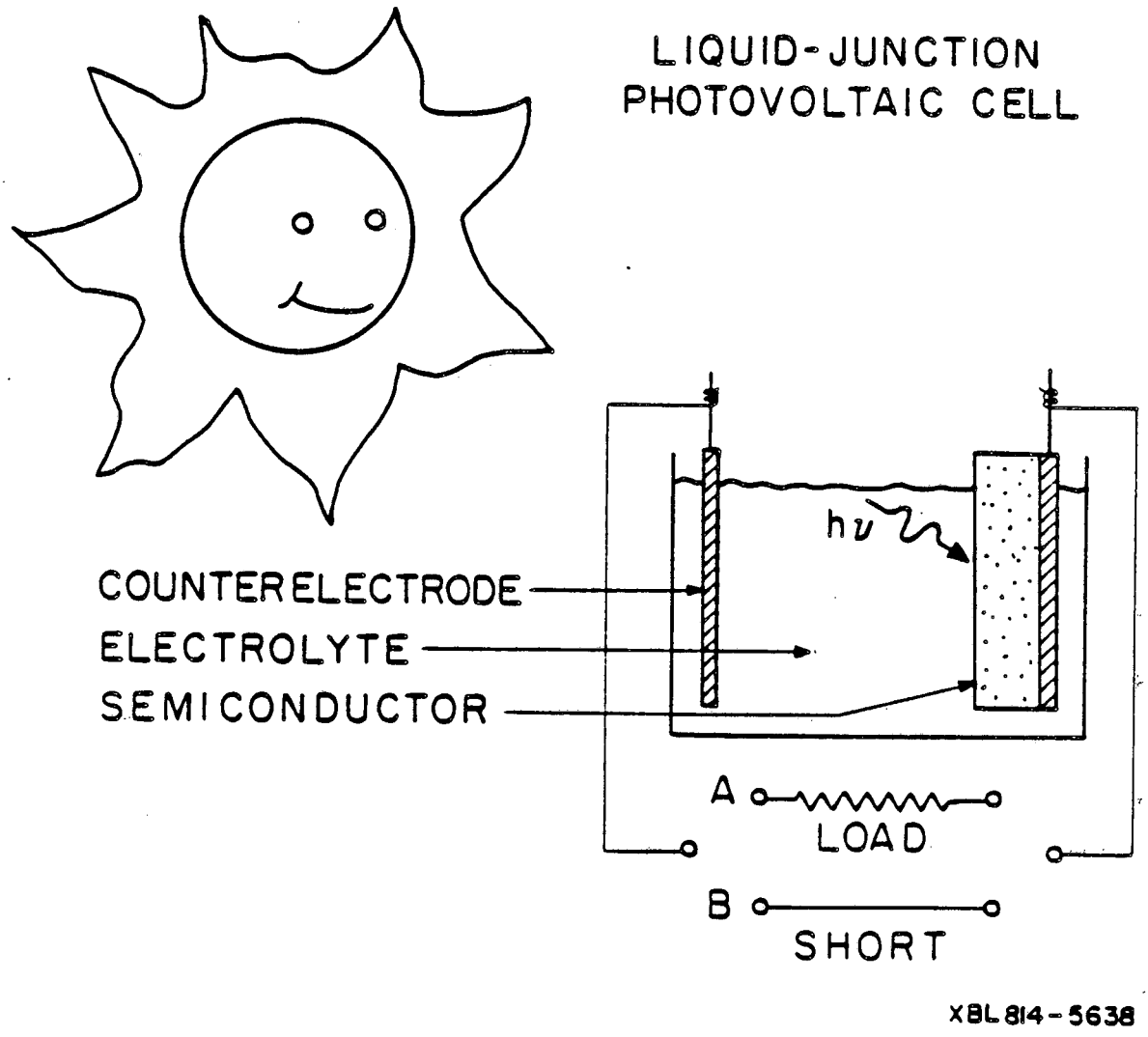


Figure 2-4; The Photoelectrochemical Cell.

The semiconductor bandgap must lie within a narrow range to be optimum for solar energy conversion as shown in Figure 1-1. Once a semiconductor is chosen, it must be matched from both a thermodynamic and kinetic standpoint to a redox couple that stabilizes it. By stabilization it is meant that a redox reaction, such as polysulfide oxidation, takes place instead of a corrosion reaction such as:

$$CdSe + 2h^+ \rightarrow Cd^{++} + Se \qquad (2\text{-}18)$$

In order to understand why some redox couples stabilize a semiconductor whereas others do not, it is necessary to look in more detail at the semiconductor energetics relative to the electrolyte. A semiconductor has valence and conduction bands. The difference in energy between the highest energy level in the valence band and the lowest energy level in the conduction band is the bandgap. The Fermi level lies in this "forbidden" energy gap. For an n-type semiconductor, the Fermi level lies close to the conduction band, and for a p-type semiconductor, it lies close to the valence band. In the absence of surface states (discussed below), only redox energy states that overlap the conduction or valence band are capable of electron transfer (58). Ideally, for a PEC with an n-type photoanode, the redox energy states should be close to the valence band.

Before the semiconductor and electrolyte are in contact, there is no space charge in the semiconductor, and the bands are flat. The position of the Fermi level under these conditions is called the flat band potential (59). Certain redox electrolytes can cause the flat band potential to shift because of specific interaction with the semiconductor surface. When the semiconductor and electrolyte are brought together in the dark, the energetics are as shown in Figure 2-5. An equilibrium electric field is set up on both sides of the interface. For redox electrolytes with concentrations greater than about 0.01 M, the double layer is O(10 Å) thickness. The space charge layer (scl) on the semiconductor side of the interface is much thicker, O(0.1 μm). The degree of band bending gives the maximum photovoltage obtainable:

$$V_{oc} = V_{fb} - V_{redox} \qquad (2\text{-}19)$$

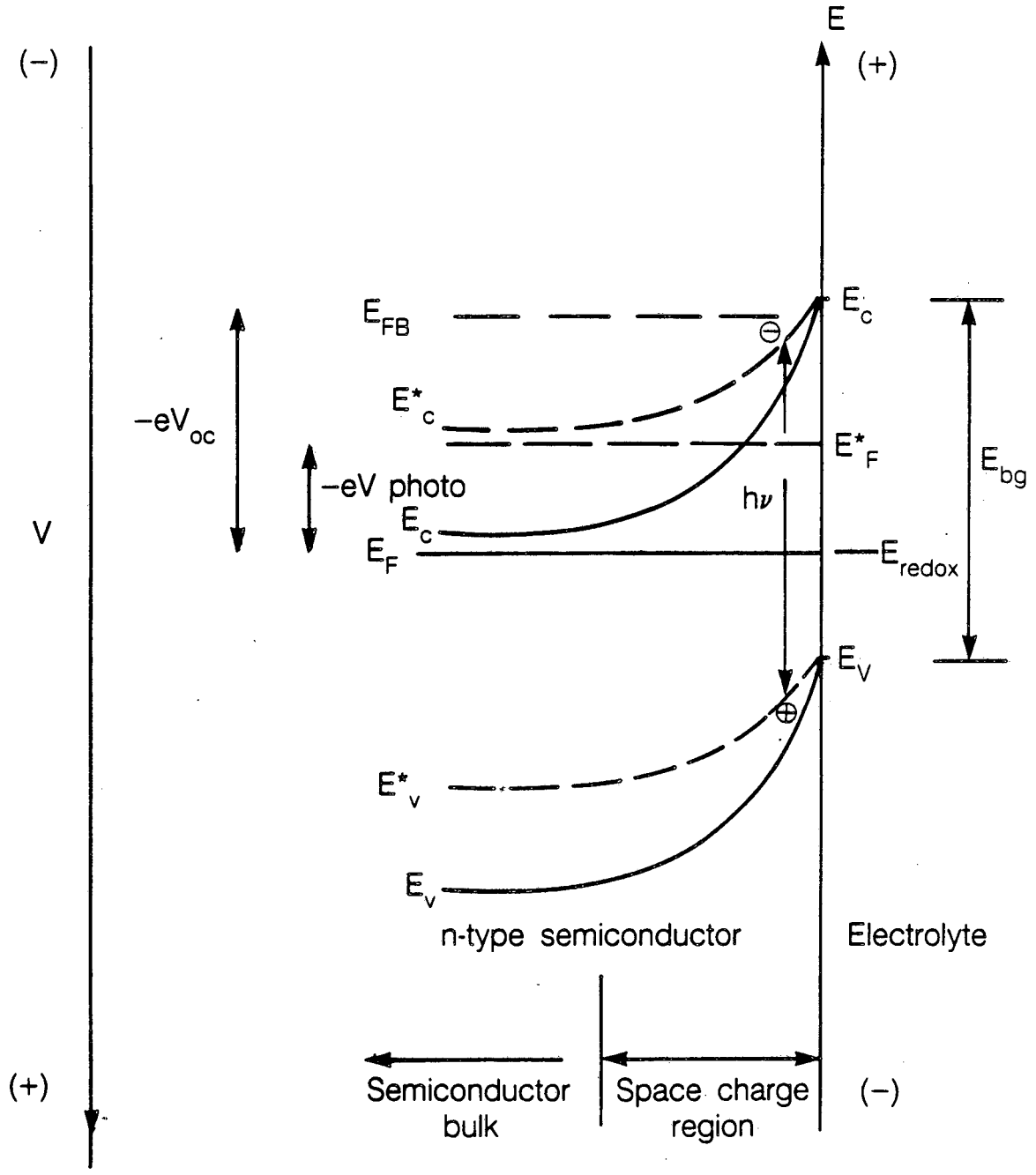


Figure 2-5: **Energy and Voltage correlations in the depeletion region of an n-type semiconductor in contact with an electrolyte:**
——————— at equilibrium;
———————, under illumination.

When light with energy greater than the bandgap is incident upon the semiconductor surface, the following processes take place (in the absence of corrosion) (59):

$$h\nu \longrightarrow h^+_{scl} + e^-_{scl}, \quad \text{light absorption} \tag{2-20a}$$

$$h^+_{scl} + e^-_{scl} \longrightarrow \text{heat}, \quad \text{recombination} \tag{2-20b}$$

$$e^-_{scl} \longrightarrow e^-_{bulk}, \quad \text{charge separation} \tag{2-20c}$$

$$h^+_{scl} \longrightarrow h^+_{surf} \quad \text{charge separation} \tag{2-20d}$$

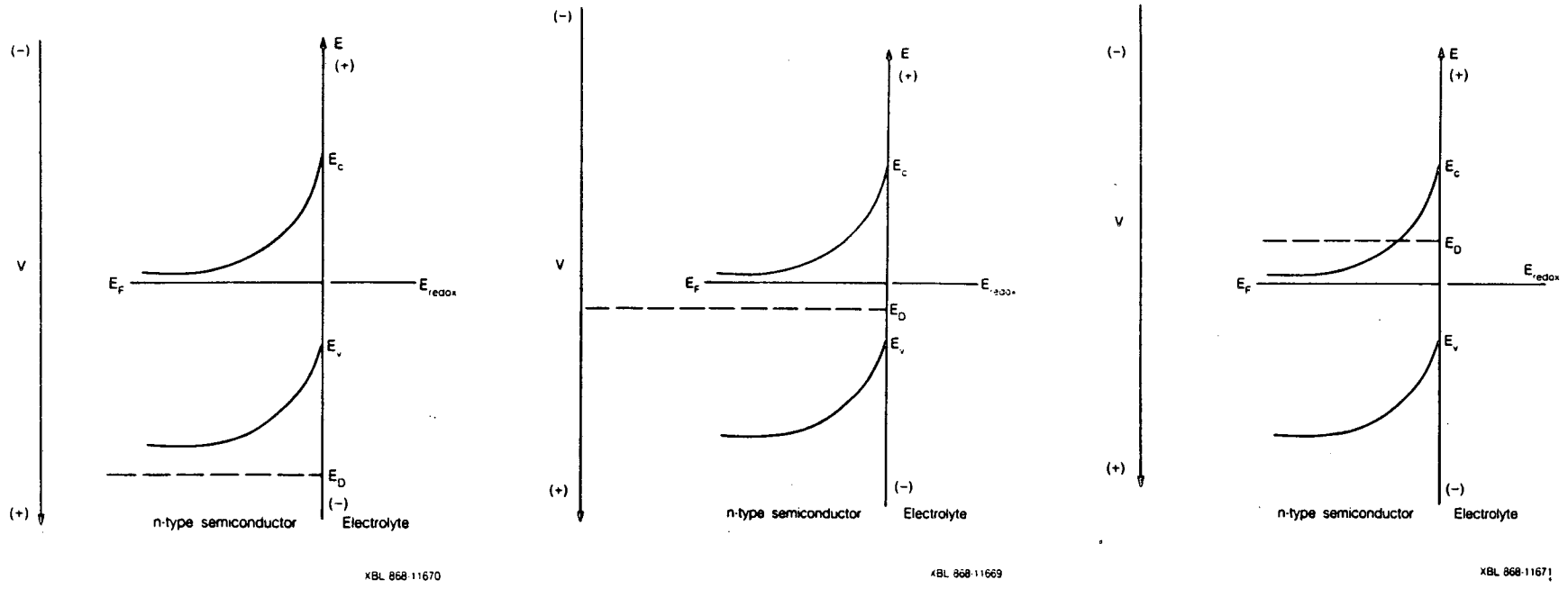
$$h^+_{surf} + R \longrightarrow O, \quad \text{photoelectrode} \tag{2-20e}$$

$$e^-_{surf} + O \longrightarrow R, \quad \text{counterelectrode} \tag{2-20f}$$

The modification of the electric field is shown in Figure 2-5. Mathematical models have been proposed to account quantitatively for the processes occurring in Reactions 2-20a-f (60-63 and references therein).

Several complications may arise that can cause a loss in performance or stability of the PEC. As Reaction 2-18 shows, photocorrosion instead of charge transfer to a redox species (Reaction 2-20e) can take place. Figure 2-6 shows the energetics for photocorrosion on an n-type semiconductor photoanode (64). In Figure 2-6a, the standard decomposition potential of the semiconductor is more positive than the redox potential of the electrolyte, and it lies outside the bandgap. Both the thermodynamic and kinetic situations for corrosion are unfavorable, and the semiconductor will be stable. In Figure 2-6b, the decomposition potential lies within the bandgap. The redox potential is more negative than the decomposition potential. Thus photocorrosion is not thermodynamically favorable. If the position of the redox potential in the bandgap moves positive of the decomposition potential, as in 2-6c, then photocorrosion will become thermodynamically favored. The oxidized form of the redox couple will also be thermodynamically able to oxidize the semiconductor surface.

Figure 2-6 implies that there is a constraint on the maximum photovoltage that a stable cell can supply because the redox potential cannot be more positive than the decomposition potential. This will also cause the redox level to be farther away from the top of the valence



(a) (b) (c)

Figure 2-6: Relation of decomposition potential to semiconductor stability:
(a) Decomposition potential lies outside of bandgap.
(b) Decomposition potential more positive than redox potential.
(c) Decomposition potential more negative than redox potential.

band and may prevent kinetic overlap of energy levels, thereby preventing charge transfer. The prospects for development of stable PECs would be dim indeed if it were not for the presence of surface states which can modify PEC energetics.

Surface states arise because of defects at the surface and can be the cause of three major processes:

1. Recombination of electrons and holes
2. Fermi level pinning
3. Mediation of charge transfer between the semiconductor and electrolyte

Recombination of electrons and holes is an undesirable result caused by some types of surface states because a cell's efficiency is thereby reduced. Fermi level pinning (65) is also not desirable. It can cause a reduction in the maximum photovoltage obtainable. On the other hand, charge transfer mediation can be beneficial for photoelectrode operation. Normally no charge transfer can occur for a photoanode unless the valence band and redox electrolyte energy states overlap. The presence of surface states can relax this requirement. The surface states may act as "intermediates" in the transfer of the hole from the semiconductor to the electrolyte. This allows redox electrolytes with redox potentials substantially more negative than the top of the valence band to be used. Thus kinetic requirements can be met while maintaining a redox potential negative of the electrode decomposition potential.

The concepts discussed above can be applied to semiconductor/aqueous polysulfide systems to help understand the limitations of these systems and to provide guidance in designing better semiconductor photoelectrodes for PECs. The energetics for aqueous polysulfide-based PECs on CdS (64) and CdSe (66) have been measured. The anodic decomposition potential for both of these semiconductors lies within the bandgap. Photocorrosion is possible, but the redox potential of the polysulfide couple is more negative than the decomposition potential, making the oxidation of polysulfide thermodynamically favored. However, the negative polysulfide redox potential limits V_{oc} (see Equation 2-19) and makes charge transfer via direct overlap of valence and redox energy states unlikely.

The approximately 1.6 V difference between V_{vb} and V_{redox} for CdS and the 0.75 V difference for CdSe suggest that surface states mediate hole transfer between the valence band and the polysulfide redox couple (66). Etching and/or photoetching treatments (67) can have a profound effect on the performance of aqueous-polysulfide-based PECs. One effect of these treatments might be to modify the number of surface states and their energetics. The quantitative measurements on the effect of surface treatments on surface states have been sparse and thus the treatment of semiconductor surfaces is at present more of an art than a science.

Differences in preparation of the semiconductors can lead to changes in bulk transport and kinetic parameters and therefore a change in cell performance. Such parameters as minority carrier diffusion length and the density of bulk recombination centers are affected by changing the way the bulk semiconductor is deposited and post-deposition annealing.

Early investigations into improving aqueous polysulfide PEC performance concentrated almost totally on semiconductor processing to improve cell performance; more recently it has been recognized that modification of the electrolyte can also lead to performance improvements. Changing X_s (46), pH (13), cation (14), and combinations of these changes (8) have all led to stability and/or efficiency improvements.

2.4. Summary

Polysulfides (S_x^{2-}), monosulfides (H_2S, HS^-, S^{2-}), and sulfur radical anions are present in aqueous, alkaline solutions in which sulfide and sulfur are dissolved. Equilibrium constants have been measured by several investigators; one such set is presented in Table 2-1. The electrochemical thermodynamic data of Teder (54) were analyzed using these equilibrium constants. The electrochemical data were consistent with the equilibrium data, which were determined by independent spectroscopic and chemical methods, except at X_s=3 (at 80 °C). Several reasons for this deviation were suggested.

Alkaline disproportionation of polysulfides to sulfide and thiosulfate is an important degradation mechanism (Reaction 2-9). The rate of this reaction can be decreased by lowering the pH,

and by decreasing X_s. The electrolyte composition chosen for some of the experiments in this thesis (Table 2-2) is a compromise between that which minimizes the rate of disproportionation and the need to work at realistic pH and X_s values.

Most of the previous work on aqueous polysulfide electrode kinetics has been qualitative or semiquantitative in nature. For application to PECs and redox batteries, the electrolyte should have a substantial concentration of both sulfur and sulfide, and the electrodes would need to support the required current densities at low overpotentials. Most previous work has involved solutions that are dilute in sulfur, Tafel-region measurements, or has been qualitative in nature. However, these works have shown that several transition metals and transition metal sulfides are good electrocatalysts and that variation in solution composition can be used to improve kinetics.

Recent work has concentrated on electrochemistry at photoelectrodes. Interpretation of results at photoelectrodes is more complicated than on dark electrocatalyts because photogeneration of charge carriers and transport of these carriers to the surface of the semiconductor must be accounted for in addition to the transport in the electrolyte phase and interfacial reaction. Improvements in efficiency and stability have been made by semiconductor modifications such as annealing, etching, and photoetching. The use of these treatments is more of an art than a science at present. Some improvement has also been made by changing polysulfide solution composition. This indicates that transport in the electrolyte and/or interfacial kinetics may be an important factor in PEC cell design.

Chapter 3

Kinetics and Mechanism of the Aqueous Sulfide/Polysulfide Electrode Reaction by the Potential-Step Method

3.1. Introduction

The conversion of sulfur into sulfide involves the transfer of two electrons, and There is more than one sulfur-bearing species in solution. These factors suggest that the aqueous polysulfide electrode reaction is a multi-step combination of elementary chemical and electrochemical reactions. For design purposes it is necessary to determine active species concentrations, exchange current densities, and homogeneous kinetic parameters. If the solvent does not decompose and the electrode reaction and mechanism do not change over a sufficiently wide range of potential, then there are several well-developed techniques for determining these parameters. These techniques include linear sweep voltammetry (68,69), ac impedance methods (70), and the rotating disk and ring-disk techniques (71). Techniques such as sweep voltammetry yield useful information only at potentials far from the equilibrium potential.

Energy conversion and storage devices (such as batteries) typically operate at low overpotentials in order to maximize energy efficiency, and they often use electrolytes that are concentrated mixtures of several species. The aqueous polysulfide electrolyte falls into this category. These characteristics suggest the use of dc relaxation techniques (such as current step and potential step) which can often be used to obtain both diffusion and kinetic information in the low-overpotential region. Nagy (72) has recently analyzed the applicability of these techniques and determined the maximum measurable rate constants.

This chapter is concerned with the use of the potential step method to measure exchange current densities and active species concentration in the aqueous polysulfide electrolyte. The

equations and assumptions that go into the derivation of the analytic form of the current-time transient in the linear overpotential region are discussed. The experimental results are then presented and compared to the closed-form solution. Since the closed-form solution did not adequately represent the experimental data of this work, an extension to the theory is presented and discussed in terms of possible electrode reaction mechanisms.

3.2. Background

Before the potential step is applied, the solution is at a uniform composition. At t=0, a small potential step (versus a reference electrode of the same kind) is applied. A one-dimensional geometry is assumed with the z coordinate denoting the distance from the working electrode surface. If at the working electrode the multi-step electrode reaction:

$$s_o O + ne^- \rightleftarrows s_r R \tag{3-1}$$

takes place, the current will follow the transient given by (72-74)

$$i = W \exp(\lambda^2 t)\ \mathrm{erfc}\ (\lambda t^{1/2}) \tag{3-2}$$

if the following assumptions hold:

1. The electrolyte is well-supported
2. Reaction 3-1 has only one rate-determining step
3. No diffusion of intermediates into the bulk occurs
4. No strong specific adsorption is present
5. The rise of the potential across the double layer is fast
6. Non-faradaic processes do not contribute significantly to the total current.

Other species besides O and R may be involved in the electrode reaction. Their concentrations are assumed to be higher than those of O and R, and they therefore do not contribute to the concentration overpotential. Reaction 3-1 and the equations derived represent a generalization of the reaction $O + ne^- \rightleftarrows R$ where the overall stoichiometric coefficients are not necessarily equal. In the linear overpotential region, W and λ have the following definitions:

$$W = \frac{V}{R_s + R_r} \tag{3-3}$$

$$\lambda = \frac{i_o}{\nu nF} \cdot \frac{R_r}{R_s+R_r}\left(\frac{s_o^2}{D_o^{1/2}C_{ob}} + \frac{s_r^2}{D_r^{1/2}C_{rb}}\right) \tag{3-4}$$

The diffusion parameter, $\left(\frac{s_o^2}{D_o^{1/2}C_{ob}}+\frac{s_r^2}{D_r^{1/2}C_{rb}}\right)$, and $\frac{i_o}{\nu}$ can be determined from W and λ.

Assumptions 1 and 3 allow a simplification of the material balance and flux equations, and assumptions 2 and 4 are consistent with the assumed form of the electrode kinetic expression. The flux equation for dilute solutions can be written (75):

$$N_i = -z_iU_iFC_i\nabla\Phi - D_i\nabla C_i + C_i\mathbf{v} \tag{3-5}$$

Since convection is not expected to play a role at very short times, in an unstirred system, the last term of Equation 3-5 can be eliminated. The first term on the right side of Equation 3-5 represents the transport of ions by migration in the electric field. Only if assumption 1 holds can this term be eliminated. The material balance for species O or R can then be written:

$$\frac{\partial C_i}{\partial t} = D_i\frac{\partial^2 C_i}{\partial z^2} + R_i \tag{3-6}$$

If Reaction 3-1 has only one rate-determining step (the other steps in the electrode reaction are assumed to be in quasi-equilibrium) and it is assumed that none of the intermediates are strongly adsorbed, then the relation between current density and surface overpotential is:

$$i = i_o'\left\{\exp\left[\frac{\alpha_a F\eta_s}{RT}\right] - \exp\left[\frac{-\alpha_c F\eta_s}{RT}\right]\right\} \tag{3-7}$$

This is the multi-step Butler-Volmer equation. The transfer coefficients and the reaction orders are related to the stoichiometry of Reaction 3-1 and the stoichiometric number by (76-78):

$$\alpha_a + \alpha_c = n/\nu \tag{3-8a}$$

$$z_{oc} - z_{oa} = s_o \tag{3-8b}$$

$$z_{ra} - z_{rc} = s_r \tag{3-8c}$$

The exchange current density, i_o', contains the *surface* concentrations of species O and R:

$$i_o' = \text{const} \cdot C_o^{(z_{oa}/\nu - s_o\alpha_a/n)}\Big|_{z=0} C_r^{(z_{ra}/\nu - s_r\alpha_a/n)}\Big|_{z=0} \tag{3-9}$$

The constant in Equation 3-9 is independent of the concentrations of O and R, but depends on the rate constant of the rate-determining step and the equilibrium constants of the quasi-reversible steps (76,77). The relationship between the transfer coefficients, α, and the mechanism of the overall reaction are (76,77):

$$\alpha_a = \frac{n-s}{\nu} - r\beta \tag{3-10a}$$

$$\alpha_c = \frac{s}{\nu} + r\beta \tag{3-10b}$$

The concentration overpotential in a well-supported electrolyte is:

$$\eta_d = \frac{RT}{nF}\left[s_o \ln\left[\frac{C_o \mid_{z=0}}{C_{ob}}\right] - s_r \ln\left[\frac{C_r \mid_{z=0}}{C_{rb}}\right]\right] \tag{3-11}$$

Equation 3-11 neglects a small term which is of the order of the reactant concentration divided by the supporting electrolyte concentration (79). In addition, activity coefficient variations between the bulk electrolyte and the region adjacent to the surface of the electrode are ignored.

Equations 3-7 through 3-9 and 3-11 can be combined (78) to give:

$$i = i_o\left\{\left(\frac{C_r \mid_{z=0}}{C_{rb}}\right)^{s_{ra}/\nu}\left(\frac{C_o \mid_{z=0}}{C_{ob}}\right)^{s_{oa}/\nu} \exp\left[\frac{\alpha_a F(\eta_s+\eta_d)}{RT}\right] - \left(\frac{C_o \mid_{z=0}}{C_{ob}}\right)^{s_{oc}/\nu}\left(\frac{C_r \mid_{z=0}}{C_{rb}}\right)^{s_{rc}/\nu} \exp\left[\frac{-\alpha_c F(\eta_s+\eta_d)}{RT}\right]\right\} \tag{3-12}$$

In Equation 3-12, i_o contains the *bulk* concentrations of O and R. If the size of the potential step is sufficiently small then Equation 3-12 can be linearized (78):

$$i = \frac{nFi_o}{\nu RT}\left[\eta_s+\eta_d - \frac{RT}{nF}\left[s_o\left\{\frac{C_o \mid_{z=0}}{C_{ob}} - 1\right\} - s_r\left\{\frac{C_r \mid_{z=0}}{C_{rb}} - 1\right\}\right]\right] \tag{3-13}$$

The conditions under which this linearization is valid for dc relaxation techniques has been discussed by Nagy (80).

Three additional equations are needed to derive Equation 3-2. A voltage balance between the working and reference electrode:

$$V = iR_s + \eta_s + \eta_d \tag{3-14}$$

a relation between the faradaic current (anodic current and overpotentials are taken to be positive) and species flux:

$$i = -\frac{nFD_o}{s_o}\frac{\partial C_o}{\partial z}\bigg|_{z=0} \tag{3-15}$$

and a relation between the fluxes of O and R at the surface:

$$\frac{D_o}{s_o}\frac{\partial C_o}{\partial z} + \frac{D_r}{s_r}\frac{\partial C_r}{\partial z} = 0 \tag{3-16}$$

Equation 3-2 is the solution to Equation 3-6 (for species O and R and with R_i=0) subject to Equations 3-13 through 3-16 and the boundary conditions of semi-infinite linear diffusion:

$$\text{as } z\rightarrow\infty,\ C_o\rightarrow C_{ob},\ C_r\rightarrow C_{rb} \tag{3-17}$$

It is applicable after the non-faradaic current due to the charging of the double layer has decayed to a small value ($\approx 4R_sC_{dl}$). The maximum time of observation is set by the decreasing amount of kinetic information as time increases (the total overpotential is dominated by concentration rather than activation overpotential as time increases). At longer times, natural convection may also influence the current.

Nagy (81) has derived a form of Equation 3-2 wherein assumption 5 can be relaxed. The potential rises linearly with time across the double layer up to time t_2. This finite rise time could be due to the risetime of the potentiostat or due to the time required for double layer charging. For double layer charging, t_2 should be set equal to $4R_sC_{dl}$ (72). The current-time transient takes the form:

$$i=\left(\frac{W}{t_2\lambda^2}\right)\left[\exp(\lambda^2 t)\operatorname{erfc}(\lambda t^{1/2})+2\lambda(t/\pi)^{1/2}-\exp(\lambda^2(t-t_2))\operatorname{erfc}(\lambda(t-t_2))^{1/2}-2\lambda((t-t_2)/\pi)^{1/2}\right] \tag{3-18}$$

Under certain conditions (72), neglecting the risetime of the potential can lead to considerable error in the determination of the exchange current density. Nagy has also considered the case where both faradaic and non-faradaic contributions to the current are taken into account

explicitly (72).

Equation 3-2 is also applicable in the non-linear overpotential range, but then W and λ will not have the meanings given by Equations 3-3 and 3-4, and uncompensated solution resistance cannot be taken into account explicitly (*cf.* Bard and Faulkner (82) and Macdonald (83)). Nagy *et al.* (80) have considered the case where an equation similar to Equation 3-12 replaces Equation 3-13 and has accounted for the uncompensated resistance. A numerical solution is required. Where the parameters are determined by a non-linear least squares fit (for example MINPACK-1 (84)), substantially more computer time is needed for this case than for the linear case. Holub (85) and Susbielles and Delahay (86) consider the linear overpotential case where specific adsorption cannot be neglected. In that case the electrode kinetic expression must be modified to take into account surface excess charge. They obtain an equation that is similar to Equation 3-2, but has extra terms that account for this specific adsorption.

Macdonald (83) presents a solution for a coupled chemical-electrochemical reaction where the overpotential is large enough so that the electrochemical reaction is under diffusion control only. The concentration of species O at the electrode surface is zero. The homogeneous kinetic parameters can be obtained from the current transient, but no information about the electrochemical kinetics can be derived under these conditions.

3.3. Experimental Procedure

Selection of Electrocatalyst

Several criteria determined the choice of an electrocatalyst for this study. The preliminary choice of the electrocatalyst was based on the experiments of Allen and Hickling (51), Hodes *et al.* (15,16), and Remick and Camara (17). These investigators showed that electrocatalysts such as Co, NiS, and CuS had activities high enough to suggest their use in a practical redox electrode.

The electrocatalyst must be stable both chemically and electrochemically in the aqueous polysulfide electrolyte. Chemical corrosion can occur by attack of the polysulfide ions on the electrode surface.

$$M + S_x^{2-} \rightarrow MS + S_{x-1}^{2-} \quad (3\text{-}19)$$

In Reaction 3-19, M represents a metal. The possibility of a metal sulfide chemically reacting to form a more stable phase should not be ruled out. Some metal sulfides can form stable complexes in aqueous sulfide solutions (87,88) and will dissolve. Electrochemical instability can be caused by cathodic

$$MS + 2e^- \rightarrow M + S^{2-} \quad (3\text{-}20a)$$

or anodic decomposition.

$$MS \rightarrow M^{2+} + S + 2e^- \quad (3\text{-}20b)$$

In Reaction 3-20b, the metal ion would probably precipitate to form a porous metal sulfide phase. The sulfur could either dissolve into the solution (as polysulfide) or form an insulating layer on the electrode surface. Two indicators of stability are the rest potential and any change in electrode response with time.

A final criterion for the choice of electrocatalyst for these experiments was the ability of the electrode to be polished to a reproducible surface. This is important for the accurate determination of the parameters W and λ. Several electrocatalysts were evaluated using the above criteria in preliminary experiments, and Table 3-1 shows the results of those experiments. Cobalt (Alfa Chemical, polycrystalline rod, 99.998%) was chosen as the electrocatalyst to be used in most of these studies, and platinum (99.95%) was used for comparison purposes.

Electronics and Cell Design

Figure 3-1 shows a block diagram of the experimental apparatus. A PAR model 175 function generator was used to apply potential pulses to a PAR model 371 potentiostat/galvanostat, which controlled a three-electrode cell. The potentiostat has an internal current/voltage meter which is between the power amplifier output of the potentiostat and the external cell connection.

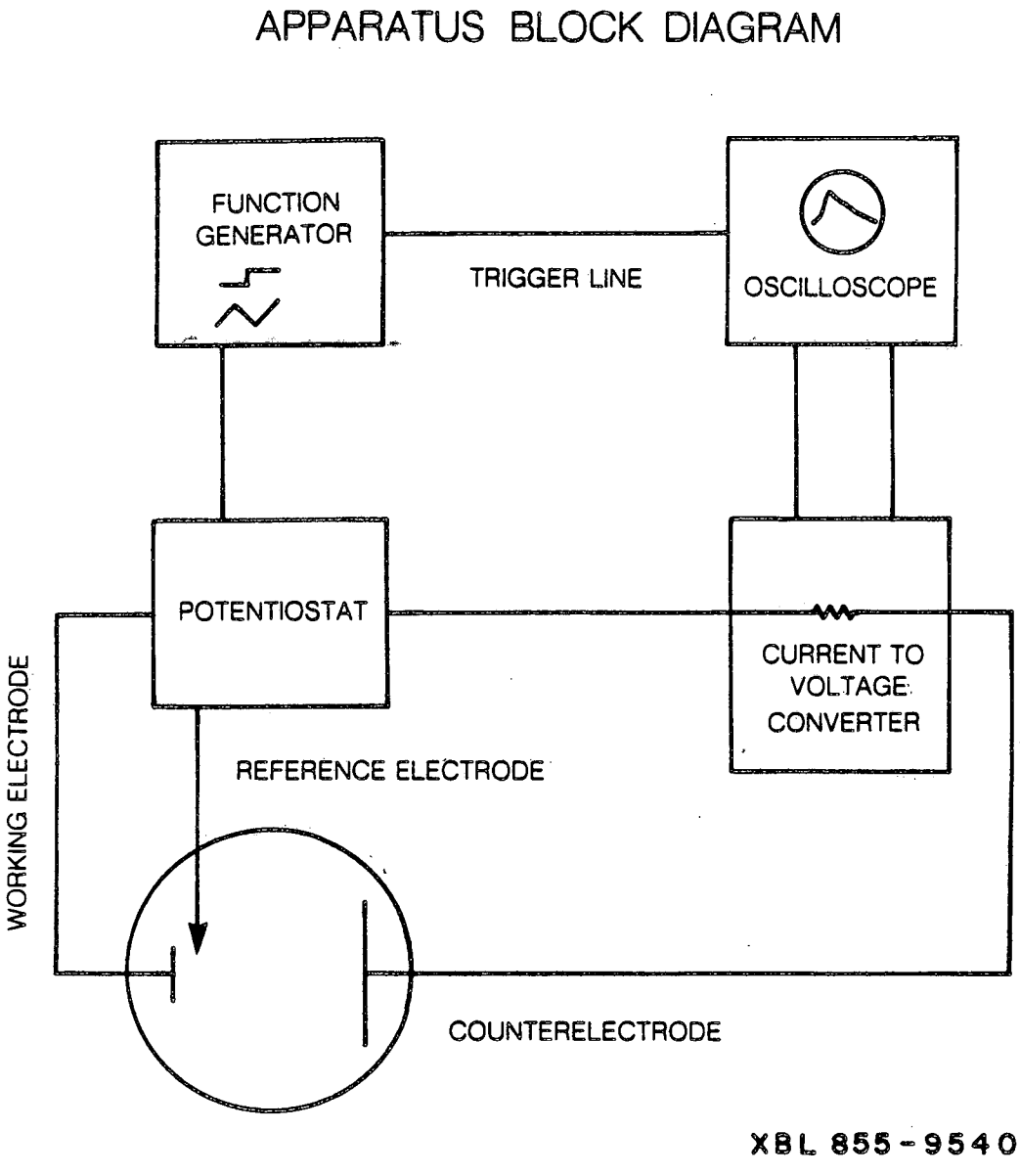


Figure 3-1: Apparatus Block Diagram.

Table 3-1: Selection of Electrocatalyst

Electrocatalyst	Smooth and Reproducible Surface?	Corrosion?	Takes on Polysulfide Redox Potential?	Comments
Cu	Yes	Very Rapid	No	Mixed Potential
Ag	Yes	Rapid	No	Mixed Potential
Mo	Yes	Yes	No	Film on surface
MoS_2	No	No	Yes	Grown by reaction of Mo disk with sulfur at 400 °C
Ni	Yes	Yes	Yes	Response changes with time due to visible surface corrosion
NiS	No	No	Yes	Pressed from powder
Co	Yes	No	Yes	No visible chemical corrosion even at elevated temperatures
Pt	Yes	No	Yes	Current response less than that of Co

The meter coil represents an extra inductance in the circuit which degrades the transient response of the system. The meter was shorted by a copper wire to remove this inductance. The pulse was applied by using an electronic switch on the function generator. The shape of this pulse was checked by placing a resistor across the output of the function generator and applying a pulse. The pulse was bounce-free and had a risetime of about 2.5 μs. The frame sync connector of the function generator supplied a pulse that triggered the oscilloscope at t=0. Potentials could be set with a precision of about $\pm$0.1 mV.

The transient current responses were stored on a Nicolet digital oscilloscope which at its maximum rate allows data to be recorded at 500 ns intervals. The full-scale output from the current monitor of the potentiostat was 10 mV, and the smallest current range was $\pm$200 μA. The most sensitive range on the ocilloscope was $\pm$100 mV. At small currents this led to a poor signal to noise ratio when the output of the current monitor was fed directly into the input of the oscilloscope. To increase the voltage signal for a given current level, the cell current was monitored via a resistor placed between the counter electrode and the potentiostat. Voltage-time

pairs were read directly from the screen via a cursor, and the voltages were converted to currents via Ohm's law. Typically 10 to 20 points were read for each transient.

The potentiostat/galvanostat was operated in the galvanostatic mode in order to obtain double layer capacity data and the ohmic potential drop in solution using the current step and current interrupt methods. The current step was applied between the working electrode and counter electrode, and the potential between the working electrode and reference electrode was monitored. The potential drop across the uncompensated solution resistance occurs almost instantaneously upon a change in current. This step change in potential was used in Ohm's law to evaluate the uncompensated resistance.

$$R_s = \frac{\left[V_{t=0_+} - V_{t=0_-}\right]}{i} \tag{3-21}$$

According the Newman (89), the resistance measured corresponds to that due to the primary current distribution. In the first few microseconds, the potential-time transient is dominated by ohmic and capacitative effects. The double layer capacitance was evaluated from the initial slope of the potential-time transient:

$$C_{dl} = \frac{i}{dV/dt} \tag{3-22}$$

Cells designed for use with methods such as potential step should have as uniform a current distribution as possible over the working electrode, and a low uncompensated resistance (90). Initial experiments were performed in a cell designed for use with a rotating disk electrode (see Figure 4-1). The uncompensated resistance between the working and reference electrodes was fairly high (on the order of 5 ohm-cm^2). The exchange current densities measured from the initial experiments were higher than expected based on previous steady-state results (15-17,51). High exchange current densities can only be determined accurately if the uncompensated resistance between the working and reference electrodes is low (81). This cell design was therefore abandoned in favor of one with a lower uncompensated resistance. A diagram of the final cell design used in these experiments is shown in Figure 3-2. The body of the cell is a 1/2" nylon

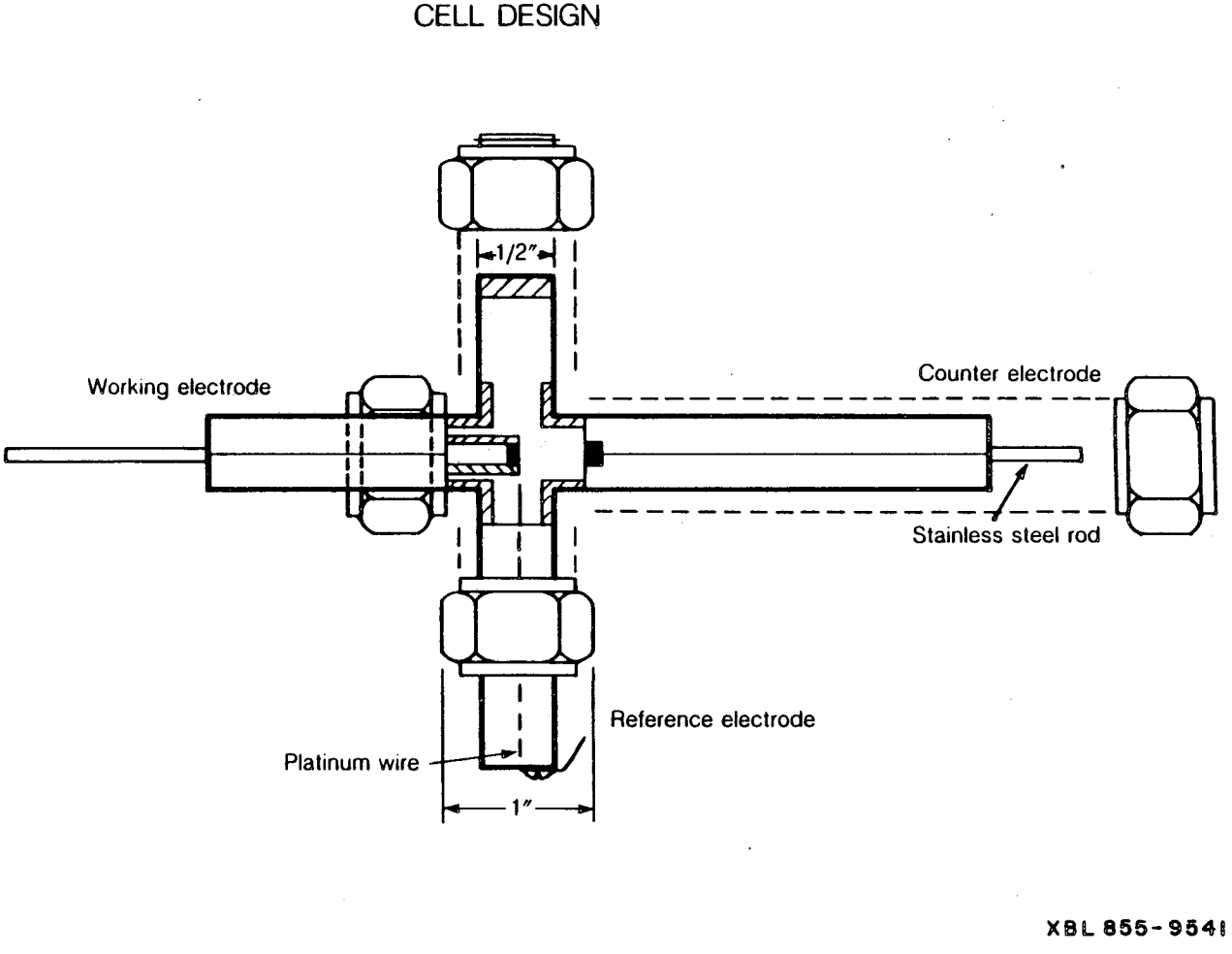


Figure 3-2: Cell design for potential step experiments.

tube cross. For operation at temperatures higher than ambient, a thermocouple was placed against the cell body, and the cell was wrapped in heating tape, asbestos pipe tape, and high-temperature furnace insulation. The temperature could be controlled within 0.2 °C for several hours by setting the power input to the heating tape.

Electrode Preparation

The working (0.2 cm^2 Co and 0.32 cm^2 Pt) and counter electrode disks were mounted in nylon rods. A hole was drilled in the back of each disk, and ohmic contact was made with a 3.16 mm stainless steel rod and silver epoxy (TRA-CON, TRA-DUCT BA-2902). For some initial experiments, this assembly was epoxied into the rod; however, due to different thermal coefficients of expansion among the different materials, the epoxy cracked allowing the corrosive polysulfide electrolyte to leak around the electrode and attack the ohmic contact. Silcone sealant (Dow Corning, Silastic 732 RTV) was found to work better due to its flexibility. Immersion tests of the cured sealant showed that it was resistant to the polysulfide electrolyte. In the final design, a PTFE heat-shrink tube was shrunk around the electrode disk. The ohmic contact was then made, and the silver epoxy was cured. Silicone sealant was placed in the electrode holder, and the electrode assembly was friction fitted into the nylon rod. The reference electrode was a platinum wire. The working electrode was placed in the center of the channel in order to minimize the ohmic drop between it and the reference electrode, and the electrodes were attached to the cell via ferrules to assure a leak-tight seal.

The mounted electrodes were pressed into a PTFE holder and then polished with a succession of silicon carbide and emery abrasives. The order was 240, 320, 400, and 600 grit silicon carbide paper with water as a lubricant and then 0000 grade emery paper with kerosene as a lubricant. The electrodes were rotated 90° after each grade of abrasive. A 10 inch polishing wheel was then covered with a nylon polishing cloth, and the electrodes were polished with 6 μm diamond paste. Final polishing was performed with 1 μm diamond paste using either a nylon or texmet (Buehler) polishing cloth. Kerosene was used a a lubricant for all polishing done with the

diamond paste. The electrodes were removed from the holder and cleaned in an ultrasonic bath with soapy distilled water to remove the kerosene and polishing material. The electrodes were rinsed with acetone and distilled water before use.

Electrolyte Preparation

The electrolyte was prepared by adding weighed amounts of 99.999% sulfur (Noah Chemical) and $Na_2S \bullet 9H_2O$ (ACS reagent-grade) to water (deionized, with resistivity greater than 1.2 MΩ-cm) which had been deoxygenated for at least one hour by bubbling argon through it. Argon was used to purge continuously the space above the solution during the dissolution of the Na_2S and S. Hydrogen sulfide (Matheson, C.P. grade, 99.5%) was bubbled through the electrolyte to adjust the pH and sulfur to sulfide ratio to the desired values. The pH was monitored by a pH electrode (Orion Research, Model 810200 combination electrode). The pH electrode was calibrated in standard buffers before use. The electrolyte was then quickly transferred to a volumetric flask fitted with a rubber septum. A slight vacuum was applied to degas the solution and fill any air space in the flask with argon. When an experiment was performed, the flask was slightly pressurized, and the electrolyte was transferred via a syringe. Provisions were made to introduce the electrolyte under a vacuum, and the cell was sealed to minimize contact of the polysulfide electrolyte with air.

The amount of zero-valent sulfur added to the electrolyte could be controlled accurately by weighing the solid sulfur on an analytical balance (precise to 0.1 mg), but there was a greater uncertainty in the concentration of sulfide present. A sample of solution was analyzed for total sulfur by oxidation to sulfate (91). A volume of polysulfide containing about 2 mmoles of total sulfur was accurately measured. This was added to about 100 ml of water which was made alkaline with 10 ml of NH_4OH. 1 to 2 ml of H_2O_2 then was added. After a few minutes, the solution turned from yellow to clear indicating that the sulfur and sulfide had been oxidized to sulfate. The solution was then heated to about 80 °C to drive off the excess ammonia and decompose the excess peroxide. After cooling, 16 ml of 3 M HCl was added. The solution was reheated to

boiling, and 5 ml of 0.5 M $BaCl_2$ was added dropwise. The solution was cooled slowly, and the $BaSO_4$ was collected in a tared Gooch crucible and washed at least 10 times with water to remove any excess $BaCl_2$. The crucible was heated in a muffle furnace at 200 °C and cooled in a dessicator. This was repeated until a constant weight was obtained. The total sulfur could be calculated by multiplying the weight of $BaSO_4$ by 0.1373 (91). The concentration of zero-valent sulfur was then subtracted from the total sulfur to determine the concentration of sulfide.

3.4. Results

Preliminary experiments were performed to check the operation of the equipment on a system with a known response. A 1 mM solution of $K_3Fe(CN)_6/K_4Fe(CN)_6$ in 1 M KCl was chosen. Figure 3-3 shows the response of the system and a non-linear least squares fit to Equation 3-18. More details on the non-linear least squares analysis and the computer implementation are presented in Appendix B. As can be seen from Figure 3-3, the fit is excellent over a time range of 35 msec. The diffusion parameter calculated using Equation 3-18 agreed to within 15% with one calculated using literature values of the diffusion coefficients at infinite dilution.

Experiments using the aqueous polysulfide electrolyte were performed over the temperature range of 25 to 80 °C. The electrolyte composition used in most of the experiments reported in this chapter is shown in Table 2-2. After introduction of the electrolyte, several minutes were required for the reference and working electrodes to reach the same potential. A potential step was applied only after the potentials differed from each other by less than 2 mV. The platinum reference electrode was checked against an SCE, and its potential was found to be that of the polysulfide redox couple. The SCE junction required cleaning after extended use in polysulfide electrolyte due to precipitation of HgS in the junction. The double-layer capacitance and ohmic resistance were measured, and data were taken only at times greater than $4R_sC_{dl}$, where capacitive current is expected to contribute less than 1% to the total current. Experiments with different potential step sizes were performed at each temperature. Figures 3-4 through 3-8 show some results of typical anodic and cathodic transients at different temperatures. An attempt was

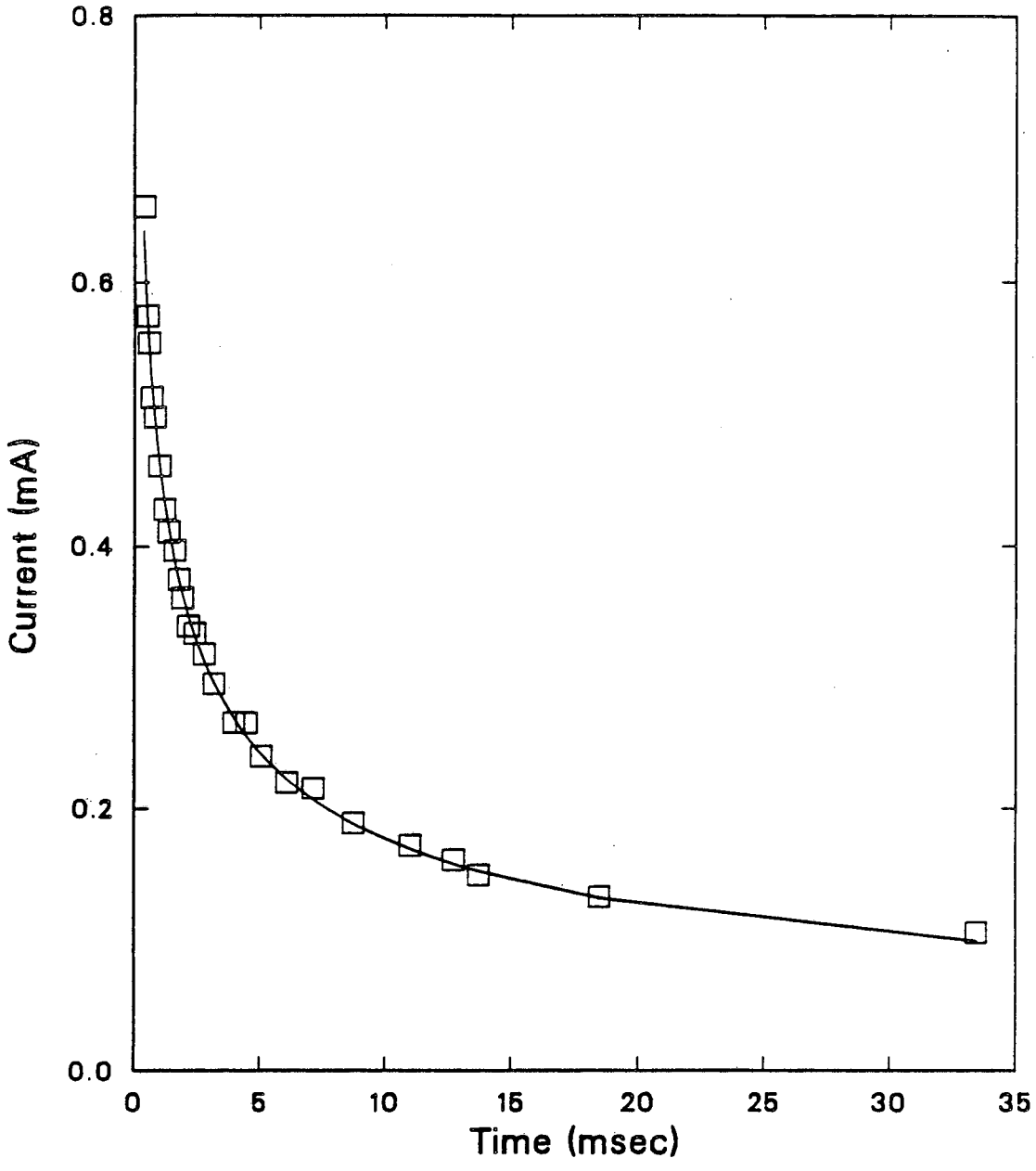


Figure 3-3: Transient current response for a 0.32 cm^2 Pt electrode in 1mM $K_3Fe(CN)_6/K_4Fe(CN)_6$-1M KCl electrolyte:
□, experimental data points for a 20 mV potential step;
_____, fit to Equation 3-18.

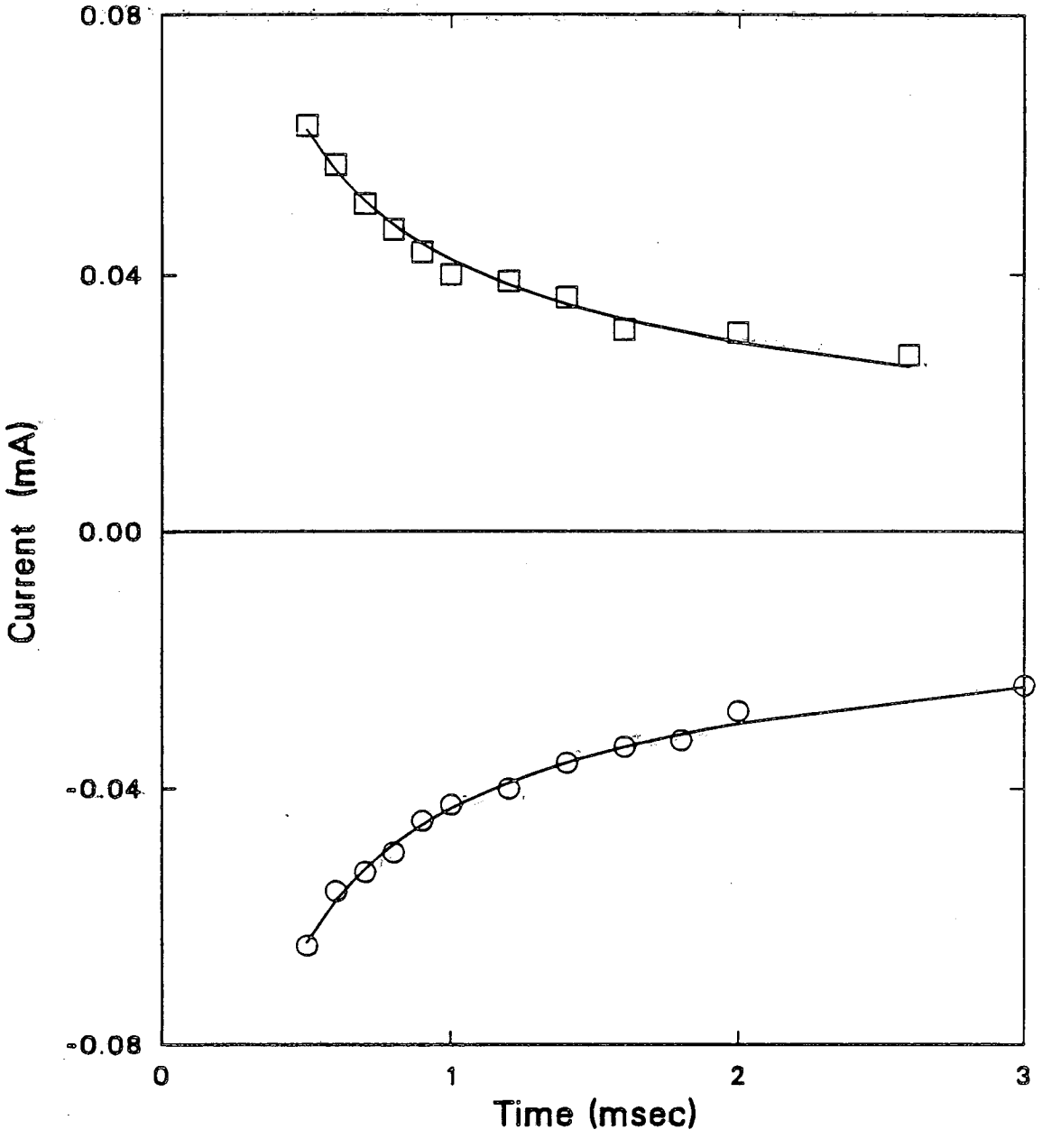


Figure 3-4: Transient current response to a potential step for a 0.2 cm^2 Co electrode in 1.3 M S^{2-}, 1 M S^0, pH=12 at 26 °C:
□, data for 19.9 mV;
○, data for -19.6 mV;
————————, fits to Equation 3-18.

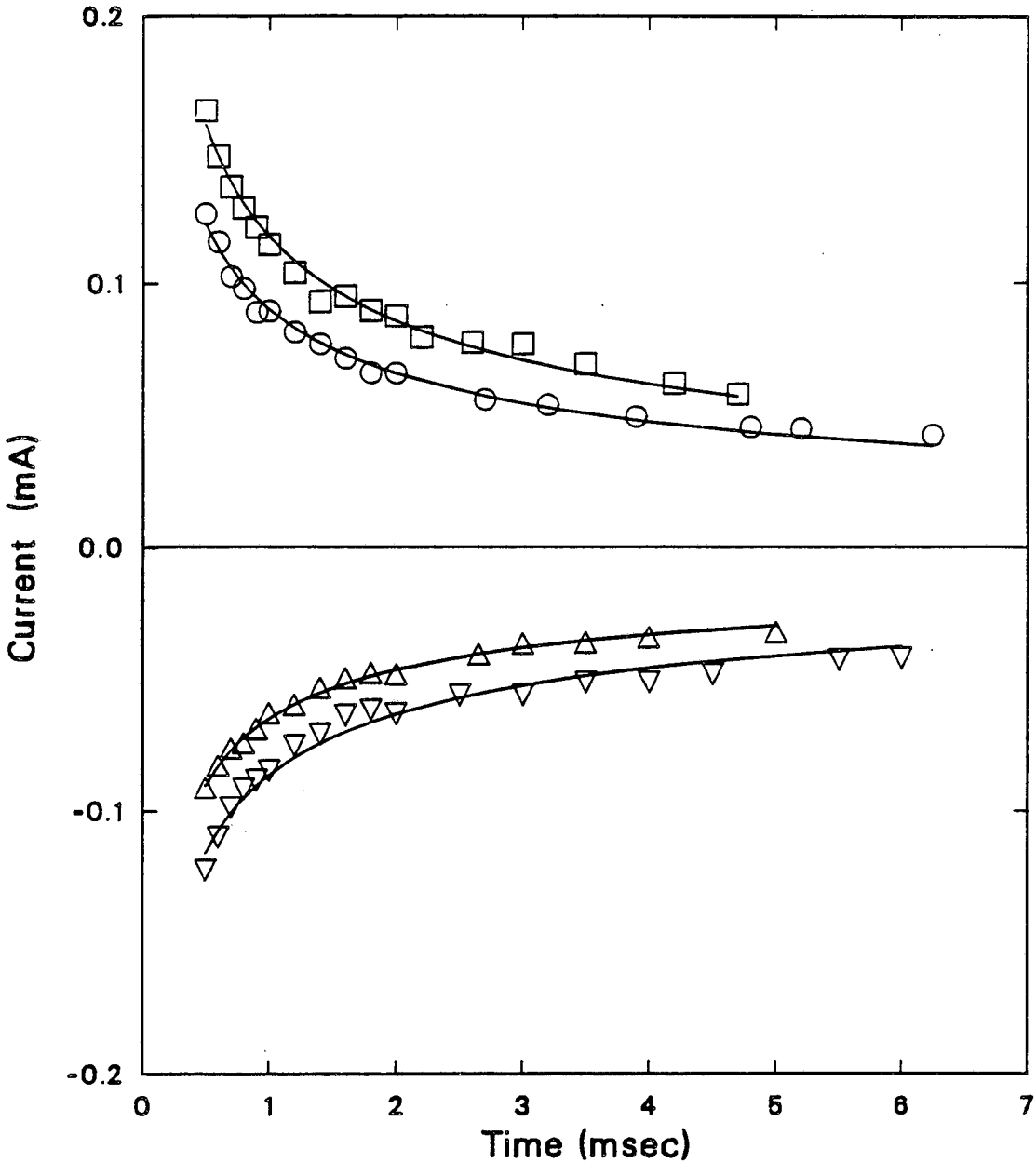


Figure 3-5: Transient current response to a potential step for a 0.2 cm^2 Co electrode in 1.3 M S^{2-}, 1 M S^0, pH=12 at 35 °C:
□, data for 25.0 mV;
○, data for 20.2 mV;
△, data for -15.0 mV;
▽, data for -20.0 mV;
_____, fits to Equation 3-18.

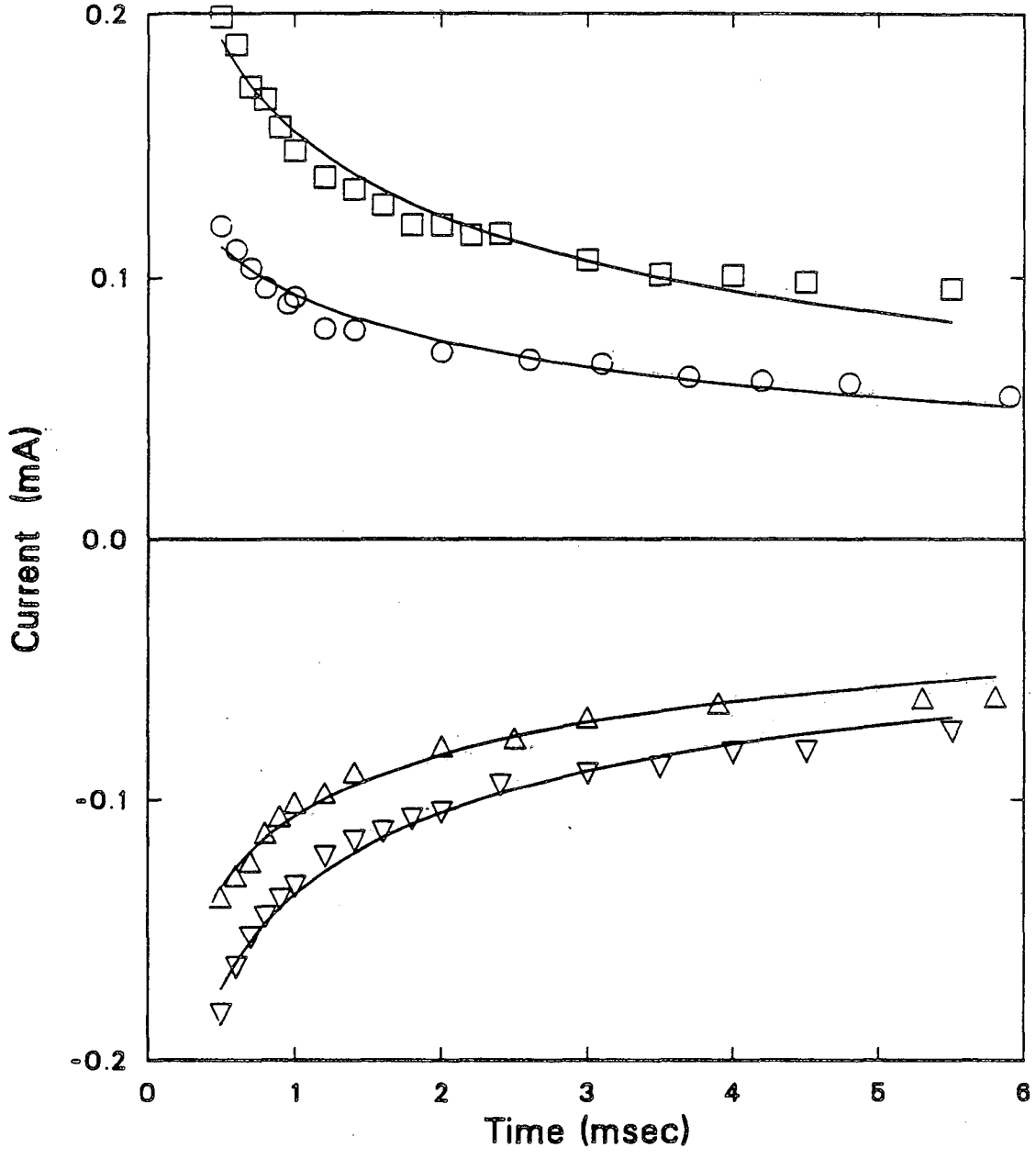


Figure 3-6: Transient current response to a potential step for a 0.2 cm^2 Co electrode in 1.3 M S^{2-}, 1 M S^0, pH=12 at 48 °C:
□, data for 25.0 mV;
○, data for 15.0 mV;
△, data for -19.9 mV;
▽, data for -25.1 mV;
_____, fits to Equation 3-18.

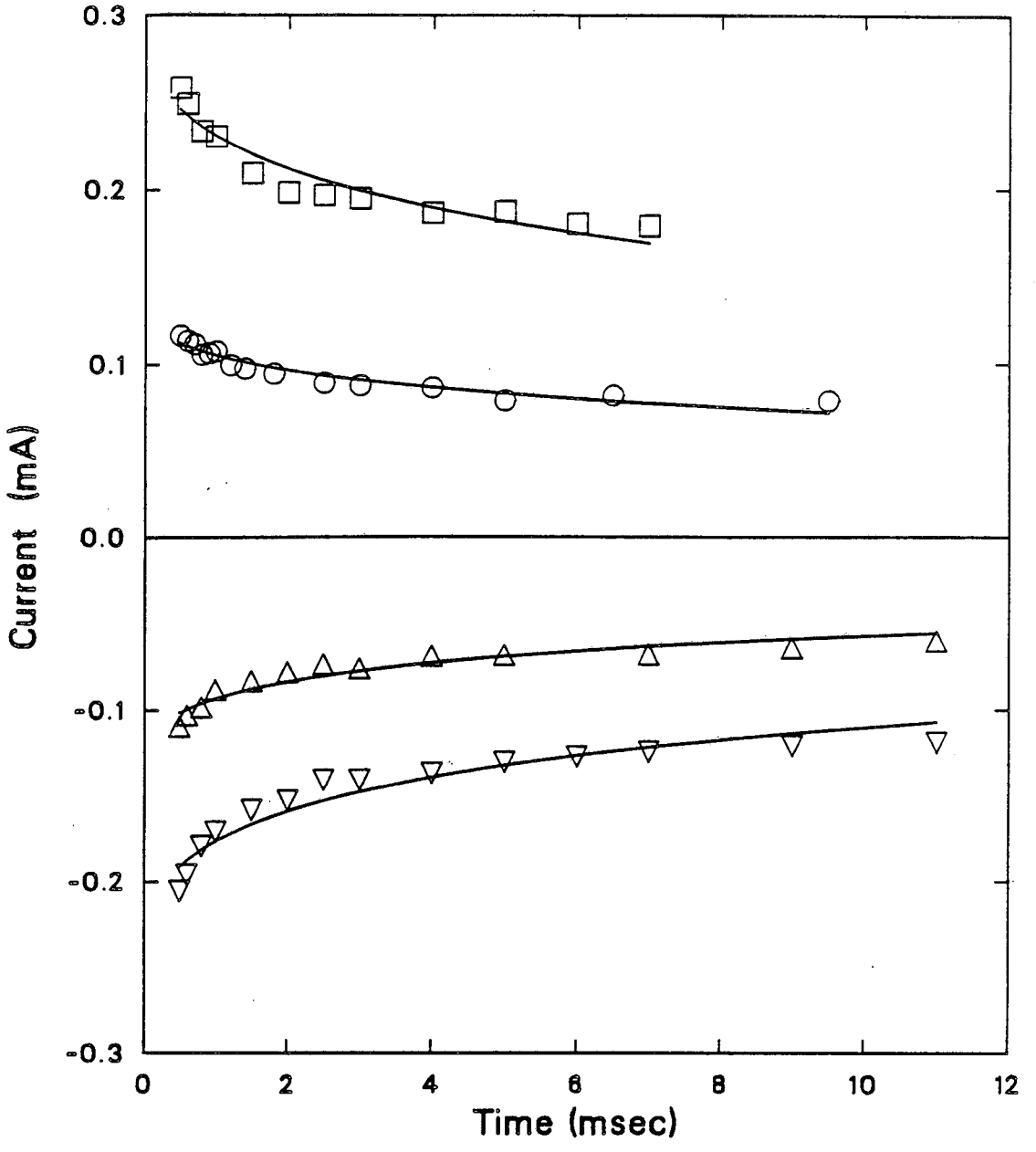


Figure 3-7: Transient current response to a potential step for a 0.2 cm^2 Co electrode in 1.3 M S^{2-}, 1 M S^0, pH=12 at 63 °C:
□, data for 19.9 mV;
○, data for 10.0 mV;
△, data for -10.0 mV;
▽, data for -19.0 mV;
————————, fits to Equation 3-18.

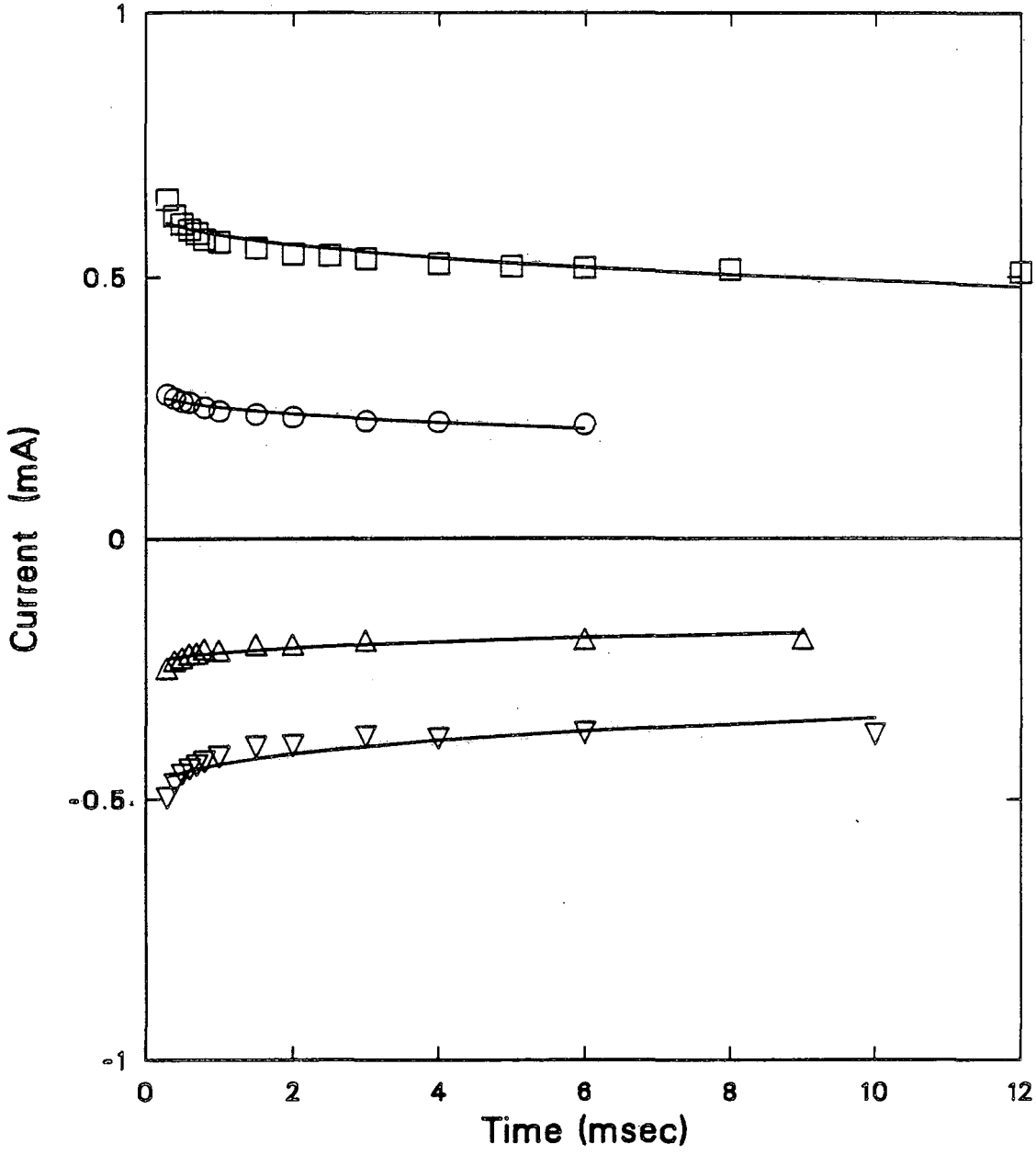


Figure 3-8: Transient current response to a potential step for a 0.2 cm^2 Co electrode in 1.3 M S^{2-}, 1 M S^0, pH=12 at 80 °C:
□, data for 20.0 mV;
○, data for 10.0 mV;
△, data for -10.0 mV;
▽, data for -20.1 mV;
————————, fits to Equation 3-18.

made to determine the exchange current density and diffusion parameter from each transient using Equation 3-18. In a few selected cases, multiple experiments were performed at a given temperature and step size. The current response was reproducible to within 5%.

At temperatures below 45 °C, a good fit could be obtained between the experimental data and Equation 3-18 in the time range of 0.5 to 10 ms. The diffusion parameter was obtained by a combination of Equations 3-3 and 3-4:

$$\left(\frac{s_o^2}{D_o^{1/2}C_{ob}}+\frac{s_r^2}{D_r^{1/2}C_{rb}}\right)=\frac{\lambda n^2 FV}{WRT} \tag{3-23}$$

A reproducible value of this quantity was obtained from all data sets, and at each temperature, but the values of λ and W were sensitive to the value chosen for t_2, the rise time of potential across the double layer, at lower temperatures. The total resistance R_s+R_r was obtained from Equation 3-3. The solution resistance was subtracted from the total resistance, and then the exchange current density was calculated from the reaction resistance:

$$\frac{i_o}{\nu}=\frac{RT}{nFR_r} \tag{3-24}$$

A check of the applicability diagrams published by Nagy (72) showed that the system was near to the edge of the applicability field at the lower temperatures.

At higher temperatures, the response curves became flatter, suggesting an increase in electroactive species concentration. Figures 3-7 and 3-8 show that the fits to the complete data sets become poorer as temperature increases.

The dashed lines in Figures 3-9 and 3-10 show the fit (using Equation 3-2) to the short-time data (less than 2 msec) of Figures 3-7 and 3-8. The fit is good, but the currents at longer times are consistently underestimated. Possible reasons for this are suggested in the discussion section.

An estimate of the active species concentration can be obtained from the diffusion parameter. Two assumptions are needed. First, the value of C_{rb} is assumed to be much greater than the value of C_{ob}. This is justified in the discussion below. Second, a value must be assumed for D_o. Values of diffusion coefficients are $O(10^{-5}$ cm^2/sec) for ions in room-temperature aqueous

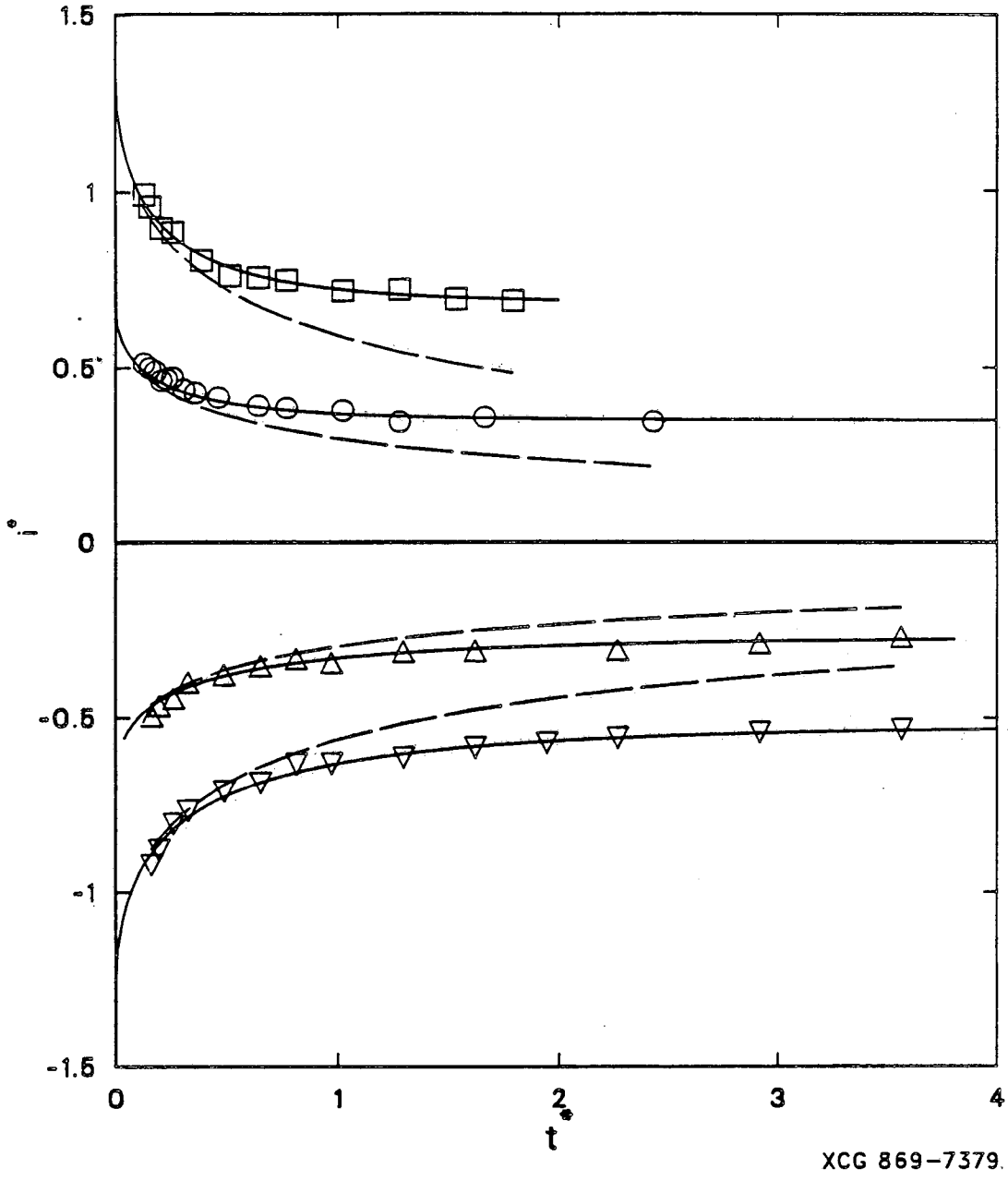


Figure 3-9: Transient current response to a potential step for a Co electrode at 63 °C: □, 19.9 mV; ○, 10.0 mV; Δ, -10.0 mV; ▽, -19.0 mV; — — — —, fit of short-time data to determine W and λ (see text); ————, computer model.

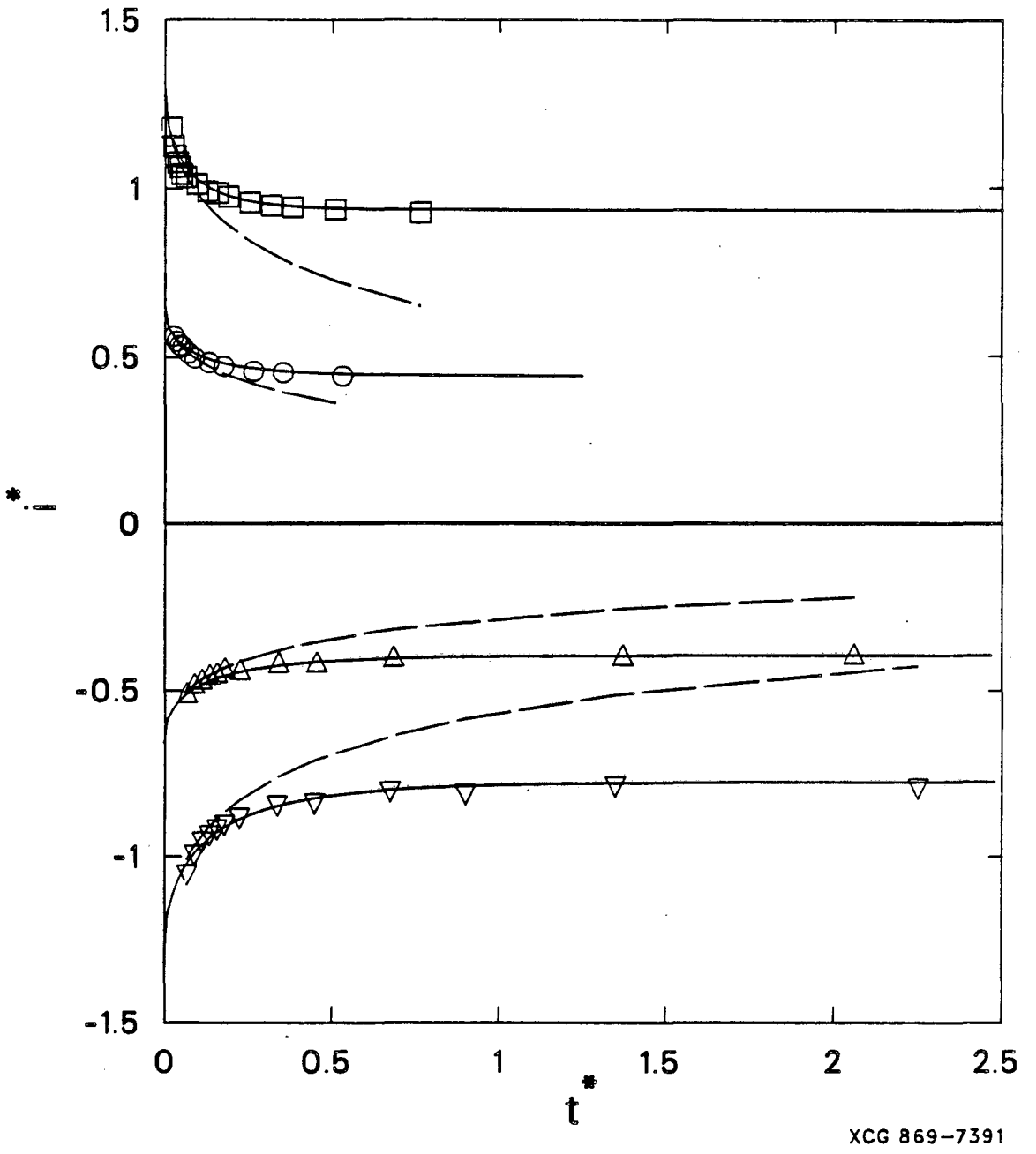


Figure 3-10: Transient current response to a potential step for a Co electrode at 80 °C: □, 20.0 mV; ○, 10.0 mV; Δ, -10.0 mV; ∇, -20.1 mV; — — — —, fit of short-time data to determine W and λ (see text); ————————, computer model.

solution (except for OH^- and H^+, which have higher diffusion coefficients). The diffusion coefficient tends to decrease as the solution becomes more concentrated. Two different values, $0.25x10^{-5}$ and $1x10^{-5}$ were assumed at room temperature. These values were adjusted for higher temperatures using the relation (92):

$$\frac{D\mu}{T} = \text{const} \tag{3-25}$$

with viscosity assumed to vary with temperature as the viscosity of water does (93):

$$\log\mu = \frac{658.25}{T} - \frac{1}{283.16} \tag{3-26}$$

Figure 3-11 shows the results of these calculations. The active species concentration is seen to be lower than any of the major polysulfide or monosulfide species, and it increases with increasing temperature with an apparent activation energy of about 10 kcal/mole.

Slow-sweep voltammetry was attempted in order to obtain kinetic and diffusion information. Observation of meaningful peaks was obscured by side reactions in both the anodic and cathodic directions. At the anodic diffusion peak, sulfur was deposited, and hydrogen was usually evolved on cathodic scan before a well-defined diffusion peak could be observed. Some potential step measurements were performed on platinum; the shapes of the transients were similar to those on cobalt, but the current densities were lower.

Fast potential sweep experiments (10 to 100 V/sec) were also performed. Figure 3-12a shows a sweep using 1 M polysulfide at a pH of about 14. The disk was a MoS_2 layer grown on a Mo disk (see Table 3-1). The total current is given by:

$$i_t = i_f + C_{dl}\frac{dV}{dt} \tag{3-27}$$

The total apparent resistance was obtained from Ohm's law. The solution resistance between the reference and working electrode was obtained from a current step (Figure 3-12b) and subtracted from the total resistance. After correcting for surface roughness, the derived reaction resistances on MoS_2 electrodes were of the same order of magnitude as those obtained from the fits to the potential step data on Co electrodes.

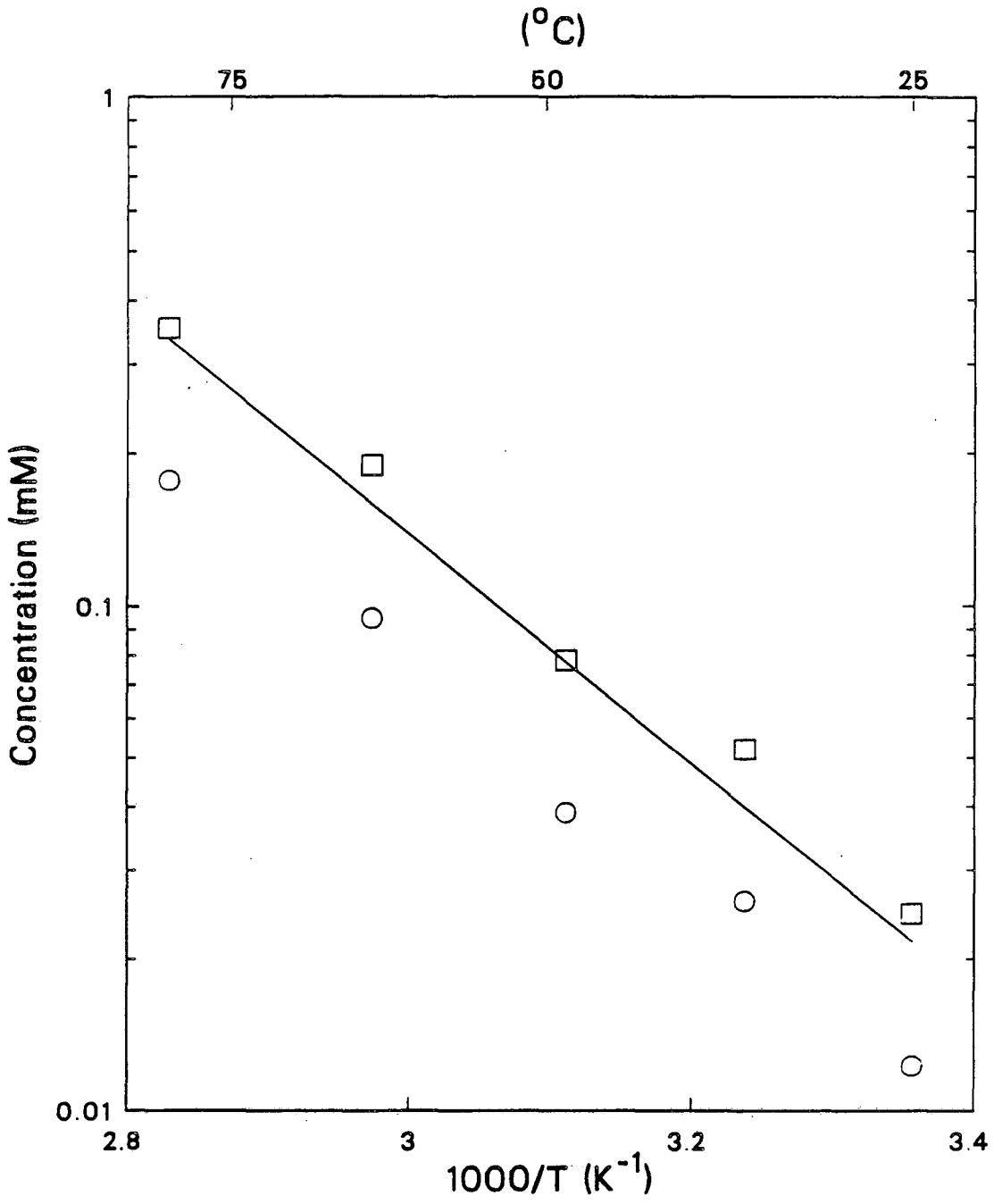


Figure 3-11: Active Species Concentration vs. Temperature:
———————, calculated from Equation 3-29;
○, calculated using experimental data and Equation 3-23 with D_o=1x10^{-6}cm^2/sec at 25 °C;
□, calculated using experimental data and Equation 3-23 with D_o=2.5x10^{-6}cm^2/sec at 25 °C.

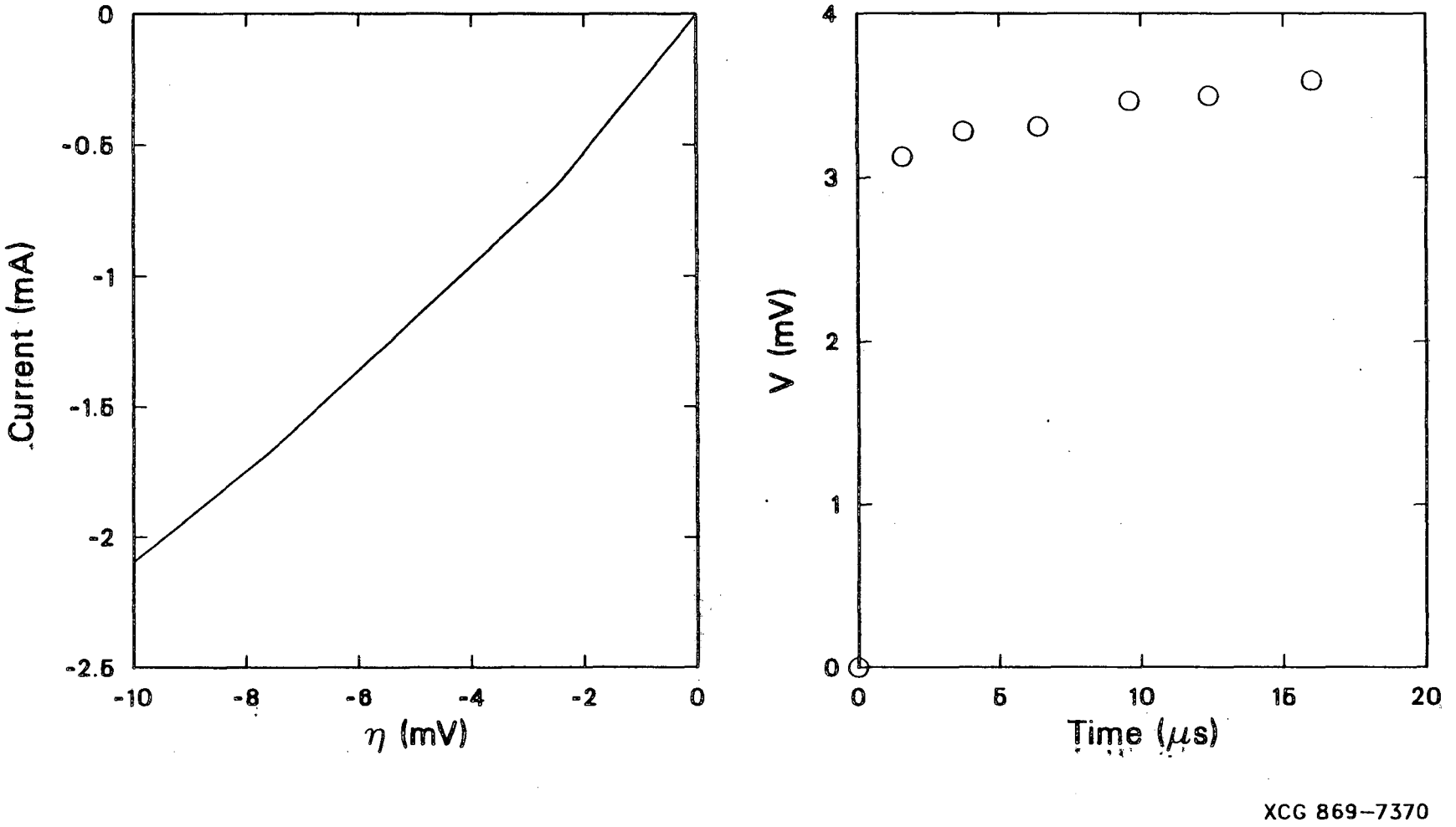


Figure 3-12: Voltage sweep and current step data at a 0.2 cm^2 MoS_2 electrode at 57 °C:
(a) 50 V/sec sweep
(b) 1.011 mA current step

3.5. Discussion

The analysis of Teder's (54) data in Section 2.2 suggested that Reaction 2-15 or a similar reaction could represent the overall polysulfide electrode reaction. Reaction 2-15 written on a per mole of zero-valent sulfur basis is:

$$\frac{1}{3}S_4^{2-} + \frac{4}{3}H_2O + 2e^- \rightleftarrows \frac{4}{3}HS^- + \frac{4}{3}OH^- \qquad (3\text{-}28)$$

It is apparent from Figure 3-11 that the calculated active species concentration is several orders of magnitude lower than that of any of the species appearing in Reaction 3-28. This leads to the conclusion that the electroactive species is none of the species in Reaction 3-28 nor is it in quasi-equilibrium with the species in Reaction 3-28 on the time scale used here.

Table 2-2 shows that there are five other species present in solution: S_2^{2-}, S_3^{2-}, S_5^{2-}, S^{2-}, and S_2^-. Because the concentration of the active species must be low and show a strong temperature dependence, only S^{2-} and S_2^- are possible candidates. The concentrations of the polysulfide ions are almost invariant with temperature and even the concentration of S_2^{2-} is too high by an order of magnitude.

Sulfide can be produced from bisulfide according to:

$$HS^- \rightleftarrows H^+ + S^{2-} \qquad (2\text{-}3)$$

This is the second dissociation reaction of hydrogen sulfide. Table 2-1 shows that the temperature dependence of Reaction 2-3 is about 6.5 kcal/mole.

Supersulfide can be produced from tetrasulfide:

$$S_4^{2-} \rightleftarrows 2S_2^- \qquad (2\text{-}8)$$

with a temperature dependence and equilibrium constant given in Table 2-1:

$$pK_d = \frac{4533}{T} - 6.42, \quad K_d = \frac{C_{S_2^-}^2}{C_{S_4^{2-}}} \qquad (3\text{-}29)$$

This represents a 10.3 kcal/mole activation energy for the temperature dependence of $C_{S_2^-}$, which is close to the temperature dependence of the active species concentration found from Figure 3-11. The line in Figure 3-11 shows $C_{S_2^-}$ predicted by Equation 3-29. The predicted

concentrations from Equation 3-29 are in close agreement with the derived concentrations if D = 0.25×10^{-6} cm^2/sec at 25 °C.

The deviations between Equation 3-18 and the experimental data can now be understood. At low temperatures and overpotentials, and for the time scales considered here, very little conversion of S_4^{2-} to S_2^- takes place (low rate of reaction and thin boundary layers). It is the S_2^- initially present that determines the response. As the temperature increases, the forward rate of Reaction 2-8 becomes a significant factor. However, at these low overpotentials it is not the sole rate-determining step. Thus the assumption of one rate-determining step used in deriving Equation 3-18 is not valid here, and deviations between Equation 3-18 and the experimental data are expected, especially at higher temperatures and longer times.

The reaction scheme can now be represented as Reaction 2-8 coupled to:

$$2S_2^- + \frac{4}{3}H_2O + 2e^- \rightleftarrows \frac{2}{3}S_4^{2-} + \frac{4}{3}HS^- + \frac{4}{3}OH^- \qquad (3\text{-}30)$$

At low overpotentials Reactions 2-8 and 3-30 occur at comparable rates. For shorthand in the following equations we represent S_4^{2-} as Y, S_2^- as O, and the products of Reaction 3-28 as R. R_i in Equation 3-6 can be written:

$$\frac{1}{2}R_o = R_y = k_f C_y - k_b C_o^2 \qquad (3\text{-}31)$$

S_4^{2-} is assumed to be electroinactive in the potential range of interest, giving a third boundary condition at the surface:

$$\left.\frac{\partial C_y}{\partial z}\right|_{z=0} = 0 \qquad (3\text{-}32)$$

It is convenient for numerical solution to make the time and distance dimensionless. The values of W and λ that would be derived if Reaction 2-8 were not a factor are used for this purpose:

$$t^* = \lambda^2 t \qquad (3\text{-}33a)$$

$$z^* = \frac{\lambda z}{D_o^{1/2}} \qquad (3\text{-}33b)$$

The concentrations are made dimensionless as:

$$C_i^* = \frac{C_i}{C_{ib}} \tag{3-34}$$

A summary of the material balance and boundary condition equations, details of the numerical methods used to solve these equations, and solutions for other homogeneous kinetic cases are given in Appendix C. In the general problem, four parameters that characterize the system need to be determined. They are W, λ, k_f, and k_b. Here we assume that k_f and k_b are related by the equilibrium constant of Equation 3-29:

$$k_b = \frac{k_f}{K_d} \tag{3-35}$$

This leaves three parameters to be determined. W and λ were found by a non-linear least squares fit to Equation 3-2 (see Appendix B). Data at short times were used; as $t \rightarrow 0$, Reaction 2-8 exerts a diminishing effect on the current response at the electrode. These values of W and λ were used to make the current and time dimensionless.

Assuming equal diffusion coefficients of S_2^-, S_4^{2-}, and the reaction products, four dimensionless parameters are needed to to calculate a computer-generated dimensionless current vs. time curve: V^*, C_{ob}/C_{rb}, K_d/C_{ob}, and k_f/λ^2. Since species R is much higher in concentration than supersulfide, C_{ob}/C_{rb} was assumed to be zero. K_d/C_{ob} was calculated from Equation 3-29, and V^* is determined by the size of the potential step. The forward reaction-rate constant (k_f) was then varied, and the computer-generated curves were compared to the experimental curves. Best agreement between the experimental data and the numerical calculations was found when the values of λ were increased slightly from the values obtained from the non-linear least squares fitting of Equation 3-2. This trend is expected because a smaller value of λ would be obtained by fitting Equation 3-2 to data influenced by Reaction 2-8. Figures 3-9 and 3-10 show samples of the calculated curves from the computer model and the experimental data at 63 and 80 °C. The agreement between the experimental data and computer-generated curves is very good. Table 3-2 lists the average values of k_f, k_b, and i_o obtained on cobalt electrodes at 63 and 80 °C.

Table 3-2: Summary of Rate Constants for Cobalt Electrodes

Temperature (°C)	k_f (sec^{-1})	k_b (liters/mole-sec)	i_o (mA/cm^2)
< 45	———	———	1
63	0.025	2.9×10^5	1.15 cathodic 1.21 anodic
80	0.13	3.3×10^5	2.54 cathodic 2.85 anodic

As mentioned in the results section, the anodic currents were higher than the cathodic currents for a given total overpotential. This leads to higher values of derived exchange current densities for the anodic potential steps. This is probably related to complexities in the reaction mechanism which are not accounted for by our model (which predicts a symmetrical response). A breakdown in the linear current density-overpotential assumption at some of the higher overpotentials employed (about 20 mV) could be one reason for this asymmetry. A change in reaction mechanism, as anodic overpotential is increased, is another possibility. The behavior of polysulfide solutions on Co and Pt electrodes outside the linear current density-overpotential region and possible complications in the reaction mechanism are discussed further in Chapter 4.

The values of k_b agree with those observed for other solution-phase dimerization reactions (94) (but are smaller those those for other dimerization reactions that are under purely diffusion control). The activation energy for k_f is about 22 kcal/mole, which is somewhat smaller than that measured (about 30 kcal/mole) for other solution-phase dissociation reactions (95). However, the uncertainties in the values of k_f are about a factor of 2. A change in the value of k_f by less than this amount would give an activation energy close to 30 kcal/mole.

The results presented here are in agreement with trends noted by other investigators. Increasing X_s (at constant sulfide concentration) lowers both the anodic and cathodic

overpotential at redox electrodes (15,17,51). Increased efficiency and stability of photoanodes has also been noted (46). In the composition range where these investigations were carried out, the predominant polysulfide species are S_3^{2-} and S_4^{2-}. Making the solution more sulfur-rich increases the concentration of S_4^{2-} at the expense of S_3^{2-}, which would increase the concentration of S_2^- according to Reaction 2-8. Decreasing the pH has also been reported to have beneficial effects on photoelectrochemical cell operation (13). In the composition ranges studied, this would also have the effect of increasing S_4^{2-} and therefore S_2^-.

The identification of supersulfide as the electroactive species suggests several modifications that could improve the kinetics at a redox electrode in addition to those mentioned above. One way of shifting the equilibrium in Reaction 2-8 toward supersulfide is to increase temperature. Photoelectrochemical cells are natural candidates for operation at elevated temperatures due to the large amount of waste heat produced by solar irradiation. While increased concentration of S_2^- would be beneficial, there are some disadvantages to increased temperature. The photocorrosion of the semiconductor, which is already a major problem near room temperature, may become a limiting factor at higher temperatures. As temperature increases, the open-circuit potential of liquid-junction photovoltaic cells decreases in a manner similar to that of solid-state photovoltaic cells (see Section 6.2). Finally, at elevated temperatures the degradation of polysulfides to thiosulfate increases as discussed in Section 2.1.

Another way of shifting the equilibrium of Reaction 2-8 toward the right would be to employ a solvent in which sulfur radical anions are stabilized relative to polysulfide ions. Aprotic, polar solvents such as dimethylformamide (DMF), dimethylsulfoxide (DMSO), and acetone have been shown to stabilize sulfur radicals (26). These solvents are stable over a wide range of potentials. However, the conductivity of such a solution is lower than that of an aqueous solutions, so higher ohmic losses might be a problem. A good strategy might be to employ the organic as a cosolvent in predominantly aqueous solutions. Results of investigations into mixed aqueous-organic electrolytes are discussed in Chapters 4 and 5.

3.6. Summary

The potential step method is a useful tool for obtaining kinetic and diffusion information at low overpotentials. This technique was used to investigate electrode reactions at the aqueous polysulfide-electrode interface. Several different species coexist in the aqueous polysulfide electrolyte (Table 2-2). Analysis of the current-time transients on Co electrodes showed that S_2^- was the electrochemically active species at low overpotentials. The conversion of S_4^{2-} into S_2^- (Reaction 2-8) affects the current response at higher temperatures and thicker boundary layers. A computer program, valid at small overpotentials, was written to model Reaction 2-8 coupled to a heterogeneous electrochemical reaction (see Appendix C). The rate constants of Reaction 2-8 were determined with the help of this model; they were similar to those measured for other dissociation-dimerization reactions.

The anodic and cathodic current-time transients were similar, but the anodic currents were slightly higher, and the transients were flatter. The computer model predicts a symmetrical response at low overpotentials. This suggests that the linear current-overpotential relation might be invalid under some of the conditions used here. A different reaction mechanism in the anodic and cathodic regions is also conceivable. These possibilities are discussed further in Chapter 4.

Chapter 4

Investigation of the Polysulfide Electrode Reaction by the Rotating Disk Method

4.1. Introduction

Photoelectrochemical cells require both an efficient photoelectrode and an efficient counterelectrode (see Chapter 1). The counterelectrode must support the same superficial current density as the photoelectrode. Typical operating current densities under normal solar illumination are 10 to 20 mA/cm^2. Since the open-circuit voltage of an aqueous polysulfide-based PEC is only about 500 to 800 mV, the total overpotential at the counterelectrode must be small. This total overpotential could include activation overpotential, concentration overpotential and ohmic losses. A reasonable design goal would be to support the required current density with less than a 10% loss at the counterelectrode. This loss would correspond to about 50 mV.

Steady-state data are needed to assess the effect of electrocatalyst, convection, and solution composition on the current density-overpotential curves. The transient data in Chapter 3 were obtained in the linear overpotential range of -25 to +25 mV. Data are also needed at higher overpotentials because 50 mV is outside the linear kinetic overpotential range, and in solutions with many species such as the polysulfide system the dominant mechanism may change with potential.

A practical counterelectrode might be a porous electrode, a flow-through porous electrode or a wire grid electrode depending on the cell configuration. It would be difficult to transfer design data gathered on one of these electrodes to an electrode of another type. Thus it was decided to use smooth electrodes of well-defined area to gather initial design data. The rotating disk electrode (rde) is a good choice to obtain steady-state data because it can be used under well-defined hydrodynamic conditions. Results of experiments on porous electrodes are discussed

in Chapter 5.

Sections 4.2 and 4.3 explain the experimental methods used and present the results obtained by use of the rde in polysulfide solution with and without the addition of an organic cosolvent. These results are discussed in Section 4.4 and Section 4.5.

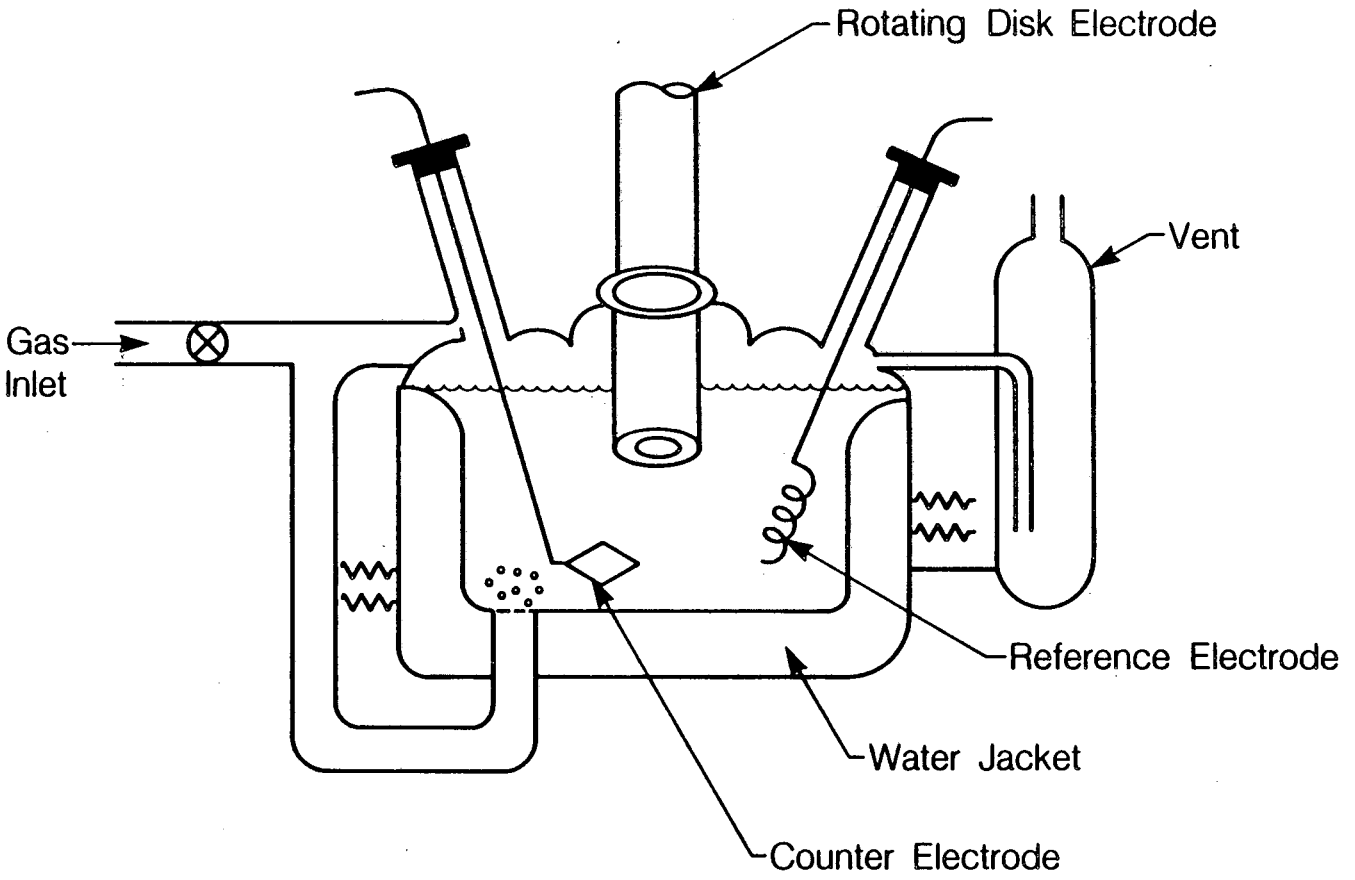
4.2. Experimental Procedure

A schematic diagram of the cell is shown in Figure 4-1. The cell is constructed of glass and has a provision for bubbling Ar through or over the solution. The cell is surrounded by a glass jacket, and cell temperature was controlled by pumping water through the jacket using a temperature controller (Techne Model TU-15). If the cell was held at a higher temperature (> 40 °C) for a significant time, there was a noticeable evaporation of solution. To solve this problem, the Ar was bubbled through a gas bubbler containing the same solution as the cell before being passed over the solution in the cell. The rotator was a Pine Instruments ASR2 capable of rotation speeds up to 10,000 rpm. A Hewlett-Packard Model 7045B X-Y recorder was used to record the steady-state data. For some experiments a PAR model 371 potentiostat/galvanostat and model 175 function generator were used. The characteristics of this equipment have been described in Section 3.3. Some other experiments were performed with a PAR model 273 potentiostat/galvanostat.

For measurements of solution resistance, both dc (current step) and ac (conductivity bridge) methods were used. The current step method was similar to that described in Section 3.3. The solution conductivity could be calculated from the measured resistance by using the relationship (96):

$$R_s = \frac{1}{4\kappa r} \tag{4-1}$$

This relationship is only strictly true when a primary current distribution prevails on the disk and the counter electrode is located infinitely far from the disk. At short times after a current step is applied, ohmic and double layer charging processes dominate, and thus Equation 4-1



XBL 868-10953

Figure 4-1: Diagram of Rotating Disk Apparatus

should allow a good approximation for κ to be calculated from the measured solution resistance.

For conductivity measurements using ac methods, a Wayne-Kerr autobalance universal bridge model B642 was used. This bridge supplies an alternating voltage at 1591.5 Hz. The bridge was used in conjunction with a Yellow Springs Instruments Co. model 3401 dipping conductivity cell. The cell constant was 1 cm^{-1}, and the cell electrodes were platinized Pt.

Both Pt and Co electrodes were used as electrocatalysts. The Pt electrode (Pine Instruments) was 0.8 cm in diameter (0.5 cm^2 area) and was surrounded by a PTFE sheath. The Co electrode was 0.5 cm diameter (0.2 cm^2 area) and was mounted in an interchangeable disk holder (Pine Instruments) with silicone sealant. Both electrodes were polished using procedures similar to those described in Section 3.3.

A Pt wire was used as the reference electrode. The counterelectrode was either a Pt foil or a porous graphite rod. Both these electrodes were positioned well outside the diffusion layer of the disk electrode.

Solution preparation was similar to that described in Section 3.3. For solutions that contained DMF as a cosolvent, the DMF and water were mixed in the correct proportion before dissolving the $Na_2S \cdot 9H_2O$, sulfur, and H_2S. The mole fraction of water, in the DMF-H_2O solvent, could be calculated from:

$$x_{H_2O} = \frac{V_{H_2O}\rho'_{H_2O}}{V_{H_2O}\rho'_{H_2O}+V_{DMF}\rho'_{DMF}} \qquad (4\text{-}2)$$

A sample of the water-DMF mixture was sent to the chemical microanalysis lab in the UC Berkeley College of Chemistry to determine carbon and nitrogen content (these components are present in DMF but not in water). Total sulfur content was determined by the methods described in Section 3.3.

4.3. Results

Experiments were performed using an aqueous polysulfide solution containing 1.3 M S^{2-} and 1 M S^0 at a pH of 12 (Table 2-2) and with polysulfides dissolved in a DMF-water mixture. Based on Equation 4-2 and an independent analysis of carbon and nitrogen, the mole percent of DMF in the mixture was 13%. The total concentrations of sulfur and sulfide were the same in both cases although the distribution of the sulfur-bearing ionic species would be expected to be different (see Section 4.5).

Figure 4-2 shows experimental current density-overpotential curves for Pt at 25 and 40 °C and a rotation rate of 1000 rpm. The potential of the working electrode was measured against a Pt reference electrode. The potential was scanned from -170 mV to 40 mV at a rate of 1 mV/sec. There is a difference in current density between the forward (positive-going) and backward (negative-going) scans (hysteresis) especially at higher cathodic overpotentials. The magnitude of the hysteresis depends on the starting point of the scan, the temperature, and the electrocatalyst used. The hysteresis decreased as the temperature was raised. In the following figures only the foward scans are shown unless otherwise noted. Figure 4-3 shows current density-overpotential plots for Pt at 60 and 77 °C. Figures 4-4 and 4-5 show analogous plots for Co. Data were taken primarily in the range of -100 to +50 mV because this was the interval of most interest for design of counterelectrodes for PECs.

Several important features of the plots should be noted. As temperature increases, two cathodic waves can be distinguished: a point of inflection occurs in the current density-overpotential curve at cathodic overpotentials. This point of inflection is most apparent on Pt electrodes at intermediate temperatures (Figure 4-2, the 40 °C curve). At temperatures above 60 °C on Pt (Figure 4-3), the current density-overpotential response is sublinear at cathodic overpotentials. In aqueous solution, Co is a better electrocatalyst than Pt: the current density at a given overpotential and temperature is higher on Co than on Pt. The inflection in the current density-overpotential curves is only noticeable above 60 °C on Co electrodes. At these tempera-

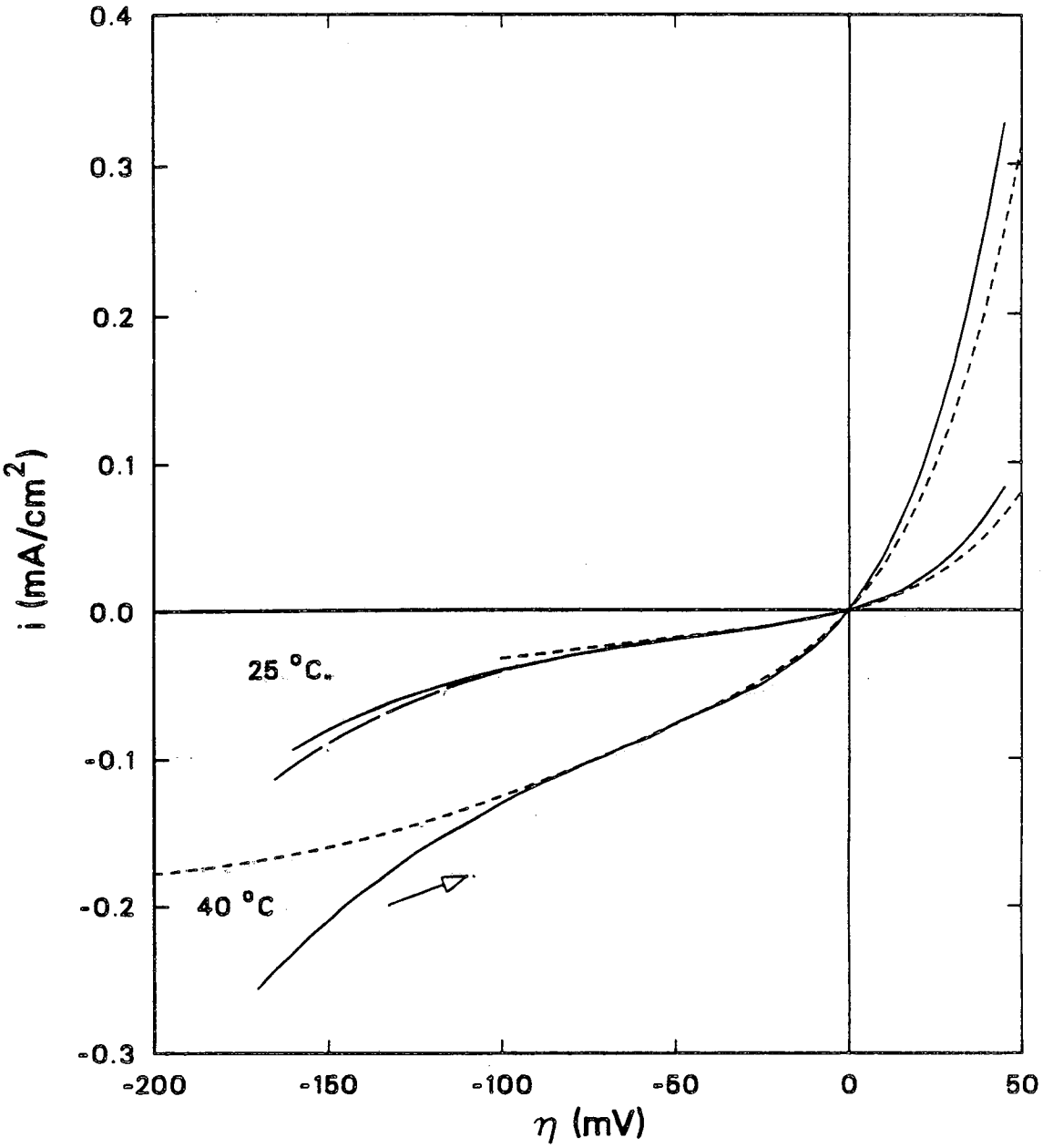


Figure 4-2: Current density-overpotential behavior for a Pt rde at 1000 rpm in 1.3 M S^{2-}, 1 M S^0, pH=12:
———————, experimental data;
— — — — —, backward (negative-going) scan;
———————, computer simulation.

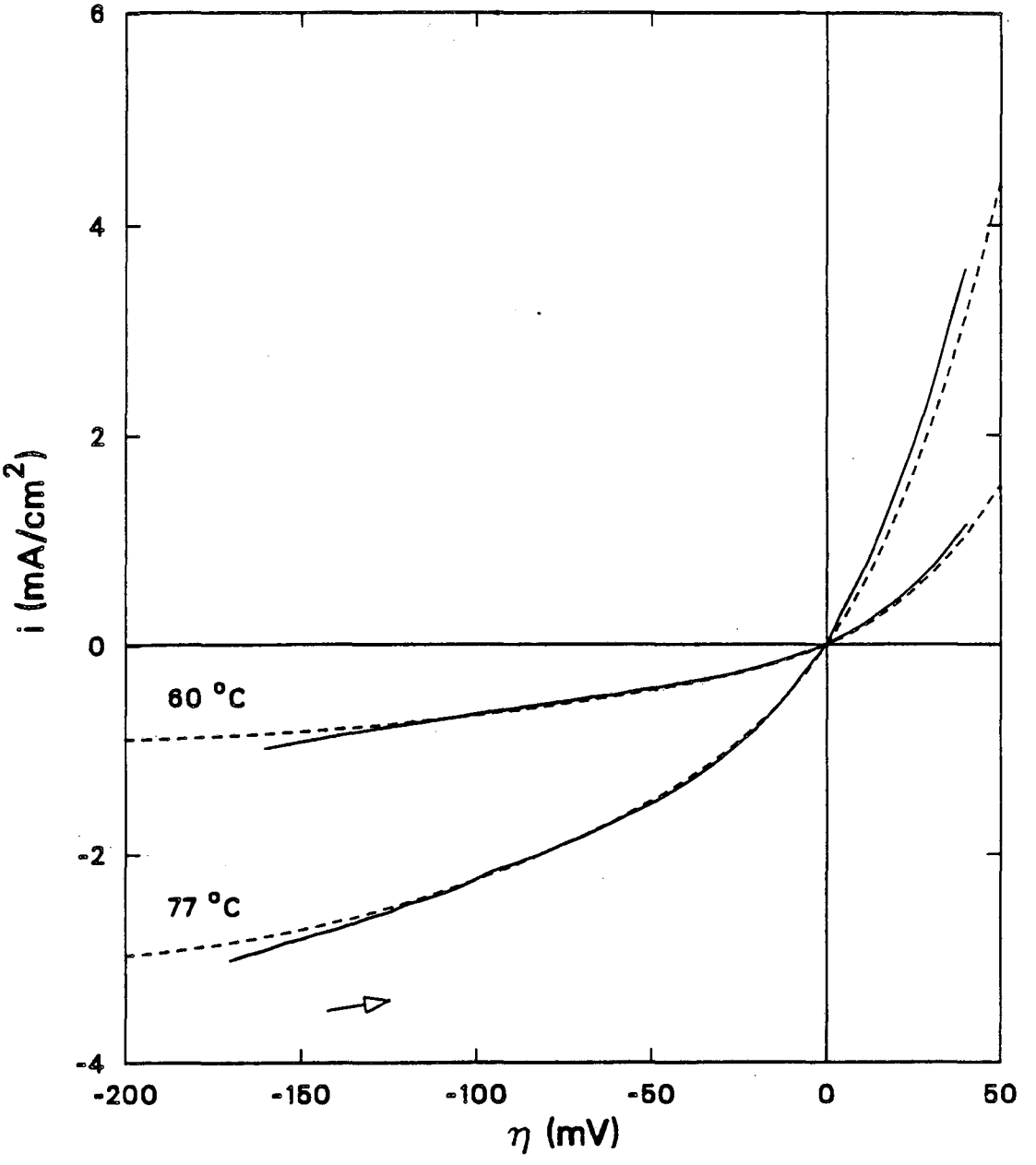


Figure 4-3: Current density-overpotential behavior for a Pt rde at 1000 rpm in 1.3 M S^{2-}, 1 M S^0, pH=12:
———————, experimental data;
– – – – – – – – – –, computer simulation.

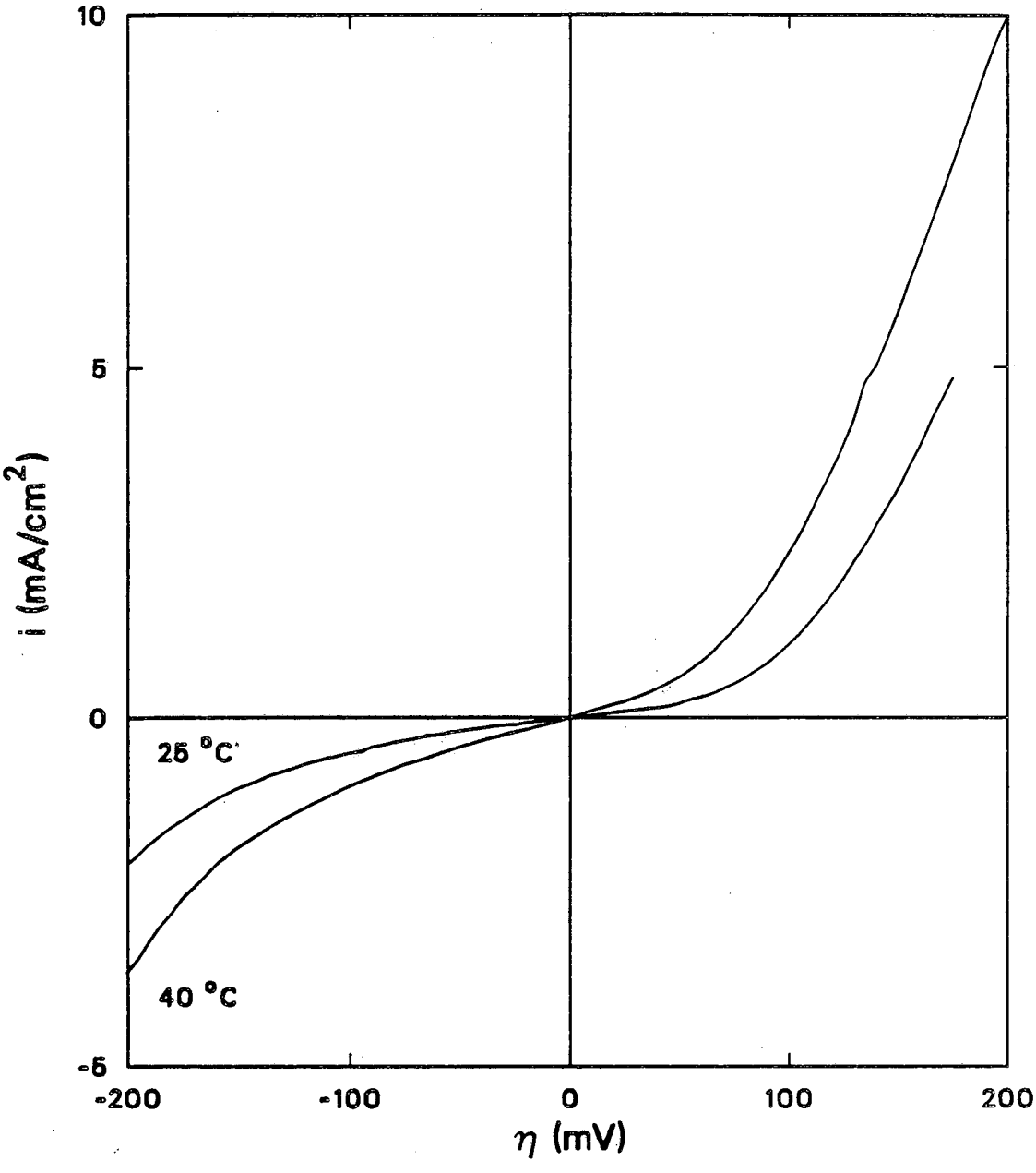
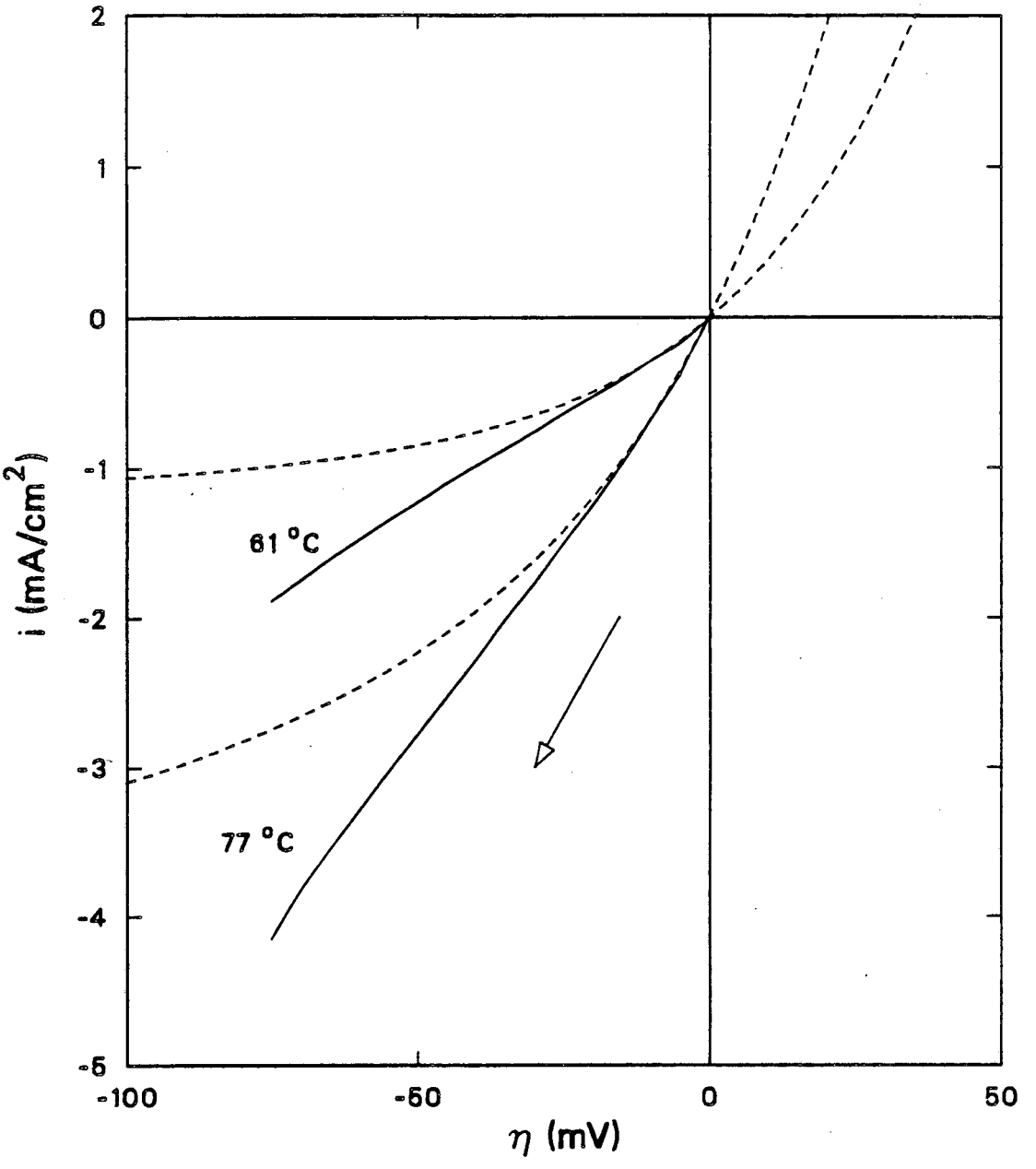


Figure 4-4: Current density-overpotential behavior for a Co rde at 400 rpm in 1.3 M S^{2-}, 1 M S^0, pH=12.



XCGT 869-7371

Figure 4-5: Current density-overpotential behavior for a Co rde at 1000 rpm in 1.3 M S^{2-}, 1 M S^0, pH=12:
———————, experimental data;
– – – – – – – – – –, computer simulation.

tures, the onset of the second cathodic wave occurs at lower overpotentials on Co than on Pt. This second cathodic wave is not due to hydrogen evolution:

$$2H_2O + 2e^- \rightleftharpoons H_2 + 2OH^- \quad (4\text{-}3)$$

In the pH 12 electrolyte used here, Reaction 4-3 has an equilibrium potential of about -0.71 V vs the SHE. The measured rest potential of the polysulfide solution was -0.70 V vs. the SCE (or about -0.46 V vs. the SHE). Hydrogen evolution is therefore not possible until an overpotential of greater than 250 mV is reached. By visual observation of the electrode surface, it was found that hydrogen evolution did not begin to take place until overpotentials somewhat greater than about 300 mV were reached. No limiting current was reached before solvent decomposition took place.

The anodic branch of the current density-overpotential curve shows quite different behavior. The current continued to rise until bulk sulfur was deposited, and sulfur oxyanions began to be produced (50,51). Therefore, overpotentials above 200 mV were avoided in the anodic scans. The anodic current density is higher than the cathodic current density at the same absolute value of overpotential. Similar behavior was reported by Remick and Camara (17). Plots of log(i) vs. η are shown in Figure 4-6. The plots are linear in the range of 50 to 120 mV. The data were fit to the Tafel equation:

$$\eta = \frac{RT}{\alpha_a F}[\ln(i) - \ln(i_o)] \quad (4\text{-}4)$$

in this range of overpotentials. The Tafel equation is a simplification of Equation 3-12; it is valid at high enough overpotentials so that one of the exponential terms in Equation 3-12 can be ignored. The value of exchange current density on Co is 50 $\mu A/cm^2$ whereas on Pt it is 15 $\mu A/cm^2$. The derived value for α_a on Pt is 1.0 while on Co it is 0.8. The derived values of α_a and i_o are consistent with the results reported by Allen and Hickling (51). At higher overpotentials, the slope of the curves decreases. The current densities on Pt and Co become nearly equal above 125 mV. Allen and Hickling (51) found similar behavior on Au, W, and Ni electrodes.

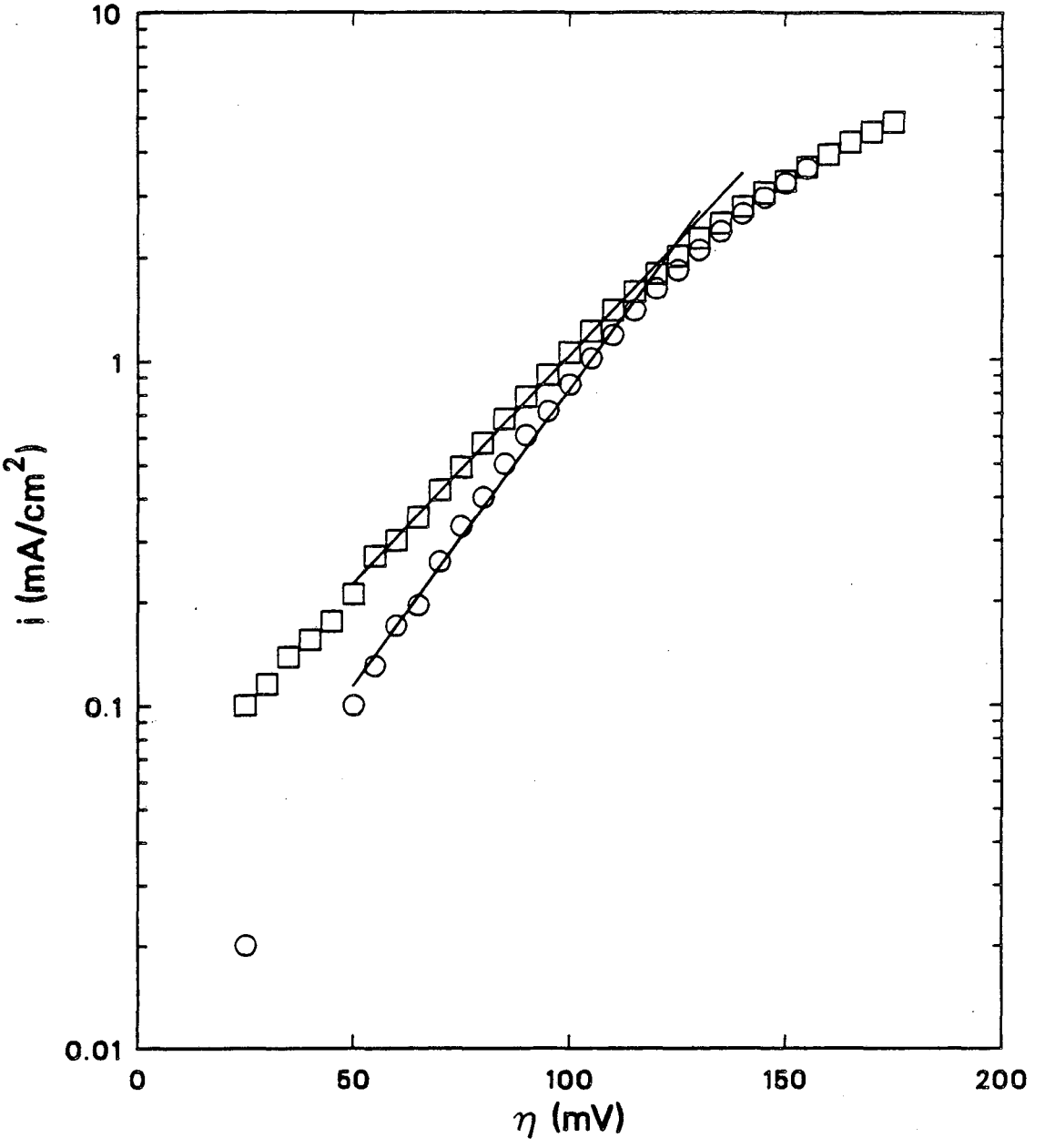


Figure 4-6: Current density-overpotential behavior at rde, 25 °C, 400 rpm:
○, Pt electrode;
□, Co electrode;
————————, regression line.

There is little effect of rotation speed on the response at Co and Pt electrodes, from 400 to 3600 rpm. The only significant effects of convection in the cathodic branch were on the second cathodic wave at 61 and 77 °C.

The addition of 13 mole-% DMF increases the current density at a given temperature and overpotential on both Co and Pt electrodes. Figures 4-7 and 4-8 show the response at Co and Pt electrodes over the temperature range of 25 to 77 °C. At 60 °C and -50 mV, the current density on Co is increased from -1.2 to -3.0 mA/cm^2 (an increase by a factor of about 2.5). The addition of DMF has even a greater effect on the response at Pt electrodes. In aqueous solution, Co was a much better catalyst than Pt, but in the water-DMF mixture, the current density-overpotential response for both catalysts is nearly the same. The first cathodic wave and the sublinear response are much more pronounced in the DMF-water mixture. This change in shape is most noticeable on Co at lower temperatures (compare Figures 4-4 and 4-7). Raising the temperature of the pure aqueous system and adding DMF have analogous effects on the shape of the cathodic curve. At 77 °C the current density-overpotential curve is almost straight over the entire potential range studied. Both the aqueous and the DMF-water solutions became visibly darker as temperature increased. At 77 °C the DMF-water solution was dark blue, and this color change was reversible.

The conductivity of the polysulfide solutions with and without the addition of DMF were measured as described in Section 4.2. Figure 4-9 shows a plot of log(κT) vs. 1/T. As expected, the conductivity of the solution without the addition of DMF is greater. At 25 °C the conductivity of the pure aqueous solution is 0.09 Ω^{-1}cm^{-1} versus 0.04 Ω^{-1}cm^{-1} for the solution with 13 mole-% DMF. The conductivity rises with an activation energy of about 4 kcal/mole for both solutions.

4.4. Discussion

One possible explanation for the shape of the steady-state current density-overpotential curves is that a single electrode reaction with unequal anodic and cathodic transfer coefficients is

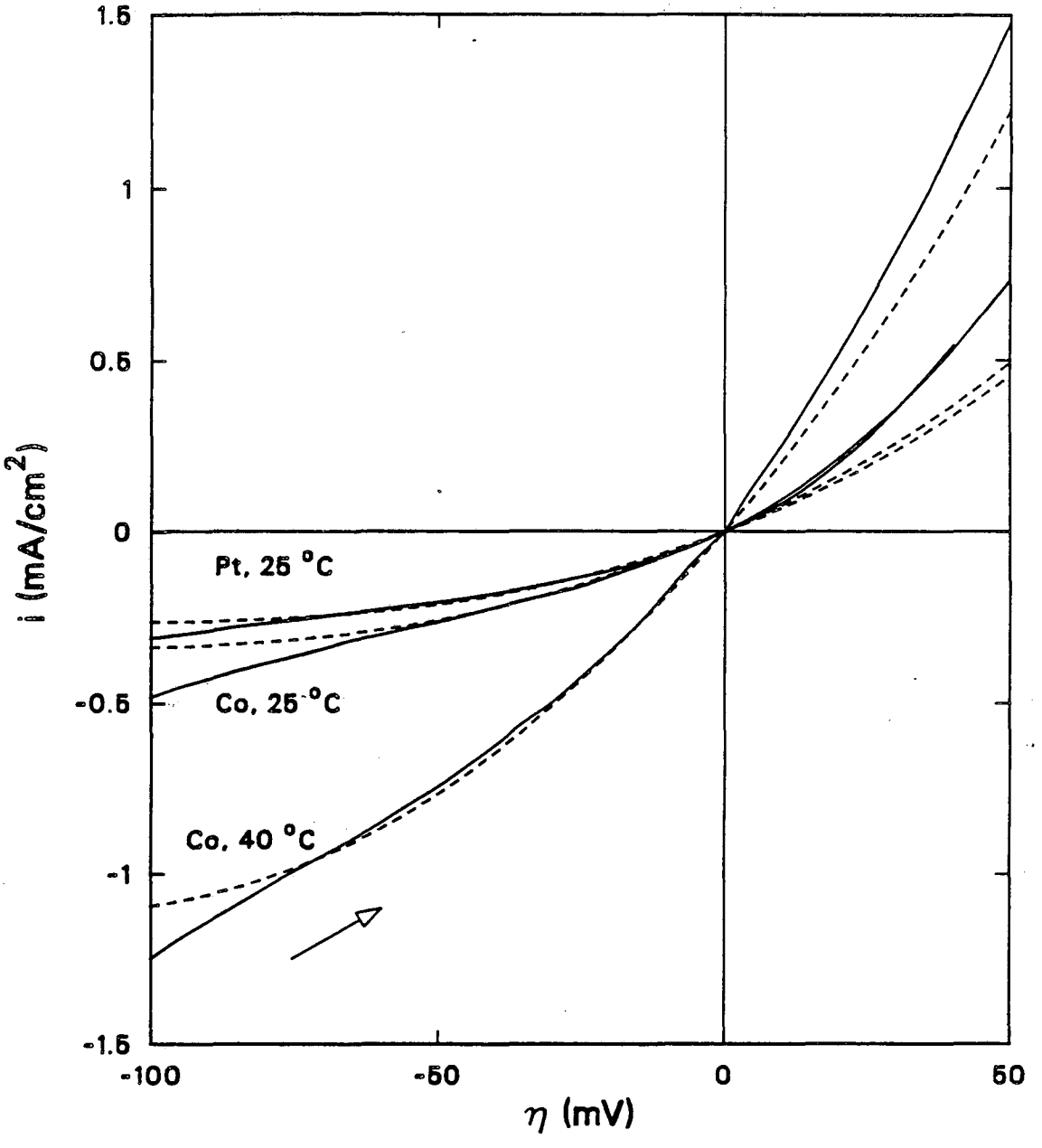
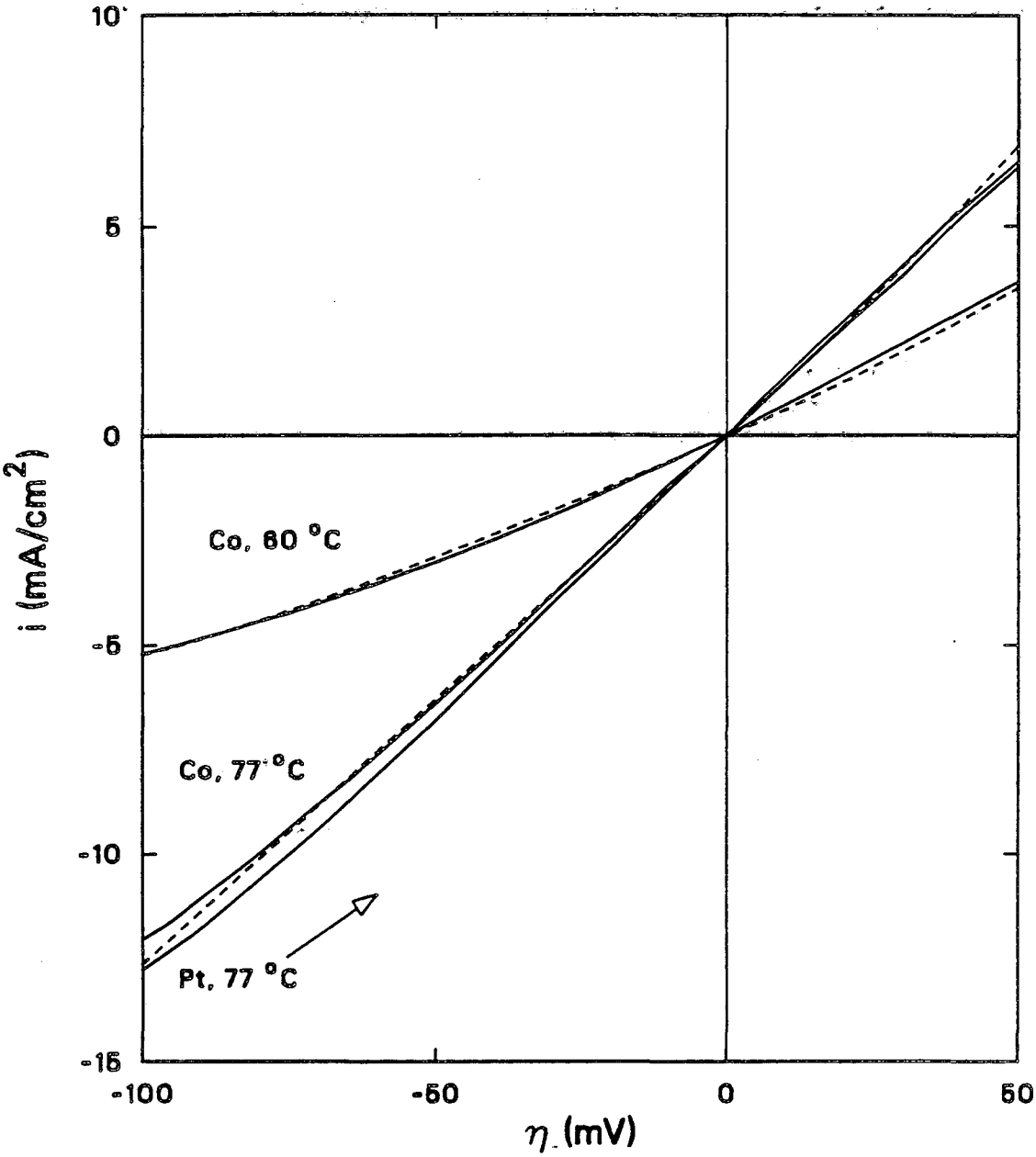


Figure 4-7: Current density-overpotential behavior at rde in 1.3 M S^{2-}, 1 M S^0 with 13 mole-% of DMF as a cosolvent at 1000 rpm:
_____, experimental data;
- - - - - - - - - -, computer simulation.



XCG 869-7396

Figure 4-8: Current density-overpotential behavior at rde in 1.3 M S^{2-}, 1 M S^0 with 13 mole-% of DMF as a cosolvent at 1000 rpm:
———————, experimental data;
– – – – – – – – – –, computer simulation.

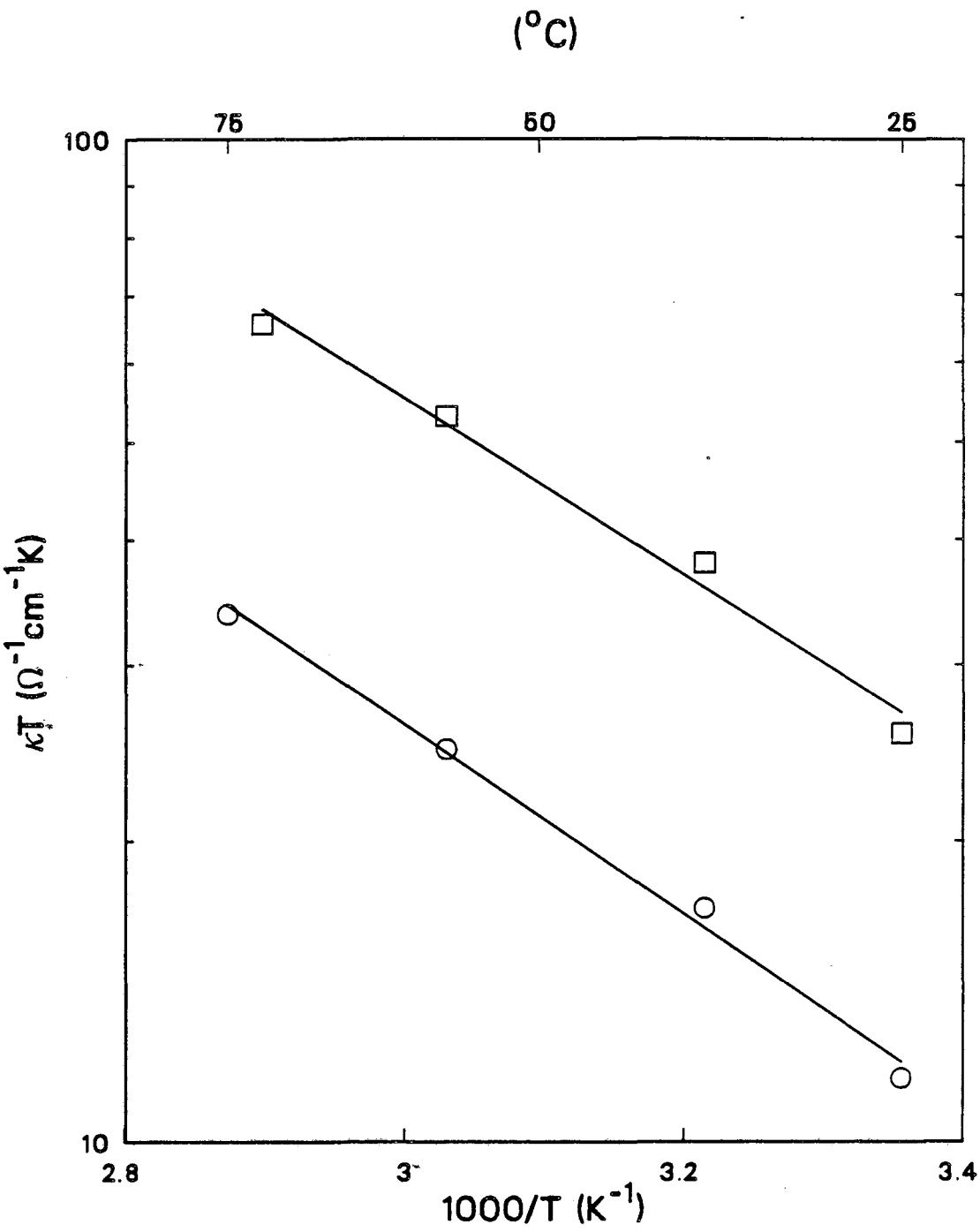


Figure 4-9: Conductivity of 1.3 M S^{2-}, 1 M S^0 solutions:
□, Aqueous (pH=12);
○, 13 mole-% DMF added.

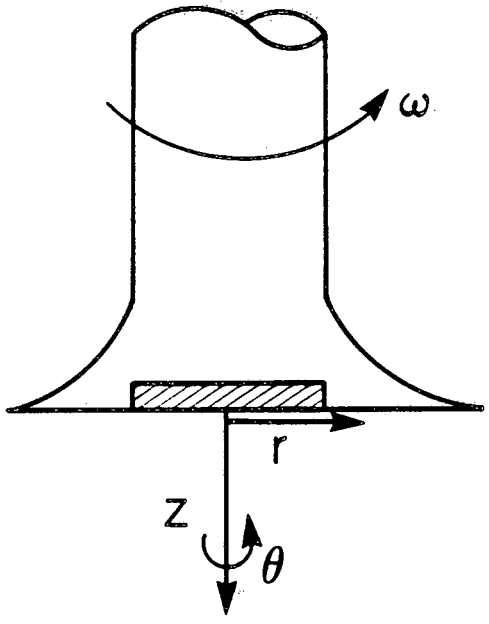
occurring. An electrode process obeying Equation 3-7 will have a point of inflection at:

$$\eta = \frac{2RT}{F} \frac{\ln\left(\alpha_c/\alpha_a\right)}{\left(\alpha_a+\alpha_c\right)} \tag{4-5}$$

If $\alpha_a=\alpha_c$, the point of inflection occurs at $\eta=0$ and the familiar $\sinh(\eta)$ behavior is observed. For $\alpha_c<\alpha_a$, the point of inflection occurs in the cathodic branch of the curve. Equation 4-5 predicts that for $\alpha_c=0.5$ and $\alpha_a=1.5$ the point of inflection will move more cathodic by 5 mV when the temperature goes from 25 to 80 °C. Figures 4-2 through 4-5 show the change with temperature is much greater than this.

Another possibility is that two electrode processes occur over the range of cathodic potentials studied. The sublinear response at small cathodic overpotentials could be due to a mass transfer or homogeneous kinetic limitation. Almost no effect of varying the rotation rate was found at these small cathodic overpotentials. The results of Chapter 3 suggest that the cathodic current response at the cobalt electrode is limited by a homogeneous reaction in solution and heterogeneous charge transfer at the interface. A model for these processes valid in the rotating disk electrode system will now be developed.

Figure 4-10 shows a schematic representation of the coordinate system and the velocity field around a rotating disk electrode. The disk is surrounded by an insulating sheath and rotates about its axis with an angular velocity ω. The rotating fluid is swept toward the disk and then expelled in the radial direction. The most convenient coordinate system to represent the hydrodynamic and mass transfer problem is cylindrical coordinates. The three velocity components, v_r, v_ϕ, and v_z plus the dynamic pressure P all are non-zero. Four partial differential equations (the continuity equation plus the three components of the Navier-Stokes equations) specify the system. Von Kármán (97) used a separation of variables scheme to reduce the four PDE's to four non-linear ODE's. White *et al.* (98) present several alternative methods for the solution of these equations.



XBL 868-10955

Figure 4-10: Rotating Disk Electrode Coordinate System.

The velocity component in the z direction depends on z only and not on r or θ. In the absence of edge effects, the concentration profile would be expected to depend only on z (99). If we assume steady-state and the absence of migration, then Equations 3-5 and 3-6 can be combined to give:

$$v_z \frac{dC_i}{dz} = D_i \frac{d^2C_i}{dz^2} + R_i \tag{4-6}$$

The boundary conditions far away from the disk can be represented by Equation 3-17. The boundary conditions at the disk surface will depend on the particular system being considered.

If $R_i=0$, then Equation 4-6 can be integrated, and C_i can be solved for in terms of two constants which are determined by the boundary conditions. For some simple cases of the Butler-Volmer equation, an explicit representation can be found for the current (100). This can lead to a scheme of correcting the currents for mass transfer effects and determining the true kinetic currents. When the heterogeneous kinetics are more complex, a solution for the current can still be obtained, but it may be in the form of a non-linear algebraic or transcendental equation (99).

When $R_i \neq 0$, it is not possible to integrate Equation 4-6 unless simplifying assumptions are made. Koutecky and Levich (101-103) present solutions for Equation 4-6 when R_i can be represented by first-order, dissociation-dimerization or catalytic type kinetics. They ignore convective terms, and their solution is only valid at the limiting current. Here we seek a solution of Equation 4-6 which includes convection and is valid where the system is under charge transfer as well as homogeneous kinetic control.

A numerical solution is required. As in Chapter 3, Equation 3-31 represents the homogeneous reaction rate expression, and Equation 3-34 is used to make the concentrations dimensionless. The boundary conditions at the interface are represented by Equations 3-12, 3-14 through 3-16, and 3-32. The dimensionless representation of the z coordinate is:

$$\varsigma = \left(\frac{\omega\rho}{\mu}\right)^{1/2} z \tag{4-7}$$

For the high Schmidt numbers encountered in electrolyte solutions, $\delta_d << \delta_h$. The z component

of the velocity can be represented in a form that is valid near the disk surface (99):

$$v_z = -a\left(\frac{\mu\omega}{\rho}\right)^{1/2}\varsigma^2 \tag{4-8}$$

The dimensionless equations and the details of the computer implementation are given in Appendix D.

The potential step experiments of Chapter 3 were carried out in the linear current density-overpotential region. In that region, no direct information can be obtained about the reaction orders, transfer coefficients, and stoichiometric number. These parameters, as well as the exchange current densities and homogeneous rate constants, are needed for the simulation of rotating disk curves outside the linear region. It is necessary to limit the choices for these parameters to a manageable number.

Reaction 3-28 is represented according to the scheme of Reactions 2-8 and 3-30:

$$S_4^{2-} \rightleftarrows 2S_2^- \tag{2-8}$$

$$2S_2^- + \frac{4}{3}H_2O + 2e^- \rightleftarrows \frac{2}{3}S_4^{2-} + \frac{4}{3}HS^- + \frac{4}{3}OH^- \tag{3-30}$$

Reaction 3-30 is a multi-step electrochemical reaction made up of elementary chemical and electrochemical steps. One of the steps, which may be chemical or electrochemical, is rate determining. For Reaction 3-30, a two-electron reaction, the possibilities for the transfer coefficients are listed in Table 4-1. The α's are computed from Equations 3-10a and b.

The cases where one of the transfer coefficients is zero (Case I, III, VI, and VIII) can be eliminated because both the anodic and cathodic reactions show some potential dependence. The values of the transfer coefficients, reaction orders, and stoichiometric number chosen should represent the data on both cobalt and platinum over a range of temperatures, and the homogeneous rate constants should not depend on the electrocatalyst. In the vicinity of the first cathodic wave, an α_c of 0.5 best represented the data. Table 4-2 shows the values of the homogeneous rate constants and exchange current densities that best fit the data for α_c=0.5 and z_{oc}/ν=1/2 and z_{oc}/ν=1. For z_{oc}/ν=1/2, the homogeneous rate constants that best represent the

Table 4-1: Possible Values of the Transfer Coefficients

n=2, β=0.5

		Case	ν=1	Case	ν=2
r=0	s=0	I	α_a=2 α_c=0	VI	α_a=1 α_c=0
	s=1	II	α_a=1 α_c=1	VII	α_a=0.5 α_c=0.5
	s=2	III	α_a=0 α_c=2	VIII	α_a=0 α_c=1
r=1	s=0	IV	α_a=1.5 α_c=0.5	IX	α_a=0.5 α_c=0.5
	s=1	V	α_a=0.5 α_c=1.5		

Table 4-2: Values of Parameters

z_{oc}/ν=1/2				
	Platinum		Cobalt	
Temperature (°C)	k_f (sec^{-1})	i_o/ν (mA/cm^2)	k_f (sec^{-1})	i_o/ν (mA/cm^2)
40	0.00071	0.04		
60	0.0075	0.24	0.02	1.0
77	0.045	0.9	0.075	2.0
z_{oc}/ν=1				
	Platinum		Cobalt	
Temperature (°C)	k_f (sec^{-1})	i_o/ν (mA/cm^2)	k_f (sec^{-1})	i_o/ν (mA/cm^2)
40	0.002	0.05		
60	0.02	0.33	0.03	1.5
77	0.1	1.3	0.15	2.5

data are somewhat different for cobalt and platinum. However, when z_{oc}/ν=1, the values of the homogeneous rate constants are nearly the same for cobalt and platinum. Furthermore, above 60 °C, the values of exchange current density found for cobalt are close to those found from the potential step data of Chapter 3. The dashed lines in Figures 4-2, 4-3, and 4-5 show the fit to the data using these parameters.

On Pt, the first cathodic wave becomes more prominent as temperature increases, and the agreement between predicted and measured currents reflects this. At the Co electrode, the data are well represented by the model only at smaller overpotentials (in the region of the potential step experiments of Chapter 3). At higher cathodic overpotentials, the model predicts a limiting kinetic current. $C_{S_2^-}$ becomes zero at the surface even though $C_{S_4^{2-}}$ is still a large fraction of its bulk concentration. The (hypothetical) limiting current would be reached at smaller overpotentials on Co because of the higher exchange current density on that electrode. The second cathodic reaction might become dominant at some fraction of that limiting current.

The results of the computer model predict little effect of convection on the response of the system. Homogeneous reaction and diffusion terms dominate over convective terms in the material balance equations. In the region where the model agrees with the data, there is almost

no effect of convection. This lends support to the hypothesis that the sublinear response at small cathodic overpotentials is due to a homogeneous-kinetic limitation rather than a mass-transfer limitation.

Table 4-3 shows two mechanistic possibilities that are consistent with the derived values of α_c=0.5 (α_a is either 0.5: Case VII and IX, or 1.5: Case IV) and z_{oc}/ν=1.

If Reaction 4-9a is the rate determining step in Mechanism I, then ν=2 because the rds occurs twice for each overall occurrence of Reaction 3-30. Reaction 4-9b (which is a combination of Reactions 2-4 and 2-5) is assumed to be in quasi-equilibrium. For this mechanism $\alpha_a=\alpha_c=0.5$, and the rate expression can be written:

$$\frac{i}{nF} = k_a C_{S_2^-}^{2/3} C_{OH^-}^{4/3} C_{HS^-}^{4/3} \exp(F\phi/2RT) - k_c C_{S_2^-} \exp(-F\phi/2RT) \qquad (4\text{-}11)$$

The constants k_a and k_c represent rate constants for Reaction 4-9a modified by the equilibrium constant of Reaction 4-9b. Consistent with the stoichiometry of Reaction 3-30 and with Equa-

Table 4-3: Mechanistic Possibilities

MECHANISM I	
$2(S_2^- + e^- \rightleftarrows S_2^{2-})$	(4-9a)
$2S_2^{2-} + \frac{4}{3}H_2O \rightleftarrows \frac{2}{3}S_4^{2-} + \frac{4}{3}HS^- + \frac{4}{3}OH^-$	(4-9b)
MECHANISM II	
$S_2^- + e^- \rightleftarrows S_2^{2-}$	(4-10a)
$S_2^{2-} \rightleftarrows S_{ad} + S^{2-}$	(4-10b)
$S^{2-} + H_2O \rightleftarrows HS^- + OH^-$	(4-10c)
$S_{ad} + e^- \rightleftarrows S_{ad}^-$	(4-10d)
$S_{ad}^- + S_2^- \rightleftarrows S_3^{2-}$	(4-10e)
$S_3^{2-} + \frac{1}{3}H_2O \rightleftarrows \frac{2}{3}S_4^{2-} + \frac{1}{3}HS^- + \frac{1}{3}OH^-$	(4-10f)

tion 3-8b, $z_{oc}=2$ and $z_{oa}=0$. Since $\nu=2$, $z_{oc}/\nu=1$. Thus this mechanism can represent the data at low cathodic overpotentials.

Mechanism II is consistent with the cathodic data (on the first reaction wave) if Reaction 4-10a is taken to be the rds. For that choice of rds, $\nu=1$, $\alpha_a=1.5$, and $\alpha_c=0.5$. The rate expression takes the following form:

$$\frac{i}{nF} = k_a' \frac{C_{S_4^{2-}}^{2/3} C_{OH^-}^{4/3} C_{HS^-}^{4/3}}{C_{S_2^{2-}}} \exp(1.5F\phi/RT) - k_c' C_{S_2^{2-}} \exp(-F\phi/2RT) \qquad (4\text{-}12)$$

In this case, $z_{oc}=1$ and $z_{oa}=-1$. As above, these reaction orders are consistent with Reaction 3-30 and Equation 3-8b and $z_{oc}/\nu=1$. Thus this mechanism can also represent the data at low cathodic overpotentials.

Neither of the above mechanisms adequately represents the anodic data. Mechanism I predicts an $\alpha_a=0.5$. At anodic overpotentials in the quasi-reversible region, this mechanism considerably underestimates the experimentally-measured currents. Mechanism II, with Reaction 4-10a as the rds, also underestimates the experimental currents, but to a smaller extent. The dashed lines in the anodic region of the graphs of Figures 4-2, 4-3, and 4-5 show the currents predicted by this mechanism.

It is apparent from the potential step data on Co electrodes in Chapter 3 that there are similarities between the processes in the low overpotential cathodic and anodic regions. However, even in that region the anodic currents are higher than the cathodic currents at the same absolute value of overpotential, and the shape of the anodic transients are flatter. As the overpotential increases anodically, there might be a change in the rate determining step in the reaction mechanism, more than one electrode process might take place or specific adsorption could become important.

In the above mechanisms, no explicit account has been taken of adsorbed sulfur species and changes of the coverage of an adsorbed species with potential. Reaction 4-10b or a similar reaction could represent an adsorption process at the electrocatalyst. Investigations on Au electrodes

showed that adsorbed sulfur layers can be formed (104,105). At low overpotentials, submonolayers of sulfur were formed. As potential increased, monolayers and multilayers were deposited. Hamilton and Woods (105) found that sulfur adsorption proceeded in parallel with polysulfide formation. Allen and Hickling (51) rationalized their experimental results in the anodic region in terms of the removal of adsorbed sulfur being the rate determining step (such as Reaction 4-10b proceeding from right to left). Lando *et al.* (12) and Tenne *et al.* (106) were able to explain some aspects of the response of CdSe photoanodes by using sulfur removal as the rds. Frese and Canfield (107) proposed a model involving sulfur adsorption and removal to explain the competition between faradaic reaction and photocorrosion at CdSe photoanodes. Hartler, Libert, and Teder (108) studied the dissolution rate of elemental sulfur in aqueous sulfide and polysulfide solutions. Conversion of their measured rates into current density gives a current density of about 20 mA/cm^2 corresponding to the slowest rates found in polysulfide solutions (at 25 °C). Sulfur dissolution could become a limiting factor at some of the highest anodic overpotentials used here (Figure 4-6) and under galvanostatic operation of efficient PEC's (where current densities of 10 to 20 mA/cm^2 have been reported under normal solar illumination). An adsorbed layer of sulfur might be bound to the electrode surface tightly, making its dissolution rate slower than that of elemental sulfur. The adsorbed sulfur might lead to blocking of catalytic sites and be responsible for the decrease in slope on the log(i) vs η plot at higher values of η.

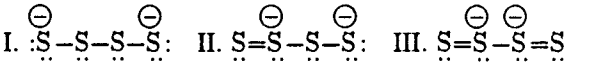
4.5. Discussion of Results with the Addition of DMF

The results of Chapter 3 indicated that the sulfur radical anion S_2^- might be involved in the polysulfide redox reaction at low overpotentials. Supersulfide accounts for only a small part of the total sulfur in aqueous solution (see Table 2-2), and the polysulfide-supersulfide equilibrium is strongly affected by temperature and choice of solvent. Polysulfides have an optical absorption band around 420 nm while sulfur radicals absorb around 620 nm (see Table 6-2). The dominant species can often be ascertained by noting the color of solution; solutions containing predominantly polysulfides are yellow-red while sulfur radical solutions are blue. Solutions

that contain a substantial amount of both types of species are green. Sulfur radicals are also thought to be responsible for the color of certain minerals such as ultramarine (109).

Abraham *et al.* (110) and Rauh *et al.* (26) report the color, spectral properties, and solubility of sodium and lithium polysulfides dissolved in a variety of aprotic media. Polysulfide solubility ranges from almost insoluble in solvents like nitromethane to a solubility greater than 10 M in dimethylsulfoxide (DMSO). Solubility increases with an increase in the basicity of the solvent, while the average size of the polysulfide ions depends on the dielectric constant of the solvent (26). The equilibrium between polysulfide ions and sulfur radicals is related to the specific structure of the solvent. Equilibrium is shifted toward sulfur radicals in aprotic solvents that contain C=O, S=O, and P=O structural units. For example, dimethylformamide (DMF), DMSO, and hexamethylphosphoramide (HMPA) all show this shift, whereas in a solvent such as tetrahydrofuran (THF), which does not contain any of these units, polysulfides are dominant.

Giggenbach (111) investigated the tetrasulfide-supersulfide equilibrium in mixtures of water and DMF at room temperature. As DMF was added to an aqueous polysulfide solution, the equilibrium was shifted toward supersulfide. Rauh *et al.* (26) have shown that similar equilibrium shifts occur when DMSO is added to a polysulfide solution in THF. Giggenbach explains the stability of S_4^{2-} in water by postulating three electronic structures:



(4-13)

In water Structure I is stabilized because of hydrogen bonding, whereas Structures II and III become more prevalent in aprotic solvents with high basicity. The accumulation of charge on the inner sulfur atoms leads to a weakening of the middle bond. The equilibrium expression in water-DMF mixtures was found to take the form:

$$(S_4^{2-}{-}H_2O) + 8DMF \rightleftharpoons 2(S_2^{-}{-}4DMF) + H_2O \qquad (4\text{-}14)$$

The participation of 4 DMF molecules per S_2^- suggests the formation of a "cage-like" structure by the DMF around the supersulfide. Solvents with S=O and P=O structural units might form similar cages. The destabilization of S_4^{2-} coupled with the solvent-specific interactions with S_2^-

shifts the equilibrium of Reaction 2-8 to the right.

The results presented in Figures 4-7 and 4-8 can be rationalized on the basis of the information presented above. The addition of DMF to the aqueous solution shifts the equilibrium of Reaction 2-8 toward the right. The equilibrium constant and the rate constants are related by Equation 3-35. The foward rate constant k_f is probably increased somewhat because of the destabilization of S_4^{2-} by the formation of Structure III in 4-13. The dimerization rate constant is probably decreased by the formation of the cage-like structure around S_2^-. Quantitative information on the temperature dependence of S_2^- concentrations, and of homogeneous reaction rates in DMF-water mixtures is lacking. The experiments reported in (111) were carried out under experimental condition which make it difficult to calculate the exact concentration of S_2^- (112). However, by choosing reasonable values for some of the parameters, the trends of Figures 4-7 and 4-8 can be predicted. The concentration of S_2^- at 25 °C is assumed to be 0.22 mM. The dependence of the equilibrium constant of Reaction 2-8 on temperature is taken to be the same as for the purely aqueous solution. The homogeneous reaction rates and the exchange current densities were adjusted to give the best fit at each temperature.

The dashed lines in Figures 4-7 and 4-8 show the results of the model predictions. Figure 4-11 shows the values of k_f and i_o/ν used. The activation energy for k_f is about 24 kcal/mole, which is close to the value found for the aqueous solutions. The value of k_f is about four times the value in the aqueous solutions at the same temperature. By using these values of k_f and the equilibrium constant, the value of k_b can be shown to be about 1.5 to 2 times lower in the DMF-water mixture than in the purely aqueous solution.

As in the aqueous solutions, the model does not predict the anodic data very well. The reasons for this might be similar to those discussed in Section 4.4.

The exchange current densities on Co electrodes are only slightly higher than those in the aqueous solutions. This suggests that the improved response in the DMF-water mixtures comes from the shift in the equilibrium toward S_2^-, and the corresponding modification of the rate con-

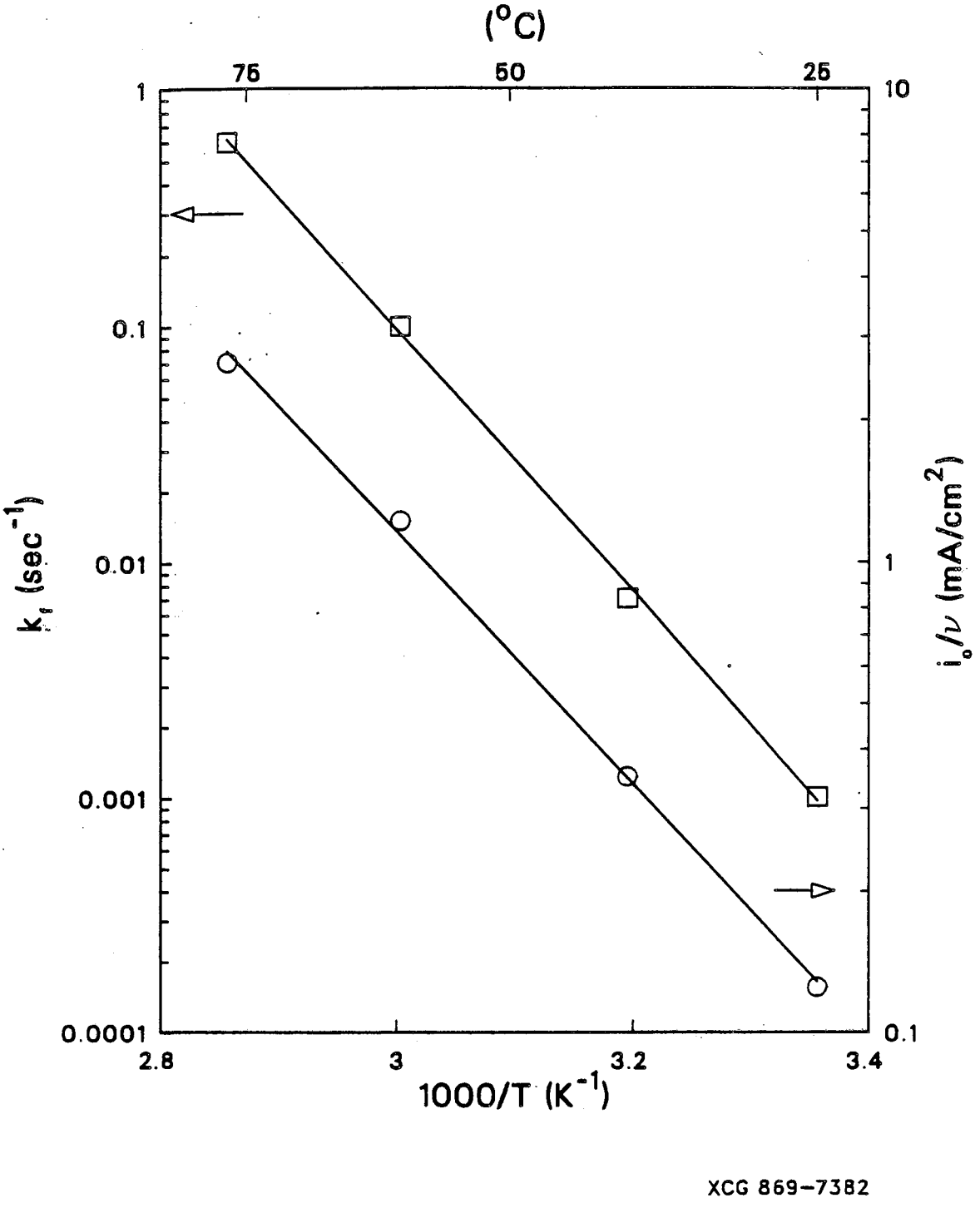


Figure 4-11: Values of k_f and i_o/ν used in Figures 4-7 and 4-8.

stants of Reaction 2-8, rather than a change in the reaction rate at the interface.

4.6. Summary

The current density-overpotential responses at cobalt and platinum rotating disk electrodes in a 1.3 M S^{2-}, 1 M S^0, pH=12 solution were determined. A model was developed to take into account a slow homogeneous reaction in solution as well as a finite heterogeneous reaction rate for this geometry. The parameters determined in Chapter 3 by the potential step method could be used with this model to explain the current density-overpotential behavior in the low-overpotential cathodic region. At higher overpotentials in the cathodic region a second cathodic reaction was evident. This second cathodic reaction was less prominent when the current densities were lower (as on Pt electrodes) or when the S_2^- concentrations were higher (as temperature increased).

The addition of DMF to the aqueous polysulfide solution increases the current density at a given temperature and overpotential. In the range of overpotentials studied, the first cathodic reaction wave becomes much more prominent. Although independent quantitative data are lacking for the DMF-water mixtures, the assumption of reasonable values for k_f and i_o/ν allows the prediction of the observed cathodic behavior in the temperature range of 25 to 77 °C.

Chapter 5

Performance of Aqueous Polysulfide Flow-Through Electrodes

5.1. Introduction

The results discussed in Chapters 3 and 4 showed that the current density at an electrode carrying out the sulfide/polysulfide redox reaction is limited by the combined effects of reactions in solution and slow electrochemical kinetics (at low cathodic overpotentials). An examination of the rotating disk data of Chapter 4 shows that the design goal of supporting 10 to 20 mA/cm^2 with an overpotential of less than 50 mV at the counterelectrode of a PEC cannot be met at a smooth planar electrode. For example, at 77 °C, the current density at -50 mV polarization on a smooth Co electrode is -2.5 mA/cm^2 in aqueous solution and -6.4 mA/cm^2 in the solution with 13 mole-% DMF added. An increase in current density of 3 to 5 times is needed in order to meet the design goals.

Porous electrodes consist of a solid phase and a liquid phase in intimate contact and therefore have a high interfacial area per unit volume (a_o). They have been used for removal of materials from waste streams (113), in redox batteries (21), and in stationary battery electrodes (114). The electrode structure can be invariant with time as in most redox battery and fuel cell applications, or solid reactants can be part of the electrode matrix (for example in the Zn/NiOOH battery). Mass transfer in the liquid phase can take place by diffusion, migration, natural convection and/or forced convection.

In our case an electrode that carries an electric current and acts as an electrocatalyst, yet does not change its structure with time, is desired. A metal or metal sulfide deposited on a wire screen or expanded-metal mesh should meet these requirements, and a structure of this type could be used as a flow-through electrode. Electrolyte flow would be useful in a redox battery

employing the aqueous polysulfide electrolyte, because in redox batteries the electrolyte is typically stored in a location remote from the cell stack, or in a PEC, where flow could be used to remove waste heat.

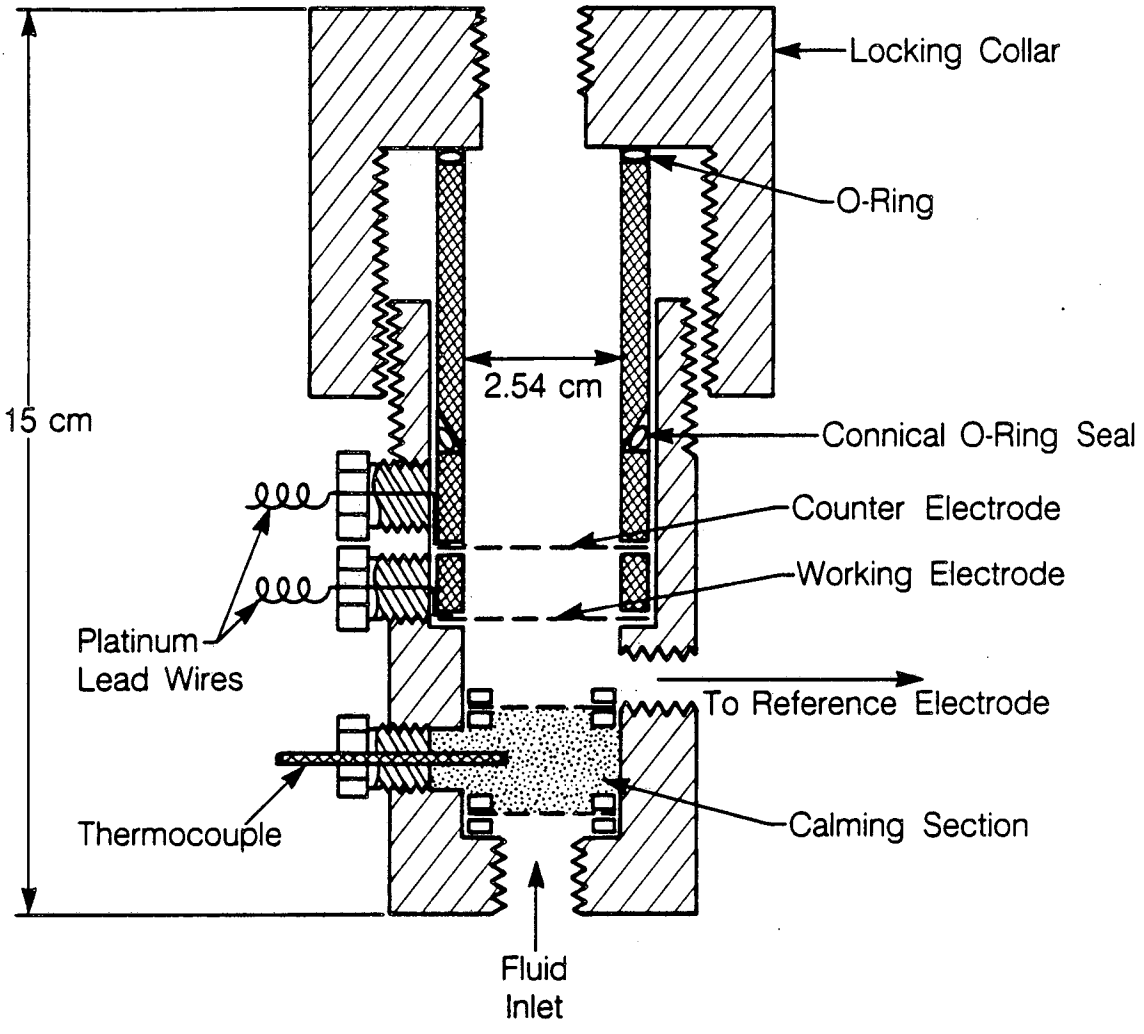
The focus of this Chapter is the preparation and testing of electrocatalytic porous electrodes for the aqueous polysulfide redox system. Section 5.2 describes the prepartion of the electrodes and the construction and operation of the flow cell. Section 5.3 discusses the effect of different catalyst materials, the effect of temperature, and the effect of the addition of DMF. These results are compared with those of Chapters 3 and 4.

5.2. Experimental Procedure

Cell and Flow System Construction

A cross-sectional view of the cell is shown in Figure 5-1. Fluropolymers such as PTFE, FEP and PFA were used as materials of construction wherever practical. The cell body is fabricated from PTFE. The flow channel is 2.54 cm in diameter (cross sectional area 5.07 cm^2). The electrolyte enters through the bottom of the cell. Channeling of the fluid through one part of the electrode would decrease the effectiveness of the electrode. To insure uniform flow distribution, a flow distributor of quartz (sand) particles is placed 0.5 cm above the inlet. The sand is composed of irregularly shaped particles 0.5 to 1 mm in diameter, resulting in a column to particle diameter ratio of greater than 25, and the packed depth of the sand is 0.75 cm. Pt-10% Rh screens (80 mesh) hold the sand in place. The screens are sandwiched between PTFE washers for mechanical stability.

A type K thermocouple (Ni-Cr vs. Ni-Al, Omega Engineering) is used to measure the temperature of the entering fluid, and it is coated with 0.020" thick FEP in order to protect if from the corrosive electrolyte. The thermocouple is attached to a 1/8" PTFE pipe plug. To form a leak-tight seal between the parts, a hole slightly smaller than the thermocouple is drilled in the plug. The hole is expanded by heating the plug to 150 °C, and the thermocouple is pushed



XBL 868-10956

Figure 5-1: Cross-Section of the flow cell.

through at this elevated temperature. Upon cooling the hole shrinks and a leak-tight seal is formed. The assembly is then mounted on the cell via a 1/8" FNPT pipe thread that was tapped into the cell body. The thermocouple tip protrudes about 3 mm into the fluid flow path.

The reference electrode is a 3.18 mm diameter Pt rod (99.95%). It is sealed into a pipe plug in a manner similar to that used for the thermocouple probe. This electrode is mounted in the branch of a 1/8" PTFE pipe tee. Part of the fluid entering the cell is tapped off to flow through the tee and over the reference electrode. This arrangement insures that the reference electrode is at the same temperature as the working electrode. The flow rate through the reference electrode is adjusted by a PTFE stopcock valve.

The working electrode is held in place between a 4.76 mm lip in the body of the cell and a 1.25 cm long piston sleeve. A stack of screen electrodes up to 0.5 cm in length can be accommodated in the space between the lip and the piston sleeve. Electrical contact to the external circuit is made by a 0.020" soft-temper Pt wire which is compressed between the piston sleeve and the electrode stack. The Pt lead wire is friction fit into a 1/8" pipe plug, and a special treating agent (Chemplast Inc., Chemgrip Hi-Viscosity) is applied to the plug so that an epoxy backup seal can be made. The contact resistance between the wire and the working electrode was found to be negligible, so long as the working electrode was a metal.

The counter electrode has an external electrical contact which is similar to that used for the working electrode. Two pistons sleeves are placed above the counter electrode. First, a 1.25 cm long piston sleeve is placed on top of the electrode to hold it in place. A 1-1/16" ID by 1/8" cross section O-ring is pressed against the top of this piston sleeve and against the cell body by a 5 cm long piston sleeve with a conical taper cut into the end that contacts the O-ring. This conical O-ring seal was found to be necessary to prevent electrolyte from leaking between the piston sleeves and the cell body.

A locking collar holds the piston sleeves in place and provides compression for the O-ring seals and between the electrodes and the contact wires. A 1-1/8" ID by 1/16" cross section O-

ring seal between the 5 cm long piston sleeve and the locking collar prevents fluid leakage.

A schematic diagram of the complete flow system is shown in Figure 5-2, and a photograph of the system is presented in Figure 5-3. A 1-liter PTFE tank acts as a storage reservoir for the electrolyte, and its volume is about twenty times that of the cell. The tank cover has a 3-1/2" ID by 1/8" cross section O-ring which is compressed against the top lip of the tank with an external flange. Three 1/4" FNPT fittings are tapped in both the top and bottom surfaces of the tank cover. The suction line of the pump is connected to the bottom of the tank via one fitting, and another fitting connects to a common discharge line for the cell, bypass loop, and reference electrode compartment. The third fitting is connected to a stopcock valve which can be used to either vent the system or allow the introduction of an inert gas above the liquid.

A positive-displacement pump (Flurocarbon, Model Saturn SP-3000) is used to move the fluid through the system. The pump is capable of providing a head of 15 psig, and its wetted parts are PTFE. Two PTFE needle values are used to control the flow rate through the cell and bypass loop. The flow rate through the cell was measured by a rotameter (Omega Engineering, FL-215). The minimum flow rate that could be read precisely was about 0.1 liter/min, and the maximum flow rate attainable (about 1.6 liters/min) depended on the number of electrode screens, the electrolyte, and the temperature. The maximum scale reading on the rotameter corresponded to 2.0 liters/min. The rotameter tube and float are made of glass.

A stopcock valve is placed between the top of the cell and the rotameter inlet, and during operation this valve is normally open. When changing electrodes this valve and the flow-control valves can be closed to allow the cell to be isolated from the rest of the system. The electrolyte in the cell is drained through the reference electrode port.

The components of the system are mounted so that easy access to all the parts was possible. The pump is mounted on a wooden base which is covered with FEP film to protect it from any leaking electrolyte. The other parts of the system are attached to a frame of 1/2" aluminum rods which are held together by metal clamps. The pump transmitted some vibration to the rest

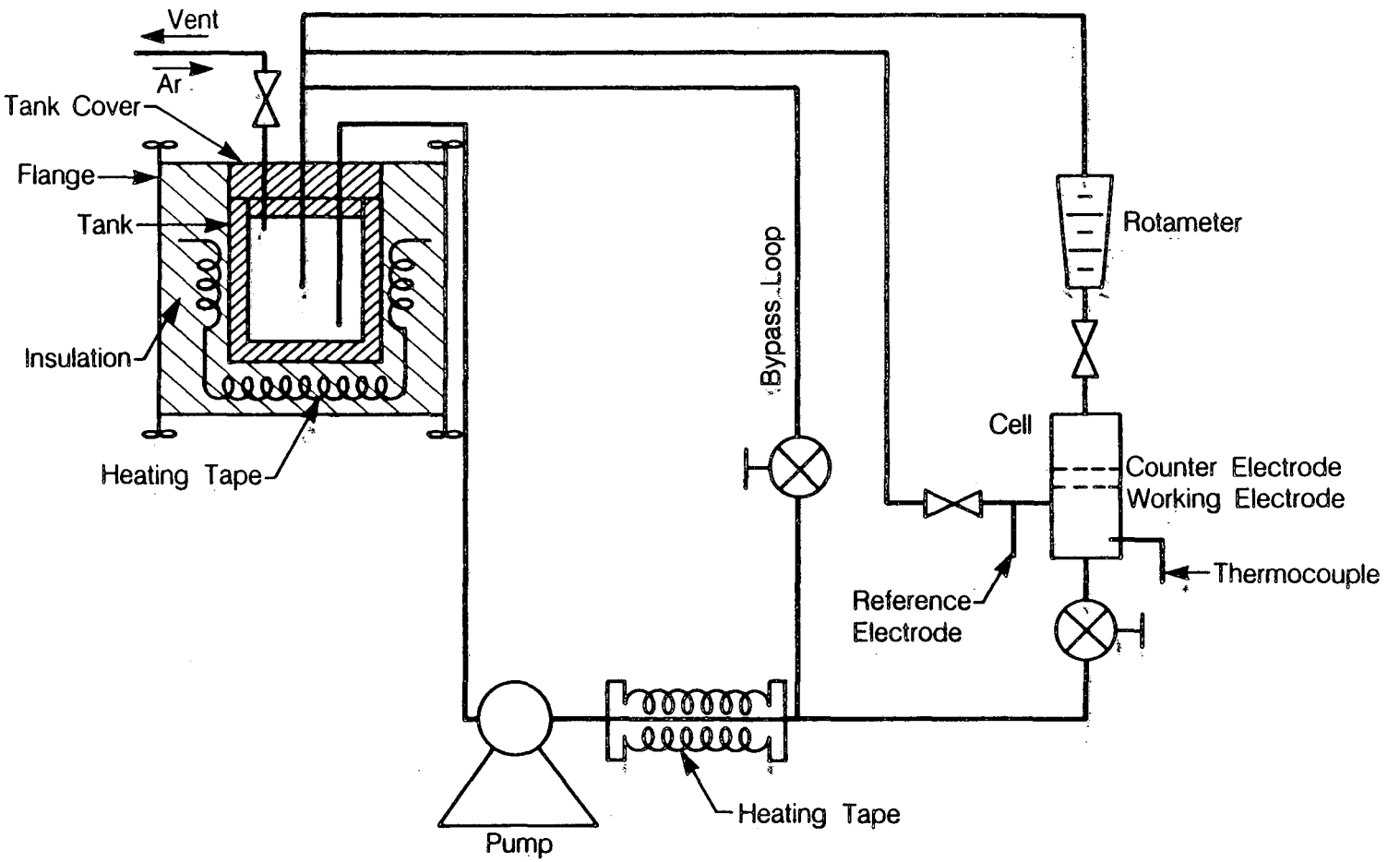
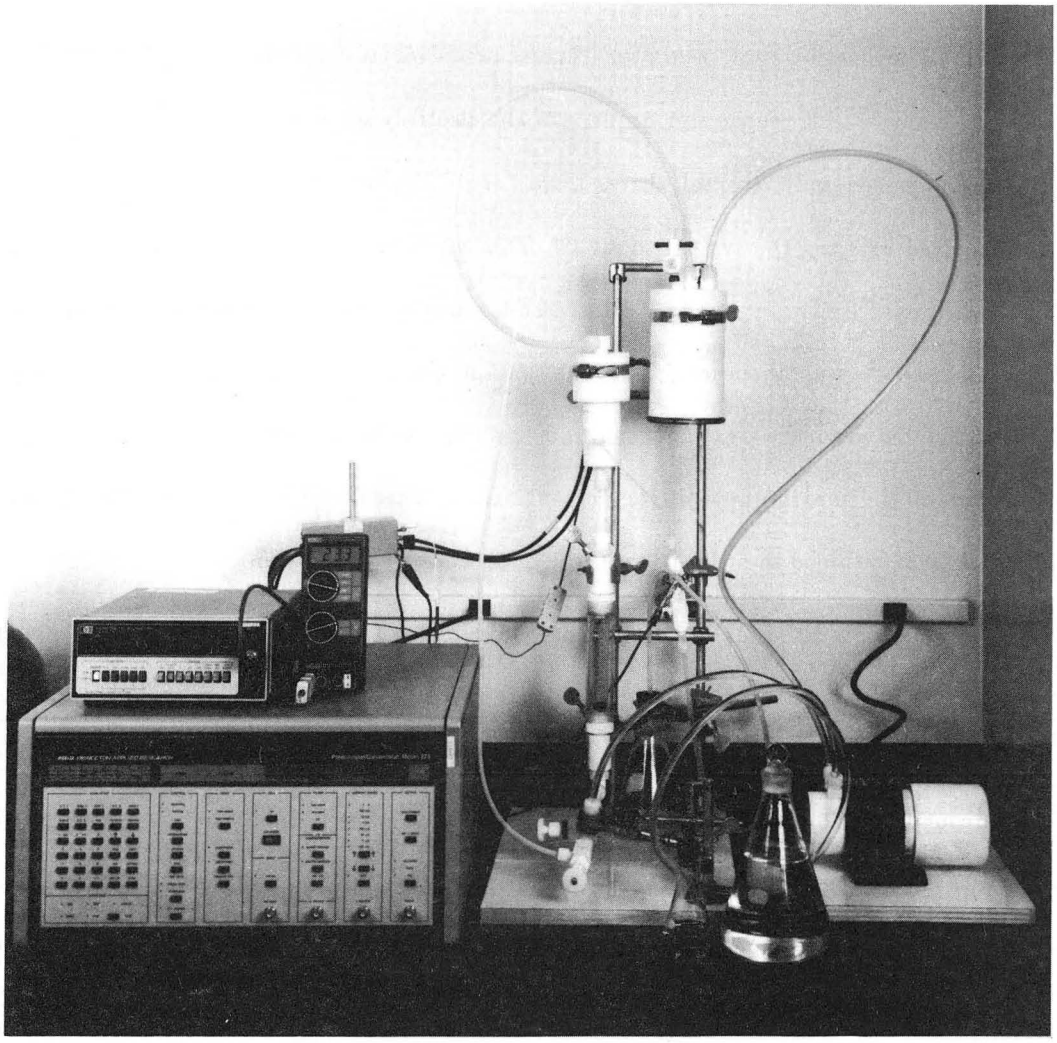


Figure 5-2: Diagram of the flow system.



CBB 863-1918

Figure 5-3: Photograph of the flow system.

of the system; placing 1 cm thick foam-rubber mats under the pump and flow system mounting boards helped reduce the vibration.

The heating and insulation requirements for the system were determined in preliminary experiments that used water in place of the electrolyte. The initial design called for heating tape to be placed only around the storage tank. Experiments indicated that several hours were required to bring the system to 80 °C. This was due to the slow heat transfer rate through the 4 mm thick PTFE tank wall. To increase the heating rate, heating tape was wrapped around the thin (0.032" wall thickness) FEP tube of the pump discharge line. A thermocouple probe was placed between the heating tape and the FEP tube to monitor the temperature, in order to prevent the maximum wall temperature from exceeding 150 °C. The heating tape around the tank was retained in order to keep the main body of fluid warm.

Providing thermal insulation on the outside of the heating tape was important because of the large convective air flow in the fume hood (0.51 m/sec). The heating tapes were wrapped with 1.27 cm thick fiberglass insulation which was held in place with duct tape. Heat loss through the flow tubes was significant, so foamed plastic tubing of 1.27 cm wall thickness and 1.27 cm inside diameter was placed around the tubes. A plug of fiberglass was placed at the end of the foamed tubing so that a stagnant air layer was trapped between the fluid flow tubing and the foamed plastic insulation. Heat loss through the cell was small because its walls were thick PTFE, so no insulation was required.

Selection and Preparation of Electrocatalysts

In Section 3.3, prerequisites for the selection of electrocatalysts for use in the potential step and rotating disk experiments were given:

1. Be chemically and electrochemically stable
2. Exhibit good electrocatalytic activity
3. Have a smooth surface

The electrodes used here should meet the first two requirements. The third requirement is not

necessary; instead we seek as much active area for a given projected area as possible.

An examination of Table 3-1 shows that Co and MoS_2 should be considered for use as electrocatalysts. Nickel (or NiS_x) would be acceptable if its corrosion rate is small. To obtain the required current densities on these electrocatalysts, an increase in surface area is needed.

Wire screen and expanded-metal mesh electrodes can provide the increase in surface area required to meet the design goals. For a square-weave wire mesh, the interfacial area per unit volume is given by (115):

$$a_o = \frac{2\pi m^2 dl}{\delta} \tag{5-1a}$$

where

$$l = \sqrt{\frac{d^2}{4} + \frac{1}{m^2}} \tag{5-1b}$$

The open area ratio ϵ can be determined by weighing a sample of screen:

$$\epsilon = 1 - \frac{w}{\rho A \delta} \tag{5-2}$$

Table 5-1 shows the properties of the screens and expanded metal used here. The real-to-projected area ratio of a single screen is given by:

$$\frac{\text{Real Area}}{\text{Projected Area}} = a_o \delta \tag{5-3}$$

A single screen or a stack of a few screens should be able to meet the design requirements.

Table 5-1 : Properties of Screens and Expanded Metal

Material	d (mm)	δ (mm)	a_o (cm^{-1})	ϵ	$\frac{\text{Real Area}}{\text{Projected Area}}$
Pt-10% Rh 80x80 mesh	0.076	0.200	75.7	0.82	1.51
Ni 100x100 mesh	0.114	0.254	122	0.67	3.10
Mo 5-Mo 20-2/0E	0.127	0.381		0.78	

The electrodes were punched out from stock material by use of a 1-1/4" rotex die punch. Cardboard sheets were used to protect the screens from damage during the punching operation. After punching, the screens were carefully trimmed with a scissors.

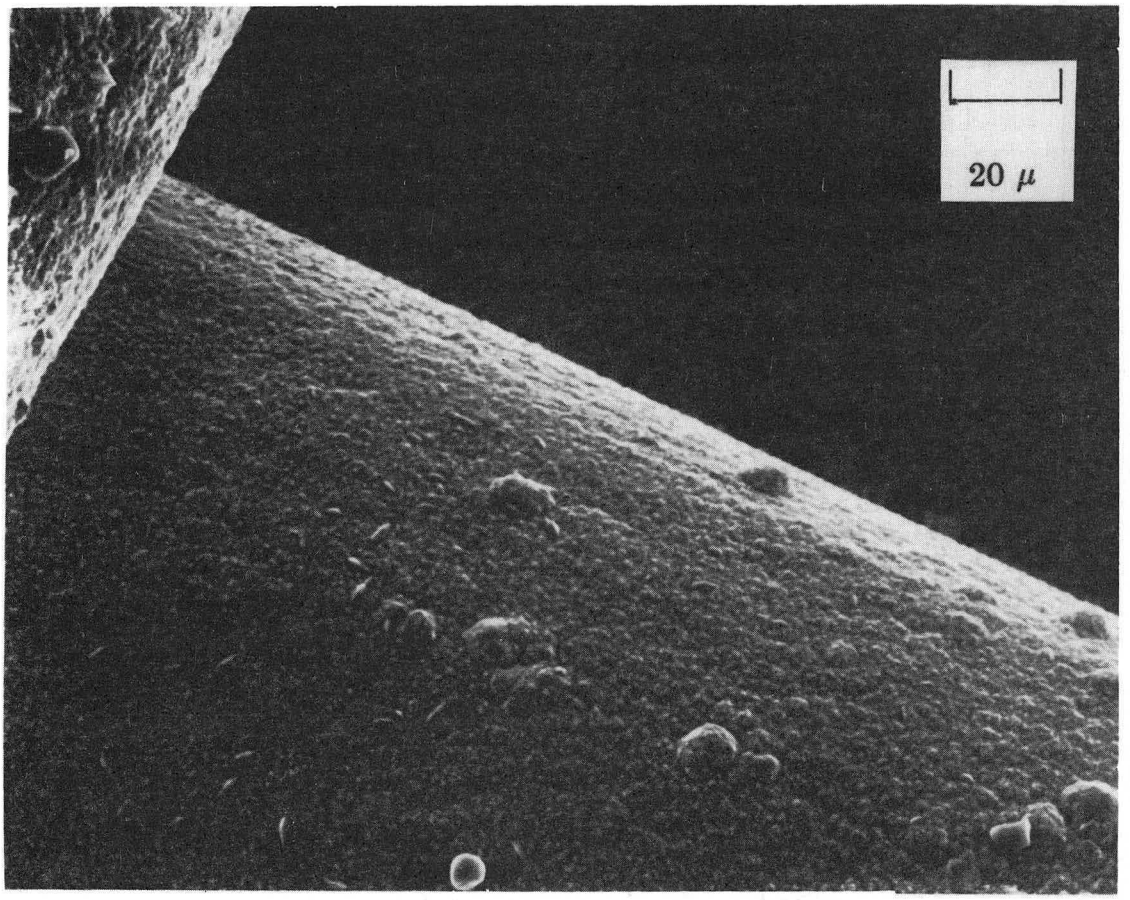
Cobalt screens were not available commercially, so cobalt was electroplated onto the nickel screens. The plating bath composition is given in Table 5-2 (116), and the conditions for periodic-reversal plating are given at the bottom of the table. The nickel screens were degreased with soapy water, soaked in acetone, and then rinsed with distilled water before being electroplated with cobalt. The Co plate was approximately 25 μm thick, and it was bright and adherent. An SEM examination (Figure 5-4) shows that the deposit was somewhat granular and rough.

MoS_2 is a semiconductor, so to be an effective electrocatalyst it must be deposited on a conductive support. Layers of MoS_2 can be grown on Mo in a H_2S/H_2 (17) or sulfur (117) atmosphere. A Mo expanded-metal mesh (Exmet Corporation) and an excess of sulfur were placed in the quartz ampoule shown in Figure 5-5. The ampoule was sealed under a vacuum, and the contents were heated for 24 hours at 450 °C in a muffle furnace and then cooled slowly to room temperature. Calculations using the data in (117) predict that a layer about 0.7 μm thick will grow under these conditions. An adherent layer of MoS_2 was formed.

Preparation of Electrolyte

Table 5-2: Cobalt Plating Bath and Conditions

Plating Bath Composition	
Chemical	Concentration
$CoCl_2 \bullet 6H_2O$	435 g/l
H_3BO_3	45 g/l
Operating Conditions	
Temperature 25 to 50 °C	
Current Density 40 mA/cm^2	
Plating Time 140 minutes	
Cathodic Period	Anodic Period
40 ms	8 ms



XBB 869-6989

Figure 5-4: Cobalt electrodeposit on a 40-mesh Ni screen.

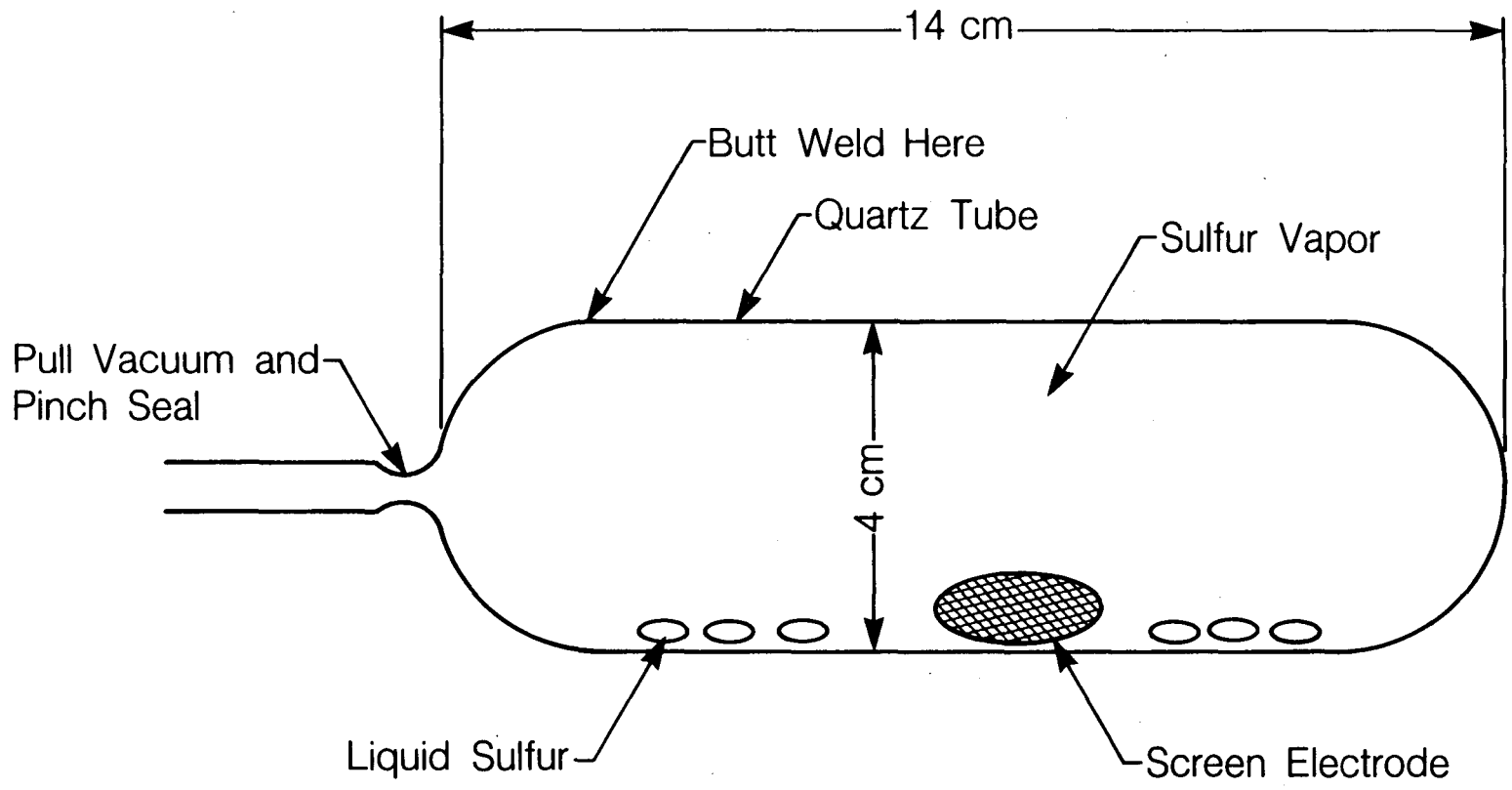


Figure 5-5: Quartz ampoule for sulfiding the surface of metal electrodes.

The procedure for electrolyte preparation presented in Section 3.3 was modified in order to produce the greater quantities required (about 1.5 liters for each run) for the flow cell experiments. A stock solution of twice the concentration of the working electrolyte was prepared. Water was deaerated by bubbling Ar through it, and a vacuum was applied with an aspirator in order to remove as much of the dissolved Ar as possible. This helped prevent gas bubbles from forming at the (suction) inlet of the pump. After dissolving the calculated quantities of $Na_2S \bullet 9H_2O$ and sulfur in 750 ml of water, the solution was placed in the PTFE tank. First air was swept out with argon, and then H_2S was used to displace the argon. The tank was pressurized with the H_2S to 6 psig, and the solution in the tank was agitated with a magnetic stirrer while H_2S was absorbed from the vapor space above the solution. Samples were withdrawn at intervals, and when the desired concentration was reached the flow of H_2S was stopped.

The above procedure was performed twice to make 1.5 liters of stock solution. One-half of the stock solution was diluted with water, and the other half was diluted with a water-DMF mixture to bring the concentration of DMF to 13 mole-%. Both working solutions were found to contain the same amount of total sulfur using the procedure outlined in Section 3.3. The solutions were stored in 2-liter polyethylene bottles under an Ar atmosphere.

Operating Procedure

To begin an experiment, the cell was assembled and connected to the flow system, which was completely contained in a laboratory fume hood. The tank was filled with electrolyte through the suction port and then connected to the rest of the system. The tank was elevated to assist in priming the pump and to allow any trapped gas to escape via the vent valve. During normal operation, Ar gas was connected to the vent valve. A pressure of 1 to 3 psig above the liquid in the tank was found to be helpful in preventing bubble formation at the pump inlet.

When the flow rate through the cell was low, fluid was diverted through the bypass line in order to prevent undue wear on the pump. Steady flow could be maintained for an indefinite period after adjustment of the two needle valves. By adjusting the stopcock valve at the cell

outlet, flow could be maintained through the reference electrode even at low cell flow rates (<0.3 liters/min).

The temperature was controlled by varying the power input to two variacs connected to the heating tape on the tank and pump discharge lines. At a steady flow rate, the temperature could be maintained within $\pm 1\,^{\circ}C$ for several hours without changing the variac settings. If the flow rate was changed, the variac settings had to be reset to maintain the same temperature.

Before changing electrodes the system was cooled to room temperature. All valves, including the normally-open stopcock valve at the cell outlet, were closed off. The fluid in the cell and reference electrode compartment (about 75 ml) was drained out through the reference electrode line, and then the open ports were plugged. The cell could then be disassembled, and the electrodes changed, while the rest of the system was protected from exposure to air.

Water was used to calibrate the rotameter. The water was collected in a graduated cylinder after a steady flow rate was attained. The correlation between rotameter scale reading and flow rate was:

$$Q_w = 16.3 \cdot y^{1.068} \tag{5-4}$$

5.3. Results and Discussion

The electrochemical performance of the flow system was checked with 10 mM $K_3Fe(CN)_6/K_4Fe(CN)_6$ in 1 M KCl. Figure 5-6 shows the current density vs. overpotential (measured against the Pt rod reference electrode described above), at various flow rates, on a 80 mesh Pt-10% Rh screen. The potential was swept in the positive direction at 5 mV/sec. In experiments that included a return sweep, no hysteresis was found. The flow rate calculated from Equation 5-4 needs to be corrected for the difference in physical properties between the electrolyte solution and water. The flow rate of water and of the electrolyte solution, at the same rotameter reading, are related by:

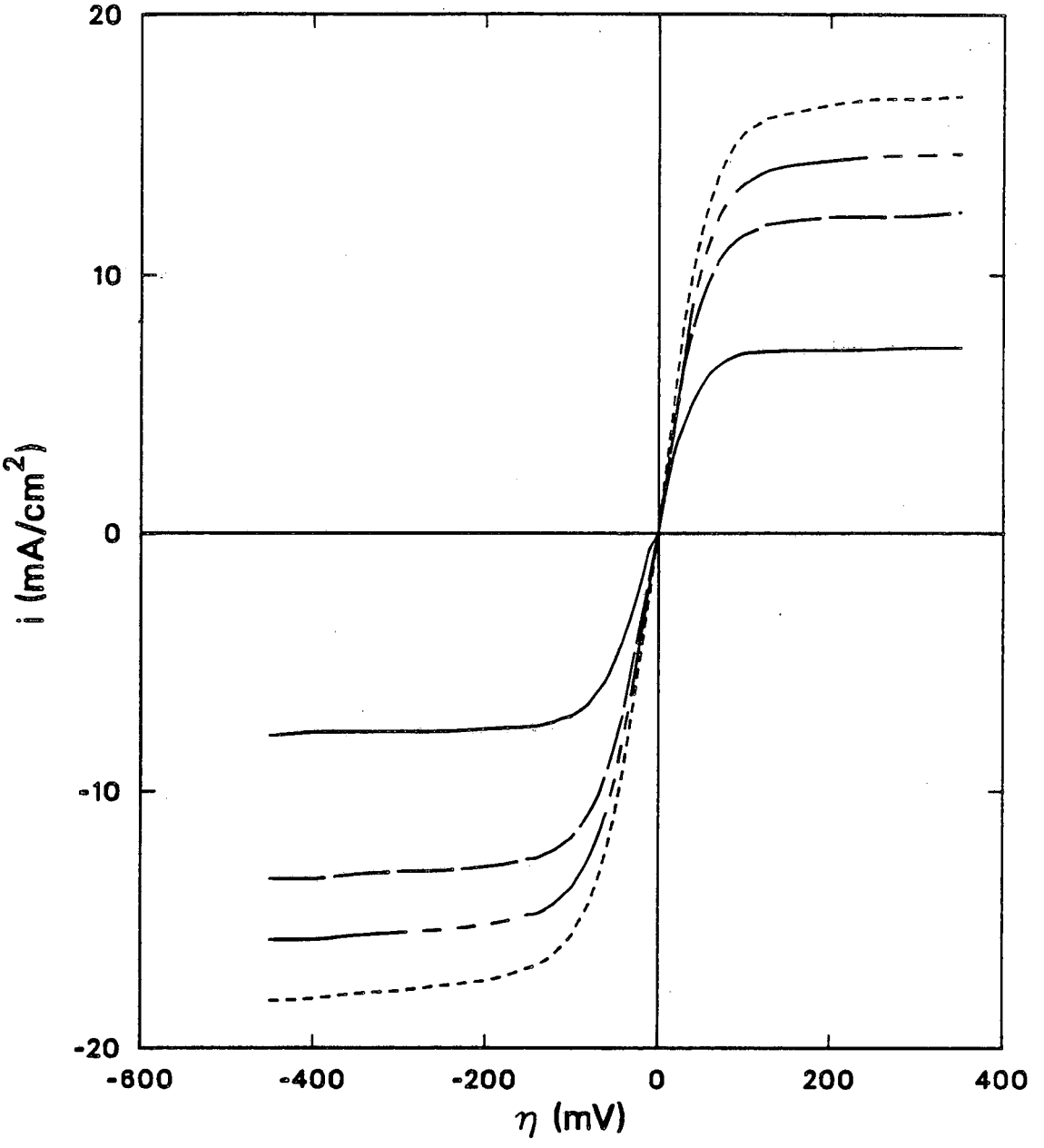


Figure 5-6: Current density versus overpotential on an 80-mesh Pt-10% Rh electrode at 25 °C with 10 mM $K_3Fe(CN)_6/K_4Fe(CN)_6$-1 M KCl electrolyte:
——————, 0.086 liters/min;
— — — — — —, 0.377 liters/min;
—— — — ——, 0.685 liters/min;
——————, 1.002 liters/min.

$$Q_e=Q_w\frac{2.53-\rho_e}{1.53\mu_e} \tag{5-5}$$

The physical properties of an electrolyte solution, similar to that used here, are given in (118). Using those properties and substituting Equation 5-5 into Equation 5-4 yields:

$$Q_e=16.7\cdot y^{1.068} \tag{5-6}$$

The mass transfer coefficient can be calculated from the limiting current density plateau at each flow rate:

$$m_o=\frac{i_L}{nFC_{ib}} \tag{5-7}$$

An appropriate definition for Re for this geometry is (118):

$$Re=\frac{\rho Q_e d}{\mu\epsilon A} \tag{5-8}$$

The dimensionless mass transfer rate (Sherwood number) is defined as:

$$Sh=\frac{m_o d}{D_i} \tag{5-9}$$

Based on the cathodic portion of the data presented in Figure 5-6, the relationship between Sh and Re is:

$$Sh=14.29Re^{0.348} \tag{5-10}$$

The functional dependence on Re is in excellent agreement with previous work (118,119), but the constant term is slightly higher than values presented in these references. This could be due to pump vibration or differences in physical properties between the solutions used here and in those references.

Figures 5-7 through 5-9 show current density-overpotential curves obtained on Mo expanded-metal mesh on which MoS_2 has been deposited. Two expanded-metal screens were used as the working electrode. Due to the MoS_2 coating, a contact resistance of a few ohms was measured between the two electrodes. The electrolyte was 1.3 M S^{2-}, 1 M S^0 at pH 12. Table 2-2 gives the distribution of ionic species in the aqueous solution. Figure 5-7 shows the response at 25 °C and 46 °C with and without the addition of 13 mole-% DMF as a cosolvent. Figure 5-8

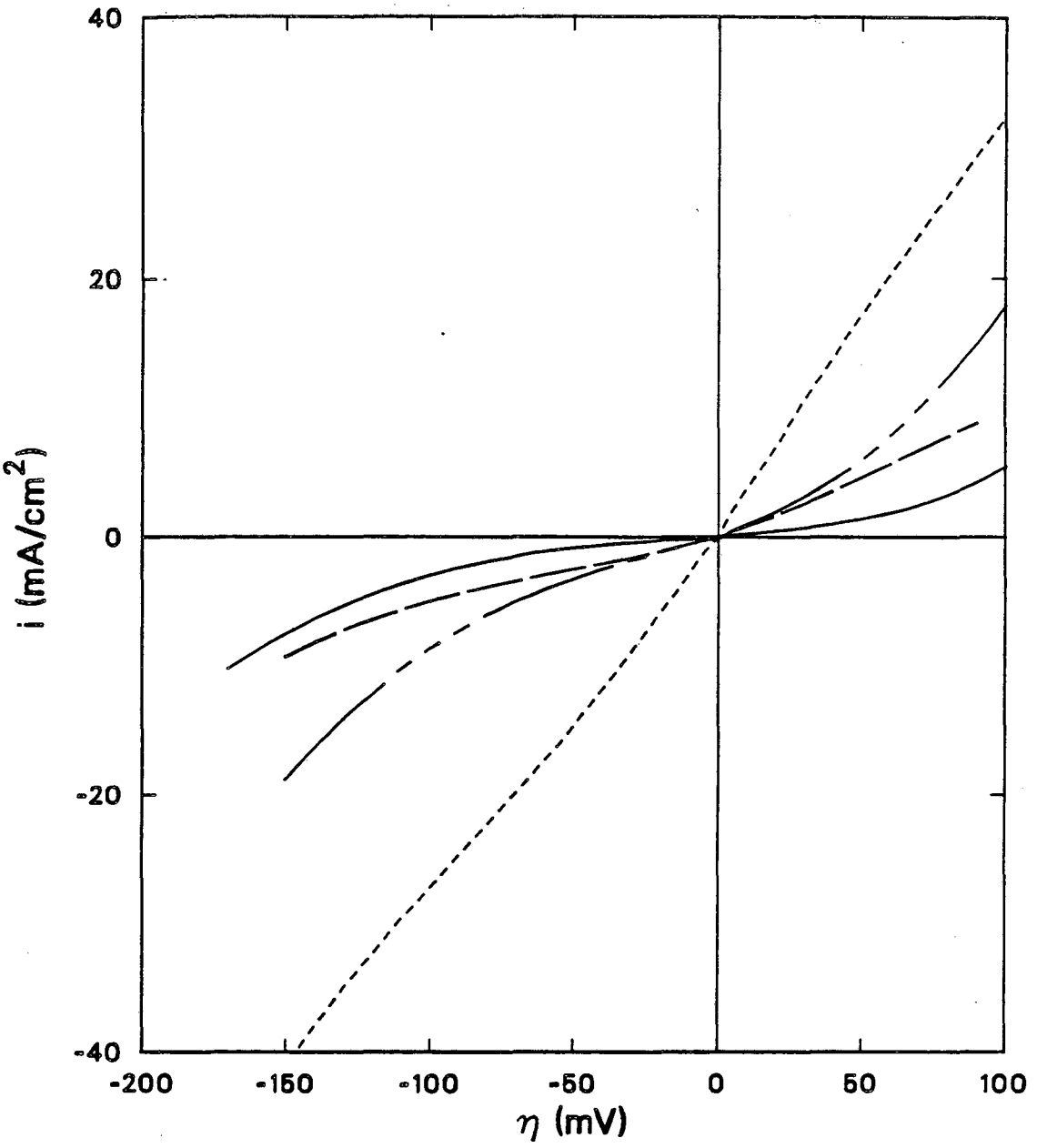


Figure 5-7: Current density versus overpotential on 2 Mo/MoS_2 expanded-metal screens at 1 liter/min flow rate:
———————, 25 °C, aqueous electrolyte;
— — — — — — —, 23 °C, 13 mole-% DMF added;
—— — — ——, 47 °C, aqueous electrolyte;
———————, 46 °C, 13 mole-% DMF added.

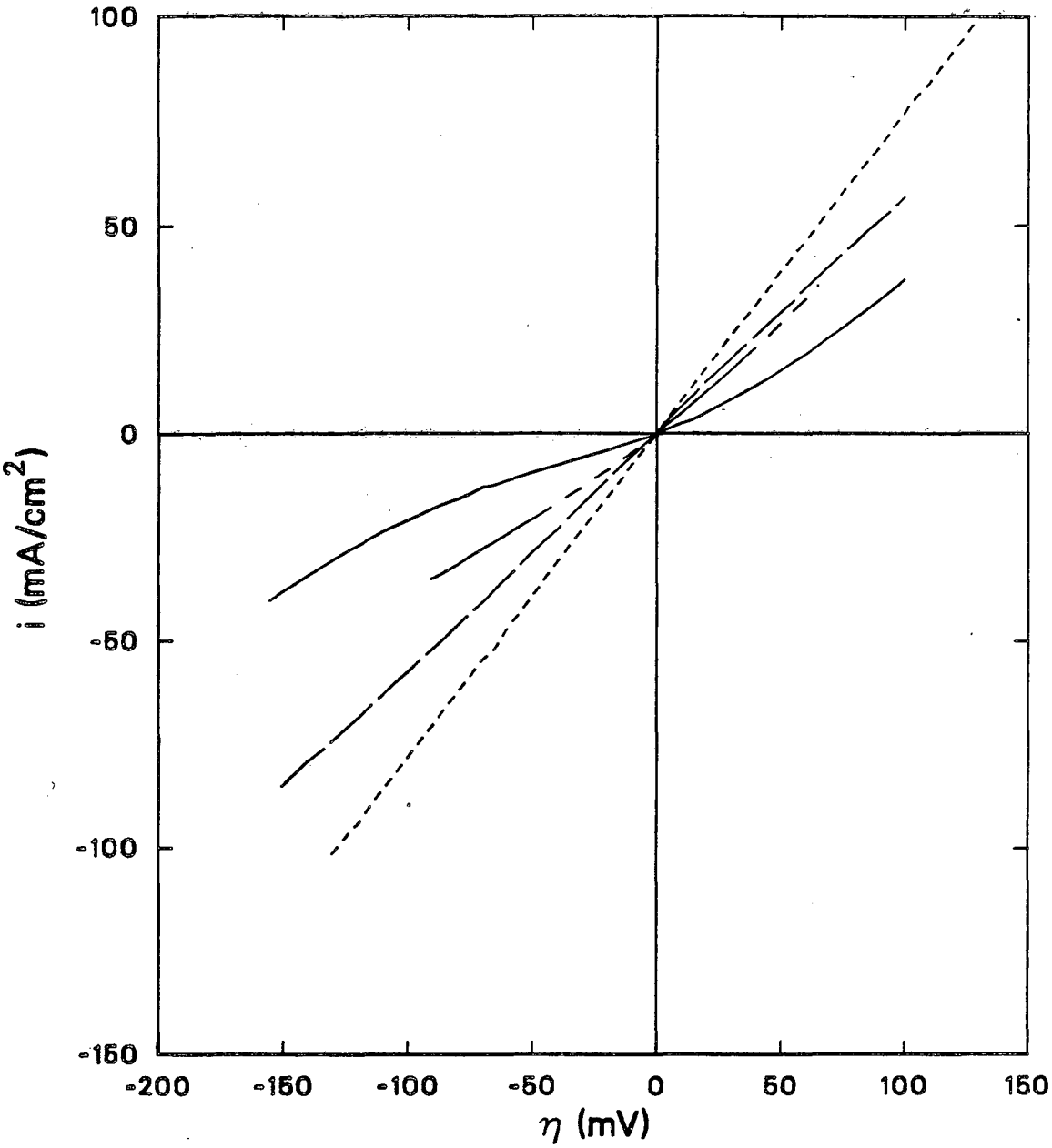


Figure 5-8: Current density versus overpotential on 2 Mo/MoS_2 expanded-metal screens at 1 liter/min flow rate:
———————, 64 °C, aqueous electrolyte;
— — — — — — —, 64 °C, 13 mole-% DMF added;
—— — — ——, 80 °C, aqueous electrolyte;
———————, 78 °C, 13 mole-% DMF added.

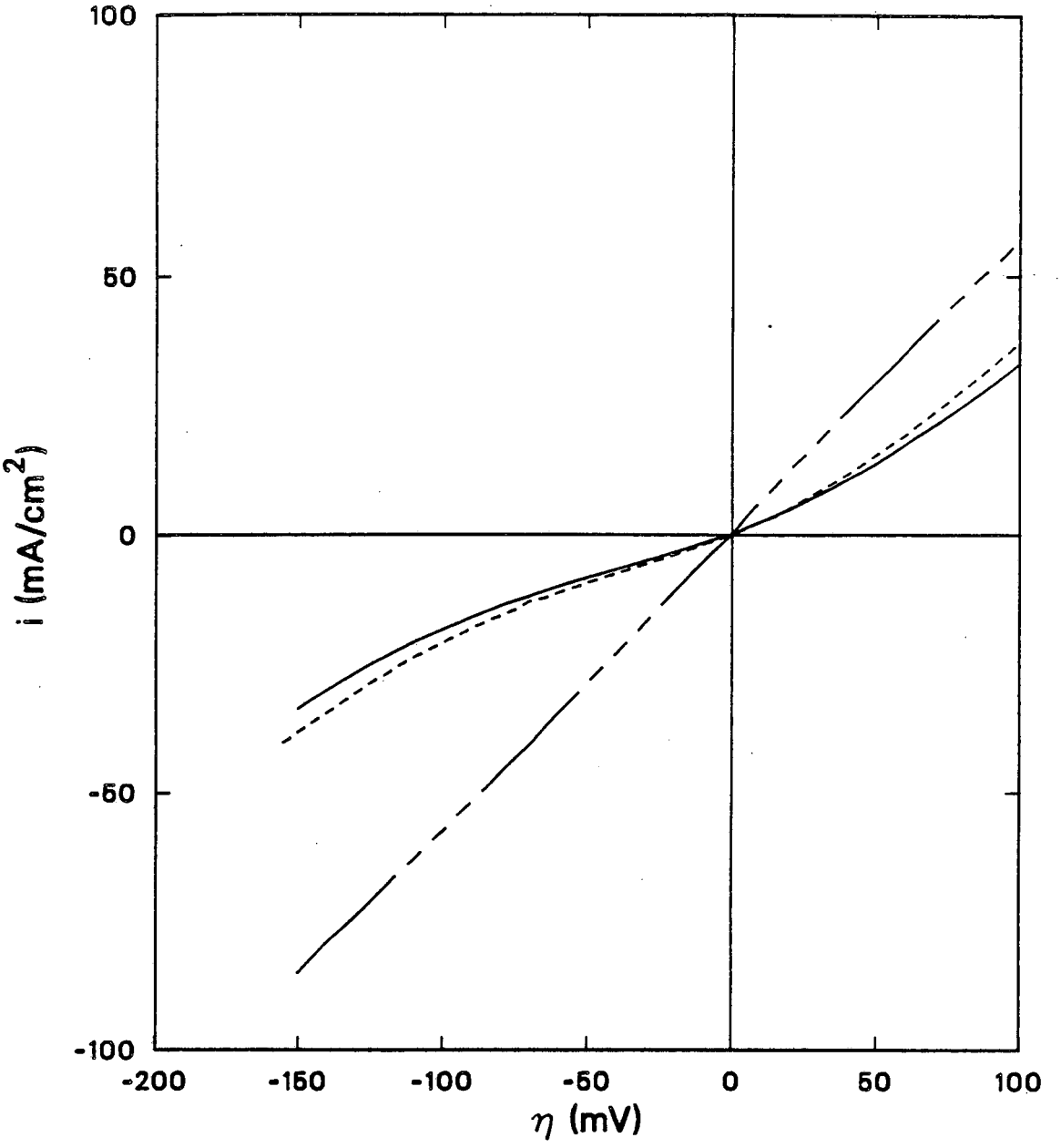


Figure 5-9: Current density versus overpotential on 2 Mo/MoS_2 expanded-metal screens:
——————, 0.1 liter/min, 64 °C, aqueous electrolyte;
——————, 1 liter/min, 64 °C, aqueous electrolyte;
—— — — ——, 1 liter/min, 64 °C with 13 mole-% DMF added.

presents corresponding results at 64 °C and 80 °C. As in the rotating disk experiments on Co and Pt, the addition of DMF increases the current density at a given overpotential and temperature. At low overpotentials, the current density using the solution with DMF at 23 °C is approximately the same as the current density at 46 °C using the solution with no DMF added. At all overpotentials, the current density at 64 °C using the solution with DMF is greater than the current density at 80 °C using the solution with no DMF.

Figure 5-9 compares the effect of flow rate and DMF addition at 64 °C. Changing the flow rate by an order of magnitude (0.1 liter/min to 1 liter/min) gives a small increase in current density. The addition of DMF results in a much larger increase in current density than that produced by an order of magnitude increase in the flow rate.

Five 100-mesh Ni screens were tested in aqueous polysulfide solution containing 1.3 M S^{2-} and 1 M S^0 at a pH of about 13.8. Figure 5-10 shows how the response changed with repeated scans at 46 °C. The electrodes were held on open circuit for 10 minutes between each scan, and the current reached a steady-state value after the 6^{th} scan. After the initial corrosion of the Ni electrodes at 46 °C, no further change in response with time was noted. The Ni electrodes were examined when the cell was disassembled; the metallic luster of the original electrodes was replaced by a grey-black coating, which did not peel off the electrode. Examination with a powder X-Ray diffractometer could not detect lines due to any NiS_x phase above the Ni background lines. The evidence suggests that a thin layer of sulfide was probably formed *in-situ* during the experiment. The layer is catalytic toward the polysulfide redox reaction and probably is protective of the Ni surface (at least on the time scale of the experiments here -- several hours).

Figure 5-11 presents results of experiments that used two Ni screens electroplated with Co. The electrolyte was 1.3 M S^{2-}, 1 M S^0 at pH 12. A photograph of the Co deposit was shown in Figure 5-4. Unlike the Ni screens, the response at the Co plated screens did not change with time. Visual examination of the Co-plated screens after the experiment showed some loss of metallic luster. This might be due to sulfidation of the underlying Ni due to incomplete coverage

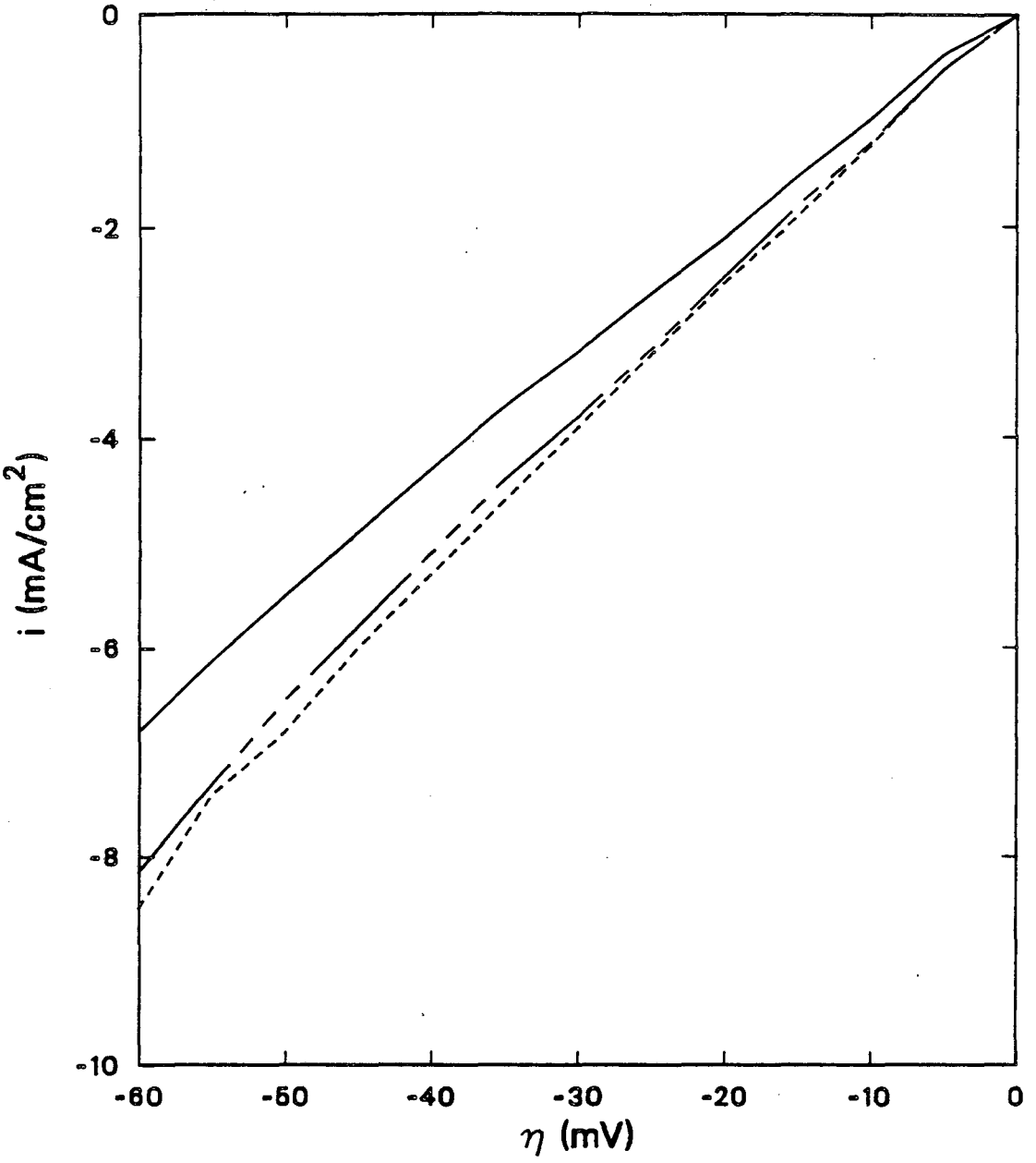


Figure 5-10: Current density versus overpotential on 5, 100-mesh Ni screens at 46 °C:
——————, initial response;
—— — — ——, 3rd scan;
- - - - - - - - - -, 6th scan.

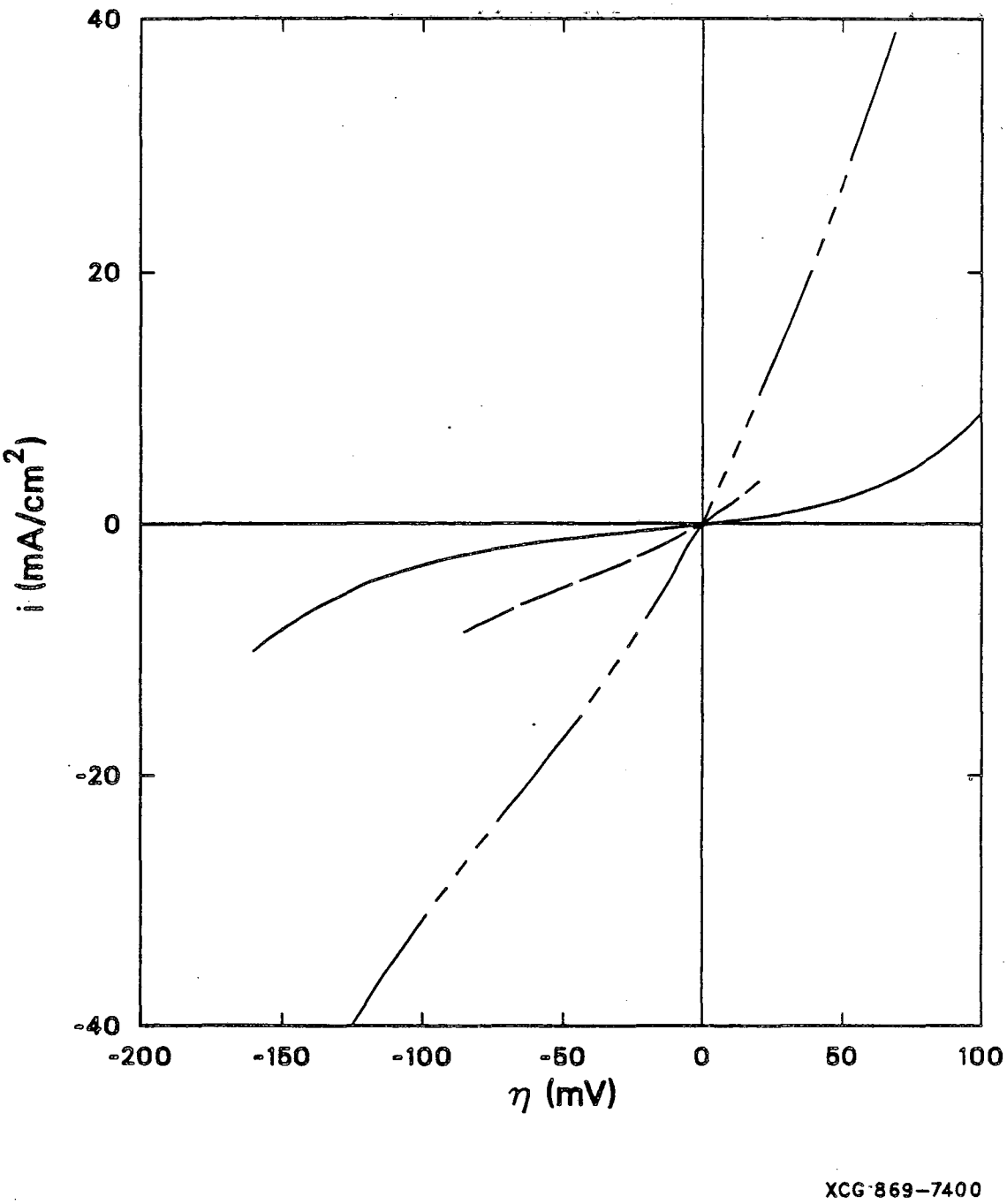


Figure 5-11: Current density versus overpotential on 2, Co plated, 100-mesh Ni screens at 1 liter/min flow rate:
———————, 23 °C;
— — — — — —, 46 °C;
—— — —— ——, 65 °C.

by the Co plate.

The Co and MoS_2 responses were similar. Table 5-3 compares the current density at -50 mV overpotential on MoS_2 and Co. The design goal of 10 to 20 mA/cm^2 at 50 mV overpotential can be met using these electrodes.

5.4. Summary

The results discussed in Chapter 4 indicated that porous electrodes were required for the counterelectrode in a PEC utilizing the aqueous sulfide/polysulfide redox couple in order to meet the design goal of supporting 10 to 20 mA/cm^2 at less than 50 mV overpotential. A flow cell for testing flow-through porous electrodes was designed and constructed using, wherever practical, wetted parts fabricated from a fluoropolymer. The system allowed testing of flow-through electrodes up to 0.5 cm in length. The cell had an upstream counter electrode and a reference electrode, and the volumetric flow rate through the 5.07 cm^2 channel could be measured precisely from 0.1 to 1.6 liters/min. External heaters allowed the temperature of the system to be varied from room temperature to 80 °C.

Pt-10% Rh electrodes and a 10 mM $K_3Fe(CN)_6/K_4Fe(CN)_6$ in 1 M KCl electrolyte were used to test the mass-transfer characteristics of the system. Mass-transfer coefficients were calculated from the limiting current plateaus at different flow rates. The results were generally in accord with previous work; the value of the Sherwood number obtained was slightly higher.

Table 5-3: Performance of Co and MoS_2 Electrodes:
Current Density (mA/cm^2) at -50 mV Overpotential

Temperature (°C)	Two 100-mesh Ni Screens Plated with Co No DMF	Two Mo expanded-metal mesh with a Deposited MoS_2 layer No DMF	Two Mo expanded metal mesh with a Deposited MoS_2 layer 13 mole-% DMF
25	-1.2	-0.8	-2.4
46	-5.0	-3.2	-14.6
65	-17	-9.2	-28.6
79		-20.5	-39.0

Ni wire mesh and Mo expanded-metal mesh were used in the aqueous polysulfide electrolyte. The Mo had a MoS_2 layer grown by reaction with S vapor at 450 °C. Some of the Ni screens were plated with Co.

The effect of electrode material, temperature, flow rate, and the addition of DMF were studied. Flow rate variation between 0.1 liter/min and 1.6 liter/min had only a small effect on the current density-overpotential curves. Raising the temperature and/or the addition of DMF had much larger effects. These observations are in accord with the steady-state results obtained on the rotating disk electrodes. The Ni electrodes showed some evidence of initial corrosion. The Co and MoS_2 electrodes gave similar responses which were more than adequate to meet the design goals.

Chapter 6

Conclusions and Recommendations

6.1. Introduction

The experimental investigations of Chapters 3 through 5 were confined to a few electrolyte compositions and electrode geometries. Those results, combined with the results of previous (photo)electrochemical investigations, are used in this chapter to derive preliminary design recommendations for electrolyte composition and electrode geometry suitable for use in practical photoelectrochemical cells and redox batteries. Section 6.2 discusses the optimization of photoelectrochemical cells. Issues relating to electrolyte composition, electrode placement, and heat and mass transfer are examined. Section 6.3 explores chemical changes that occur in a redox half-cell during cycling. In Section 6.4, suggestions for further experiments are offered.

6.2. Photoelectrochemical Cell Optimization

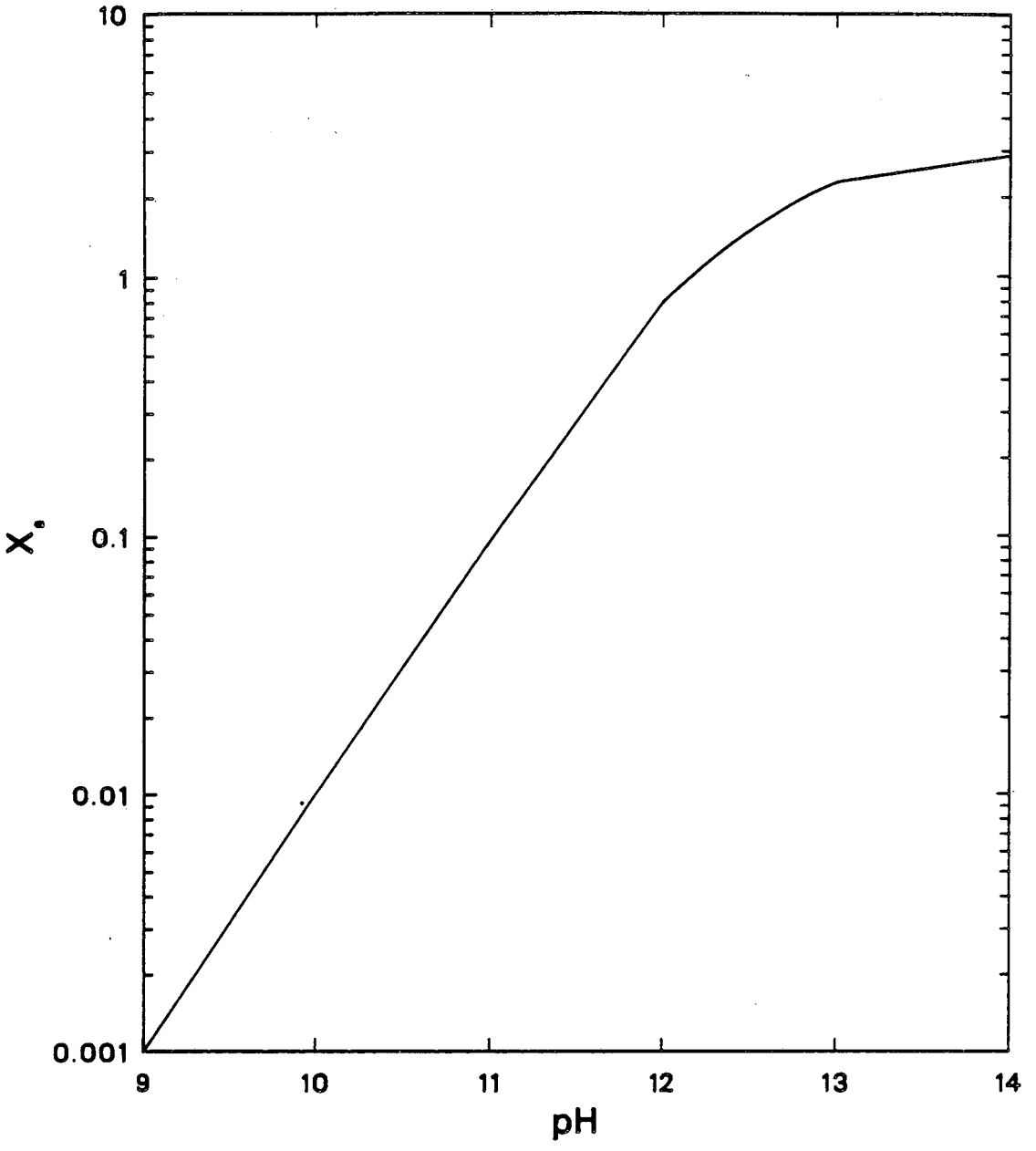
Electrolyte Composition: Stability vs. Electroactive Species Content

A regenerative photoelectrochemical cell employs an electrolyte of fixed composition; the electrochemical reaction at the counterelectrode is the reverse of the reaction at the photoelectrode. The "best" electrolyte will maximize kinetic activity at the photoelectrode and counterelectrode, be stable toward undesired chemical reactions (i.e., disproportionation), exhibit suitable transport properties, and absorb a minimum of light. It may not be possible to optimize all of the above factors at once: the best electrolyte may be a compromise among the various factors. Optimization of the electrolyte depends on the electrode configuration. For example, in a back-illuminated configuration (Figure 6-5c) absorption of light by the electrolyte may not be a factor in cell performance while in a front-illuminated configuration (Figure 6-5a) it can be a critical factor.

Strong evidence is presented in Chapters 3 and 4 for S_2^- as the electroactive species at low cathodic overpotentials; $C_{S_2^-}$ is greatest at maximum $C_{S_4^{2-}}$. Licht *et al.* (45,46) found maximum efficiencies at photoelectrodes when $C_{S_4^{2-}}$ was increased relative to the concentrations of the other polysulfide ions. Our investigations and Licht's work point toward an optimum solution composition with maximum $C_{S_4^{2-}}$. The X_s and pH that maximize $C_{S_4^{2-}}$ can be found from the equilibrium constants of Table 2-1, a material balance for sulfide and for sulfur, and a charge balance (see Appendix A). In order for oxidation of the sulfide/polysulfide couple to compete successfully with photocorrosion on semiconductor photoanodes, $C_{S(0)}$ should be near 1 M. The optimum $C_{S_4^{2-}}$ may not be achievable over a range of pH at this value of $C_{S(0)}$ because of limited sulfide solubility. The rate of disproportionation at the optimum concentration needs to be considered.

Figure 6-1 shows the value of X_s that maximizes the fraction of sulfur present as tetrasulfide (u_3) at a given pH, and Figure 6-2 shows the sensitivity of u_3 to a change in X_s. At low pH, this value of X_s is small; a large amount of uncomplexed S^{2-} (present as HS^-) is therefore needed to shift the polysulfide equilibrium toward S_4^{2-}. At a pH of 10 and a $C_{S(0)}$ of 1 M, the required value of C_{HS^-} is about 100 M. This far exceeds the solubility limit of either NaHS or KHS. Figure 6-3 shows the solubility of Na_2S and K_2S as a function of temperature (45); it is seen that the solubility of K_2S is greater than the solubility of Na_2S (8.9 m vs. 2.5 m at 25 °C). The solubilities were measured in pure M_2S (M = K^+ and Na^+) solutions; the effect of M_2S_x on M_2S solubility was not measured. The minimum X_s, i.e. that which can be achieved at 1 M $C_{S(0)}$ without sulfide precipitation, is about 0.4 with Na_2S and about 0.11 with K_2S. As pH increases, the X_s where u_3 is maximum also increases. At pH values between 11 and 14, the optimum X_s ranges from about 0.1 to 2.9. Figure 6-2 shows that the maximum is fairly broad; at pH 9 to 10, a change in X_s by a factor of five will not change u_3 by more than a few percent.

While the minimum useful pH is determined by sulfide solubility, the maximum useful pH is determined by the stability of the polysulfide solutions. Table 6-1 shows the initial rate of disproportionation at different pH values relative to the rate at pH=12. The relative rates in



XCG 869-7374

Figure 6-1: Value of X_* $\left(\frac{\sum nC_{S_nS^{2-}}}{C_{H_2S}+C_{HS^-}+C_{S^{2-}}+\sum C_{S_nS^{2-}}}\right)$ at which u_3 $\left(\frac{3 \cdot C_{S_3S^{2-}}}{C_{S(0)}}\right)$ is maximum as a function of pH.

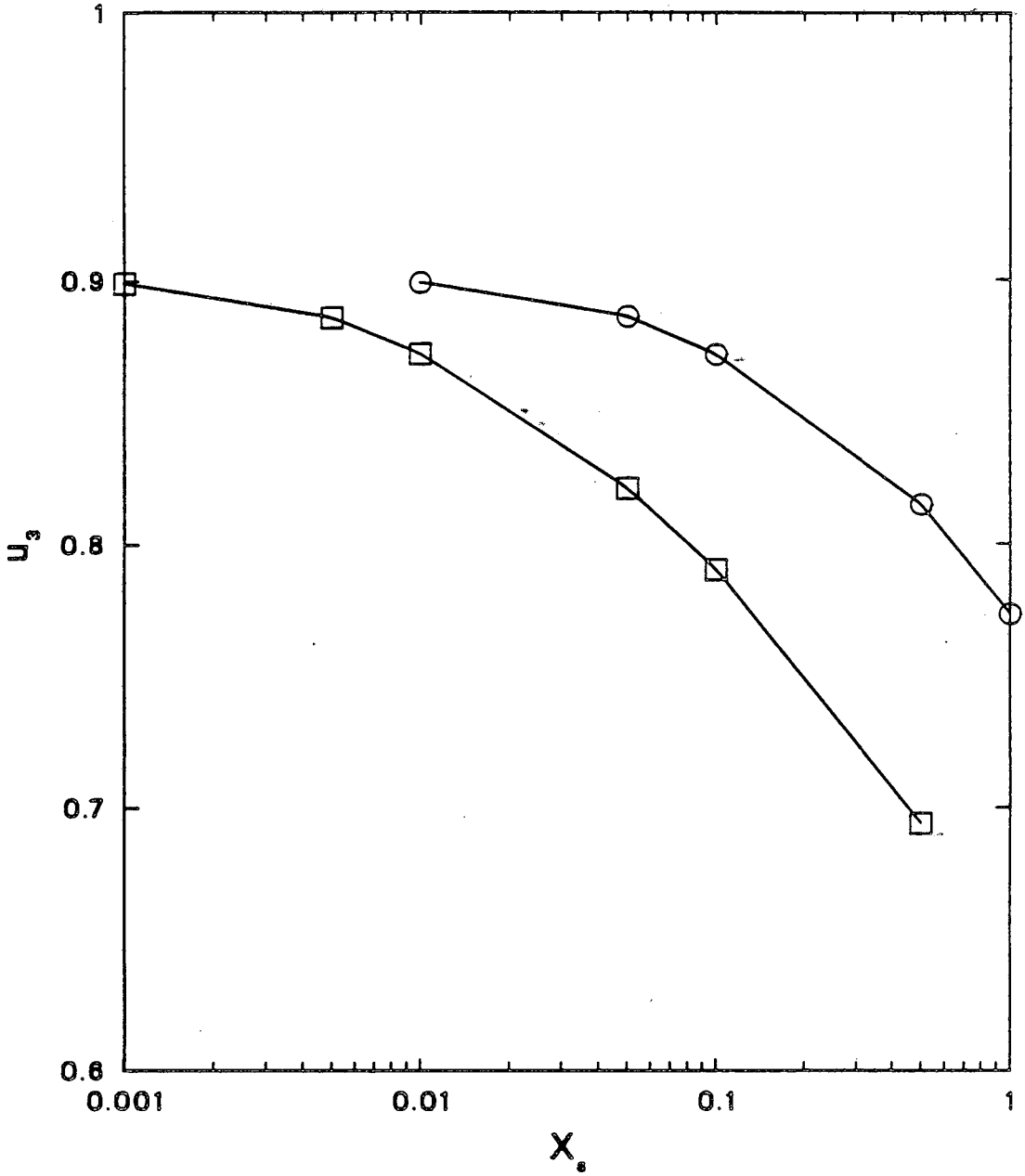


Figure 6-2: Sensitivity of u_3 $\left(\frac{3 \cdot C_{S_3S^{2-}}}{C_{S(0)}}\right)$ to a change in X_s $\left(\frac{\sum n C_{S_nS^{2-}}}{C_{H_2S}+C_{HS^-}+C_{S^{2-}}+\sum C_{S_nS^{2-}}}\right)$:

□, pH 9;
○, pH 10.

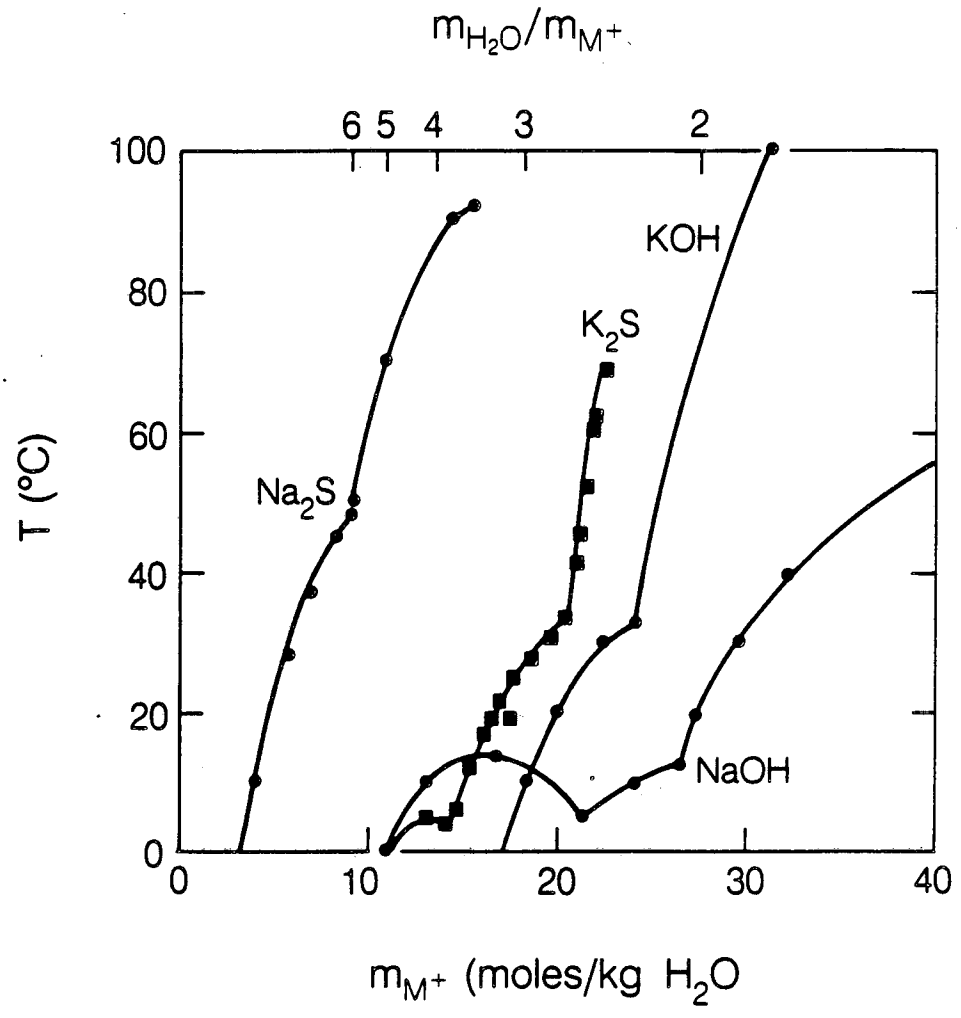


Figure 6-3: Solubility versus Temperature.
[From S. Licht, J. Manassen and G. Hodes, *J. Electrochem. Soc.*, **133**, 272 (1986), with permission of the publisher, The Electrochemical Society, Inc.]

Table 6-1: Relative Rate of Disproportionation

pH	Relative Rate
9	$1.7x10^{-3}$
10	$9.8x10^{-3}$
11	$5.1x10^{-2}$
12	1.0
13	860
14	$1.3x10^{6}$

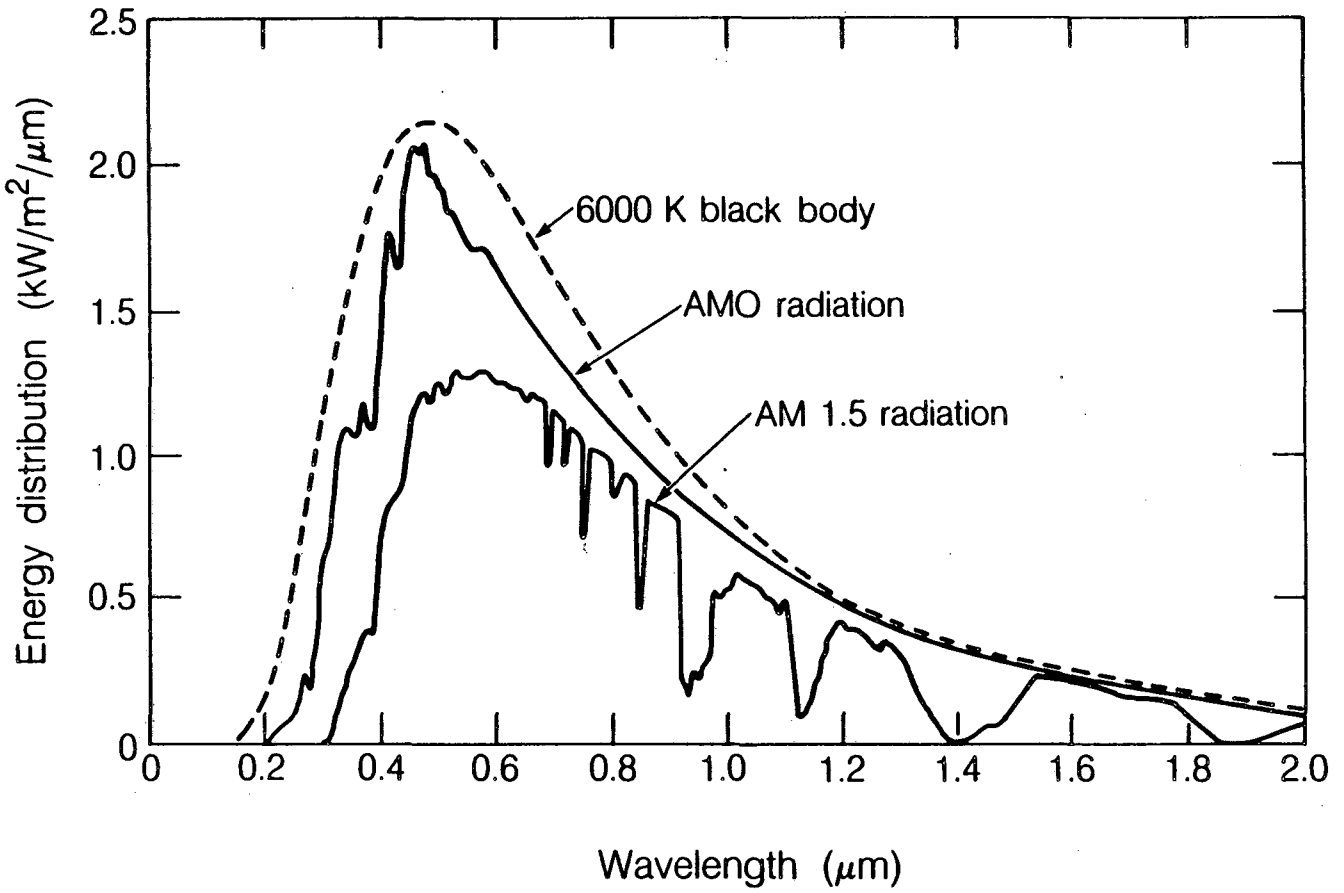
Table 6-1 are computed from Equation 2-12. At a pH of 11 and below, an X_s of 0.5 was used in the computations whereas at a pH of 12 and above the X_s used is the optimum value from Figure 6-1. The relative rate of disproportionation is increased at higher pH's because of the increased C_{OH^-} and the higher X_s needed to achieve an optimum u_3.

The best pH represents a compromise between the large amounts of uncomplexed sulfide needed at low pH to maximize u_3, and the higher disproportionation rates at high pH. At pH values from 11 to 13, reasonable values of X_s are required for an optimum u_3, and the loss of polysulfide with time due to disproportionation is reasonably low (see also Figure 2-1).

Electrolyte Composition: Light Absorption Considerations

The spectral distribution of sunlight is shown in Figure 6-4. Below about 210 nm there is very little photon flux because molecular oxygen absorbs the radiation before it can reach the earths' surface. The ultraviolet region extends from 210 nm to the visible region (380 to 780 nm). The region of maximum solar intensity is from 400 to 600 nm. Sulfide ions, polysulfide ions, and sulfur radical ions absorb light in the ultraviolet and visible regions. Due to the number of species, the absorption of light is a complicated function of wavelength. Table 6-2 shows the wavelengths of greatest molar absorptivity for the species listed in Table 2-2 (27,111).

Both HS^- and S^{2-} absorb only in the ultraviolet region, whereas the polysulfide ions show two absorption peaks. The molar absorptivity falls off rapidly away from the absorption peaks (each peak is described by a normal distribution about its maximum (27)). Thus the polysulfide peaks near 300 nm absorb very little of the solar photon flux. However, the absorption peaks in



XBL 868-11667

Figure 6-4: Spectral Distribution of Sunlight.

Table 6-2: Wavelength of Maximum Absorption[a]

Ion	λ_1 (nm)	ϵ_{m1} (liter/cm-mole)	λ_2 (nm)	ϵ_{m2} (liter/cm-mole)
HS^-	229			
S^{2-}	250			
S_2^{2-}	358	850		
S_3^{2-}	417	95	303	1140
S_4^{2-}	368	320	303	1140
S_5^{2-}	375	640	299	2000
S_2^-	595	2400		
	617[b]			

[a]Values from (27) and in
aqueous solution except where noted
[b]In DMF (111)

the range of 358 to 417 nm can significantly reduce the amount of light reaching the photoelectrode. Near 500 nm, the molar absorptivities of S_3^{2-} and S_5^{2-} are significantly greater than the molar absorptivities of S_2^{2-} and S_4^{2-}. When Licht (45) decreased X_s by adding K_2S to a solution of constant $C_{S(0)}$, the absorbance of the solution increased because of the decrease in $C_{S_4^{2-}}$ and increase in $C_{S_3^{2-}}$.

The S_2^- ion absorbs near the longer wavelength side of the region of maximum solar intensity. During the experiments reported in Chapters 4 and 5, observation of the aqueous solutions showed that they became distinctly darker as the temperature was raised. Also, the solution with 13 mole-% DMF was significantly darker than the aqueous solution. At temperatures above 70 °C, the water-DMF solution was so dark that a flashlight was needed to read the rotameter scale. Upon cooling, all solutions returned to their original state. Figure 1 of (111) shows that a 13 mole-% DMF solution has an absorbance about three times that of an aqueous polysulfide solution. Figure 1 of (32) shows large increases in absorption in the visible region when the temperature of an aqueous polysulfide solution is raised. This increase in absorption is due to an increase in $C_{S_2^-}$. These results are in accord with our visual observations.

Electrode Placement

Figure 1-1 shows a schematic representation of the major parts of a PEC. A working PEC will have to be sealed in order to protect the electrolyte from the atmosphere and prevent evaporation of the electrolyte. Figure 6-5 shows three possible cell configurations (61,120). In the front-illuminated configuration (Figure 6-5a), light passes through a counterelectrode and the electrolyte before reaching the photoelectrode. The counterelectrode must be semi-transparent: a wire grid electrode is shown in the figure, and a transparent conductor (e.g., SnO_2 or a thin metal film on SnO_2) is also a possibility. The light intensity at the photoelectrode is reduced by shadowing (due to the counterelectrode grid) and absorption of light in the electrolyte. Shadowing can be reduced by decreasing the opaque area of the counterelectrode relative to its projected area. By decreasing the active area, the activation overpotential will be increased if any interfacial kinetic limitations are present. This might be overcome by stacking high-open-area screens in a regular way such that a three-dimensional counterelectrode is formed. This has the disadvantage of increasing the thickness of the cell and thereby increasing the absorption of light by the electrolyte.

Another front-illuminated system is the slotted semiconductor configuration of Figure 6-5b. Here the counterelectrode is not in the path of the photoelectrode; a wider choice of counterelectrodes is therefore possible. The photoelectrode and counterelectrode compartments can be separated. The path length of light through the electrolyte can also be decreased. Under certain conditions, the current distribution on the photoelectrode can become non-uniform; Orazem (61) has analyzed the primary current distribution in detail. Since the photoelectrode is slotted, the photoactive area will be less than the projected area of the cell. Some thought must also be given to protection of the photoelectrode current collector from the electrolyte.

The back-illuminated configuration is shown in Figure 6-5c. As for the slotted configuration, considerable flexibility in the counterelectrode design is possible, and a separator can be used. Light does not pass through the electrolyte. The requirements for the photoelec-

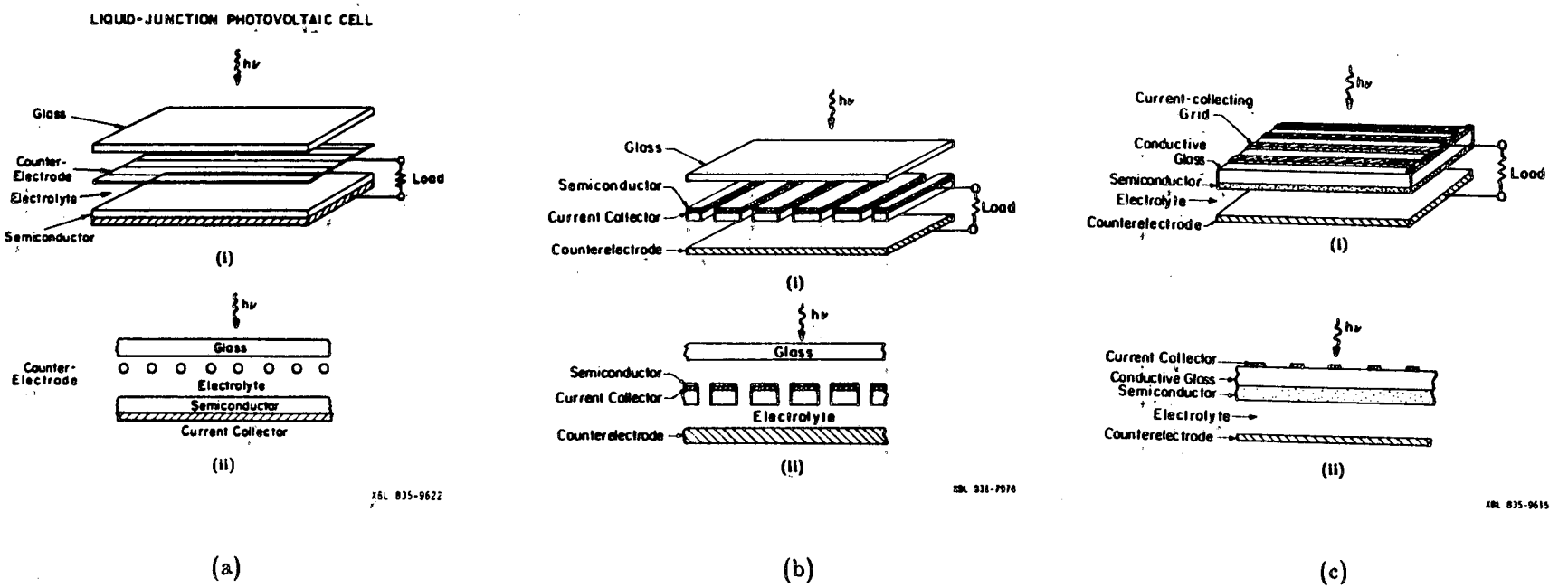


Figure 6-5: Photoelectrochemical cell designs:
(a) Front-illuminated with a wire counterelectrode
(b) Front-illuminated with a slotted semiconductor photoelectrode
(c) Back-illuminated
[From M. E. Orazem and J. Newman, *J. Electrochem. Soc.*, **131**, 2582 (1984), with permission of the publisher, The Electrochemical Society, Inc.]

trode and its current collector are somewhat different than in the front-illuminated cases. For example, because light passes directly through the current collector, it must be semi-transparent. Many such grid designs, for use in solid-state solar cells, have been considered (*cf.* Green (121)). Since light is incident on the ohmic contact instead of the semiconductor-electrolyte interface, the space charge region should extend throughout the semiconductor (in order to have efficient charge separation). This implies a thin film deposit with a thickness of a few μm. Reichman and Russak (10) discuss the practical construction of a back-illuminated system for the n-CdSe/S_x^{2-} system.

Heat Transfer

A thermal energy balance between the PEC and its surroundings will determine the operating temperature of the cell. The solar power incident on the cell is either converted into electrical power or generates heat. At the counterelectrode, heat is generated due to overpotential losses:

$$q_{ce} = i\eta_{ce} \tag{6-1}$$

In the electrolyte, infrared radiation excites rotational and vibrational modes of the molecules which is disspated as heat. Absorption of ultraviolet and visible radiation causes electronic transitions; this can also lead to heat generation. Power is also dissipated in the electrolyte by resistive heating. Thus:

$$q_e = q_{rad} + i^2R_e \tag{6-2}$$

Out of the total energy E of a photon incident on the semiconductor, only the energy E_g is used. The rest of the energy is dissipated as heat:

$$q_{pe} = \int_{E_g}^{\infty} f(E)(E-E_g)dE \tag{6-3}$$

Since all the energy incident on the cell must be accounted for, the sum of the heat produced (Equation 6-1 to 6-3) and the electrical power generated must be equal to the incident solar power:

$$q = (1-\eta_{eff})P_i \tag{6-4}$$

At steady state, the heat generation inside the cell is balanced by the heat rejection to the atmosphere. Natural convection is driven by the density difference between the hot air adjacent to the cell and the cooler air a distance from the cell. The heat transfer coefficient for natural convection (heated, horizontal plate facing upwards) is (122):

$$h_{nc} = 0.54 \cdot \frac{k'}{L}(Gr \cdot Pr)^{1/4} \tag{6-5a}$$

where

$$Gr = \frac{\rho^2 \beta g L^3 \Delta T}{\mu^2} \tag{6-5b}$$

and

$$Pr = \frac{C_p \mu}{k'} \tag{6-5c}$$

The fluid properties in Equations 6-5 are evaluated at the film temperature: $T_f=(T_c+T_a)/2$. Radiation of heat to the atmosphere is described by the Stefan-Boltzman law (122):

$$q = \sigma\left(e_c T_c^4 - e_a T_a^4\right) \tag{6-6}$$

For a transparent medium (the air), radiative heat transfer is additive with other forms of heat transfer. It is not affected by the velocity profile of the air above the cell. Forced convection heat transfer may be caused by wind currents above the cell. The forced convection heat transfer coefficient can be approximated as that due to flow over a flat plate (averaged over a plate of length L) (122):

$$h_{fc} = 0.664 \cdot \frac{k'}{L} Re'^{0.5} Pr^{0.33} \tag{6-7a}$$

where

$$Re' = \frac{\rho v_\infty L}{\mu} \tag{6-7b}$$

As in the correlation for h_{nc}, the fluid properties are evaluated at T_f.

At steady state, the heat loss is balanced by the heat input:

$$(1-\eta_{eff})P_i = h_{nc}\Delta T + \sigma\left(e_c T_c^4 - e_a T_a^4\right) + h_{fc}\Delta T \qquad (6\text{-}8)$$

Equation 6-8 can be solved iteratively for the unknown cell temperature. Appendix E discusses the solution method and shows how the physical properties of air were estimated. Figure 6-6 shows the results of these calculations. In stagnant air, the cell temperature will be 45 °C greater than the ambient air temperature; heat loss by radiation and heat loss by natural convection are equally important. The temperature difference drops quickly if wind is present; heat removal by forced convection becomes the dominant mechanism as the wind speed increases. At 1 m/sec, the model predicts a temperature difference of 21 °C. This result is in agreement with measured temperature increases for solid-state solar cells under similar atmospheric conditions (123). The temperature difference drops slowly as the wind velocity increases above 1 m/sec.

PEC's show a different behavior with temperature than solid-state photovoltaic cells. In solid-state cells, the short-circuit current is almost independent of temperature, whereas the open-circuit voltage decreases with temperature at a rate of about 2 mV/ °C. Due to the constant I_{sc} and the decrease in V_{oc}, the power output of solid-state cells decreases with increasing temperature.

In PEC's the decrease in V_{oc} with temperature is similar to that of solid-state cells. For example, McCann *et al.* (124) and Lokhande and Pawar (125) found a decrease in V_{oc} of 2-3 mV/ °C. Under load the behavior of PEC's is different from that of solid-state cells. The resistance of the electrolyte decreases with increasing temperature (see Figure 4-9). The overpotential required to support a given current density at the counterelectrode decreases with temperature. Absorption of light, due to increased $C_{S_2^-}$, increases with temperature. The disproportionation rate to thiosulfate increases rapidly with temperature. In experiments performed on CdX/S_x^{2-} systems, a maximum was found in I_{sc} with temperature (124-126). McCann *et al.* (124) attributed this increase to improved interfacial kinetics on the photoelectrode and the CoS counterelectrode plus a decrease in electrolyte resistance. Lokhande and Pawar (125) attribute the decrease in current above about 40 °C to increasing light absorption by the electrolyte. Licht

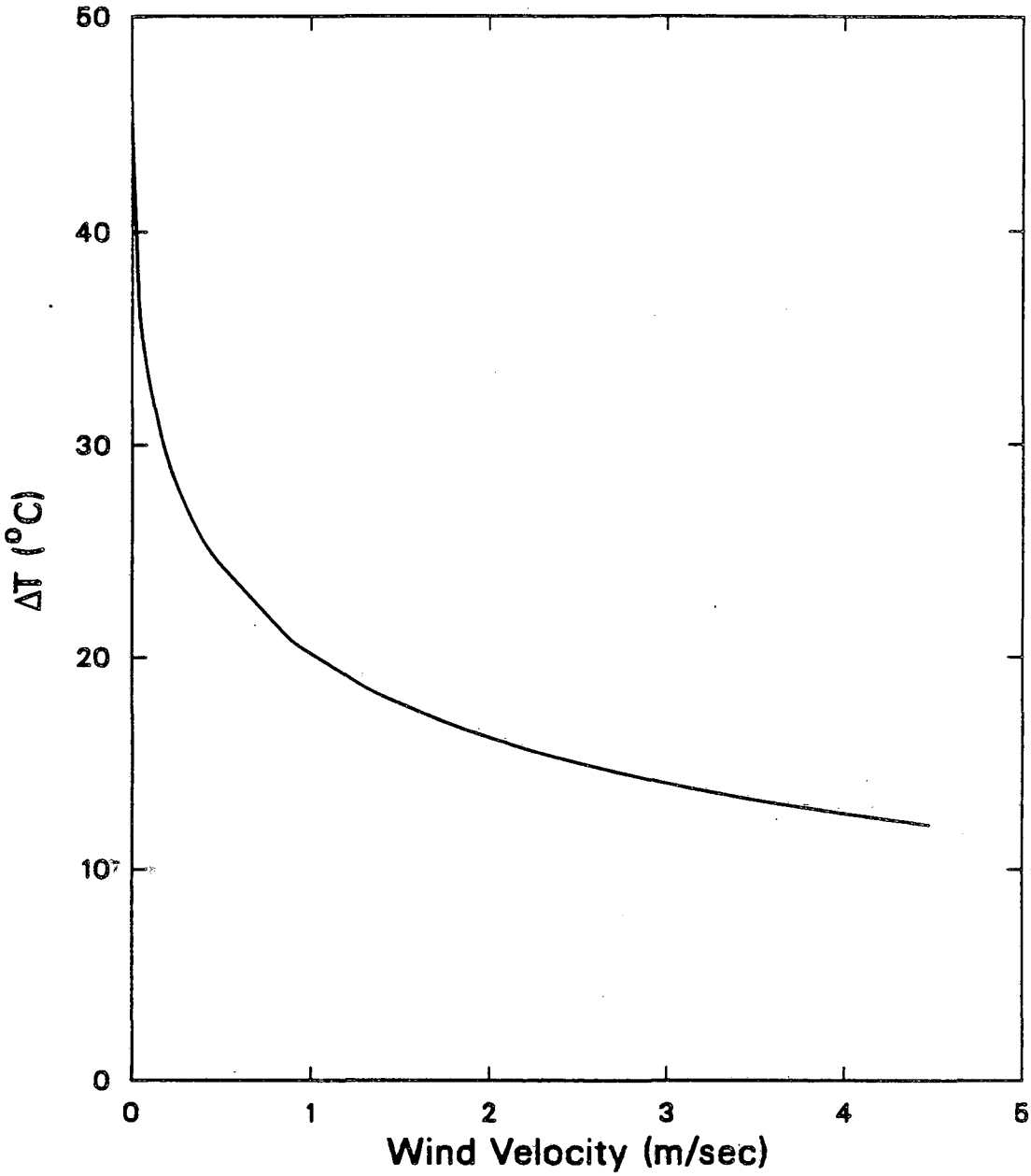


Figure 6-6: Temperature difference between a photoelectrochemical cell and ambient air at 25 °C. Cell is 3 cm long and operates at 10% efficiency under 80 mW/cm^2 solar illumination.

(127) found that roof-mounted cells at the Weizmann Institute in Israel reached 60 °C and suffered long-term degradation in performance due to polysulfide disproportionation to thiosulfate.

Mass Transfer

This thesis has been concerned primarily with improving the interfacial and homogeneous kinetics of the aqueous sulfide/polysulfide couple. Under the forced convection conditions of the rotating disk and flow-through porous electrode experiments (Chapters 4 and 5), the current density at an overpotential of 50 mV is only a small fraction of the limiting current density based on the total sulfur or sulfide concentration. The finite rate of dissociation of S_4^{2-} and slow interfacial kinetics keep the current low. The interfacial reaction rate can be increased by choosing the best electrocatalyst. Thus Co and MoS_2 are better choices than Pt. The homogeneous equilibria and reaction rates can be modified by the addition of DMF.

If heterogeneous and homogeneous kinetics could be significantly improved beyond the present state of the art, then mass transfer may become important at lower overpotentials. Cell design would then need to be considered from a mass transfer viewpoint. In a typical PEC the electrodes will be close together in order to eliminate light absorption and ohmic losses. In the absence of forced convection, stagnant diffusion and natural convection will be the mass transfer mechanisms used to supply the reactants to the electrodes. Mass transfer rates in forced convection are higher, and the electrolyte could be passed through a heat exchanger for temperature control. However, the power output of the PEC module will be reduced due to pumping losses.

6.3. Redox Batteries

Table 1-2 demonstrates that the sulfide/polysulfide redox couple is a viable candidate for a redox battery half-cell. Storage capacity (A-hr/liter) is high because polysulfide ions are fairly soluble in aqueous solution and two Faradays of electrons are released per mole of S. The redox potential of the sulfur/polysulfide couple is about -0.5 V vs. SHE. Because the complete redox

cell should have an open circuit voltage greater than 1.5 V, the standard potential of the other redox couple should be less than -2.0 V or greater than +1.0 V vs. SHE. A redox couple with a standard potential near +1.0 V is more desirable; the electrochemistry of a couple with a redox potential near -2.0 V might be complicated by hydrogen evolution, which would lead to low energy storage efficiency.

In addition to electrochemical requirements, the two redox couples must be chemically compatible. A more detailed consideration of the changes in the composition of the polysulfide electrolyte during a charge/discharge cycle is in order. If the polysulfide half-cell is the negative electrode, then sulfide will be oxidized to sulfur during discharge, i.e.

$$S^{2-} \rightleftarrows S + 2e^{-} \tag{6-9}$$

Equation 6-9 is only a schematic representation of the processes occurring in the polysulfide half-cell. A model is needed to keep track of the changes in species concentration during a charge/discharge cycle. Appendix A presents a model that calculates, at equilibrium, the species concentrations as a function of the state of charge.

The maximum amount of sulfur is present at the beginning of charge. If sulfur is present in excess of its solubility limit, then it can precipitate both from the bulk solution and at the electrode surface. Precipitation at the electrode surface will cause rapid masking of the electrode surface, which is undesirable. The sulfur solubility depends on the pH of solution and the total amount of sulfide present. Using the information presented in (27) and (37), the maximum value of X_s at a given pH is:

$$X_s = \frac{6}{\frac{6\times10^{-6}}{C_{OH^-}} + 1.75} \tag{6-10}$$

Figure 6-7 plots this maximum X_s versus pH. At a pH below 9, the sulfur solubility falls rapidly.

At the end of charging, the concentration of sulfide is at its maximum. The solubility of sulfide may be exceeded. Figure 6-3 shows the solubility of Na_2S and K_2S. K^+ is a more desirable cation from the solubility standpoint. However, Na_2S and Na_2S_4 are available commer-

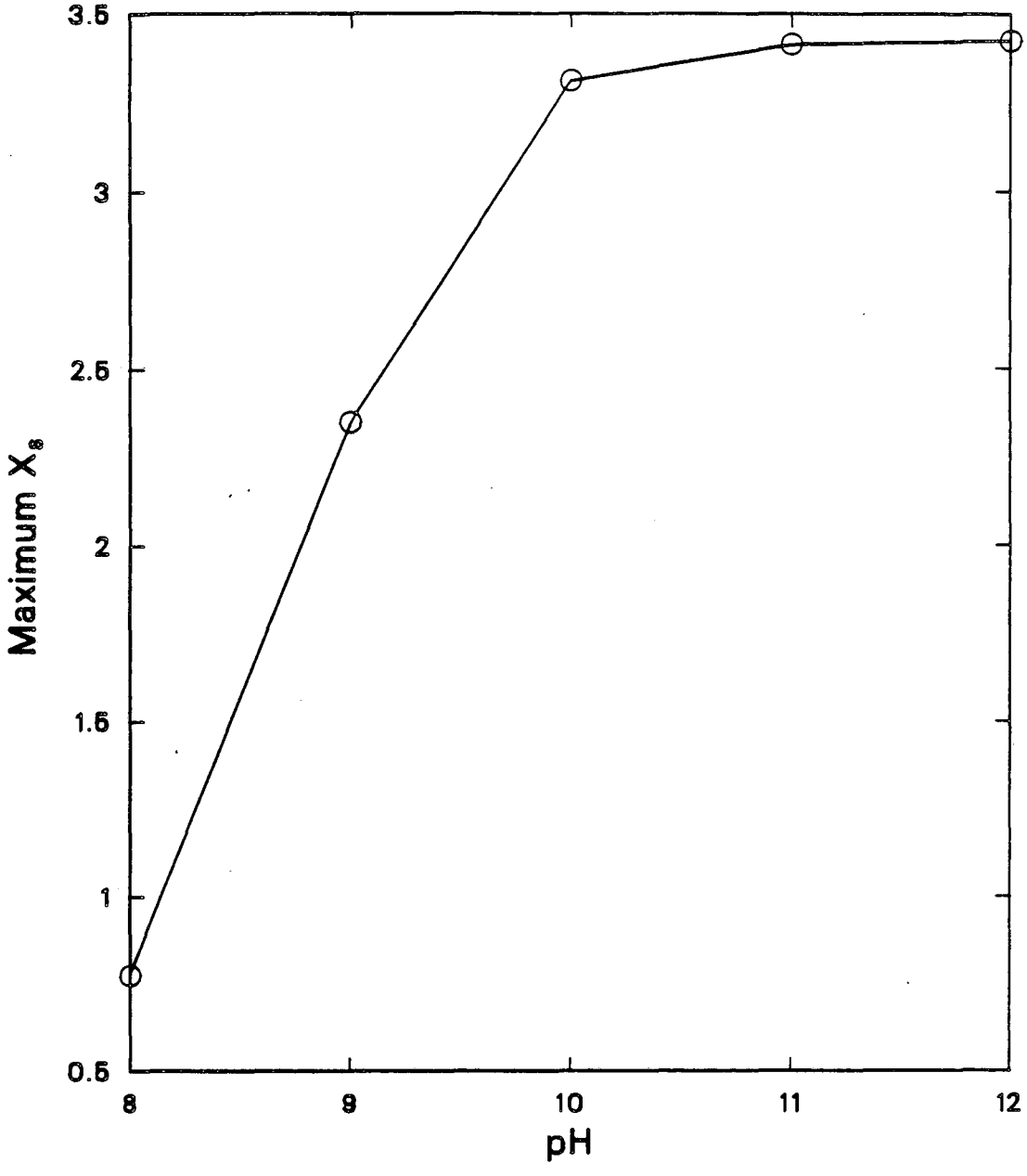


Figure 6-7: Maximum X_s $\left(\frac{\sum nC_{S_nS^{2-}}}{C_{H_2S}+C_{HS^-}+C_{S^{2-}}+\sum C_{S_nS^{2-}}}\right)$ without sulfur precipitation as a function of pH.

cially, while K_2S has to be synthesized from KOH and H_2S. This will have an effect of the overall cost of the electrolyte.

Consider an aqueous polysulfide half-cell which has at the beginning of charge: X_s=3, $C_{S(0)}$=2M, and pH=13. Under these conditions, most of the sulfide is complexed with S as polysulfides. During charge, the concentration of the polysulfides drop, and C_{HS^-} rises. Charging therefore causes the pH of the anolyte solution to rise because the polysulfides are not protonated while HS^- is protonated. Figure 6-8a shows the changes in C_{OH^-} and C_{HS^-} as the redox half-cell is charged. The pH changes from 13 at the beginning of charge to about 14.4 at a 90% state of charge. At 90% state of charge, C_{HS^-} is 2.38 M, which is near the solubility limit for Na_2S.

There are also major changes in the distribution of the polysulfide species during a charge/discharge cycle. Figure 6-8b shows the changes in the fraction of S present as S_nS^{2-} (n = 2, 3 or 4) and changes in the average polysulfide chain length as a function of the state of charge. At the beginning of charge, S_4^{2-} is by far the dominant species. At a 90% state of charge, nearly 50% of the sulfur is present as S_3^{2-}. These changes could affect the electrode kinetics and homogeneous kinetics in solution.

Due to changes in species concentration, the rate of polysulfide disproportionation varies with the state of charge. Figure 6-9b shows the disproportionation rate calculated from Equation 2-12. The rate drops as charging proceeds; the decrease in $C_{S_5^{2-}}$ and increase in C_{HS^-} more than offset the increase in pH. The greatest rate of degradation will occur if the cell is left to stand in the fully discharged state.

The aqueous polysulfide redox system is a one-phase system in the absence of any solid sulfur or sulfide phases. The electrode potential will therefore vary as the half-cell is charged and discharged. Equation 2-16 shows how the redox potential changes with composition; Figure 6-9a is an illustration of this for the example considered here. The potential changes rapidly near the beginning of charge because of the large changes in C_{OH^-} that occur there. At the end of charge,

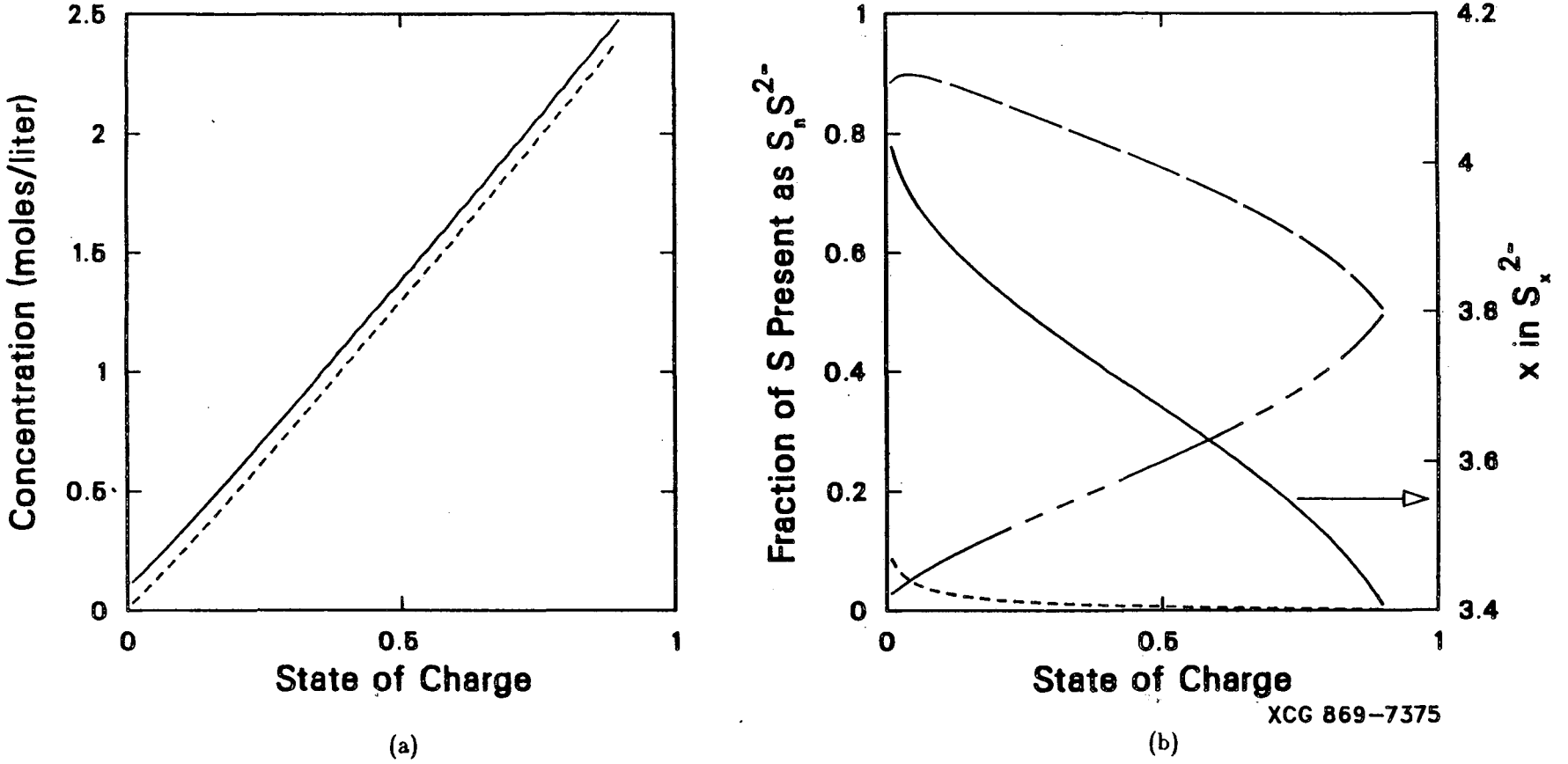


Figure 6-8: Discharge of an aqueous polysulfide half-cell with $C_{S(0)}$ = 2 M, X_s = 3, and pH = 13 at the begining of charge:
(a) Concentration versus state of charge: _____, OH^-; ----------, HS^-.
(b) Change in distribution of polysulfide species:
Fraction of sulfur present as: —— — — ——, S_3^{2-}; — — — —, S_4^{2-}; ----------, S_5^{2-};
_____, average chain length.

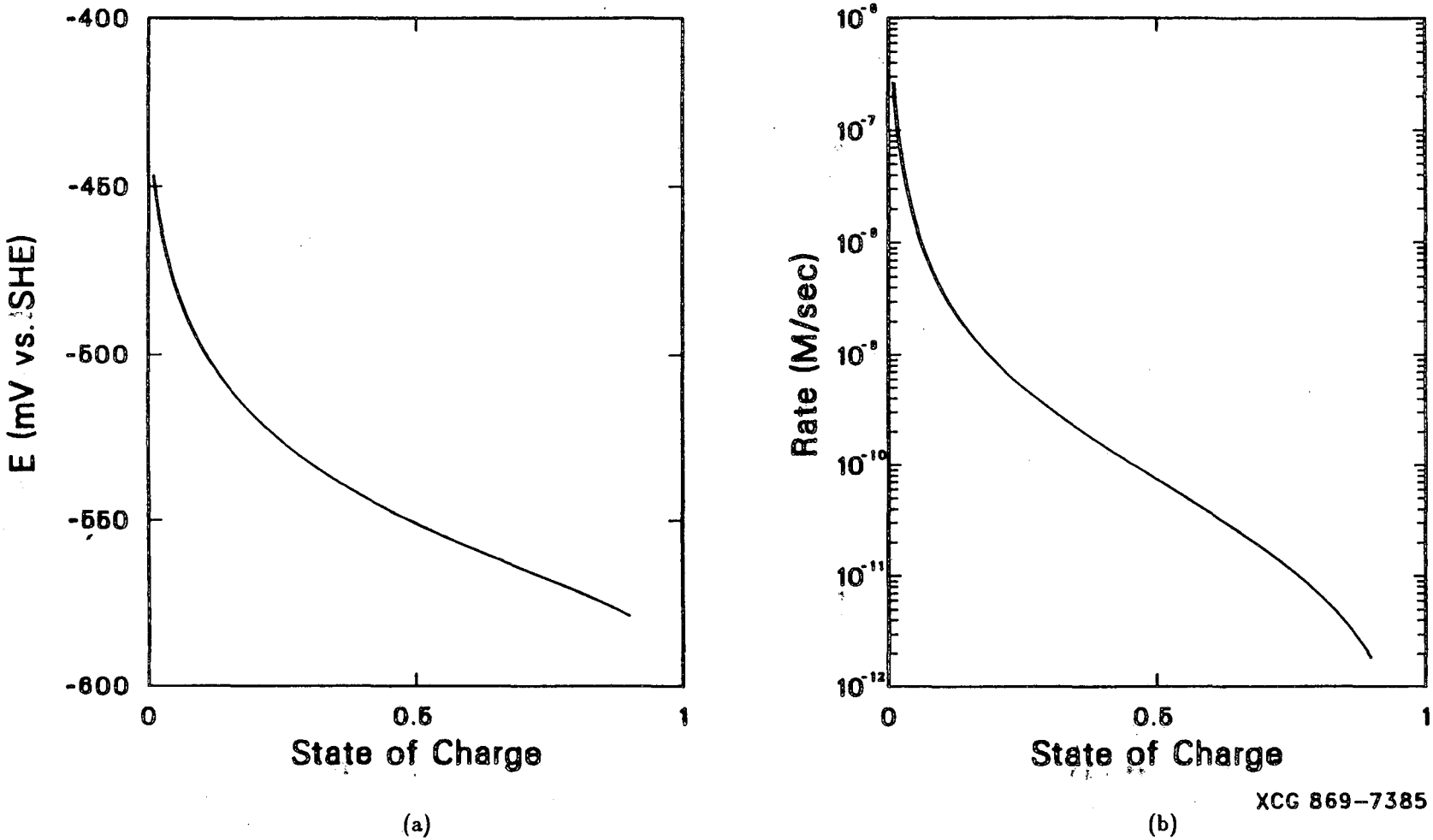


Figure 6-9: Discharge of an aqueous polysulfide half-cell with $C_{S(0)} = 2$ M, $X_s = 3$, and pH = 13 at the begining of charge:
(a) Redox potential versus state of charge.
(b) Rate of disproportionation to thiosulfate versus state of charge.

the potential again changes rapidly because $C_{S_4^{2-}} \rightarrow 0$; at a 100% state of charge the redox potential is undefined.

6.4. Recommendations

The discussion in Chapters 2 to 5 show that the mechanism of aqueous polysulfide reactions is complicated. This section discusses experiments to help further determine the mechanism of aqueous polysulfide electrode reactions and help design better aqueous polysulfide-based PEC's and redox batteries.

The addition of DMF to aqueous polysulfide solutions gives dramatic improvement in current densities on redox electrodes at a given overpotential and temperature. Yet little is known about polysulfides in water-DMF mixtures: the only investigation is that of Giggenbach (111). The equilibrium is shifted toward S_2^-, and the average polysulfide chain length is probably longer in water-DMF mixtures. Experiments using dimethylacetimide (DMAC) as a solvent have shown that polysulfides up to S_{30}^{2-} can be formed (110). Investigations into the water-DMSO system have shown that the solubility of sulfide is decreased relative to the pure aqueous solution (128), and the polysulfides in DMAC (110) could only be discharged as far as S_2^{2-} before sulfide precipitation. The solubility limits need to be quantified in order to estimate the capacity of the redox half-cell for redox batteries. The detailed distribution of species should be determined as a function of DMF content and temperature. This can be done by ultraviolet-visible spectroscopy; the absorbance values will also be useful in PEC cell design.

The long-term stability of water-DMF mixtures needs closer examination. Amides undergo hydrolysis, which is catalyzed in basic or acidic solution, e.g:

$$HCON(CH_3)_2 + H_2O \rightarrow HCOOH + HN(CH_3)_2 \qquad (6\text{-}11)$$

This hydrolysis is irreversible, but it is also slow. Preparation usually calls for refluxing over concentrated acid or base, whereas the alkalinity of the polysulfide solutions is much more mild. Giggenbach (111) did not report any decomposition of the alkaline solutions used in his study, and we have found no direct evidence for DMF decomposition in our studies. If hydrolysis is a

problem, then other organic cosolvents, that might be chemically more stable and also shift equilibrium toward S_2^-, can be evaluated. These include DMSO and acetonitrile.

Additional electrochemical studies in water-DMF mixtures should be performed. The performance of the photoanode in water-DMF mixtures should be determined. In addition to the electrochemical performance of the photoanode, its chemical stability in DMF solutions is also important. There may be an optimum amount of cosolvent; this should be found by varying the percentage of DMF in the water-DMF mixtures.

The absorption peak of S_2^- is near 600 nm, whereas the polysulfide ions absorb near 400 nm. This wide peak separation can provide the basis for coupling optical methods with electrochemical methods for mechanism determination. A cell with an optically transparent electrode (e.g., a thin film of Pt on SnO_2) can be used to determine the changes in S_2^- during an electrochemical experiment.

It was postulated that sulfur adsorption and bulk sulfur deposition are important at high anodic overpotentials, and these processes occur in parallel with polysulfide formation. In concentrated solutions it is difficult to study these adsorption processes by purely electrochemical means. Optical methods, such as reflectance spectroscopy, can be used to complement electrochemical studies.

6.5. Summary

Experiments reported in this thesis show that more efficient counterelectrodes for PEC's can be produced by increasing $C_{S_2^-}$. One method of achieving this is to increase $C_{S_4^{2-}}$. Other workers (45,46) have shown that the efficiency of photoanodes (n-CdSe, etc.) in polysulfide-based PEC's is improved when $C_{S_4^{2-}}$ is maximum. Section 6.2 discusses practical means of achieving this optimum concentration and minimizing factors detrimental to long-term PEC performance.

An optimum cell temperature may exist. A working cell may have to operate in a range around this optimum temperature. Heat generation in the cell and heat transfer between the cell

and the atmosphere will then be important. A heat transfer model is presented, and the predicted temperatures agree well with experimentally measured solid-state photovoltaic cell temperatures under similar insolation conditions.

Important aspects of polysulfide chemistry in its relation to redox battery cycling are discussed. The pH and polysulfide species distribution vary significantly during a charge/discharge cycle. This has a marked effect on the redox electrode potential and rate of disproportionation to thiosulfate.

Nomenclature

Roman

a	0.51023, Equation 4-8
a	activity
a_o	interfacial area per unit volume (cm^{-1})
A	area (cm^2)
B	$C_{HS^-}C_{OH^-}/C_{S(0)}$
C	concentration (mole/cm^3 or mole/liter)
C_{dl}	double layer capacity (F/cm^2)
C_p	heat capacity (J/g-K)
d	wire diameter (cm)
D	diffusion coefficient (cm^2/sec)
e	emissivity
e^-	electron
E	energy (eV)
E	equilibrium potential, Equations 2-16 and 2-17 (volts)
E^o	standard potential (volts)
F	Faraday (96,487 C/equiv)
f	residual
f(E)	spectral distribution of sunlight (W/cm^2-nm)
Gr	Grashof number
g(z)	defined by Equation B-8
h	distance interval
h	heat transfer coefficient (W/cm^2-°C)
h^+	hole

I	ionic strength (mole/liter)
I_{sc}	short circuit current density (A/cm^2)
i	current density (A/cm^2)
i_o	exchange current density referenced to bulk concentrations (A/cm^2)
i_o'	exchange current density referenced to surface concentrations (A/cm^2)
J	Jacobian Matrix
K_{eq}	equilibrium constant
k	rate constant
k'	thermal conductivity (W/cm-°C)
l	defined by Equation 5-1b (cm)
L	electrode length (cm)
m	mesh size (wires/inch or wires/cm)
m_o	mass transfer coefficient (cm/sec)
n	number of electrons
N	flux ($mole/cm^2$-sec)
P_i	incident solar power (W/cm^2)
Pr	Prandtl number
q	heat flux (W/cm^2)
Q	volumetric flow rate (cm^3/sec)
r	radius of disk (cm)
r	number of electrons transferred in rate determining step, Equation 3-10
R	gas constant (J/mole-K)
R_i	homogeneous reaction rates ($mole/cm^3$—sec)
R_s	uncompensated solution resistance (ohm-cm^2)
R_r	linear reaction resistance, $RT\nu/nFi_o$ (ohm—cm^2)
Re	Reynolds number
Re'	Reynolds number (Equation 6-7b)

s	number of e^- transfers occuring before the rate determining step with the electrode reaction written in the cathodic direction
s	Laplace variable (Appendix B and C)
S	sum of squares of residuals
s_o, s_r	stoichiometric coefficients for overall reaction
t	time (sec)
t_2	rise time of potential across double layer (sec)
T	temperature (K)
U	ionic mobility (cm^2–mole/J–sec)
u_n	fraction of sulfur present in S_nS^{2-}, $nC_{S_nS^{2-}}/C_{S(0)}$
v	velocity (cm/sec)
V	total overpotential between the working electrode and a reference electrode of the same kind (volts)
V_{oc}	open circuit voltage (volts)
V_{H_2O}	V_{DMF}, volume fraction of water and DMF
w	mass (grams)
W	defined by Equation 3-3 (A/cm^2)
X_k	k^{th} weight factor of 20^{th} order Hermite polynomial
X_s	$\sum nC_{S_nS^{2-}}/C_{H_2S}+C_{HS^-}+C_{S^{2-}}+\sum C_{S_nS^{2-}}$
z	distance from working electrode surface (cm)
z_i	multiple of electron charge carried by species i, Equation 3-5
z_a	anodic reaction order
z_c	cathodic reaction order

Greek

α_a, α_c	transfer coefficients
α_k	k^{th} zero of 20^{th} order Hermite polynomial

β	symmetry factor
β	in Appendix C defined by Equation C-22
β	volume coefficient of expansion (K^{-1})
γ	$nFDC_{ob}R_s(\rho\omega/\mu)^{1/2}$
γ	activity coefficient, Equation 2-17
δ	boundary layer thickness (cm)
δ	electrode thickness (Chapter 5) (cm)
ϵ	porosity
ϵ_m	molar absorptivity (liter/mole-cm)
η_{eff}	solar to electrical conversion efficiency
η_s	activation overpotential (volts)
η_d	concentration overpotential (volts)
κ	conductivity ($\Omega^{-1}cm^{-1}$)
λ	defined by Equation 3-4 ($sec^{-1/2}$)
λ_i	wavelength of maximum absorption (nm)
μ	viscosity (g/cm-sec)
ν	stoichiometric number
ρ	density (g/cm^3)
ρ'	density ($mole/cm^3$)
σ	Stefan-Boltzmann constant (W/cm^2-K^4)
σ	collision diameter, Equation E-1 (A)
Φ	potential (volts)
ω	rotation rate (rad/sec)
Ω_μ	collision integral
ς	dimensionless distance from disk

Subscripts

a	air
b	bulk
c	cell
cb	conduction band
e	electrolyte
f	film
fc	forced convection
i	species i
m	measured
L	limiting
nc	natural convection
o	species O
oc	open circuit
p	predicted
r	species R
rad	radiation
vb	valence band
w	water
y	species Y

Superscripts

*	dimensionless variable
′	first derivative

Diacritical Marks

-	Laplace transform of a variable

Abbreviations

AM	air mass
DMF	dimethylformamide
DMSO	dimethylsulfoxide
FEP	fluorinated ethylenepropylene
HMPA	hexamethylphosphoramide
PEC	photoelectrochemical cell
PTFE	polytetrafluoroethylene
rde	rotating disk electrode
rds	rate determining step
SCE	saturated calomel electrode
SHE	standard hydrogen electrode
THF	tetrahydrofuran

References

1. S. W. Angrist, *Direct Energy Conversion,* Allyn and Bacon Inc., Boston (1976).

2. F. R. Kalhammer and P. S. Zygielbaum, "Potential for Large Scale Energy Storage in Electric Utility Systems," ASME Paper No. 74-WA/Ener-9 (1974).

3. N. P. Yao and J. R. Selman, *Load Leveling,* in The Electrochemical Society Symposium Proceeding Series, The Electrochemical Society, Princeton, New Jersey (1977).

4. E. J. Cairns and E. H. Hietbrink, "Electrochemical Power For Transportation," in *Comprehensive Treatise of Electrochemistry* Volume 3, J. O'M Bockris, B. E. Conway, E. Yeager, and R. E. White, eds., Plenum Publishing Corporation, New York, 1981, p.421.

5. A. Podder and M. Kapner, *Analysis of Batteries For Use In Photovoltaic Systems,* Volumes 1 and 2, U.S. Department of Energy Report No. DOE/ET/25202-1 (1981).

6. A. Heller, K. C. Chang, and B. Miller, "Spectral Response and Efficiency Relations In Semiconductor Liquid Junction Solar Cells," *J. Electrochem. Soc.,* **124,** 697 (1977).

7. M. A. Russak, J. Reichman, H. Witzke, S. K. Deb, and S.N. Chen, "Thin Film CdSe Photoanodes For Electrochemical Photovoltaic Cells," *J. Electrochem. Soc.* **127,** 725 (1980).

8. S. Licht, R. Tenne, G. Dagen, G. Hodes, J. Manassen, D. Cahen, R. Triboulet, J. Rioux, and C. Levy-Clement, "High Efficiency n-Cd(Se,Te)/$S^{=}$ Photoelectrochemical Cell Resulting From Solution Chemistry Control," *Appl. Phys. Lett.* **46,** 608 (1985).

9. D. Cahen, G. Dagan, Y. Mirovsky, G. Hodes, W. Giriat, and M. Lubke, "Ternary Chalcogenide-Based Photoelectrochemical Cells: IV. Further Characterization of the n-$CuInS_2$ and n-$CuInSe_2$/Aqueous Polysulfide Systems," *J. Electrochem. Soc.* **132,** 1062 (1985).

10. J. Reichman and M. A. Russak, "Properties of CdSe Thin Film Electrodes For Photoelectrochemical Cells," *J. Electrochem. Soc.,* **128,** 2025 (1981).

11. M. A. Russak and C. Creter, "Vacuum Evaporated $CdSe_{1-x}Te_x$ Thin Films for Electrochemical Photovoltaic Cells," *J. Electrochem. Soc.*, **131**, 556 (1984).

12. D. Lando, J. Manassen, G. Hodes, and D. Cahen, "Transient Photocurrents and Conversion Losses In Polysulfide-Based Photoelectrochemical Cells," *J. Am. Chem. Soc.*, **101**, 3969 (1979).

13. S. Licht and J. Manassen, "The Effect of Hydroxide Ion on Cd-Chalcogenide/Aqueous Polysulfide Photoelectrochemical Cells," *J. Electrochem. Soc.*, **132**, 1079 (1985).

14. S. Licht, R. Tenne, H. Flaisher, and J. Manassen, "Cation Effects on the Electrochemistry of Anions in Polysulfide Photoelectrochemical Cells," *J. Electrochem. Soc.*, **133**, 52 (1986).

15. G. Hodes, J. Manassen, and D. Cahen, "Electrocatalytic Electrodes For The Polysulfide Redox System," *J. Electrochem. Soc.*, **127**, 544 (1980).

16. G. Hodes, J. Manassen, and D. Cahen, "Photo-electrochemical Energy Conversion: Electrocatalytic Sulphur Electrodes," *J. Appl. Electrochem.*, **7**, 181 (1977).

17. R. J. Remick and E. H. Camara, "Electrochemistry of the Sulfide/Polysulfide Couple," Lawrence Berkeley Laboratory Report No. LBL-16850 (1983).

18. M. Warshay and L. O. Wright, "Cost and Size Estimates For a Redox Bulk Energy Storage Concept," *J. Electrochem. Soc.*, **124**, 173 (1977).

19. P. S. Fedkiw and R. W. Watts, "A Mathematical Model for the Iron-Chromium Redox Battery," *J. Electrochem Soc.* **131**, 701 (1984).

20. R. P. Hollandsworth, J. Zegarski, and J. R. Selman, "Zinc/Ferricyanide Battery Development Phase IV," Sandia National Laboratory Report No. SAND85-7195 (1985).

21. R. A. Putt, A. J. Attia, P.-Y. Lu, and J. H. Heyland, "Development of Zinc-Bromine Batteries for Utility Energy Storage," Electric Power Research Institute Report No. EM-1717 (1981).

22. D. Cahen, G. Hodes, S. Licht, and J. Manassen, "A High Efficiency Thin Film Cadmium Chalcogenide Photoelectrochemical Cell With *In Situ* Storage," in *Abstracts of Presentation,* Sixth Photoelectrochemical Cell Contractors Review Meeting, Solar Energy Research Institute, Golden, Colorado (1983).

23 P. Bratin and M. Tomkiewicz, "Transport Properties of Nafion Membranes for Use in Three-Electrode Photoelectrochemical Storage Cells," *J. Electrochem. Soc.*, **129**, 2469 (1982).

24. B. Cleaver, "Properties of Polysulfide Melts," in *The Sulfur Electrode,* R. P. Tischer ed., Academic Press, New York, 1983, Chapter 2.

25. D. A. Aikens, "The Sulfur Electrode in Molten Polysulfide and in Thiocyanate Melts," *ibid.*, Chapter 4.

26. R. D. Rauh, F. S. Shuker, J. M. Marston, and S. B. Brummer, "Formation of Lithium Polysulfides In Aprotic Media," *J. Inorg. Nucl. Chem.*, **39**, 1761 (1977).

27. W. Giggenbach, "Optical Spectra and Equilibrium Distribution of Polysulfide Ions in Aqueous Solution at 20°," *Inorg. Chem.*, **11**, 1201 (1972).

28. G. Schwarzenbach and A. Fischer, "Die Acidität der Sulfane und die Zusammensetzung Wässeriger Polysulfidlösungen," *Helv. Chim. Acta.*, **43**, 1365 (1960).

29. S. R. Rao and L. G. Hepler, "Equlibrium Constants And Thermodynamics of Ionization of Aqueous Hydrogen Sulfide," *Hydrometallurgy*, **2**, 293 (1977).

30. W. Giggenbach, "Optical Spectra of Highly Alkaline Sulfide Solutions and The Second Dissociation Constant of Hydrogen Sulfide," *Inorg. Chem.*, **10**, 1333 (1971).

31. W. Giggenbach, "Equilibria Involving Polysulfide Ions in Aqueous Sulfide Solutions up to 240°," *Inorg. Chem.* **13**, 1724 (1974).

32. W. Giggenbach, "The Blue Solutions of Sulfur in Water at Elevated Temperatures," *Inorg. Chem.*, **10**, 1306 (1971).

33. A. Teder, "The Rates of Rearrangement Reactions in Aqueous Polysulfide Solutions," *Sv. Papperstidn.*, **72**, 245 (1969).

34. G. Maronny, "Fonctions Thermodynamiques Standards des Ions Sulfurés et Polysulfures en Solution Aqueuse: I. Etudes Préliminaires," *J. Chim. Phys.*, **56**, 140 (1959).

35. G. Maronny, "Fonctions Thermodynamiques Standards des Ions Sulfurés et Polysulfures en Solution Aqueuse: II. Détermination des Tensions Standards," *J. Chim. Phys.*, **56**, 202 (1959).

36. G. Maronny, "Fonctions Thermodynamiques Standards des Ions Sulfurés et Polysulfures en Solution Aqueuse: III. Calcul et Recoupement Calorimétrique," *J. Chim. Phys.*, **56**, 214 (1959).

37. A. Teder, "The Equilibrium Between Elementary Sulfur and Aqueous Polysulfide Solutions," *Acta Chem. Scand.*, **25**, 1722 (1971).

38. A. Teder, "The Spectra of Aqueous Polysulfide Solutions, I. The Resolution Into Transisition Energy Bands," *Ark. Kemi*, **30**, 379 (1969).

39. A. Teder, "The Spectra of Aqueous Polysulfide Solutions, II: The Effect of Alkalinity and Stoichiometric Composition At Equilibrium," *Ark. Kemi*, **31**, 173 (1969).

40. S. Licht, G. Hodes, and J. Manassen, "Numerical Analysis of Aqueous Polysulfide Solutions and Its Application to Cadmium Chalcogenide/Polysulfide Photoelectrochemical Solar Cells," *Inorg. Chem.*, **25**, 2486 (1986).

41. B. Meyer, K. Ward, K. Koshlap, and L. Peter, "Second Dissociation Constant of Hydrogen Sulfide," *Inorg. Chem.*, **22**, 2345 (1983).

42 K. Y. Chen and J. C. Morris, " Kinetics of Oxidation of Aqueous Sulfide by O_2," *Environ. Sci. Tech.*, **6**, 529 (1972).

43. L. Gustaffsson and A. Teder, "The Thermal Decomposition of Aqueous Polysulfide Solutions," *Sv. Papperstidn.*, **72**, 249 (1969).

44. W. Giggenbach, "Kinetics of the Polysulfide-Thiosulfate Disproportionation up to 240°," *Inorg. Chem.*, **13**, 1730 (1974).

45. S. Licht, J. Manassen, and G. Hodes, "The High Aqueous Solubility of K_2S and Its Effect on Bulk and Photoelectrochemical Characteristics of Cd(Se,Te)/$S_x^=$ Cells. I. Polysulfide Variation at Constant Sulfur/Sulfide Ratio," *J. Electrochem. Soc.* **133**, 272 (1986).

46. S. Licht and J. Manassen, "The High Aqueous Solubility of K_2S and Its Effect On Bulk and Photoelectrochemical Characteristics of Cd(Se,Te)/$S_x^=$ Cells. II. Variation of Sulfur/Sulfide Ratio," *J. Electrochem. Soc.*, **133**, 277 (1986).

47. F. W. Küster, "Beiträge Zur Kenetnis der Polysulfide. III. Die Periodischen Vorgänge bei der Elektrolyse der Polysulfide," *Z. anorg. Chem.*, **46**, 113 (1905).

48. W. R. Fetzer, "The Electrolysis of Sodium Sulphide Solutions," *J. Phys. Chem.*, **32**, 1787 (1928).

49. H. Gerischer, "Über die Auflösungsqeschwindigkeit von Schwefel in Sulfid-und Polysulfidlösungen," *Z. anorg. Chem.*, **259**, 221 (1949).

50. H. Gerischer, "Reaktionen Und periodische Vorgänge an einer Platinanode in Alkalisufidlösungen," *Z. Electrochem.*, **54**, 541 (1950).

51. P. L. Allen and A. Hickling, "Electrochemistry of Sulfur, Part 1. Overpotential in the Discharge of the Sulphide Ion," *Trans. Faraday Soc.*, **53**, 1626 (1957).

52. N. Härler, J. Libert, and A. Teder, "Beredning av Polysulfidkokvätska ur Svavel Och Vitlut," *Sv. Papperstidn.*, **71**, 65 (1968).

53. A. Teder, "Some Aspects of the Chemistry of Polysulfide Pulping," *Sv. Papperstidn.*, **72**, 294 (1969).

54. A. Teder, "Redox Potential of Polysulfide Solutions and Carbohydrate Stabilization," *Sv. Papperstidn.*, **71**, 149 (1968).

55. Z. V. Bogomolova, K. I. Tikhonov, and A. L. Rotinyan, "Redox Potentials of Sulfur in Polysulfide Solutions," *Elektrokhimiya,* **15,** 1237 (1979).

56. R. J. Remick, P. G. P. Ang, and A. F. Sammells, "On The Feasibility of Sulfur-Iodine Redox Storage Batteries," The Electrochemical Society Extended Abstracts, Volume 80-2, Hollywood, Florida, Paper No. 151 (1980).

57. R. J. Remick and P. G. P. Ang, "Electrically Recharageable Anionically Active Reduction-Oxidation Electrical Storage-Supply System," U.S. Patent 4,485,154 (1984).

58. H. Gerischer, "Semiconductor Electrochemistry," in *Physical Chemistry An Advanced Treatise,* Volume IXA, Eyring, ed., Academic Press, New York, 1970, Chapter 5.

59. H. Gerischer, "Electrochemical Photo and Solar Cells Principles and Some Experiments," *J. Electroanal. Chem.*, **58,** 263 (1975).

60. J. Reichman, "The Current-Voltage Characteristics of Semiconductor-Electrolyte Junction Photovoltaic Cells," *Appl. Phys. Lett.*, **36,** 574 (1980).

61. M. E. Orazem, "Mathematical Modeling and Optimization of Liquid-Junction Photovoltaic Cells," Lawerence Berkeley Laboratory Report, LBL-16131 (1983).

62. M. E. Orazem and J. Newman, "Mathematical Modeling of Liquid-Junction Photovoltaic Cells: I. Governing Equations," *J. Electrochem. Soc.*, **131,** 2569 (1984).

63. M. E. Orazem and J. Newman, "Mathematical Modeling of Liquid-Junction Photovoltaic Cells: II. Effect of System Parameters on Current-Potential Curves," *J. Electrochem. Soc.*, **131,** 2574 (1984).

64. A. J. Bard and M. S. Wrighton, "Thermodynamic Potential for the Anodic Dissolution of n-Type Semiconductors," *J. Electrochem. Soc.*, **124,** 1706 (1977).

65. A. J. Bard, A. B. Bocarsly, F-R. F. Fan, E. G. Walton, and M. S. Wrighton, "The Concept of Fermi Level Pinning at Semiconductor/Liquid Junctions. Consequences for Energy Conversion Efficiency and Selection of Useful Solution Redox Couples," *J. Am. Chem.*

Soc., **102**, 3671 (1980).

66. R. Haak, D. Tench, and M. Russak, "Charge Transfer via Interface States at Polycrystalline Cadmium Selenide Electrodes," *J. Electrochem. Soc.*, **131**, 2709 (1984).

67. G. Hodes, "A Thin-Film Polyscrystalline Photoelectrochemical Cell with 8% Solar Conversion Efficiency," *Nature*, **285**, 29 (1980).

68. R. S. Nicholson and I. Shain, "Theory of Stationary Electrode Polargraphy. Single Scan and Cyclic Methods Applied to Reversible, Irreversible, and Kinetic Systems," *Anal. Chem.*, **36**, 706 (1964).

69. M. L. Olmstead, R. G. Hamilton, and R. S. Nicholson, "Theory of Cyclic Voltammetry for a Dimerization Reaction Initiated Electrochemically," *Anal. Chem.*, **41**, 260 (1969).

70. A. J. Bard and L. R. Faulkner, *Electrochemical Methods*, John Wiley and Sons, New York, 1980, Chapter 9.

71. S. Bruckenstein and B. Miller, "Unraveling Reactions with Rotating Electrodes," *Accounts Chem. Res.*, **10**, 54 (1977).

72. Z. Nagy, "Error Analysis of the Potential and Voltage Step Relaxation Techniques for the Measurement of Kinetics of Electrode Reactions," *J. Electrochem. Soc.*, **129**, 1943 (1982).

73. H. Gerischer and W. Vielstich, "Zur Elektrolyse bei Konstantem Elektrodenpotential. I. Der Strom-Zeit-Verlauf bei gehemmter Entladung Mit Nachlieferung Durch Diffusion und Rückschlüsse auf die Kinetik," *Z. physik Chem. (Frankfurt)*, **3**, 16 (1955).

74. W. Vielstich and P. Delahay, "Voltage-step Method for the Kinetic Study of Fast Electrode Reactions," *J. Am. Chem. Soc.*, **79**, 1874 (1957).

75. J. Newman, *Electrochemical Systems*, Prentice-Hall, Englewood Cliffs, 1973, page 217.

76. J. O'M Bockris and A. K. N. Reddy, *Modern Electrochemistry*, Plenum Press, New York, 1970, Chapter 9.

77. J. O'M Bockris and Z. Nagy, "Symmetry Factor and Transfer Coefficient," *J. Chem. Ed.*, **50,** 839 (1973).

78. H. Reller and E. Kirowa-Eisner, "The Coulostatic Method: Mathematical Development for Multi-Step Processes," *J. Electroanal. Chem.*, **103,** 335 (1979).

79. J. Newman, *op. cit.*, pp. 385-386.

80. Z. Nagy, R. H. Land, G. K. Leaf, and M. Minkoff, "Extension of DC Transient Techniuqes to the Nonlinear Current Density-Overpotential Range and the Limitations of Linearized Approximations," *J. Electrochem. Soc.*, **132,** 2626 (1985).

81. Z. Nagy, "On The Theory Of The Potential And Voltage Step Relaxation Techniques For The Investigation Of Fast Electrode Reactions," *Electrochim. Acta,* **25,** 575 (1980).

82. A. J. Bard and L. R. Faulkner, *op. cit.*, Chapter 5.

83. D. D. Macdonald, *Transient Techniques in Electrochemistry,* Plenum Press, New York (1977).

84. J. J. More, B. S. Garbow, and K. E. Hillstrom, "User Guide for MINPACK-1," Argonne National Laboratory Report ANL-80-74 (1980).

85. K. Holub, "Relaxation of Electrode Processes with Simultaneous Consideration of Double-Layer Charging and Faradaic Current. Part I," *J. Electroanal. Chem.*, **17,** 277 (1968).

86. G. G. Susbielles and P. Delahay, "Relaxation of Electrode Processes with Simultaneous Consideration of Double-Layer Charging and Faradaic Current. Part II," *J. Electroanal. Chem.*, **17,** 289 (1968).

87. I. R. Polyvyannyi, D. A. Taraskin, and L. N. Terzeman, "Study of Equilibrium in the Mercury (II) Sulfide-Sodium Sulfide-Water System," *Chem. Abs.*, **88,** 55555g (1976).

88. P. L. Cloke, "II. Solubility of Acanthite and Covellite in Sodium Polysulfide Solutions," *Geochim. Cosmochim. Acta,* **27,** 1299 (1963).

89. J. Newman, "Ohmic Potential Measured by Interrupter Techniques," *J. Electrochem. Soc.*, **117**, 507 (1970).

90. Z. Nagy and J. L. Settle, "Cell Design Principles for the Measurement of Fast Electrode Reactions," in *Molten Salts*, M. Blander, D. S. Newman, M. L. Saboungi, G. Mamatov, and K. Johnson, ed., The Electrochemical Society Softbound Proceedings Series, Pennington, NJ, 1984, p. 534.

91. Scott, *Standard Methods of Chemical Analysis*, Volume I, Fifth ed., D. Van Nostrand Co., 1939, p. 908.

92. R. C. Reid, J. M. Prausnitz, and T. K. Sherwood, *The Properties of Gases and Liquids*, 3rd Ed., McGraw-Hill, New York, 1977, pp. 590-595.

93. *ibid*, p. 629.

94. J. E. O'Reilly and P. J. Elving, "Electrochemical Reduction of Pyrimidine in Acetonitrile: Behavior of the Anion Free Radical," *J. Am. Chem. Soc.*, **93**, 1871 (1971).

95. K. J. Laidler, *Chemical Kinetics*, 2nd ed., McGraw-Hill, New York (1965), p.200.

96. J. Newman, "Resistance for Flow of Current to a Disk," *J. Electrochem. Soc.*, **113**, 501 (1966).

97. T. Von Kármán, "Uber Laminare und Turbulente Reibung," *Z. angew. Math. i. Mech.*, **1**, 233 (1921).

98. R. White, C. M. Mohr Jr., P. Fedkiw, and J. Newman, "The Fluid Motion Generated By a Rotating Disk: A Comparison of Solution Techniques," Lawrence Berkeley Laboratory Report No. LBL-3910 (1975).

99. V. G. Levich, *Physicochemical Hydrodynamics*, Prentice-Hall, Englewood Cliffs, New Jersey 1962, Chapter 2.

100. A. J. Bard and L. R. Faulkner, *op. cit.*, Chapter 8.

101. J. Koutecky and V. G. Levich, "The Application of the Rotating Disk Electrode to the Study of Kinetic and Catalytic Processes in Electrochemistry," *Dolk. Akad. Nauk. SSSR,* **117,** 441 (1957).

102. J. Koutecky and V. G. Levich, "The Application of the Rotating Disk Electrode to the Study of Kinetic and Catalytic Processes," *Zhur. Fiz. Khim.,* **32,** 1565 (1958).

103. V. G. Levich, *op. cit.,* Chapter 6.

104. D. G. Wierse, M. M. Lohrengel, and J. W. Shultze, "Electrochemical Properties of Sulfur Adsorbed on Gold Electrodes," *J. Electroanal. Chem.,* **92,** 121 (1978).

105. I. C. Hamilton and R. Woods, "An Investigation of the Deposition and Reactions of Sulphur on Gold Electrodes," *J. Appl. Electrochem.,* **13,** 783 (1983).

106. R. Tenne, N. Müller, Y. Mirovsky, and D. Lando, "The Relation Between Performance and Stability of Cd-Chalcogenide/Polysulfide Photoelectrochemical Cells. I. Model and the Effect of Photoetching," *J. Electrochem. Soc.,* **130,** 852 (1983).

107. K. W. Frese, Jr. and D. Canfield, "Photocorrosion of n-CdSe in Sulfide Electrolytes," *J. Electrochem. Soc.,* **132,** 1649 (1985).

108. N. Hartler, J. Libert, and A. Teder, "Rate of Sulfur Dissolution in Aqueous Sodium Sulfide," *I&EC Proc. Design. Dev.,* **6,** 398 (1967).

109. R. J. H. Clark and D. G. Cobbold, "Characterization of Sulfur Radical Anions in Solutions of Alkali Polysulfides in Dimethylformamide and Hexamethylphosphoramide and in the Solid State in Ultramarine Blue, Green and Red," *Inorg. Chem.,* **17,** 3169 (1978).

110. K. M. Abraham, R. D. Rauh, and S. B. Brummer, "A Low Temperature Na-S Battery Incorporating a Soluble S Cathode," *Electrochim. Acta,* **23,** 501 (1978).

111. W. Giggenbach, "On the Nature of the Blue Solutions of Sulfur," *J. inorg. nucl. Chem.,* **30,** 3189 (1968).

112. W. Giggenbach, personal communication (1986).

113. M. Matlosz and J. Newman, "Use of a Flow-Through Porous Electrode for Removal of Mercury from Contaminated Brine Solutions," in *Transport Processes in Electrochemical Systems,* R. S. Yeo, T. Katan and D. T. Chin eds., The Electrochemical Society Symposium Proceeding Series, The Electrochemical Society, Pennington, New Jersey, 1982, p.53.

114. M. Barak, *Electrochemical Power Sources. Primary and Secondary Batteries,* Institution of Electrical Engineers, London (1980).

115. J. C. Armour and J. N. Cannon, "Fluid Flow Through Woven Screens," *AIChE J.,* **14,** 415 (1968).

116. Anonymous, "Periodic Reverse Plating of Nickel and Cobalt," *Electroplating,* **3,** 89 (1951).

117. J. E. Dutrizac, "The Reaction of Sulphur Vapour with Molybdenum Metal," *Can. Met. Quart.,* **9,** 449 (1970).

118. R. E. Sioda, "Flow-Through Electrodes Composed of Parallel Screens," *Electrochim. Acta.,* **22,** 439 (1977).

119. J. Cano and U. Böhm, "Mass Transfer in Packed Beds of Screens," *Chem. Eng. Sci.,* **32,** 213 (1977).

120. M. E. Orazem and J. Newman, "Mathematical Modeling of Liquid-Junction Photovoltaic Cells: III. Optimization of Cell Configurations," *J. Electrochem. Soc.,* **131,** 2582 (1984).

121. M. A. Green, *Solar Cells,* Prentice-Hall, Englewood Cliffs, New Jersey (1982).

122. R. H. Perry and C. H. Chilton, eds., *Chemical Engineers Handbook,* Fifth Ed., McGraw-Hill, New York, 1973, Chapter 10.

123. J. W. Stultz and L. C. Wen, *Thermal Performance Testing and Analysis of Photovoltaic Modules in Natural Sunlight,* JPL Document No. 5105-31 (1977).

124. J. F. McCann, M. S. Kazacos, and D. Haneman, "Temperature Dependence for the Power Outputs of n-CdSe Liquid Junction Cells," *Nature,* **289,** 780 (1981).

125. C. D. Lokhande and S. H. Pawar, "Effect of Temperature on the Performance of the Photoelectrochemical Cells Formed with Chemically Deposited CdS Films," *Solar Energy Mat.*, **7**, 313 (1982).

126. P. Bratin and M. Tomkiewicz, "Solar to Thermal+Electrical Energy Conversion by Polycrystalline Liquid Junction Solar Cells," in *Photoelectrochemistry: Fundamental Processes and Measurement Techniques*, W. L. Wallace, A. J. Nozik, S. K. Deb, and R. H. Wilson eds., The Electrochemical Society Symposium Proceedings Series, The Electrochemical Society, Pennington, New Jersey, 1982, p. 704.

127. S. Licht, "Combined Solution Effects Yield Stable Thin-Film Cd(Se,Te)/Polysulfide Photoelectrochemical Solar Cells," *J. Phys. Chem.*, **90,** 1096 (1986).

128. B. A. Trofimov, G. K. Musorin, and S. V. Amosova, "Characteristics of Sodium Sulfide Solubility in the System Water-Dimethylsulfoxide," *Z. Prikl. Khim.*, **51,** 1190 (1978).

129. J. L. Settle and Z. Nagy, "Metal Deposition-Dissolution in Molten Halides: On the Question of Measurability of Very Fast Electrode Reaction Rates," *J. Electrochem. Soc.*, **132,** 1619 (1985).

130. E. Santos, T. Iwasita, and W. Vielstich, " On the Use of the Coulostatic Method for the Investigation of Fast Redox Systems," *Electrochim. Acta*, **31,** 431 (1986).

131. J. Mandel, *The Statistical Analysis of Experimental Data*, New York, Dover Publications Inc., 1964, Chapter 7.

132. Z. Nagy, " On Computer Curve-Fitting Data-Evalution of Relaxation Techniques for Electrode Kinetic Investigations," *Electrochim. Acta*, **29,** 917 (1984).

133. IMSL Library Reference Manual, IMSL-LIB-0009, Houston, Texas, 1982, p. ZXSSQ-1.

134. Z. Nagy, "Comparison of Computer Curve-Fitting and Graphical Data Evaluations of the Galvanostatic Double Pulse Relaxation Technique for the Measurement of Kinetics of Electrode Reactions," *J. Electrochem. Soc.*, **128,** 786 (1981).

135. Z. Nagy, "Comparison of Computer Curve-Fitting and Graphical Data Evaluation of the Galvanostatic Relaxation Technique for the Measurement of Kinetics of Electrode Reactions," *Electrochim. Acta,* **26,** 671 (1981).

136. H. E. Salzer, R. Zucker, and R. Capuano, "Table of the Zeros and Weight Factors of the First Twenty Hermite Polynomials," *J. Res. natn. Bur. Stand.,* **48,** 111 (1952).

137. A. J. Bard and L. R. Faulkner, *op. cit.,* p.683.

138. L. Lapidus, *Digital Computation for Chemical Engineers,* McGraw-Hill, New York, 1962, Chapter 4.

139. E. K. Yung and R. C. Alkire, "Analysis of Laboratory Data in Early Stages of Evaluation of Electro-Organic Reactions," *J. Electrochem. Soc.,* **132,** 2341 (1985).

140. J. Newman, "Numerical Solution of Coupled, Ordinary Differential Equations," *Ind. Eng. Chem. Fund.,* **7,** 514 (1968).

141. J. Newman, *Electrochemical Systems, op. cit.,* Appendix C.

142. H. Reller and E. Kirowa-Eisner, "The Galvanostatic Method: Analysis of Error and Computation of Parameters," *J. Electrochem. Soc.,* **129,** 1473 (1982).

143. F. B. Hildebrand, *Advanced Calculus For Applications,* Prentice-Hall, Englewood Cliffs, New Jersey, 1976, p. 477.

Appendix A

Computer Programs For Ionic Equilibrium Calculations

A.1. Introduction

To calculate the concentrations of species in solution, a charge balance and a material balance for total sulfide and total sulfur are needed in addition to the equilibrium expressions of Table 2-1. The charge balance is:

$$C_{H^+} + C_{Na^+} = C_{HS^-} + C_{OH^-} + C_{S_2^-} + 2\cdot\left(C_{S^{2-}} + C_{S_2^{2-}} + C_{S_3^{2-}} + C_{S_4^{2-}} + C_{S_5^{2-}}\right) \quad \text{(A-1)}$$

The material balance for sulfide is:

$$\text{total sulfide} = C_{H_2S} + C_{HS^-} + C_{S^{2-}} + C_{S_2^{2-}} + C_{S_3^{2-}} + C_{S_4^{2-}} + C_{S_5^{2-}} + 0.5\cdot C_{S_2^-} \quad \text{(A-2)}$$

And the material balance for sulfur:

$$C_{S(0)} = C_{S_2^{2-}} + 1.5\cdot C_{S_2^-} + 2\cdot C_{S_3^{2-}} + 3\cdot C_{S_4^{2-}} + 4\cdot C_{S_5^{2-}} \quad \text{(A-3)}$$

In the pH range of 9-14, the major species are:

Na^+
OH^-
HS^-
S_3^{2-}
S_4^{2-}
S_5^{2-}

The charge and material balances were solved for these species. The concentrations of the (stoichiometric) minor species were then found from their equilibrium expressions.

A.2. Programs for Calculating Quatities of Chemicals Required

```
C Calculate amount of hydrogen sulfide to add to a sodium sulfide-sulfur
C solution to get a given final pH
C Also calculate distribution of polysulfide ions, average polysulfide
C chain length and sulfur to sulfide ratio


      Real*8 wk(182),x(6),par(7),fnorm
      Integer n,itmax,ier
      External fcn

C Equilibrium constants from Giggenbach
      par(5) = 2.e-4
      par(6) = 1.8e-2
      par(7) = 4.e5

C Get sodium sulfide concentration, final pH and sulfur concentration
      Read (5,10) par(1),par(3),par(4)
10    Format (3f16.7)

C Concentration of Na ions is twice that of sodium sulfide
C Calculate hydrogen ion concentration
      par(1) = 2.*par(1)
      par(2) = 1.e-14/par(3)

      n=6
      nsig=7
      itmax=100

C Initial guesses
      x(1) = par(4)
      x(2) = 0.0
      x(3) = 0.0
      x(4) = par(4)/3.
      x(5) = 0.0
      x(6) = 0.5*par(4)
      Call ZSCNT(fcn,nsig,n,itmax,par,x,fnorm,wk,ier)

      Write (6,15) par(1)/2.,par(4),-dlog10(par(2))
15    Format (' Sodium Sulfide added = ',f8.4,' M',/
     1,' Sulfur added = ',f8.4,' M',/
     2,' pH = ',f8.4)
      Write (6,18) x(6)
18    Format (' Hydrogen Sulfide needed = ',f8.4,' M')
      Write (6,20) par(4)/x(1)
20    Format (' Sulfur to Sulfide ratio = ',f8.4)

      avgn=(x(2)+2.*x(3)+3.*x(4)+4.*x(5))/(x(2)+x(3)+x(4)+x(5))
      Write (6,25) avgn+1.
25    Format (' Average Polysulfide Chain Length = ',f8.4)
      Write (6,27)
```

```
27      Format (' Distribution of Polysulfide Ions',/,
   1' Polysulfide Ion',4x,'moles/liter',2x,'Percent of Sulfur')
        Write (6,28) x(2),x(2)*100./par(4),x(3),x(3)*200./par(4)
28      Format (' disulfide',9x,1pe11.3,4x,0pf8.4,/
   1,' trisulfide',8x,1pe11.3,4x,0pf8.4)
        Write (6,29) x(4),300.*x(4)/par(4),x(5),400.*x(5)/par(4)
29      Format (' tetrasulfide',6x,1pe11.3,4x,0pf8.4,/
   1,' pentasulfide',6x,1pe11.3,4x,0pf8.4)
        Stop
        End
```

```
      Subroutine fcn (x,f,n,par)
      Real*8 x(6),f(6),par(7)

      f(1) = par(1)+par(2)-par(3)-x(1)-2.*(x(2)+x(3)+x(4)+x(5))
      f(2) = par(4)-x(2)-2.*x(3)-3.*x(4)-4.*x(5)
      f(3) = par(1)/2. +x(6)-x(1)-x(2)-x(3)-x(4)-x(5)
      f(4) = par(5)*x(3)*x(1)*par(3)-x(2)*x(2)
      f(5) = par(6)*x(4)*x(4)*x(1)*par(3)-x(3)*x(3)*x(3)
      f(6) = par(7)*x(5)*x(5)*x(5)*x(1)*par(3)
     1-x(4)*x(4)*x(4)*x(4)
      Return
      End
```

A.3.
Programs for Electrochemical Equilibria

```
      Real*8 x(5),par(5),fnorm,wk(138),save(8,90)
      Real*8 B,nbar,cterm,rate,kf
      Real*8 xsubs,R,T,F,E,E0,OH0,S0
      Real*8 dlog,dfloat,dlog10,add
      Integer nsig,n,itmax,ier
      External fcn1,fcn2
      Data R,F /8.314,96487.0/
      Data E0 /-536.0/

C Variables and parameters
C B, HS*OH/S(0)
C F, Faraday (96487 coul/equiv)
C fcn1, subroutine containing material balances, equil. express., etc.
C ier, error parameter from ZSCNT, ier of 129 or 130 indicates error
C itmax, maximum number of iterations
C kf, foward rate constant for disproportionation
C n, number of variables
C nsig, number of decimal places that solution is good to
C par(1), OH concentration (moles/liter)
C par(2), S(0) concentration (moles/liter)
C par(3), upon input is Xs and then changed to total Sulfide
C par(4), K2/3
C par(5), K3/4
C R, gas constant (8.314 J/mole-K)
C rate, initial rate of disproportionation (moles/liter-sec)
C T; temperature (K)
C x(1), Na concentration (moles/liter)
C x(2), HS concentration (moles/liter)
C x(3), trisulfide concentration (moles/liter)
C x(4), tetrasulfide concentration (moles/liter)
C x(5), pentasulfide concentration (moles/liter)
C xsubs, S(0)/total sulfide
C wk, work array for ZSCNT

      Open (Unit=7, File='redox.out',Status='New')
      Open (Unit=8, File='redox.gph',Status='New')
      n=5
      itmax=100
      nsig=5
      par(4)=1.8e-2
      par(5)=4.e5

C Read initial OH, S(0) and Xs
      Read (5,10)par(1),par(2),par(3)
10    Format(3f16.7)
      Read (5,12) T
12    Format (f16.7)

      kf = 10**(-5600./T + 10.9)

      xsubs = par(3)
```

```
      OH0=par(1)
      S0=par(2)
      par(3)=par(2)/par(3)

C Initial guesses
      x(4) = par(2)/3.
      x(2) = par(3)-x(4)
      x(1) = x(2)+par(1)+2.*x(4)

      Call ZSCNT (fcn1,nsig,n,itmax,par,x,fnorm,wk,ier)


C Print out diagnostic information from ZSCNT
      Write (7,13) ier,fnorm
13    Format (' **Diagnostic Information**',/
     1,' IER= ',i3,5x,' FNORM =',f8.4,/)

C Results
      Write (7,14)
14    Format (' **Results**',/)
      Write (7,15) par(1),par(2),xsubs
15    Format (' [OH] = ',1pe10.2,/,' [S(0)] = ',0pf8.3,/
     1,' Xs = ',f8.3,/)

      Write (7,18)
18    Format (' Ion',7x,'Conc.',7x,'Frac. of S')
      Write (7,20) x(1),x(2)
20    Format (' Na',4x,1pe11.3,/,' HS',4x,e11.3)
      Write (7,21) x(3),2.*x(3)/par(2),x(4),3.*x(4)/par(2)
21    Format (' triS',2x,1pe11.3,5x,0pf8.4,/
     1,' tetraS',1pe11.3,5x,0pf8.4)
      Write (7,22) x(5),4.*x(5)/par(2)
22    Format (' pentaS',1pe11.3,5x,0pf8.4,/)

      B= x(2)*par(1)/par(2)
      nbar = (2.*x(3)+3.*x(4)+4.*x(5))/(x(3)+x(4)+x(5))
      Write (7,30) B,nbar
30    Format (' B =',1pe10.2,/,' nbar = ',0pf6.2)

      rate = kf*4.*x(5)*par(1)/(x(2)*x(2))
      Write (7,35) rate
35    Format (' initial rate of disprop. =',1pe12.4
     1,' moles/liter-sec',/)

      cterm = dlog (((x(2)*par(1))**4)/x(4))
      Write (7,40) cterm
40    Format (' Conc term (for tetrasulfide) =',f11.3)

      temp = x(1)
      x(1) = par(1)
C Sodium ion concentration is now known
      par(1) = temp
      add=par(2)*0.01
```

```
      do 100 j =1,90

      par(1) = par(1)+2.*add
      par(2) = par(2)-add
      par(3) = par(3)+add
      Call ZSCNT (fcn2,nsig,n,itmax,par,x,fnorm,wk,ier)

      save (1,j) = x(1)
      save(2,j) = x(2)
      save(3,j)=2.*x(3)/par(2)
      save(4,j)=3.*x(4)/par(2)
      save(5,j)=4.*x(5)/par(2)
C Redox potential
      E = E0-4.08*dlog (((x(2)*x(1))**4)/x(4))
      save(6,j)=E
      B= x(2)*x(1)/par(2)
      rate = kf*4.*x(5)*x(1)/(x(2)*x(2))
      save(8,j) = rate
      nbar = (2.*x(3)+3.*x(4)+4.*x(5))/(x(3)+x(4)+x(5))
      save(7,j) = nbar+1.0
      Write (6,50) dfloat(j)*0.01,nbar,E
50    Format (3f12.4)

      If (dfloat(j)/10. .eq. dfloat(int(j/10))) Then
      Write (7,55) dfloat(j)*0.01,E
55    Format (/,' Depth of (dis)charge=',f8.2,3x
     1,'Electrode Potential=',f10.2,/)
      Write (7,15) x(1),par(2);par(2)/par(3)
      Write (7,18)
      Write (7,20) par(1),x(2)
      Write (7,21) x(3),2.*x(3)/par(2),x(4),3.*x(4)/par(2)
      Write (7,22) x(5),4.*x(5)/par(2)
      Write (7,30) B,nbar
      Write (7,35) rate
      Endif

100   Continue

C Tellagraph file for OH and HS concentration
      Write (8,57) S0,xsubs,14.+dlog10(OH0)
57    Format (' GENERATE A PLOT.',/
     1,' X AXIS LENGTH IS  7.',/
     2,' X AXIS TICK-MARKS MODE IS REVERSED.',/
     3,' Y AXIS LENGTH IS  6.',/
     4,' Y AXIS TICK-MARKS MODE IS REVERSED.',/
     5,' AXIS FRAME IS  1.',/
     6,' AXIS FRAME THICKNESS IS  2.',/
     7,' X AXIS MAXIMUM IS 1.',/
     8,' PAGE-BORDER IS  0.',/
     9,' ALL MESSAGE UNITS PLOT %.',/
     9,' MESSAGE 1 X 80.',/,' MESSAGE 1 Y 95.',/
     9,' MESSAGE 1 TEXT "[S(0)]=',f5.1,'".',/
     9,' MESSAGE 2 X 80.',/,' MESSAGE 2 Y 85.',/
```

```
     9,' MESSAGE 2 TEXT "X<LH.5)s<LXHX)=',f5.1,'".',/
     9,' MESSAGE 3 X 80.',/,' MESSAGE 3 Y 75.',/
     9,' MESSAGE 3 TEXT "pH=',f5.1,'".',/
     9,' X AXIS LABEL TEXT IS "State of Charge".')
          Write (8,59)
59      Format (' Y AXIS LABEL TEXT',1x
     2,'IS "Concentration (moles/liter)".',/
     3,' INPUT DATA.')

          Write (8,500)
500       Format (' "OH<EH.8)-<EXHX)"')
          Write (8,60) (dfloat(j)*0.01,save(1,j), j=1,90)
60        Format (4(f8.2,e11.3))

          Write (8,550)
550       Format (' "HS<EH.8)-<EXHX)"')
          Write (8,60) (dfloat(j)*0.01,save(2,j), j=1,90)
          Write (8,63)
63        Format (' END OF DATA.',/
     1,' CURVE 1.',/
     2,' CURVE COLOR IS NO.',/
     3,' CURVE THICKNESS IS  2.',/
     4,' CURVE SYMBOL COUNT IS  0.',/
     4,' CURVE 2.',/
     4,' CURVE TEXTURE 11.',/
     5,' CURVE COLOR IS NO.',/
     6,' CURVE THICKNESS IS  2.',/
     7,' CURVE SYMBOL COUNT IS  0.',/
     5,' GO.',/,' **FILE**')

C Tellagraph file for polysulfide fractions
          Write (8,57) S0,xsubs,14.+dlog10(OH0)
          Write (8,240)
240       Format (' Y AXIS LABEL IS',1x
     1,'"Fraction of S Present as S<LH.5)n<LXHX)S<EH.8)2-".',/
     2,' INPUT DATA.')

          Write (8,245)
245       Format (' "u<LH.5)2<LXHX)"')
          Write (8,250) (dfloat(j)*0.01,save(3,j), j=1,90)
250       Format (4(f8.2,f11.4))
          Write (8,255)
255       Format (' "u<LH.5)3<LXHX)"')
          Write (8,250) (dfloat(j)*0.01,save(4,j), j=1,90)
          Write (8,265)
265       Format (' "u<LH.5)4<LXHX)"')
          Write (8,250) (dfloat(j)*0.01,save(5,j), j=1,90)

          Write (8,270)
270       Format (' END OF DATA.',/,' CURVE 1.',/
     1,' CURVE COLOR IS NO.',/
     1,' CURVE TEXTURE 11.',/
     2,' CURVE THICKNESS IS  2.',/
```

```
     3,' CURVE SYMBOL COUNT IS  0.',/
     4,' CURVE 2.',/
     4,' CURVE TEXTURE 1.',/
     5,' CURVE COLOR IS NO.',/
     6,' CURVE THICKNESS IS  2.',/
     7,' CURVE SYMBOL COUNT IS  0.',/
     8,' CURVE 3.',/
     8,' CURVE TEXTURE 13.',/
     9,' CURVE COLOR IS NO.',/
     1,' CURVE THICKNESS IS  2.',/
     2,' CURVE SYMBOL COUNT IS  0.',/
     3,' GO.',/,' **FILE**')
C Tellagraph file for Electrode Potential
          Write (8,57) S0,xsubs,14.+dlog10(OH0)
          Write (8,64)
64        Format (' Y AXIS LABEL TEXT',1x
     1,'IS "E (mV vs. SHE)".',/
     2,' INPUT DATA.')

          Write (8,65) (dfloat(j)*0.01,save(6,j), j=1,90)
65        Format (4(f8.2,f11.3))

          Write (8,63)

C Tellagraph file for polysulfide chain length
          Write (8,57) S0,xsubs,14.+dlog10(OH0)
          Write (8,70)
70      Format(' Y AXIS LABEL TEXT',1x
     1,'IS "x in S<LH.5)x<LXHXEH.8)2-<EXHX)".',/
     2,' INPUT DATA.')

          Write (8,65) (dfloat(j)*0.01,save(7,j), j=1,90)

          Write (8,63)

C Rate of disproportionation
          Write (8,57) S0,xsubs,14.+dlog10(OH0)
          Write (8,600)
600       Format (' Y AXIS LABEL TEXT IS "Rate (M/sec)".',/
     1,' Y AXIS TYPE LOG.',/
     2,' INPUT DATA.')
          Write (8,60) (dfloat(j)*0.01, save(8,j), j=1,90)
          Write (8,63)

          Stop
          End
```

```
C This subroutine calculates (using ZSCNT) the sodium ion concentration
C given hydroxide, total sulfide and total sulfur.
      Subroutine fcn1 (x,f,n,par)
      Real*8 x(5),f(5),par(5)
      f(1) = par(1)+x(2)+2.*x(3)+2.*x(4)+2.*x(5)-x(1)
      f(2) = par(2)-2.*x(3)-3.*x(4)-4.*x(5)
      f(3) = par(3)-x(2)-x(3)-x(4)-x(5)
      f(4) = x(3)*x(3)*x(3)-par(4)*par(1)*x(4)*x(4)*x(2)
      f(5) = x(4)*x(4)*x(4)*x(4)-
     1par(5)*par(1)*x(5)*x(5)*x(5)*x(2)
      Return
      End
```

```
C This subroutine calculates (using ZSCNT) the hydroxide ion concentration
C given sodium, total sulfide and total sulfur.
      Subroutine fcn2 (x,f,n,par)
      Real*8 x(5),f(5),par(5)
      f(1) = x(1)+x(2)+2.*x(3)+2.*x(4)+2.*x(5)-par(1)
      f(2) = par(2)-2.*x(3)-3.*x(4)-4.*x(5)
      f(3) = par(3)-x(2)-x(3)-x(4)-x(5)
      f(4) = x(3)*x(3)*x(3)-par(4)*x(1)*x(4)*x(4)*x(2)
      f(5) = x(4)*x(4)*x(4)*x(4)-
     1par(5)*x(1)*x(5)*x(5)*x(5)*x(2)
      Return
      End
```

```
C Do a linear regression
      Real*8 xy(100,2), pred(100,7),albap(3),des(5),anova(14)
      Real*8 stat(9),save(100)
      Real*8 Temp,R,F
      Integer ix,n,imod,ipred,ip,nn,ier
      Data R,F /8.314,96487.0/

C Open files
      Open (Unit=7,File='pot.dat',Status='Old')
      Open (Unit=8,File='pot.out',Status='New')

      ix=100
      Read (7,2) n
2     Format (i3)
      imod=0
      ipred=1
      albap(1)=0.05
      albap(2)=0.05
      albap(3)=0.01
      ip=100
      nn=n

C Temperature
      Read (7,5) Temp
5     Format (f16.7)

      do 20 j=1,n
            Read (7,10) xy(j,1),xy(j,2)
10          Format (2f16.7)
            pred(j,1)=xy(j,1)
            save(j)=xy(j,2)
20    Continue

      Call RLONE (xy,ix,n,imod,ipred,albap,des,anova,stat,
     1pred,ip,nn,ier)

C Write Header
      Write (8,12) Temp
12    Format (' Temperature=',f7.1,' K',/)
      Write (8,15)
15    Format (2x,' Log Term',3x,' Electrode Potential',5x
     1,' Predicted Potential',5x,'Residual',/)
      do 100 j=1,n
      Write (8,21) pred(j,1),save(j),pred(j,2),
     1pred(j,2)-save(j)
21    Format (f9.3,10x,f7.1,19x,f7.1,10x,f8.2)
100   Continue

      Write (8,25) des(5)
25    Format (/,' Correlation Coeff.=',f10.4)
      Write (8,30) stat(1),stat(5)
30    Format (' Slope =',f6.2,' mv',/
     1,' E0=',f8.2,' mV')
```

```
      Write (8,40) stat(2),stat(6)
40    Format (' Est. of error in slope=',f9.3,/
     1,' Est. of error in E0=',f9.3)
      Write (8,60) -R*Temp*1000.0/(6.*F)
60    Format (' Theoretical Slope=',f7.2,' mV')
      Stop
      End
```

A.4.
Sample Output
Temperature= 298.0 K

Log Term	Electrode Potential	Predicted Potential	Residual
-0.611	-540.0	-533.7	6.25
-4.411	-519.0	-518.2	0.77
-5.444	-514.0	-514.0	-0.01
-9.239	-497.0	-498.5	-1.51
-10.246	-494.0	-494.4	-0.40
-10.815	-494.0	-492.1	1.92
-14.521	-475.0	-476.9	-1.94
-15.074	-473.0	-474.7	-1.69
-15.643	-471.0	-472.4	-1.36
-19.350	-455.0	-457.2	-2.22
-20.025	-457.0	-454.5	2.53
-20.098	-455.0	-454.2	0.83
-23.674	-438.0	-439.6	-1.56
-24.853	-431.0	-434.7	-3.75
-24.926	-433.0	-434.5	-1.45
-28.510	-417.0	-419.8	-2.82
-29.063	-419.0	-417.6	1.44
-29.178	-420.0	-417.1	2.91
-32.770	-401.0	-402.4	-1.42
-33.892	-396.0	-397.8	-1.84
-34.007	-394.0	-397.4	-3.37
-37.606	-381.0	-382.7	-1.67
-37.954	-383.0	-381.2	1.75
-38.262	-384.0	-380.0	4.01
-41.783	-366.0	-365.6	0.39
-42.782	-362.0	-361.5	0.47
-43.091	-359.0	-360.3	-1.27
-46.612	-345.0	-345.9	-0.89
-46.728	-349.0	-345.4	3.58
-51.556	-328.0	-325.7	2.30

Correlation Coeff.= -0.9991
Slope = -4.08 mv
E0= -536.24 mV
Est. of error in slope= 0.032
Est. of error in E0= 0.951
Theoretical Slope= -4.28 mV

Appendix B

Non-Linear Least Squares Analysis of Potential-Step Data

B.1. Introduction

Several methods have been suggested to determine exchange current density and active species concentration from potential step current-time transients. If Equation 3-2 is restricted so that $\lambda t^{1/2} << 1$, the right side can be expanded in a Taylor series. If the series is truncated after the first term, this yields (82):

$$i = W\left[1 - 2\lambda(t/\pi)^{1/2}\right] \tag{B-1}$$

Unlike Equation 3-2, Equation B-1 is convenient for graphical analysis. If i is plotted versus $t^{1/2}$, then W can be obtained from the intercept and λ can be obtained from the slope. Equation B-1 has restricted applicability to fast reactions because then λ is large and the region where $\lambda t^{1/2} << 1$ may overlap the double layer charging regime. However, Equation B-1 could provide estimates of W and λ for a more sophisticated analysis based on Equation 3-2 (or 3-18). Settle and Nagy (129) have indicated that a plot of Equation B-1 can also provide information on the reliability of the potential step data.

The Laplace transform of Equation 3-2 is:

$$\bar{i} = \frac{W}{s^{1/2}(s^{1/2} + \lambda)} \tag{B-2}$$

which can be rearranged to give:

$$\frac{1}{\bar{i}s^{1/2}} = \frac{s^{1/2}}{W} + \frac{\lambda}{W} \tag{B-3}$$

A plot of the left side of Equation B-3 versus $s^{1/2}$ would allow determination of W from the slope and λ/W from the intercept. Macdonald (83) has suggested analysis in Laplace space to evaluate the parameters. $\bar{i}(s)$ can be generated from i(t) by applying the Laplace transform to the experimental data:

$$\bar{i}(s)=\int_{t=0}^{t=\infty} i(t)e^{-st}dt \qquad \text{(B-4)}$$

The integration in Equation B-4 is carried out for several values of s and the set of points $[\bar{i}(s),s]$ is plotted as in Equation B-3. There are some practical problems in applying Equation B-3 and B-4 to the experimental data. Equation B-4 requires that the integration be carried out between t=0 and t=∞. Values for i(t) are not available near t=0 due to double layer charging effects. At longer times natural convection may influence the response, and therefore a long-time cuttoff for the integration must be chosen. An appropriate method of evaluating the integral from the discrete current-time points also needs to be considered. Santos *et al.* (130) have dealt with some of these problems in the application of Laplace space analysis to the coulostatic method.

Least squares analysis can be used to estimate parameters from experimental data. The model can be non-linear and contain one or more parameters. In applying Equation B-1, only the data at short times can be used, and in applying Equations B-3 and B-4, the complete data set must be used. In the non-linear least squares method, either the full data set or a restricted portion of the data set can be used. Thus non-linear least squares analysis of Equation 3-2 (or 3-18) has an advantage over the other methods of analysis.

The object of least squares analysis is to provide the best "fit" of experimental data to a theoretical model containing parameters. This is done by varying the parameters so that the sum of the squares of the residuals is minimized. The residual is defined as the difference between the measured current and that predicted from the model equation:

$$f=i_m-i_p \qquad \text{(B-5)}$$

and the sum of the squares is:

$$S=\sum_j f^2 \qquad \text{(B-6)}$$

The sum of the squares is minimized by setting the partial derivatives of S with respect to each parameter to zero. For the linear case, an analytical expression for the best parameter values can be obtained. In the non-linear case, an iterative solution is required. More information on least squares is available in (131). Nagy (132) has discussed the statistical information that can

be derived in applying non-linear least squares analysis to the determination of kinetic parameters using dc relaxation techniques. The computer implementation and its application to the experimental data of Chapter 3 are discussed in the next section.

B.2. Computer Implementation

Several computer programs are availible for non-linear least squares analysis of data (84,133), so it was not necessary to write new programs. The MINPACK program LMDER1 (84) was chosen because it has been applied, with success, to similar problems (134). It uses a modification of the Levenberg-Marquardt algorithm. A subroutine for evaluation of the residuals and the Jacobian matrix of the residuals is required.

The Jacobian matrix for this problem is:

$$J=\begin{bmatrix} \frac{\partial f(1)}{\partial W} & \frac{\partial f(1)}{\partial \lambda} \\ \vdots & \vdots \\ \frac{\partial f(n)}{\partial W} & \frac{\partial f(n)}{\partial \lambda} \end{bmatrix} \tag{B-7}$$

Let us denote:

$$g(z)=\exp(z^2)\mathrm{erfc}(z) \tag{B-8}$$

If Equation 3-2 represents the model, then the partial derivatives required for the Jacobian are:

$$\frac{\partial f}{\partial W}=-g(\lambda t^{1/2}) \tag{B-9a}$$

$$\frac{\partial f}{\partial \lambda}=-2\lambda W t\, g(\lambda t^{1/2}) + 2W\left(\frac{t}{\pi}\right)^{1/2}[\exp(\lambda^2 t)]^2 \tag{B-9b}$$

For Equation 3-18 as the model:

$$\frac{\partial f}{\partial W}=\frac{-1}{t_2\lambda^2}\left[g(\lambda t^{1/2})+2\lambda\left(\frac{t}{\pi}\right)^{1/2}-g(\lambda(t-t_2)^{1/2})-2\lambda\left(\frac{(t-t_2)}{\pi}\right)^{1/2}\right] \tag{B-10a}$$

$$\frac{\partial f}{\partial \lambda}=g(\lambda t^{1/2})\left[\frac{2W}{t_2\lambda^3}-\frac{2Wt}{t_2\lambda}\right]+g(\lambda(t-t_2)^{1/2})\left[\frac{2W(t-t_2)}{t_2\lambda}-\frac{2W}{t_2\lambda^3}\right]+\frac{4W}{t_2\lambda^2}\left[\left(\frac{t}{\pi}\right)^{1/2}-\left(\frac{(t-t_2)}{\pi}\right)^{1/2}\right] \tag{B-10b}$$

The computer programs consist of pstep, fullfunc, the IMSL routine DERFC, gofz, and the MINPACK supplied program LMDER1. The main program collects the data and other information about the experiment. LMDER1 is then referenced, and it uses fullfunc to calculate the residuals and the Jacobian matrix. The program continues to refine its guesses for the best values of the parameters until certain tolerance criteria are satisfied. Section B.4 shows some sample output from the fitting routine.

The function subroutine gofz was written because the IMSL-supplied library function for erfc was inaccurate at large values of the argument. At large values of z in Equation B-8, the value of erfc(z) is small. The VAX 8600 compiler in double precision mode treats any number less than about 10^{-38} as zero. To overcome this problem, a method is needed to evaluate g(z) in Equation B-8 directly without multiplying a very large number ($\exp(z^2)$) by a very small number (erfc(z)). Nagy (135) has indicated that the following expression is valid for large arguments of z (mod(z) $>$ 3.5):

$$g(z)=\frac{i}{\pi}\sum_{k=1}^{k=20}\left[\frac{\alpha_k}{iz-X_k}\right] \qquad \text{(B-11)}$$

In Equation B-11, $i=(-1)^{1/2}$. The weight factors (α_k) and zeros (X_k) of the 20th order Hermite polynomial are available (136). This equation is valid in both the real and complex domain. For the potential step program only real arguments of z are encountered. Program storage space can be saved by deriving a form of Equation B-11 that is valid in the real domain only:

$$g(z)=\frac{2}{\pi}\sum_{k=1}^{k=10}\left[\frac{\alpha_k z}{z^2+X_k^2}\right] \qquad \text{(B-12)}$$

At small values of z, the FORTRAN library function dexp and the IMSL function derfc were used to calculate g(z). For z $>$ 3.5, Equation B-12 was used to evaluate g(z). There was a smooth transition between the two methods of calculation.

B.3. Program Listings

```
      Program pstep
C ***************************************************************
C * This program finds the best fit parameters                  *
C * for a potential step experiment using                       *
C * non-linear least squares analysis                           *
C * The main program does the input and output                  *
C * and calls the fitting program                               *
C ***************************************************************

C ***************************************************************
C * Area, electrode area (cm**2)                                *
C * curr, measured current (mA)                                 *
C * currp, predicted current (mA)                               *
C * Dparm, diffusion parameter (cm**2-sec**1/2/mole)            *
C * elecn, number of electrons                                  *
C * excur, exchange current density (mA/cm**2)                  *
C * F, Faraday (C/equiv)                                        *
C * fvec, residual (mA)                                         *
C * R, gas constant (J/mole-K)                                  *
C * Rct, charge transfer resistance (ohm-cm**2)                 *
C * Rohm, uncompensated ohmic resistance (ohm-cm**2)            *
C * Rtot, sum of activation and ohmic resistance (ohm-cm**2)    *
C * stpsz, total overpotential (mV)                             *
C * Temp, temperature (C)                                       *
C * x(1), W (mA)                                                *
C * x(2), lambda (sec**-1/2)                                    *
C ***************************************************************
      Real*8 dexp,derfc,dsqrt,dpmpar
      Real*8 x(2),fvec(30),wa(100)
      Real*8 tol,t(30),curr(30)
      Real*8 fjac(30,2)
      Integer ldfjac,ipvt(2)
      Real*8 currp,perr,t2
      Real*4 Area, stpsz, Rohm, Rct, Rtot, excur
      Real*4 Temp, Dparm, Kappa, F, R, elecn
      Integer iwa(2),info,mp,n
      Character*25 infile
      Character*100 msg
      Common /dat/ curr,t,t2
      External fcn
      Data R,F /8.314,96500.0/
C ***************************************************************
C *                    Open Files                               *
C ***************************************************************
      Write (6,1)
1     Format (' Name of input file ? ',$)
      Read (5,2) infile
2     Format(A)
      Open (Unit=7, File=infile//'.dat', Status='Old')
      Open (Unit=8, File=infile//'.out', Status='New')
```

```
C Number of parameters equals 2
      n=2
      lwa = 100
      ldfjac = 30
C Set tolerance
C dpmpar is machine tolerance
      tol = dsqrt(dpmpar(1))

C ***************************************************************
C *                      Read Data                              *
C ***************************************************************
      Read (7,10) mp
10    Format (i2)
      do 30 i = 1,mp
            Read (7,20) t(i), curr(i)
20          Format (2f16.7)
30          Continue

C Initial guess
      Read (7,36) x(1),x(2),t2
36    Format (3f16.7)

C ***************************************************************
C *            Additional information about experiment          *
C ***************************************************************
      Read (7,38) Area, stpsz, elecn, Rohm, Temp
38    Format (5f16.7)
      Read (7,2) msg
C ***************************************************************
C *            Now call subroutine that fits parameters *
C ***************************************************************
      Call LMDER1 (fcn,mp,n,x,fvec,fjac,ldfjac,tol,
     1info,ipvt,wa,lwa)

C ***************************************************************
C *                    Compute results of experiment            *
C ***************************************************************

C Total resistance in ohm-cm**2
      Rtot = stpsz*Area/x(1)

C Charge transfer resistance in ohm-cm**2
      Rct = Rtot - Rohm

C Exchange current in mA/cm**2
      excur = R*1000.*(Temp+273.)/(elecn*F*Rct)

C Rate constant in sec**-1/2
      Kappa = x(2)*Rtot/Rct

C Diffusion parameter in cm**2-sec**1/2/mole
      Dparm = x(2)*Area*elecn*elecn*F*F*stpsz/(x(1)*R*(Temp+273.))
```

```
C Compute final L2 norm of residuals
      fnorm= enorm(mp,fvec)

C ***************************************************************
C *                      Write Out Results                      *
C ***************************************************************
      Write (8,37) infile,msg
37    Format(' ****INFORMATION****',/
     1,' Original Data File-- ',A,/
     2,1x,A)

      Write (8,39) stpsz,Temp,Area
39    Format (' Step size =',f7.2,' mV',2x,'Temperature =',
     1f6.1,' C',2x,'Elec. Area =',f8.3,' cm**2',/)

      Write (8,49)
49    Format (1x,'**** RESULTS ****',/)
      Write (8,50) x(1),x(2)
50    Format (' W=',1Pe14.3,/, ' lambda =',e13.2)
C Write value of t2 used in fitting program
      Write (8,55) 1.e6*t2
55    Format ( ' t2 = ',f10.1, ' microseconds',/)

      Write (8,56) Rtot,Rohm,Rct
56    Format (/,1x,'Rtot =',f8.4,' ohm-cm**2',2x,'Rohm =',
     1f8.4,' ohm-cm**2',2x,'Rct =',f8.4,' ohm-cm**2',/)
      Write (8,57) excur,Kappa,Dparm
57    Format(/,1x,' Exch. current =',f7.3,' ma/cm**2',2x,
     1'Kappa =',f12.2,' sec**-1/2',/,1x,'Diff. parm. =',1pe10.2,/)

C Write out measured and predicted results
      Write (8,250)
250   Format (12x,'Time',6x,'Meas. Current',3x,'Pred. Current',
     15x,'Pdiff')
      Write (8,251)
251   Format (11x,'(msec)',/)

      do 500 i=1,mp

      currp = curr(i)-fvec(i)
      perr = fvec(i)*100.0/curr(i)
            Write (8,300) 1.e3*t(i),curr(i),currp,perr
300         Format (f15.2,f15.4,f15.4,f15.2)
500   Continue

C Statistical and program information
      Write (8,40) fnorm,info
40    Format (/,1x,'Final L2 norm of residuals =',e20.7,/
     1,1x,'Exit parameter =',i2,/)
      Stop
      End
```

```
      Subroutine fcn (mp,n,x,fvec,fjac,ldfjac,iflag)
C This is the subroutine that contains the fitting function for
C the potential step experiment.
C This functions is valid under the following conditions:
C 1. The overpotential and concentration variations are such that
C the linerized kinetic and Nernst equations can be used.
C 2. There are no adsorption or double layer effects and any intermediates
C are not lost by diffusion.
C 3. The proper t1 is chosen. t1 is the rise time of the potentiostat
C or the rise time of potential across the double layer (4RC) --
C whichever is longer.

C Declare variables
      Double Precision dexp,dsqrt,derfc,g
      Double Precision x(2),fvec(30),fjac(ldfjac,n)
      Double Precision term1,term2,term3
      Double Precision t1,y1,y2, curr(30),t(30)
      Integer mp,n,iflag,ldfjac
      Common /dat/ curr,t,t1

      If (iflag .eq. 1) then
C Compute functions
      do 10 i = 1,mp
            y1= x(2)*dsqrt(t(i))
            y2= x(2)*dsqrt(t(i)-t1)
            fvec(i) = curr(i)- (x(1)/(t1*x(2)*x(2)))*(g(y1)
     1+2.0*x(2)*dsqrt(t(i)/3.14159) - g(y2)
     2-2.0*x(2)*dsqrt((t(i)-t1)/3.14159))
10    Continue
      Else
C Compute Jacobian
      do 30 i = 1,mp
            y1 = x(2)*dsqrt(t(i))
            y2 = x(2)*dsqrt(t(i)-t1)
            fjac(i,1) = (-1./(t1*x(2)*x(2)))*(g(y1)
     1+2.*x(2)*dsqrt(t(i)/3.14159) - g(y2) -
     22.*x(2)*dsqrt((t(i)-t1)/3.14159))
            term1 = (2.*x(1)/(t1*x(2)**3.) - 2.*x(1)*t(i)/
     1(x(2)*t1)) * g(y1)
            term2 = (4.*x(1)/(t1*x(2)**2.))*(
     1dsqrt(t(i)/3.14159) - dsqrt((t(i)-t1)/3.14159))
            term3 = (2.*x(1)*(t(i)-t1)/(x(2)*t1) -
     12.*x(1)/(t1*x(2)**3.))* g(y2)
            fjac(i,2) = term1+term2+term3
30    Continue
      Endif
      Return
      End
```

```
      Double Precision Function g(z)
C
C This function computes exp(z*z)erfc(z) for both large and small
C values of z.
C Only real arguments are permitted.
C For values of z less than or equal to 3.5 the fortran and imsl
C library functions are used.
C For values of z greater than 3.5 an asymptotic expansion based on
C Hermite polynomials is used.
C For the functions that are valid in the complex domain also
C see Z. Nagy, Electrochimica Acta, 26(5), 671, (1981).
C
C The values of the zeros and weight factors are from:
C H. Salzer, et. al., J. Res. natn. Bur. Stand., 48, 111, (1952).
C

      Double Precision z,alpha(10),zero(10)
      Double Precision sum
      Double Precision derfc,dexp
      Data alpha /0.4622436696006,0.2866755053628,0.1090172060200,
     10.2481052088746D-01,0.3243773342238D-02,0.2283386360163D-03,
     20.7802556478532D-05,0.1086069370769D-06,0.4399340992273D-09,
     30.2229393645534D-12/
      Data zero /0.2453407083009,0.7374737285454,1.2340762153953,
     11.7385377121166,2.2549740020893,2.7888060584281,
     23.3478545673832,3.9447640401156,4.6036824495507,
     35.3874808900112/
      If (z.le.3.5) then
            g=dexp(z*z)*derfc(z)
            Return
      endif
      sum = 0.0
      do 100 i=1,10
            sum=sum+alpha(i)*z/(z*z+zero(i)*zero(i))
100   Continue
      g=2.0*sum/3.14159
      Return
      End
```

B.4.
Sample Output

****INFORMATION****
Original Data File-- fer01
Pt, feri/ferro
Step size = 20.00 mV Temperature = 25.0 C Elec. Area = 0.320 cm**2

**** RESULTS ****

W= 1.223E+00
lambda = 3.81E+01
t2 = 100.0 microseconds

Rtot = 5.2313 ohm-cm**2 Rohm = 1.5000 ohm-cm**2 Rct = 3.7313 ohm-cm**2

Exch. current = 6.881 ma/cm**2 Kappa = 53.44 sec**-1/2
Diff. parm. = 7.49E+08

Time (msec)	Meas. Current	Pred. Current	Pdiff
0.40	0.6560	0.6377	2.78
0.55	0.5740	0.5772	-0.56
0.61	0.5535	0.5580	-0.81
0.73	0.5125	0.5253	-2.50
0.85	0.4975	0.4982	-0.14
1.03	0.4605	0.4650	-0.98
1.23	0.4275	0.4353	-1.83
1.41	0.4105	0.4132	-0.66
1.64	0.3965	0.3895	1.76
1.82	0.3745	0.3737	0.22
1.95	0.3605	0.3634	-0.80
2.18	0.3390	0.3472	-2.41
2.43	0.3335	0.3319	0.49
2.81	0.3175	0.3121	1.69
3.20	0.2950	0.2952	-0.07
3.98	0.2655	0.2683	-1.07
4.49	0.2650	0.2543	4.03
5.08	0.2395	0.2406	-0.46
6.10	0.2195	0.2214	-0.85
7.15	0.2150	0.2057	4.31
8.74	0.1885	0.1873	0.62
11.01	0.1715	0.1680	2.05
12.73	0.1605	0.1568	2.33
13.72	0.1490	0.1512	-1.50
18.48	0.1325	0.1310	1.11
33.44	0.1050	0.0981	6.56

Final L2 norm of residuals = 0.3268858E-01
Exit parameter = 1

Appendix C

Coupled Electrochemical and Chemical Reactions: Response to a Potential Step

C.1. Introduction

This appendix describes a model for a homogeneous solution reaction coupled to a heterogeneous charge transfer step. The response to a small potential step is solved for when neither the homogeneous reaction nor the heterogeneous reaction can be considered to be the rate-limiting step. Table C-1 shows the reaction sequence for the two homogeneous kinetic cases considered in this appendix. In Case I the homogeneous reaction is first order. In Case II it follows dissociation-dimerization kinetics. These reactions may be multi-step so long as the overall kinetics correspond to one of these cases.

The chemical reactions can be accounted for explicitly by replacing R_i in Equation 3-6 with the homogeneous reaction terms shown in Table C-1. For Case I this leads to a set of linear equations; for Case II some of the equations are non-linear. The following electrode reaction is considered to obey the assumptions that make the multi-step Butler-Volmer equation valid.

Table C-1: Reaction Schemes

Case I	Case II
1st Order Reaction	Dissociation-Dimerization Reaction
$Y \rightleftarrows O$	$Y \rightleftarrows 2O$
$s_oO + ne^- \rightleftarrows s_rR$	$s_oO + ne^- \rightleftarrows s_rR$
$R_o = -R_y = k_fC_y - k_bC_o$	$\frac{1}{2}R_o = -R_y = k_fC_y - k_bC_o^2$

Since the potential step experiments in Chapter 3 were carried out in the linear current-overpotential region, the linearized form of this equation was used (see Equation 3-13). Table C-2 shows the set of material balances, initial conditions and boundary conditions for both cases.

Table C-2.

Case I	Case II
First-Order Reaction	Dissociation-Dimerization Reaction
Material Balances	Material Balances
$\frac{\partial C_o}{\partial t}=D_o\frac{\partial^2 C_o}{\partial z^2}+(k_f C_y-k_b C_o)$ (C-1)	$\frac{\partial C_o}{\partial t}=D_o\frac{\partial^2 C_o}{\partial z^2}+2(k_f C_y-k_b C_o^2)$ (C-4)
$\frac{\partial C_r}{\partial t}=D_r\frac{\partial^2 C_r}{\partial z^2}$ (C-2)	$\frac{\partial C_r}{\partial t}=D_r\frac{\partial^2 C_r}{\partial z^2}$ (C-5)
$\frac{\partial C_y}{\partial t}=D_y\frac{\partial^2 C_y}{\partial z^2}-(k_f C_y-k_b C_o)$ (C-3)	$\frac{\partial C_y}{\partial t}=D_y\frac{\partial^2 C_y}{\partial z^2}-(k_f C_y-k_b C_o^2)$ (C-6)

Initial Conditions

at $t=0$, $z\geq 0$: $C_o=C_{ob}$, $C_r=C_{rb}$, $C_y=C_{yb}$ (C-7)

Boundary Conditions

as $z\rightarrow\infty$, $t\geq 0$: $C_o\rightarrow C_{ob}$, $C_r\rightarrow C_{rb}$, $C_y\rightarrow C_{yb}$ (C-8)

at $z=0$, $t\geq 0$:

$$\frac{-D_o}{s_o}\frac{\partial C_o}{\partial z}=\frac{D_r}{s_r}\frac{\partial C_r}{\partial z} \quad \text{(C-9a)}$$

$$\frac{\partial C_y}{\partial z}=0 \quad \text{(C-9b)}$$

$$i=\frac{-nFD_o}{s_o}\frac{\partial C_o}{\partial z}=\frac{1}{R_r+R_s}\left(V-\frac{RT}{nF}\left[s_o\left\{\frac{C_o}{C_{ob}}-1\right\}-s_r\left\{\frac{C_r}{C_{rb}}-1\right\}\right]\right) \quad \text{(C-9c)}$$

For ease of solution and interpretation, it is desirable to make the equations and boundary conditions dimensionless. The parameters W and λ as defined by Equations 3-3 and 3-4 are used in the non-dimensionalization. These are the parameters that would be derived if the preceding chemical reaction was not a factor. Table C-3 shows the definitions of the dimensionless groups and variables. Table C-4 lists the dimensionless form of the material balances, initial conditions, and boundary conditions. For the solutions presented in this appendix, the diffusion coefficients of all species are set equal as are the stoichiometric coefficients. Under these conditions, only the first four groups in the left-hand column of Table C-3 will affect the i^* vs. t^* curves.

Table C-3: Dimensionless Variables

Dimensionless Groups	Definitions
1. V^*	$V^*=\frac{nFV}{RT}$
2. $\frac{C_{ob}}{C_{rb}}$	$t^*=\lambda^2 t$
3. K_{eq}, case I; $\frac{K_{eq}}{C_{ob}}$, case II	$z^*=\frac{\lambda x}{D_o^{1/2}}$
4. $\frac{k_b}{\lambda^2}$	$i^*=\frac{iV^*}{s_o W(1+\frac{s_r^2 D_o^{1/2} C_{ob}}{s_o^2 D_r^{1/2} C_{rb}})}$
5. $\frac{D_o}{D_r}$	$C_o^*=\frac{C_o}{C_{ob}}$
6. $\frac{D_o}{D_y}$	$C_r^*=\frac{C_r}{C_{rb}}$
7. $\frac{s_o}{s_r}$	$C_y^*=\frac{C_y}{C_{yb}}$

Table C-4: Dimensionless Equations

Case I	Case II
First-Order Reaction	Dissociation-Dimerization Reaction
Material Balances	Material Balances
$\frac{\partial C_o^*}{\partial t^*}=\frac{\partial^2 C_o^*}{\partial z^{*2}}+\frac{k_b}{\lambda^2}(C_y^*-C_o^*)$ (C-10)	$\frac{\partial C_o^*}{\partial t^*}=\frac{\partial^2 C_o^*}{\partial z^{*2}}+\frac{2k_b C_{ob}}{\lambda^2}(C_y^*-C_o^{*2})$ (C-13)
$\frac{\partial C_r^*}{\partial t^*}=\frac{D_r}{D_o}\frac{\partial^2 C_r^*}{\partial z^{*2}}$ (C-11)	$\frac{\partial C_r^*}{\partial t^*}=\frac{D_r}{D_o}\frac{\partial^2 C_r^*}{\partial z^{*2}}$ (C-14)
$\frac{\partial C_y^*}{\partial t^*}=\frac{D_y}{D_o}\frac{\partial^2 C_y^*}{\partial z^{*2}}-\frac{k_b K_{eq}}{\lambda^2}(C_y^*-C_o^*)$ (C-12)	$\frac{\partial C_y^*}{\partial t^*}=\frac{D_y}{D_o}\frac{\partial^2 C_y^*}{\partial z^{*2}}-\frac{k_b K_{eq}}{\lambda^2}(C_y^*-C_o^{*2})$ (C-15)

Initial Conditions

$$\text{at } t^*=0,\ z^*\geq 0\text{: } C_o^*=1,\ C_r^*=1,\ C_y^*=1 \qquad \text{(C-16)}$$

Boundary Conditions

$$\text{as } z^*\to\infty,\ t^*\geq 0\text{: } C_o^*\to 1,\ C_r^*\to 1,\ C_y^*\to 1 \qquad \text{(C-17)}$$

$$\text{at } z^*=0,\ t^*\geq 0\text{:}$$

$$\frac{\partial C_r^*}{\partial z^*}+\frac{D_o}{D_r}\frac{s_r}{s_o}\frac{C_{ob}}{C_{rb}}\frac{\partial C_o^*}{\partial z^*}=0 \qquad \text{(C-18a)}$$

$$\frac{\partial C_y^*}{\partial z^*}=0 \qquad \text{(C-18b)}$$

$$V^*=s_o(C_o^*-1)-s_r(C_r^*-1)-s_o\left[1+\frac{s_r^2 D_o^{1/2} C_{ob}}{s_o^2 D_r^{1/2} C_{rb}}\right]\frac{\partial C_o^*}{\partial x^*} \qquad \text{(C-18c)}$$

C.2. Method of Solution

The sets of parabolic partial differential equations were solved by casting them into finite difference form. Central difference approximations were used to approximate the space derivatives:

$$\frac{\partial C^*}{\partial z^*}=\frac{C^*(z^*+h,t^*)-C^*(z^*-h,t^*)}{2h}+O(h^2) \tag{C-19a}$$

$$\frac{\partial^2 C^*}{\partial z^{*2}}=\frac{C^*(z^*+h,t^*)-2C^*(z^*,t^*)+C^*(z^*-h,t^*)}{h^2}+O(h^2) \tag{C-19b}$$

The boundary conditions of Table C-4 specify as a domain the semi-infinite half plane ($0\leq z^*<\infty$). A finite, maximum value of z^* must be chosen for the computer implementation. According to Bard and Faulkner (137), a safe estimate for z_{max} is:

$$z_{max}=6(Dt)^{1/2} \tag{C-20}$$

A finite difference approximation needs to be chosen for the time derivatives. This must be done with care; otherwise convergence or stability problems can result. One method is to use the foward difference approximation for the time derivative around t^*:

$$\frac{\partial C^*}{\partial t^*}=\frac{C^*(x^*,t^*+k)-C^*(x^*,t^*)}{k}+O(k) \tag{C-21}$$

Equation C-21 along with Equations C-19a and C- 19b can be substituted into the material balance and boundary condition equations (C-10 thru C-18). There are two problems. The truncation error for the time derivative is O(k) while for the space derivatives it is $O(h^2)$. A more serious problem is that the computer solution will only be stable for the ratio

$$\beta=\frac{k}{h^2} \tag{C-22}$$

less than 1/2. If h is chosen to be small (to minimize truncation error), then k must be small, and the number of time intervals will be large, leading to excessive computation time.

If Equation C-21 is replaced by the central difference approximation for the time derivative around t^*, then the equations will be unstable for all values of β. However, Equation C-21 can be considered a central difference approximation around the midpoint of the time interval. Equation C-21 can then be used with Equation C-19 averaged at the begining and end of the time interval. This is the Crank-Nicolson implicit method (138) and is stable for all positive, finite values of β. It is the method used here.

In Case II the material balance equations contain non-linear terms. This leads to a set of non-linear finite difference equations. Although methods for the solution of sets of non-linear equations have been applied to the solution of non-linear differential equations (139), here we linearize the equations and iterate. The non-linear term, C_o^{*2}, can be written as:

$$C_o^{*2}(j,i)=2C_o^{*(n)}(j,i)C_o^{*}(j,i)-C_o^{*2(n)}(j,i) \tag{C-23}$$

Here the only non-linear terms involved are from the previous (n^{th}) iteration. An initial guess is required.

Newman has developed the BAND routine (140,141) to solve sets of coupled linear (or non-linear if an iterative method like Equation C-23 is used) ordinary differential equations. This program can be adapted to solve partial differential equations. For example, using the Crank-Nicolson method, Equation C-15 can be represented in finite difference form as:

$$\begin{aligned} &-\beta C_y^{*}(j+1,i+1)+\left(2+2\beta+\frac{k_f k}{\lambda^2}\right)C_y^{*}(j,i+1)-\beta C_y^{*}(j-1,i+1)-\left(\frac{2k_f k}{\lambda^2}C_o^{*(n)}(j,i+1)\right)C_o^{*}(j,i+1) \\ &=\beta C_y^{*}(j+1,i)+\left(2-2\beta-\frac{k_f k}{\lambda^2}\right)C_y^{*}(j,i)+\beta C_y^{*}(j-1,i)+\frac{k_f k}{\lambda^2}(C_o^{*2}(j,i)-C_o^{*2(n)}(j,i+1)) \end{aligned} \tag{C-24}$$

The right side of Equation C-24 contains only values of C^* from the previous time step or the previous iteration. Thus at the i+1 time step, the equations are solved as ordinary differential equations using the known values from the previous time step. The solution at $t^*=0$ is known because Equation 3-2 is strictly valid as $t^*\rightarrow 0$. For Case II where there are iterations at each time step, the final values of the concentration from the i time step are used as the initial guess for the i+1 time step.

C.3. Results and Discussion

There are four parameters to be determined from a set of experiments: the exchange current density and diffusion parameter that characterize the electrochemical reaction, and the forward and backward rate constants that characterize the chemical reaction. If the equilibrium constant is known, then only three parameters are adjustable because the rate constants are related by $K_{eq}=k_f/k_b$. The values of the first four dimensionless groups in Table C-3 plus the

time interval of observation will determine the type of information obtainable for a given system.

We will use an example to illustrate the effect of a slow homogeneous reaction on the current-time response at an electrode. The electrochemical system is characterized by the parameters listed in the first column of Table C-5. The square points in Figure C-1 were calculated from the numerical model (first-order kinetics). The limiting cases of no coupled homogeneous reaction (k_f=0, solid line) and very fast homogeneous reaction ($k_f \rightarrow \infty$, dotted line) are shown. The current-time responses for these limiting cases are calculated from Equation 3-2 using the diffusion parameters shown in the second column of Table C-5. The diffusion parameter for the fast homogeneous reaction ($k_f \rightarrow \infty$) is obtained from Equation 3-4 by replacing C_{ob} with C_{yb}. The usual method of obtaining the kinetic and diffusion parameters is a non-linear least squares fit of the data to an assumed form of the current-time transient. The last column of Table C-5 shows the result of using Equation 3-2 to fit the data over three different time intervals. The dashed line in Figure C-1 is the non-linear least squares fit for the time interval 0-3.5 milliseconds.

Since Equation 3-2 does not describe the current-time response of the system over the entire time interval, the values of exchange current density and diffusion parameter obtained from the least squares fit will depend on the time interval selected. This can result, for example, in calculated species concentrations that do not correspond to actual species concentrations in solution. The exchange current density is underestimated because of the "flattening" of the current-time transient at longer times.

As $t \rightarrow 0$ the homogeneous reaction does not influence the current response because the boundary layer thickness is zero. As time increases, the homogeneous reaction will have an increasingly important effect. The last column of Table C-5 shows the effect of changing the time interval over which the non-linear least squares fit to Equation 3-2 is carried out. The fit to the short-time data will give a calculated response at longer times that will be below the experi-

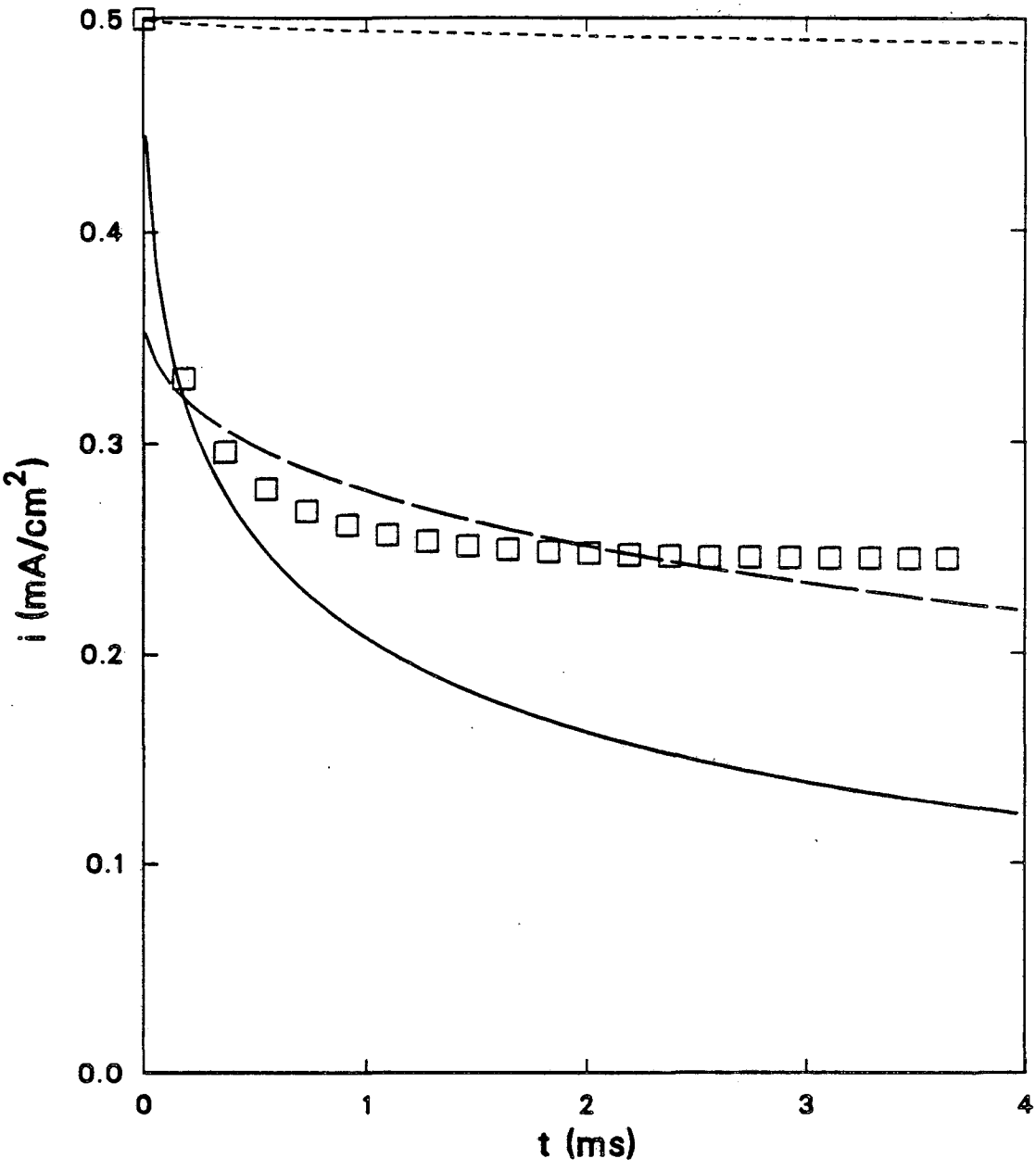


Figure C-1: Calculated transient current response to a potential step, illustrating the errors that can result from using least squares fit to Equation 3-2 when slow homogeneous reactions are coupled to a heterogeneous electrode reaction:
□, calculated from numerical model using parameters in Table IV;
————————, k_f=0;
————————, $k_f \rightarrow \infty$;
— — — —, least-squares fit of Equation 3-2 to points.

Table C-5: Parameters For Figure C-1.

Reaction Parameters	Derived Quantities	Results of Fit to Equation 3-2
$i_o/\nu = 1$ mA/cm^2 V = 12.8 mV n = 1	W = 0.5 mA/cm^2 $V^* = 0.5$ $R_r = 0.5$ ohm–cm^2	0<t<3.5 ms $i_o/\nu = 0.73$ mA/cm^2 Diffusion Parameter = 1.09x10^9 cm^2–sec$^{1/2}$/mole
$C_{ob} = 0.1$ mM $C_{rb} = 10$ mM $C_{yb} = 1$ M	$\lambda = 33.1$ sec$^{-1/2}$ Diffusion Parameter = 3.2x10^9 cm^2–sec$^{1/2}$/mole $k_b/\lambda^2 = 0.913$	0<t<2 ms $i_o/\nu = 0.83$ mA/cm^2 Diffusion Parameter = 1.66x10^9 cm^2–sec$^{1/2}$/mole
$D = 10^{-5}$ cm^2/sec $K_{eq} = 10^{-4}$ $k_f = 0.1$ sec^{-1}	if $k_f \rightarrow \infty$ $\lambda = 0.331$ sec$^{-1/2}$ Diffusion Parameter = 3.2x10^7 cm^2–sec$^{1/2}$/mole	0<t<1 ms $i_o/\nu = 0.92$ mA/cm^2 Diffusion Parameter = 2.26x10^9 cm^2–sec$^{1/2}$/mole

mental currents, but will produce exchange current density and diffusion parameter values that approach those of the unperturbed electrode reaction. These values can then be used as starting values in a least-squares fit using the model that includes the slow homogeneous reaction, with

data over the full time range.

It is useful to construct dimensionless working curves that can be used to determine the range of accessible rate constants and diffusional information. If a numerical simulation is carried out for Case I, and for a given C_{ob}/C_{rb}, k_b/λ^2, and K_{eq} but different values of V^*, all the curves will have the same shape. In fact, all the curves will collapse into one if i^*/V^* is plotted versus t^*. The proof in Section C.4 shows why this behavior is expected. The cathodic and anodic responses, for potential steps of equal size, are mirror images of each other. For Case II, i^*/V^* will, in general, not be independent of V^*. However, under the conditions where the linearization of Equation 3-12 is valid, i^*/V^* for different values of V^* do not deviate from each other by more than a few hundredths of a percent. In order to facilitate comparison among figures, $i^*(1+C_{ob}/C_{rb})/V^*$ is plotted versus t^*. The $(1+C_{ob}/C_{rb})$ term is multiplied by i^*/V^* so that curves with different values of the group C_{ob}/C_{rb} will have the same value of intercept. These dimensionless working curves are presented in Figures C-2 through C-4.

The case of most practical interest is where the electroactive species O is in much smaller concentration than species Y, and therefore K_{eq} is small. At small values of K_{eq} ($<\approx 10^{-4}$), the back reaction dominates, and the shape of the current transient is determined by k_b/λ^2 and C_{ob}/C_{rb}. Figures C-2 and C-3 show the dimensionless current transients for Case I and C_{ob}/C_{rb} of 0 and 1, respectively. The bottom curve in each figure shows the response when no preceding reaction takes place ($k_f=0$). In Figure C-2 the curves becomes almost flat as the homogeneous reaction rate increases because both Y and R are in excess. Only at short times is any transient behavior detectable. In Figure C-3, O and R are present in small and equal concentrations, and at high homogeneous reaction rates the concentration overpotential due to the depletion or production of R (depending on the sign of the potential step) dominates the shape of the current transient.

If the homogeneous reaction scheme of Case II is considered at small values of K_{eq} the curves will be qualitatively similar to those for Case I. The groups that determine the current

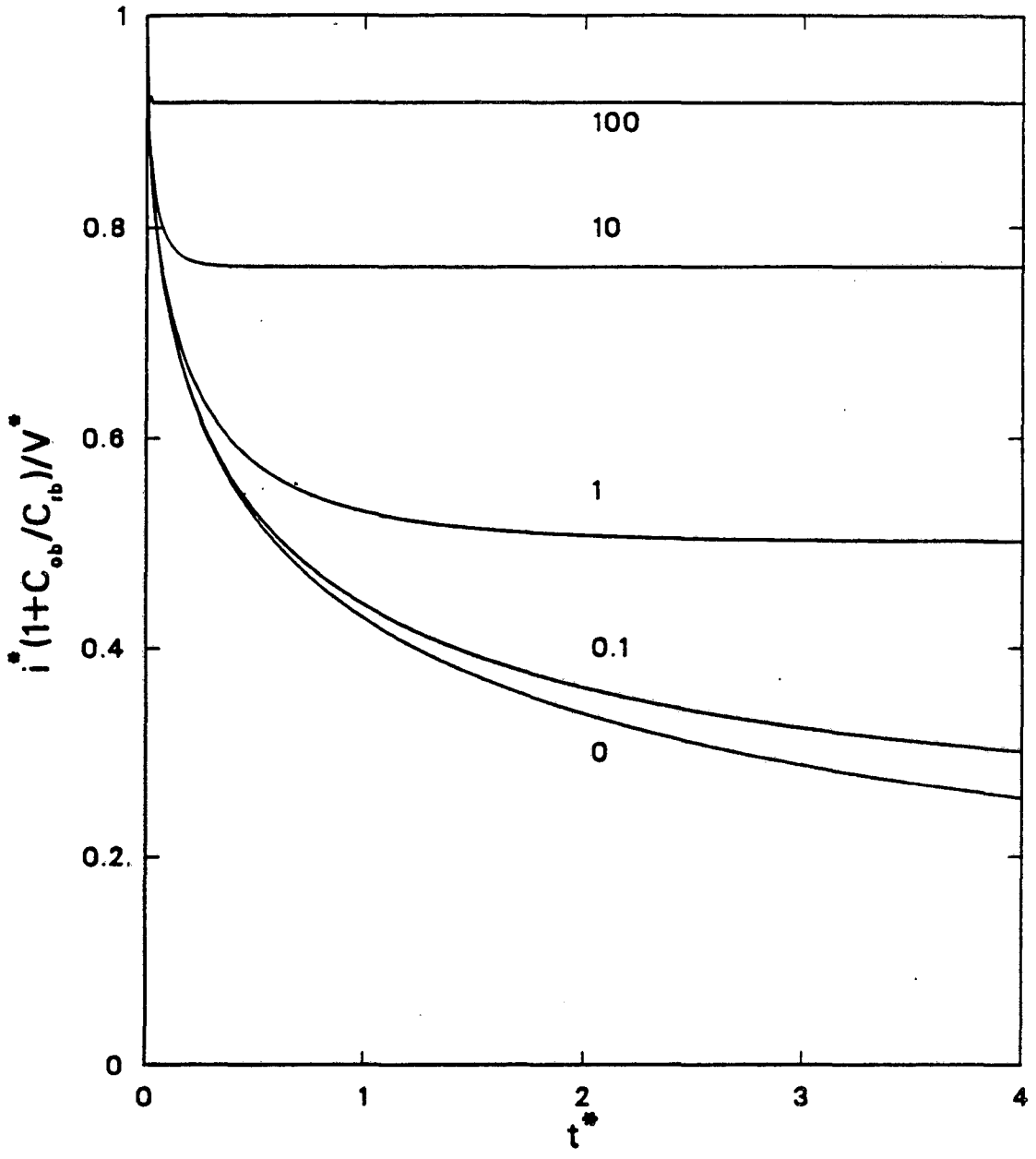
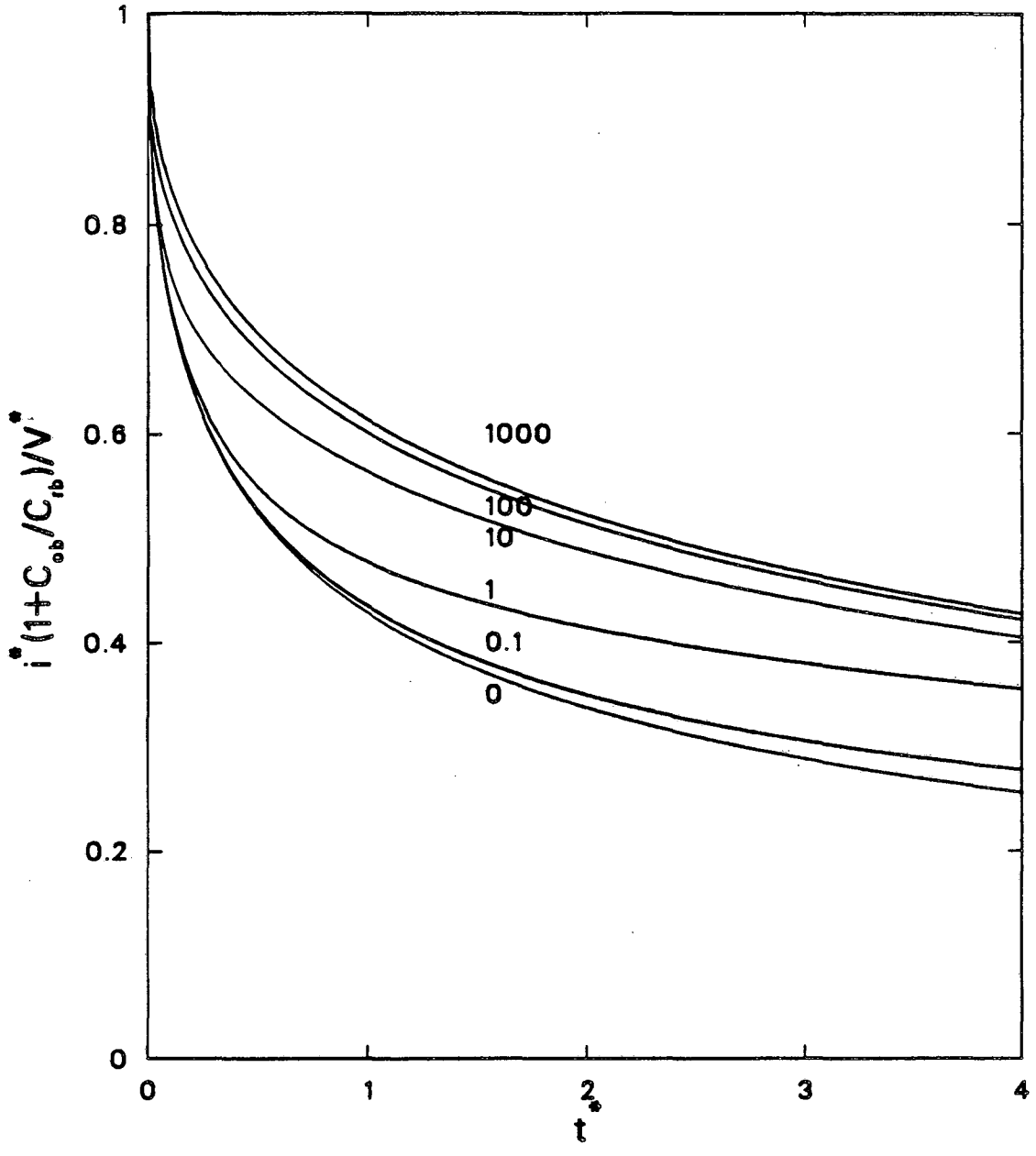
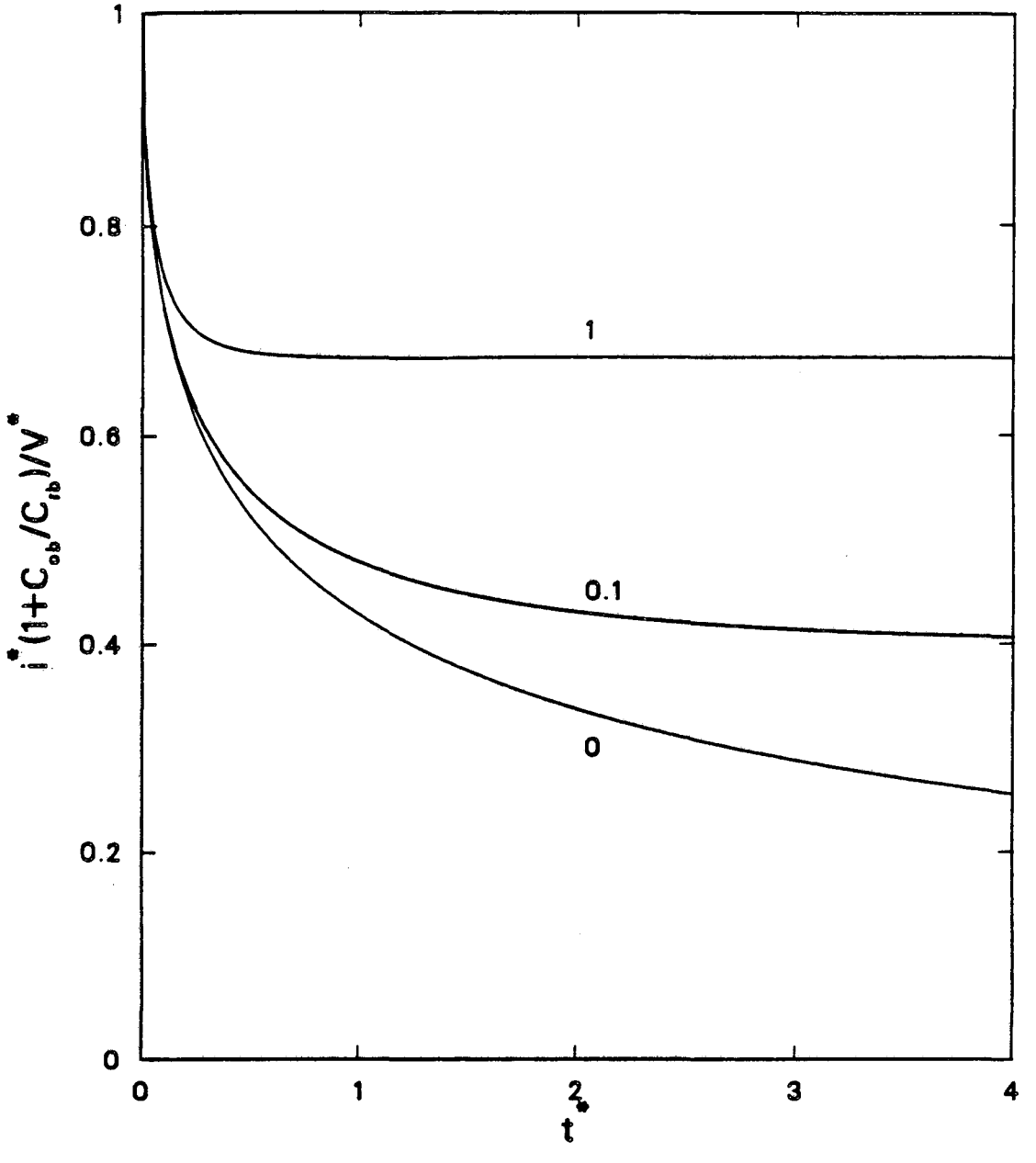


Figure C-2: Calculated dimensionless transient current response to a potential step: Case I kinetics, $C_{ob}/C_{rb}=0$, k_b/λ^2 as labeled.



XCG 869-7376

Figure C-3: Calculated dimensionless transient current response to a potential step: Case I kinetics $C_{ob}/C_{rb}=1$, k_b/λ^2 as labeled.



XCG 869-7386

Figure C-4: Calculated dimensionless transient current response to a potential step: Case II kinetics, $C_{ob}/C_{rb}=0$, k_bC_{ob}/λ^2 as labeled.

response at the electrode are $k_b C_{ob}/\lambda^2$ and C_{ob}/C_{rb}. Figure C-4 shows the normalized current transients for the condition of $C_{ob}/C_{rb} = 0$. There is a quantitative difference in response for Case I and Case II, even when $k_b C_{ob}/\lambda^2 = k_b/\lambda^2$. The range of homogeneous rate constants for which the current response is most sensitive to the rate of the homogeneous reaction is also somewhat different.

How well the model of Equation 3-2 will approximate the data depends on k_b/λ^2, C_{ob}/C_{rb}, and the time of observation (t^*). As $k_b/\lambda^2 \rightarrow 0$, Equation 3-2 fits exactly over all t^*. At the other limit, $k_b/\lambda^2 \rightarrow \infty$, Equation 3-2 also describes the relaxation curve. Here Y and O are in quasi-equilibrium, so the assumption of only one rate-determining step again holds, and in the diffusion parameter λ, O is simply replaced by Y. In the middle range of k_b/λ^2, the effect of homogeneous reaction will be most apparent. Attempts to correlate experimental data with Equation 3-2 (e.g., by a non-linear least squares fit) will lead to systematic deviations between the calculated current response and the experimental data (*cf.* Figure C-1).

The sensitivity of the current response to a change in kinetic parameters can be represented quantitatively by the term $\frac{\Delta i^*}{V^* \Delta \log k_b/\lambda^2}$. In Table C-6 this quantity is listed for the curves of Figures C-2 through C-4 at four different dimensionless times t^*. The values are normalized so that the smallest value of $\frac{\Delta i^*}{V^* \Delta \log k_b/\lambda^2}$ for each case is assigned a value of unity.

Table C-6 can be used as an aid in locating the range of k_b/λ^2 where the current response is most sensitive to a change in k_b/λ^2 and for locating the value of t^* where the current response is most sensitive to changes in kinetic parameters. For example, Table C-6 shows that for $C_{ob}/C_{rb}=1$ and first-order kinetics, the current response is most sensitive to changes in k_b/λ^2 for k_b/λ^2 between 0.1 and 10. At values of k_b/λ^2 between 0.01 and 0.1, the current response is much less sensitive. As t^* increases, the sensitivity increases somewhat because the expanding boundary layer allows homogeneous kinetics to have a greater influence.

Table C-6: Sensitivity Of Current To Change In Kinetics:
Values of the Parameter
$$\frac{\Delta i^*}{V^* \Delta \log(k_b/\lambda^2)}$$

C_{ob}/C_{rb}=0, Case I Kinetics[a] Range of k_b/λ^2	t^*=1	t^*=2	t^*=3	t^*=4
0.01-0.1	1	1.9	2.8	3.5
0.1-1	7.8	12.7	15.7	17.6
1-10	20.4	22.5	22.8	22.9
10-100	13.7	13.7	13.7	13.7
C_{ob}/C_{rb}=1, Case I Kinetics[b] Range of k_b/λ^2				
0.01-0.1	1	1.9	2.8	3.4
0.1-1	7.5	11.6	13.2	13.8
1-10	15.5	13.0	10.6	8.9
10-100	6.6	4.7	3.6	3.0
C_{ob}/C_{rb}=0, Case II Kinetics[c] Range of k_bC_{ob}/λ^2				
0.01-0.1	1	1.84	2.45	2.9
0.1-1	4.4	5.5	5.9	6.0
1-10	4.4	4.4	4.4	4.4
10-100	2.1	2.1	2.1	2.1

a $\left.\frac{\Delta i^*}{V^* \Delta \log(k_b/\lambda^2)}\right|_{min} = 0.0114$

b $\left.\frac{\Delta i^*}{V^* \Delta \log(k_b/\lambda^2)}\right|_{min} = 0.0028$

c $\left.\frac{\Delta i^*}{V^* \Delta \log(k_bC_{ob}/\lambda^2)}\right|_{min} = 0.0444$

Several strategies can be used to determine the homogeneous and heterogeneous parameters from the experimental current response curve. For example, the numerical differential equation solution routine can be coupled to a non-linear least squares optimization package (see Appendix B); this has been done recently by Nagy (80) for the extension of dc relaxation methods to the non-linear current-overpotential range. There are some caveats to be noted. The differential

equations have to be solved for each set of parameters called by the optimization package. If the initial guesses for the parameters are far from the correct values, large amounts of computer time may be required. The optimization program can also become trapped in a local minimum that does not represent the physically meaningful solution. The chances of this happening increase as the number of parameters to be fit increases or the initial guesses become worse.

Equation 3-2 is strictly valid as $t^* \rightarrow 0$. This suggests the use of Equation 3-2 to estimate the heterogeneous parameters W and λ from the data near t=0. These values could then be used as starting values in a non-linear least squares optimization, or be used as fixed values for a parameter optimization involving only homogeneous kinetic parameters. Table C-6 shows that the response curves are more sensitive to homogeneous kinetic parameters as t^* increases. This illustrates the desirability of taking data over a fairly wide range of time for maximum precision in determining both heterogeneous and homogeneous kinetic parameters. Reller *et al.* (142) and Nagy (132) have examined the errors involved in fixing a parameter and allowing the others to vary.

Figure C-5 shows some examples of the error in determining the zero-time intercepts of the curves in Figures C-2 thru C-4 when the approximate model of Equation 3-2 is used to fit the numerical data. If short-time data can be used, the error can be limited to a few percent even in those cases where the current response is most sensitive to homogeneous kinetics. The minimum time of observation is limited by factors such as the rise time of the potentiostat and double layer charging. Figure C-5 shows that the errors are larger when the time of observation is limited by these factors, but a valid estimate to start a non-linear least squares optimization can still be made.

C.4. Proof of Symmetrical Response for Linear Homogeneous Kinetics

If the potential step can be simulated by a combination of linear partial differential equations (PDE's) and linear boundary conditions, it will be shown that i^*/V^* is independent of V^*. This result will also apply to systems with no homogeneous reactions (Equation 3-2), and slow

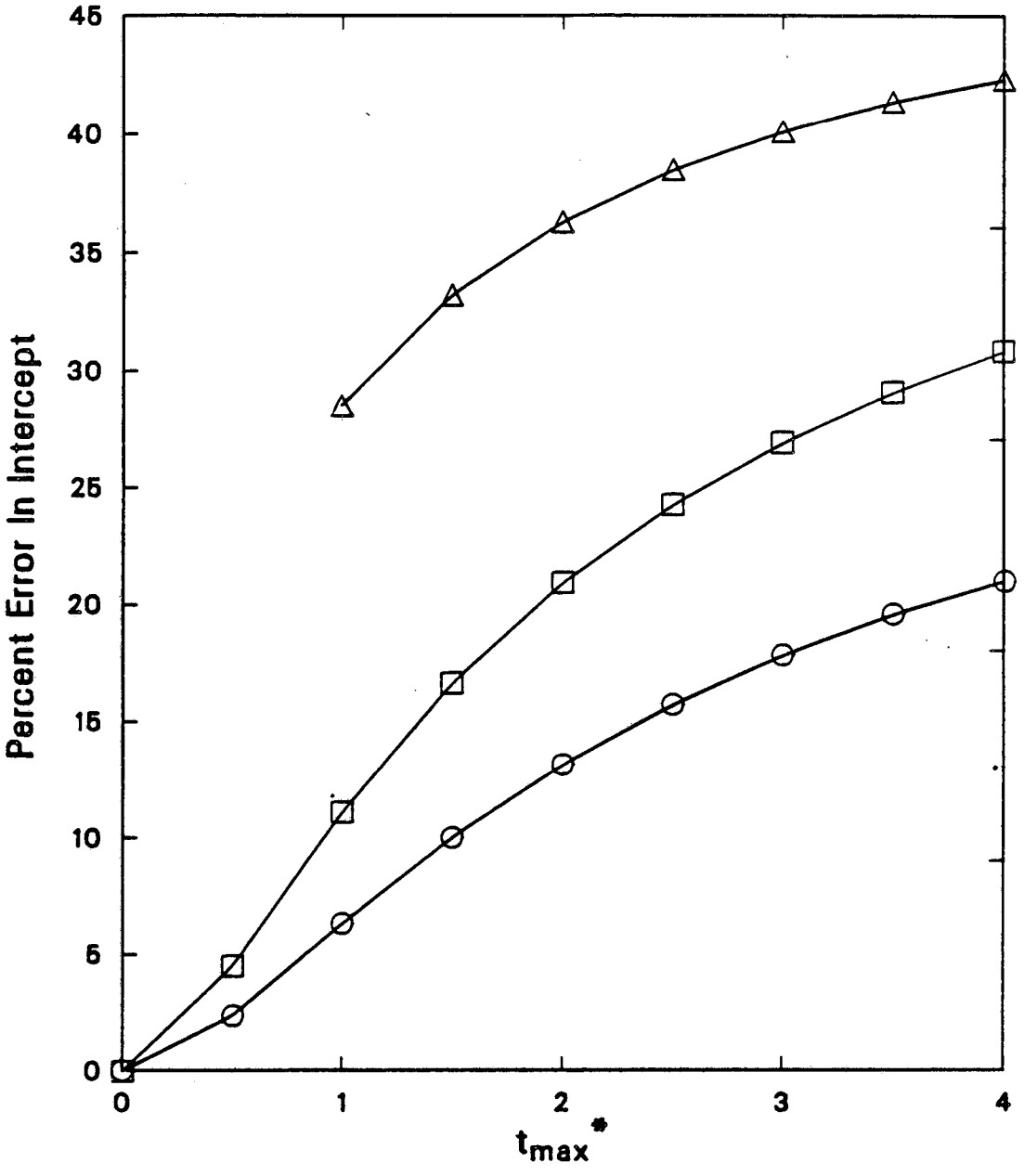


Figure C-5: Error in determination of intercept:
○, Case I kinetics, $k_b/\lambda^2=1$, $C_{ob}/C_{rb}=1$;
□, Case I kinetics, $k_b/\lambda^2=1$, $C_{ob}/C_{rb}=0$;
Δ, same but $t^*_{min}=0.5$

homogeneous reactions with zero- or first-order kinetics.

A set of linear PDE's and boundary conditions can be reduced to a set of ordinary differential equations and algebraic equations by a Laplace transform technique (143). From Equations C-10 and C-12 plus boundary conditions C-17 and C-18b we can obtain:

$$\bar{C}_o^* = A\bar{f}(s,z^*,\frac{k_f}{\lambda^2},K_{eq}) \tag{C-25}$$

From the transform of Equation C-11:

$$\bar{C}_r^* = B\bar{g}(s,z^*) \tag{C-26}$$

The constants A and B can be related by C-18a. Using that boundary condition and the relation between current density and concentration gradient (and assuming for illustrative purposes that all diffusion coefficients are equal and the stoichiometric coefficients are equal):

$$\bar{i}^* = \frac{-V^*\frac{\partial \bar{f}}{\partial z^*}}{s\left[\bar{f}-\frac{C_{ob}}{C_{rb}}\frac{\frac{\partial \bar{f}}{\partial z^*}}{\frac{\partial \bar{g}}{\partial z^*}}-(1+\frac{C_{ob}}{C_{rb}})\frac{\partial \bar{f}}{\partial z^*}\right]} \tag{C-27}$$

All the functions and derivatives in Equation C-27 are evaluated at $z^*=0$. The right side of Equation C-27 can be denoted by $\bar{h}$. The inverse transform of Equation C-27 can be taken:

$$\frac{i^*}{V^*} = h(t^*,C_{ob}/C_{rb},k_f/\lambda^2,K_{eq}) \tag{C-28}$$

Therefore i^*/V^* is independent of V^*.

C.5. Summary

The results presented here represent an extension of the small potential step technique to include reactions which have two slow steps, one of which is a homogeneous reaction in bulk solution. The material balances and boundary conditions are presented for homogeneous reactions following first-order kinetics or dissociation-dimerization kinetics. At short times, the current response at the electrode follows the current-time response given by Equation 3-2 (or Equation 3-18). Over a longer time interval, a fit of experimental data to Equation 3-2 will give

species concentrations and an exchange current density that are erroneous. Using the full numerical model, the correct diffusional and rate data for both homogeneous and heterogeneous reactions can be obtained. For a particular system, the type of information that can be obtained will depend on the time available for observation and the values of the dimensionless groups listed in Table C-3. Figures C-2 through C-5 and Table C-6 should be of help in identifying the information obtainable for a given system.

C.6. Computer Programs

```
C This program uses numerical simulation to simulate a small potential
C step with 1st order  homogeneous kinetics
C The reaction sequence simulated is:
C       Y = O
C       O + ne = R
C The equilibrium constant for the chemical reaction is Keq =Cob/Cyb
C kf = foward rate constant
C Keq = kf/kb
C crat = Cob/Crb
C lamb is a heterogeneous kinetic parameter
C Vs = dimensionless potential step



      Real*8 tsmax,xsmax,Vs,r,crat,h,dts
      Real*8 ts,cs,csp,xs,cpp,homo
      Real*8 kf,Keq,lamb
      Real*8 dsqrt,derfc,ee
      Real*8 C(3,203),Save(3,203)
      Real*8 A(3,3),B(3,3),D(3,7),X(3,3),Y(3,3),G(3)
      Real*8 dgro1,dgro2,dgro3,fac1,fac2
      Integer NJ,ni,n
      Integer nint
      Common /BLK1/ A,B,C,D
      Common /BLK2/ G,X,Y,N,NJ

C ***************************************************************************
C *                                                                         *
C *                                                                         *
C                       OPEN FILES
C *                                                                         *
C *                                                                         *
C ***************************************************************************

C Open graphics file
      Open (Unit=8, File='current.gph',Status='New')

C Open file for concentration profile
      Open (Unit = 9, File = 'conch1.pro', Status = 'New')


C ***************************************************************************
C *                                                                         *
C *                                                                         *
C                       READ PARAMETERS
C *                                                                         *
C *                                                                         *
C ***************************************************************************
      Read (5,10) tsmax,Vs,r,crat
10    Format (4f16.7)
```

```
      Read (5,11) kf,Keq,lamb
11    Format(3f16.7)

C Number of mesh points for t
      Read (5,15) ni
15    Format (i4)

C Number of equations
      n=3
C ***************************************************************************
C *                                                                         *
C *                                                                         *
C              SET UP SPACE AND TIME MESH
C *                                                                         *
C *                                                                         *
C ***************************************************************************

C t interval size
      dts = tsmax/(ni - 1)

C x interval size
      h = dsqrt(dts/r)

C Conservative estimate for x boundary layer thickness
      xsmax = 6.0*dsqrt(tsmax)

C Number of x mesh points including a image point at x=0
      NJ = nint(xsmax/h) + 2

C Define groups and factors that need to be calculated
C once for each simulation
      dgro1 = kf/(lamb*lamb)
      dgro2 = 1/Keq
      dgro3 = dgro1*dgro2
      fac1 = dgro1*dts
      fac2 = dgro3*dts

C ***************************************************************
C *                                                             *
C *                                                             *
C              WRITE OUT PARAMETERS
C *                                                             *
C *                                                             *
C ***************************************************************

C To terminal screen
      Write (6,990)
990   Format (' ****RESULTS FOR 1st ORDER KINETICS****',/)
      Write (6,16) Vs,crat
16    Format (' ** Step Size = ',f10.4,/,' ** Cob/Crb = ',f10.4,/)
      Write (6,17) dgro1,Keq
17    Format (' ** kf/lambda**2 = ',1pe10.2,/
     1,' ** Keq = (Cob/Cyb) = ',e10.2,/)
```

```
      Write (6,19) r
19    Format (' ** delta t/(delta x)**2 = ',f10.4,/)
      Write (6,20) tsmax,dts, ni-1
20    Format (' ** tmax = ',f8.2,5x
     1,'delta t = ',f10.4,5x
     2,'num of t int. = ',i4,/)
      Write (6,25) xsmax,h,NJ-2
25    Format (' ** xmax = ',f8.2,5x
     1,' delta x = ',f10.4,5x
     2,'num of x int. = ',i4,/)

C To graphics file

      Write (8,990)
      Write (8,16) Vs,crat
      Write (8,17) dgro1,Keq
      Write (8,19) r
      Write (8,20) tsmax,dts,ni-1
      Write (8,25) xsmax,h,NJ-2

C To concentration profile file
      Write (9,990)
      Write (9,16) Vs,crat
      Write (9,17) dgro1,Keq
      Write (9,19) r
      Write (9,20) tsmax,dts,ni-1
      Write (9,25) xsmax,h,NJ-2

C ***************************************************************************
C *                                                                         *
C *                                                                         *
C                       SET UP ARRAYS
C *                                                                         *
C *                                                                         *
C ***************************************************************************

      do 100 k = 1,203
            C(1,k) = 0.0
            C(2,k) = 0.0
            C(3,k) = 0.0
100   Continue

C Initial concentration profile should satisfy boundary conditions
      Save(1,1) = 2.*h*Vs/(1.+crat) +1.
      Save(2,1) = 1. - 2.*h*crat*Vs/(1.+crat)
      Save(3,1) = 1.0
      do 105 k= 2,203
            Save(1,k) = 1.0
            Save(2,k) = 1.0
            Save(3,k) = 1.0
105   Continue

C Print out initial current
```

```
      cs = -(Save(1,3) - Save(1,1))/(2.*h)
      csp = Vs/(1.+crat)
      Write (6,175) 0.0,cs/csp

      Write (8,168) dgro3
168   Format (' "kb/lambda<EH.8)2<EXHX)=',1pe9.2
     1,'"')

      Write (8,170) 0.0,cs/csp

C *********************************************************************
C *                                                                   *
C *                                                                   *
C     SOLVE DIFFERENTIAL EQUATION FOR EACH TIME STEP
C *                                                                   *
C *                                                                   *
C *********************************************************************
      do 500 i = 2,ni

C Set up for first mesh point (j = 1)
      do 125 in1 = 1,3
            do 120 in2 = 1,3
                  B(in1,in2) = 0.0
                  D(in1,in2) = 0.0
                  X(in1,in2) = 0.0
120         Continue
      G(in1) = 0.0
125   Continue
      B(1,1) = -crat
      X(1,1) = crat
      B(1,2) = -1.0
      X(1,2) = 1.0
      G(1) = Save(2,1)-Save(2,3)+crat*(Save(1,1)-Save(1,3))
      B(2,1) = 1.* (1.0 + crat)/2.0
      D(2,1) = h
      X(2,1) = -1.* (1.0 + crat)/2.0
      D(2,2) = -h
      G(2) = 2.*h*Vs
     1+h*(Save(2,2)-Save(1,2))+(1.+crat)/2.*(Save(1,3)-Save(1,1))
      B(3,3) = -1.0
      X(3,3) = 1.0
      G(3) = Save(3,1) - Save(3,3)
C Now call BAND
      Call BAND(1)
C For interior points
      do 150 j = 2,NJ-1
            do 135 in1 = 1,3
                  do 130 in2 = 1,3
                        A(in1,in2) = 0.0
                        B(in1,in2) = 0.0
                        D(in1,in2) = 0.0
130               Continue
                  G(in1) = 0.0
```

```
135             Continue
                A(1,1) = -r
                B(1,1) = 2.+2.*r+fac2
                D(1,1) = -r
                B(1,3) = -fac2
                G(1) = r*Save(1,j-1)+(2.-2.*r-fac2)*Save(1,j)
   1+r*Save(1,j+1)+fac2*Save(3,j)
                A(2,2) = -r
                B(2,2) =  2.0*(1.0 + r)
                D(2,2) = -r
                G(2) = r*Save(2,j-1)+2.0*(1.-r)*Save(2,j)+r*Save(2,j+1)
                B(3,1) = -fac1
                A(3,3) = -r
                B(3,3) = 2.+2.*r+fac1
                D(3,3) = -r
                G(3) = r*Save(3,j-1)+(2.-2.*r-fac1)*Save(3,j)
   1+r*Save(3,j+1)+fac1*Save(1,j)
                Call BAND(j)
150     Continue
C Last mesh point
        do 165 in1 = 1,3
                do 160 in2 = 1,3
                        Y(in1,in2) = 0.0
                        A(in1,in2) = 0.0
                        B(in1,in2) = 0.0
160             Continue
                G(in1) = 0.0
165     Continue
        B(1,1) = 1.0
        G(1) = 1.0
        B(2,2) = 1.0
        G(2) = 1.0
        B(3,3) = 1.0
        G(3) = 1.0
        Call BAND(NJ)
C ***************************************************************************
C *                                                                         *
C *                                                                         *
C               WRITE OUT RESULTS AT THIS TIME STEP
C *                                                                         *
C *                                                                         *
C ***************************************************************************

C Compute current
        cs = -(C(1,3) - C(1,1))/(2.0*h)

C Get value of time
        ts = dts * (i-1)

C Compute current with no homogenous kinetics
        csp = Vs/(1. + crat)*ee(dsqrt(ts))
C Compute overpotentials:
C       Mass transfer
```

```
        etacs = C(1,2) - C(2,2)
C       Sum of charge transfer and ohmic
        etaas = (1. + crat)*cs

C Write points to file for graph and every 100th point to screen
        Write (8,170) ts,cs/csp
170     Format (2f16.7)
        If(float(i-1)/100.0 .eq. float(int((i-1)/100))) Then
                Write (6,175) ts,cs/csp
175             Format (' at ts = ',f10.4,5x,'cs/csp = ',f10.4)

        Write (9,180) ts
180     Format (1H1,' ts = ',f10.4)
        Write (9,181) cs,csp
181     Format (/,' cs = ',f10.4,5x,'cs (no homo kin) = ',f10.4,/)
        Write (9,182) cs/csp,etacs,etaas
182     Format (' i(hk)/i(nohk) = ',f7.4,3x
   1,' eta(conc.) = ',f7.4,3x,'eta(ac+ohmic) = ',f7.4,/)
C Write out table header to concentration file
        Write (9,183)
183     Format (6x,'xs',8x,'Co',8x,'Cr',8x,'Cy',6x,'Co Diff'
   1,3x,'Homo Kin',/)

C Write out concentrations at image point
        Write (9,184) -h,C(1,1),C(2,1),C(3,1)
184     Format(4f10.4)

C Write out concentration profile in boundary layer
        do 190 j = 2,NJ-1
                xs = (j-2)*h
                cpp=(C(1,j+1)-2.*C(1,j)+C(1,j-1))/(h*h)
                homo =kf/(Keq*lamb*lamb)*(C(3,j)-C(1,j))
                If ((dabs(cpp) .lt. 1.e-5) .and.
   1(dabs(homo) .lt. 1.e-5) .and.
   2(dabs(1.-C(2,j)) .lt. 1.e-5)) Then
                        goto 195
                Endif
                Write (9,185) xs,C(1,j),C(2,j),C(3,j),cpp,homo
185             Format (6f10.4)
190     Continue

195     Continue
        Endif

C ***************************************************************************
C *                                                                         *
C *                                                                         *
C               SET UP FOR NEXT TIME STEP
C *                                                                         *
C *                                                                         *
C ***************************************************************************
C Save concentration values from this time step to use in next time step
C and re zero concentration array
```

```
      do 200 k = 1,NJ
            Save (1,k) = C(1,k)
            Save (2,k) = C(2,k)
            Save(3,k) = C(3,k)
            C(1,k) = 0.0
            C(2,k) = 0.0
            C(3,k) = 0.0
200   Continue
500   Continue

      Stop
      End
```

```
C This program uses numerical simulation to simulate a small potential
C step with 2nd order  homogeneous kinetics
C The reaction sequence simulated is:
C        Y = 2O
C  2x( O + ne = R)
C The equilibrium constant for the chemical rxn is Keq = Cob*Cob/Cyb
C It is related to the rate constants for the rxn by Keq = kf/kb

        Real*8 tsmax,xsmax,Vs,r,crat,h,dts
        Real*8 ts,cs,csp,xs,etacs,etaac
        Real*8 kf,Keq,lamb,Cob
        Real*8 dsqrt,derfc,dabs
        Real*8 C(3,203),Ci(3,203),Cn(3,203)
        Real*8 A(3,3),B(3,3),D(3,7),X(3,3),Y(3,3),G(3)
        Real*8 tol,cpp,homo,dgro1,dgro2,dgro3,fac1,fac2
        Integer NJ,ni,n
        Integer imax,itnum
        Integer nint
        Common /BLK1/ A,B,C,D
        Common /BLK2/ G,X,Y,N,NJ

C ***************************************************************************
C *                                                                         *
C *                                                                         *
C                       OPEN FILES
C *                                                                         *
C *                                                                         *
C ***************************************************************************
C Open graphics file
        Open (Unit=8, File='current.gph',Status='New')

C Open file for concentration profile
        Open (Unit=9,File='conch2.pro',Status='New')


C ***************************************************************************
C *                                                                         *
C *                                                                         *
C                       READ PARAMETERS
C *                                                                         *
C *                                                                         *
C ***************************************************************************
C tsmax = maximum dimensionless time that the solution is desired at
C Vs = dimensionless potential step
C r = dts/h*h
C crat = Cob/Crb

        Read (5,10) tsmax,Vs,r,crat
10      Format (4f16.7)

C kf = foward rate constant
C Keq = equilibrium constant = Cob*Cob/Cyb
C lamb = kinetic parameter
```

```
C Cob = concentration of Co initially
C tol = tolerance for iterations
      Read (5,11) kf,Keq,lamb,Cob,tol
11    Format(5f16.7)


C Maximum number of iterations
      Read (5,13) imax
13    Format (i2)
C ni = number of mesh points for t
      Read (5,15) ni
15    Format (i4)

C Number of equations
      n=3
C *****************************************************************
C *                                                               *
C *                                                               *
C                SET UP SPACE AND TIME MESH
C *                                                               *
C *                                                               *
C *****************************************************************

C t interval size
      dts = tsmax/(ni - 1)

C x interval size
      h = dsqrt(dts/r)

C Conservative estimate for x boundary layer thickness
      xsmax = 6.0*dsqrt(tsmax)

C Number of x mesh points including an image point at x=0
      NJ = nint(xsmax/h) + 2

C Define groups and factors that need only be computed once
C For each simulation
      dgro1 = kf/(lamb*lamb)
      dgro2 = Cob/Keq
      dgro3 = dgro1*dgro2
      fac1 = dgro1*dts
      fac2 = dgro3*dts
C *****************************************************************
C *                                                               *
C *                                                               *
C                WRITE OUT PARAMETERS
C *                                                               *
C *                                                               *
C *****************************************************************

C To terminal screen
      Write (6,990)
990   Format (' ****RESULTS FOR 2nd ORDER KINETICS****',/)
```

```
      Write (6,16) Vs,crat,dgro1,1/dgro2
16    Format (' ** Step Size = ',f10.4,/,' ** Cob/Crb = ',f10.4,/,
     1' ** kf/lambda**2 = ',1pe10.2,/,
     2' ** Keq/Cob = ',e10.2,/)

      Write (6,17) kf,lamb,Keq,Cob
17    Format (' ** kf = ',1pe10.2,' 1/sec',/
     1,' ** lambda = ',e10.2, ' sec**-1/2',/
     2,' ** Keq =',e10.2,' mole/liter',/,
     3' ** Cob = ',e10.2,' moles/liter',/)

      Write (6,19) r
19    Format (' ** delta t/(delta x)**2 = ',f10.4,/)

      Write (6,20) tsmax,dts, ni-1
20    Format (' ** tmax = ',f8.2,5x
     1,'delta t = ',f10.4,5x
     2,'num of t int. = ',i4,/)

      Write (6,25) xsmax,h,NJ-2
25    Format (' ** xmax = ',f8.2,5x
     1,' delta x = ',f10.4,5x
     2,'num of x int. = ',i4,/)

C To concentration profile file
      Write (9,990)
      Write (9,16) Vs,crat,dgro1,1./dgro2
      Write (9,17) kf,lamb,Keq,Cob
      Write (9,19) r
      Write (9,20) tsmax,dts,ni-1
      Write (9,25) xsmax,h,NJ-2

C To graphics file
      Write (8,990)
      Write (8,16) Vs,crat,dgro1,1./dgro2
      Write (8,17) kf,lamb,Keq,Cob
      Write (8,19) r
      Write (8,20) tsmax,dts,ni-1
      Write (8,25) xsmax,h,NJ-2

C ****************************************************************
C *                                                              *
C *                                                              *
C                      SET UP ARRAYS
C *                                                              *
C *                                                              *
C ****************************************************************

      do 100 k = 1,203
            C(1,k) = 0.0
            C(2,k) = 0.0
            C(3,k) = 0.0
100   Continue
```

```
C Initial concentration profile should satisfy boundary conditions
      Ci(1,1) = 2.*h*Vs/(1.+crat) +1.
      Ci(2,1) = 1. - 2.*h*crat*Vs/(1.+crat)
      Ci(3,1) = 1.0
      do 105 k= 2,203
            Ci(1,k) = 1.0
            Ci(2,k) = 1.0
            Ci(3,k) = 1.0
105   Continue

C Print out initial.current
      cs = -(Ci(1,3) - Ci(1,1))/(2.*h)
      csp = Vs/(1.+crat)
      Write (6,175) 0.0,cs/csp,0

      Write (8,168) dgro3
168   Format (' "kb*Cob/lambda**2 = ',1pe11.3,' " ')

      Write (8,170) 0.0,cs*(1.+crat)/Vs

C ***************************************************************************
C *                                                                         *
C *                                                                         *
C              FOR EACH TIME STEP SOLVE DIFFERENTIAL EQUATION
C *                                                                         *
C *                                                                         *
C ***************************************************************************
      do 500 i = 2,ni

C ***************************************************************************
C *                                                                         *
C *                                                                         *
C      FIRST TIME THROUGH AT EACH TIME STEP - INITAL GUESS
C *                                                                         *
C *                                                                         *
C ***************************************************************************

C Inital guess for C at the i+1 time step will be the final value
C for C at the i time step
      itnum = 1
      do 111 in1 = 1,3
            do 110 j = 1,NJ
                  Cn(in1,j) = Ci(in1,j)
110         Continue
111   Continue

C If this is not the first iteration for this time step then we will
C start here
115   Continue

C Set up for first mesh point (j = 1)
      do 125 in1 = 1,3
            do 120 in2 = 1,3
```

```
                        B(in1,in2) = 0.0
                        D(in1,in2) = 0.0
                        X(in1,in2) = 0.0
120             Continue
        G(in1) = 0.0
125     Continue
        B(1,1) = -crat
        X(1,1) = crat
        B(1,2) = -1.0
        X(1,2) = 1.0
        G(1) = Ci(2,1)-Ci(2,3)+crat*(Ci(1,1)-Ci(1,3))
        B(2,1) = 1.* (1.0 + crat)/2.0
        D(2,1) = h
        X(2,1) = -1.* (1.0 + crat)/2.0
        D(2,2) = -h
        G(2) = 2.*h*Vs
   1+h*(Ci(2,2)-Ci(1,2))+(1.+crat)/2.*(Ci(1,3)-Ci(1,1))
        B(3,3) = -1.0
        X(3,3) = 1.0
        G(3) = Ci(3,1) - Ci(3,3)
C Now call BAND
        Call BAND(1)
C For interior points
        do 150 j = 2,NJ-1
                do 135 in1 = 1,3
                        do 130 in2 = 1,3
                                A(in1,in2) = 0.0
                                B(in1,in2) = 0.0
                                D(in1,in2) = 0.0
130                     Continue
                        G(in1) = 0.0
135             Continue
                A(1,1) = -r
                B(1,1) = 2.+2.*r
   1+4.*fac2*Cn(1,j)
                D(1,1) = -r
                B(1,3) = -2.*fac2
                G(1) = r*Ci(1,j+1)
   1+(2.-2.*r-2.*fac2*Ci(1,j))*Ci(1,j)
   2+r*Ci(1,j-1)+2.*fac2*Ci(3,j)
   3+2.*fac2*Cn(1,j)*Cn(1,j)
                A(2,2) = -r
                B(2,2) =  2.0*(1.0 + r)
                D(2,2) = -r
                G(2) = r*Ci(2,j-1)+2.0*(1.-r)*Ci(2,j)+r*Ci(2,j+1)
                B(3,1) = -2.*fac1*Cn(1,j)
                A(3,3) = -r
                B(3,3) = 2.+2.*r+fac1
                D(3,3) = -r
                G(3) = r*Ci(3,j+1)+(2.-2.*r-fac1)*Ci(3,j)
   1+r*Ci(3,j-1)+fac1*Ci(1,j)*Ci(1,j)
   2-fac1*Cn(1,j)*Cn(1,j)
                Call BAND(j)
```

```
150     Continue
C Last mesh point
        do 165 in1 = 1,3
                do 160 in2 = 1,3
                        Y(in1,in2) = 0.0
                        A(in1,in2) = 0.0
                        B(in1,in2) = 0.0
160             Continue
                G(in1) = 0.0
165     Continue
        B(1,1) = 1.0
        G(1) = 1.0
        B(2,2) = 1.0
        G(2) = 1.0
        B(3,3) = 1.0
        G(3) = 1.0
        Call BAND(NJ)
C
C
C

C ***************************************************************************
C *                                                                         *
C *                                                                         *
C               CHECK FOR CONVERGENCE

C *                                                                         *
C *                                                                         *
C ***************************************************************************
        do 210 in1 = 1,3
                do 205 j = 1,NJ
                If(dabs((C(in1,j)-Cn(in1,j))/C(in1,j)) .gt. tol) Then
C This is what is done if solution has not converged
C First increment iteration number
                        itnum = itnum + 1
C Now check iteration number against maximum iteration number
                        If ( itnum .gt. imax) Then
                                Write (6,900) (i-1)*dts,imax
900                             Format(' at ts = ',f16.7,/
   1,' maximum iteration count = ',i3, 'exceeded')
                                Stop
                        Endif
C Maximum iteration number has not been exceeded so set up
C for another iteration
                        do 600 m1 = 1,3
                                do 550 m2 = 1,NJ
                                        Cn(m1,m2) = C(m1,m2)
550                             Continue
600                     Continue
C Now go back and try again
                        goto 115
                Endif
```

```
205             Continue
210     Continue
C Normal exit from do loop so equation has converged at i+1 time step

C ***************************************************************
C *                                                             *
C *                                                             *
C               WRITE OUT RESULTS AT THIS TIME STEP
C *                                                             *
C *                                                             *
C ***************************************************************

C Compute current from concentration gradient
        cs = -(C(1,3) - C(1,1))/(2.0*h)

C Compute time
        ts = dts * (i-1)

C Current in the absence of homogeneous kinetics
        csp = Vs/(1.+crat) *dexp(ts)*derfc(dsqrt(ts))

C Overpotentials:
C       Concentration overpotential
        etacs = C(1,2) - C(2,2)
C       Activation + ohmic overpotential
        etaac = (1. + crat)*cs

C Write all points to graphics file
        Write (8,170) ts,cs*(1.+crat)/Vs
170     Format (2f16.7)

C Every 100th time step to screen and concentration profile file
        If(float(i-1)/100.0 .eq. float(int((i-1)/100))) Then
                Write (6,175) ts,cs/csp,itnum
175             Format (' at ts = ',f10.4,5x
   1,'cs/csp = ',f10.4,5x,'in ',i3,' iterations')

                Write (9,180) ts
180             Format (1H1,' ts = ',f10.4)
                Write (9,181) cs,csp
181             Format (/,' cs = ',f10.4,5x,'cs (no homo kin) = ',f10.4,/)
                Write (9,182) cs/csp,etacs,etaac
182             Format (' i(HK)/i(NoHK) = ',f7.4,3x
   1,'eta(conc.) = ',f7.4,3x,'eta(ac+ohmic) = ',f7.4)
C Write out table header to concentration profile file
                Write (9,183)
183             Format (6x,'xs',8x,'Co',8x,'Cr',8x,'Cy',6x,'Co Diff'
   1,3x,'Homo Kin',/)

C Write out concentrations at image point
                Write (9,184) -h,C(1,1),C(2,1),C(3,1)
184             Format(4f10.4)
```

```
                do 190 j = 2, NJ-1
                        xs = (j-2)*h
                        cpp=(C(1,j+1)-2.*C(1,j)+C(1,j-1))/(h*h)
                        homo = 2.*dgro3*(C(3,j)-C(1,j)*C(1,j))
                        If ((dabs(cpp) .lt. 1.e-5) .and.
   1(dabs(homo) .lt. 1.e-5) .and.
   2(dabs(1.-C(2,j)) .lt. 1.e-5)) Then
                                goto 195
                        Endif
                        Write (9,185) xs,C(1,j),C(2,j),C(3,j),cpp,homo
185                     Format (6f10.4)
190             Continue

195     Continue
        Endif

C ***************************************************************
C *                                                             *
C *                                                             *
C               SET UP FOR NEXT TIME STEP
C *                                                             *
C *                                                             *
C ***************************************************************
C Save concentration values from this time step to use in next time step
C and re zero concentration array
        do 200 k = 1,NJ
                Ci (1,k) = C(1,k)
                Ci (2,k) = C(2,k)
                Ci(3,k) = C(3,k)
                C(1,k) = 0.0
                C(2,k) = 0.0
                C(3,k) = 0.0
200     Continue
500     Continue

        Stop
        End
```

```
      SUBROUTINE BAND(J)
      Real*8 E(3,4,1003)
      Real*8 A(3,3),B(3,3),C(3,1003),D(3,7)
      Real*8 G(3),X(3,3),Y(3,3)
      Real*8 DETERM
      COMMON /BLK1/ A,B,C,D
      COMMON /BLK2/ G,X,Y,N,NJ
      IF (J-2) 1,6,8
1     NP1=N+1
      DO 2 I=1,N
      D(I,2*N+1)=G(I)
      DO 2 L=1,N
      LPN=L+N
2     D(I,LPN)=X(I,L)
      CALL MATINV (N,2*N+1,DETERM)
      IF (DETERM) 4,3,4
3     WRITE (6,101) J
101   FORMAT (1X, 14HDETERM=0 AT J=,I4)
4     DO 5 K=1,N
      E(K,NP1,1)=D(K,2*N+1)
      DO 5 L=1,N
      E(K,L,1)=-1.*D(K,L)
      LPN=L+N
5     X(K,L)=-1.*D(K,LPN)
      RETURN
6     DO 7 I=1,N
      DO 7 K=1,N
      DO 7 L=1,N
7     D(I,K)=D(I,K)+A(I,L)*X(L,K)
8     IF (J-NJ) 11,9,9
9     DO 10 I=1,N
      DO 10 L=1,N
      G(I)=G(I)-Y(I,L)*E(L,NP1,J-2)
      DO 10 M=1,N
10    A(I,L)=A(I,L)+Y(I,M)*E(M,L,J-2)
11    DO 12 I=1,N
      D(I,NP1)=-1.*G(I)
      DO 12 L=1,N
      D(I,NP1)=D(I,NP1)+A(I,L)*E(L,NP1,J-1)
      DO 12 K=1,N
12    B(I,K)=B(I,K)+A(I,L)*E(L,K,J-1)
      CALL MATINV (N,NP1,DETERM)
      IF (DETERM) 14,13,14
13    WRITE (8,101) J
14    DO 15 K=1,N
      DO 15 M=1,NP1
15    E(K,M,J)=-1.*D(K,M)
      IF (J-NJ) 20,16,16
16    DO 17 K=1,N
17    C(K,J)=E(K,NP1,J)
      DO 18 JJ=2,NJ
      M=NJ-JJ+1
      DO 18 K=1,N
```

```
      C(K,M)=E(K,NP1,M)
      DO 18 L=1,N
18    C(K,M)=C(K,M)+E(K,L,M)*C(L,M+1)
      DO 19 L=1,N
      DO 19 K=1,N
19    C(K,1)=C(K,1)+X(K,L)*C(L,3)
20    RETURN
      END
```

```
      SUBROUTINE MATINV(N,M,DETERM)
      DIMENSION ID(3)
      Real*8 A(3,3),B(3,3),C(3,1003),D(3,7)
      Real*8 DETERM,BMAX,SAVE,F
      Real*8 DABS
      COMMON /BLK1/ A,B,C,D
      DETERM=1.0
      DO 1 I=1,N
1     ID(I)=0
      DO 18 NN=1,N
      BMAX=0.0
      DO 6 I=1,N
      IF (ID(I))2,2,6
2     DO 5 J=1,N
      IF (ID(J)) 3,3,5
3     IF (DABS(B(I,J))-BMAX) 5,5,4
4     BMAX=DABS(B(I,J))
      IROW=I
      JCOL=J
5     CONTINUE
6     CONTINUE
      IF (BMAX) 7,7,8
7     DETERM=0.0
      RETURN
8     ID(JCOL)=1
      IF (JCOL-IROW) 9,12,9
9     DO 10 J=1,N
      SAVE=B(IROW,J)
      B(IROW,J)=B(JCOL,J)
10    B(JCOL,J)=SAVE
      DO 11 K=1,M
      SAVE=D(IROW,K)
      D(IROW,K)=D(JCOL,K)
11    D(JCOL,K)=SAVE
12    F=1.0/B(JCOL,JCOL)
      DO 13 J=1,N
13    B(JCOL,J)=B(JCOL,J)*F
      DO 14 K=1,M
14    D(JCOL,K)=D(JCOL,K)*F
      DO 18 I=1,N
      IF (I-JCOL) 15,18,15
15    F=B(I,JCOL)
      DO 16 J=1,N
16    B(I,J)=B(I,J)-F*B(JCOL,J)
      DO 17 K=1,M
17    D(I,K)=D(I,K)-F*D(JCOL,K)
18    CONTINUE
      RETURN
      END
```

C.7.
Sample Output

****RESULTS FOR 2nd ORDER KINETICS****

** Step Size = 0.5000
** Cob/Crb = 0.5000
** kf/lambda**2 = 1.18E-03
** Keq/Cob = 1.11E-03

** kf = 2.00E-01 1/sec
** lambda = 1.30E+01 sec**-1/2
** Keq = 4.00E-07 mole/liter
** Cob = 3.60E-04 moles/liter

** delta t/(delta x)**2 = 1.0000

** tmax = 2.00 delta t = 0.0100 num of t int. = 200

** xmax = 8.49 delta x = 0.1000 num of x int. = 85

1 ts = 1.0000

cs = 0.1934 cs (no homo kin) = 0.1425

i(HK)/i(NoHK) = 1.3568 eta(conc.) = 0.2099 eta(ac+ohmic) = 0.2901

xs	Co	Cr	Cy	Co Diff	Homo Kin
-0.1000	1.1143	0.8731	1.0001		
0.0000	1.0930	0.8830	1.0001	0.4035	-0.4143
0.1000	1.0757	0.8925	1.0001	0.3255	-0.3343
0.2000	1.0616	0.9015	1.0001	0.2632	-0.2703
0.3000	1.0502	0.9100	1.0001	0.2132	-0.2189
0.4000	1.0409	0.9180	1.0001	0.1730	-0.1775
0.5000	1.0333	0.9255	1.0001	0.1405	-0.1440
0.6000	1.0271	0.9326	1.0001	0.1142	-0.1170
0.7000	1.0221	0.9392	1.0001	0.0929	-0.0950
0.8000	1.0180	0.9453	1.0001	0.0757	-0.0773
0.9000	1.0147	0.9510	1.0000	0.0616	-0.0628
1.0000	1.0119	0.9562	1.0000	0.0502	-0.0511
1.1000	1.0097	0.9611	1.0000	0.0410	-0.0415
1.2000	1.0079	0.9655	1.0000	0.0334	-0.0337
1.3000	1.0064	0.9695	1.0000	0.0273	-0.0274
1.4000	1.0052	0.9731	1.0000	0.0222	-0.0223
1.5000	1.0042	0.9764	1.0000	0.0182	-0.0181
1.6000	1.0034	0.9794	1.0000	0.0148	-0.0147
1.7000	1.0028	0.9821	1.0000	0.0121	-0.0119
1.8000	1.0023	0.9844	1.0000	0.0099	-0.0096
1.9000	1.0018	0.9866	1.0000	0.0081	-0.0078
2.0000	1.0015	0.9884	1.0000	0.0066	-0.0063
2.1000	1.0012	0.9901	1.0000	0.0054	-0.0051
2.2000	1.0010	0.9915	1.0000	0.0044	-0.0041
2.3000	1.0008	0.9928	1.0000	0.0036	-0.0033

2.4000	1.0006	0.9939	1.0000	0.0029	-0.0026
2.5000	1.0005	0.9948	1.0000	0.0024	-0.0021
2.6000	1.0004	0.9957	1.0000	0.0019	-0.0017
2.7000	1.0003	0.9964	1.0000	0.0016	-0.0014
2.8000	1.0003	0.9970	1.0000	0.0013	-0.0011
2.9000	1.0002	0.9975	1.0000	0.0010	-0.0009
3.0000	1.0002	0.9979	1.0000	0.0008	-0.0007
3.1000	1.0001	0.9983	1.0000	0.0007	-0.0005
3.2000	1.0001	0.9986	1.0000	0.0005	-0.0004
3.3000	1.0001	0.9989	1.0000	0.0004	-0.0003
3.4000	1.0001	0.9991	1.0000	0.0004	-0.0003
3.5000	1.0000	0.9992	1.0000	0.0003	-0.0002
3.6000	1.0000	0.9994	1.0000	0.0002	-0.0002
3.7000	1.0000	0.9995	1.0000	0.0002	-0.0001
3.8000	1.0000	0.9996	1.0000	0.0001	-0.0001
3.9000	1.0000	0.9997	1.0000	0.0001	-0.0001
4.0000	1.0000	0.9998	1.0000	0.0001	-0.0001
4.1000	1.0000	0.9998	1.0000	0.0001	0.0000
4.2000	1.0000	0.9998	1.0000	0.0001	0.0000
4.3000	1.0000	0.9999	1.0000	0.0000	0.0000
4.4000	1.0000	0.9999	1.0000	0.0000	0.0000
4.5000	1.0000	0.9999	1.0000	0.0000	0.0000
4.6000	1.0000	0.9999	1.0000	0.0000	0.0000
4.7000	1.0000	1.0000	1.0000	0.0000	0.0000
4.8000	1.0000	1.0000	1.0000	0.0000	0.0000
4.9000	1.0000	1.0000	1.0000	0.0000	0.0000
5.0000	1.0000	1.0000	1.0000	0.0000	0.0000
5.1000	1.0000	1.0000	1.0000	0.0000	0.0000
5.2000	1.0000	1.0000	1.0000	0.0000	0.0000

Appendix D

Coupled Electrochemical and Chemical Reactions at the RDE

D.1. Introduction

This appendix presents a model for coupled homogeneous reaction and heterogeneous charge transfer at the rotating disk electrode (rde). The homogeneous reaction is assumed to follow dissociation-dimerization type kinetics, and the heterogeneous reaction follows kinetics given by the form of the multi-step Butler-Volmer equation presented in Equation 3-12. The dimensionless form of the equations and boundary conditions are derived in this section. In Section D.2 issues pertaining to the computer implementation are discussed. Section D.3 presents the computer programs, and Section D.4 shows some sample output.

The material balance equations appropriate for the rotating disk electrode are given by Equation 4-5 with Equation 3-31 for R_i. The boundary conditions for this problem are contained in Equations 3-12, 3-16, 3-17, and 3-32. The voltage balance between the working and reference electrode is Equation 3-14, and the relation between concentration gradient and current density is Equation 3-15. Since the system is at steady-state and only the z coordinate appears in the equations, the partial derivatives can be replaced by ordinary derivatives. The dimensionless variables in Table D-1 are used to make dependent and independent variables and their derivatives dimensionless.

Table D-2 lists the dimensionless forms of the material balance equations and boundary conditions. Several dimensionless groups appear in these equations; Table D-1 lists these groups.

D.2. Computer Implementation

As in Appendix C, Newman's BAND program (140,141) was used to obtain a numerical solution. This technique requires that any non-linear equations or boundary conditions be linearized about a trial solution. The three coupled ordinary differential equations were reduced

Table D-1: Definitions

Dimensionless Groups	Dimensionless Variables
$Sc = \frac{\mu}{\rho D}$	$\varsigma = \left(\frac{\rho\omega}{\mu}\right)^{1/2} z$
$\frac{k_b C_{ob}}{\omega}$	$C_o^* = \frac{C_o}{C_{ob}}$
$\frac{K_{eq}}{C_{ob}}$	$C_r^* = \frac{C_r}{C_{rb}}$
$\frac{C_{ob}}{C_{rb}}$	$C_y^* = \frac{C_y}{C_{yb}}$
$i_o^* = i_o \frac{\left(\frac{\mu}{\rho\omega}\right)^{1/2}}{nFDC_{ob}}$	$i^* = -\frac{dC_o^*}{d\varsigma} = i \frac{\left(\frac{\mu}{\rho\omega}\right)^{1/2}}{nFDC_{ob}}$

Table D-2: Dimensionless Equations

Material Balances

$$\frac{1}{Sc}\frac{d^2C_o^*}{d\varsigma^2} + a\varsigma^2\frac{dC_o^*}{d\varsigma} + \frac{2k_bC_{ob}}{\omega}(C_y^* - C_o^{*2}) = 0 \qquad \text{(D-1)}$$

$$\frac{1}{Sc}\frac{d^2C_r^*}{d\varsigma^2} + a\varsigma^2\frac{dC_r^*}{d\varsigma} = 0 \qquad \text{(D-2)}$$

$$\frac{1}{Sc}\frac{d^2C_y^*}{d\varsigma^2} + a\varsigma^2\frac{dC_y^*}{d\varsigma} + \frac{k_bK_{eq}}{\omega}(C_o^{*2} - C_y^*) = 0 \qquad \text{(D-3)}$$

Boundary Conditions

as $\varsigma \rightarrow \infty$, $C_o^* \rightarrow 1$, $C_r^* \rightarrow 1$, $C_y^* \rightarrow 1$ (D-4)

at $\varsigma = 0$:

$$\frac{dC_r^*}{d\varsigma} + \frac{s_rC_{ob}}{s_oC_{rb}}\frac{dC_o^*}{d\varsigma} = 0 \qquad \text{(D-5a)}$$

$$\frac{dC_y^*}{d\varsigma} = 0 \qquad \text{(D-5b)}$$

$$\frac{dC_o^*}{d\varsigma} = i_o^*\left[(C_o^*)^{z_{o\infty}/\nu}(C_r^*)^{z_{r\infty}/\nu}\exp\left(\frac{-\alpha_cF\left\{V-\gamma\frac{dC_o^*}{d\varsigma}\right\}}{RT}\right) - (C_o^*)^{z_{o\infty}/\nu}(C_r^*)^{z_{r\infty}/\nu}\exp\left(\frac{\alpha_aF\left\{V-\gamma\frac{dC_o^*}{d\varsigma}\right\}}{RT}\right)\right] \qquad \text{(D-5c)}^\dagger$$

$^\dagger\gamma = nFDC_{ob}R_s\left(\frac{\rho\omega}{\mu}\right)^{1/2}$

to finite-difference form using Equations C-19. The non-linear homogeneous kinetic terms were

handled as in Equation C-23.

The heterogeneous boundary condition, Equation D-5c, is non-linear. The truncated Taylor series that can be written for the preexponential terms in Equation D-5c is:

$$(a+x)^y = a^y + y\,a^{y-1} + \cdots \tag{D-6}$$

Using this series, the first preexponential term in Equation D-5c can be written:

$$(C_o^*)^{z_\infty/\nu} = (C_o^{*(n)})^{z_\infty/\nu} + \frac{z_{oc}}{\nu}(C_o^{*(n)})^{z_\infty/\nu-1}\Delta_o \tag{D-7}$$

where $\Delta_o = C_o^* - C_o^{*(n)}$. Applying Equation D-6 to the other preexponential terms leads to equations similar to D-7.

The truncated Taylor series for the exponential term can be written:

$$\exp(x) = 1+x \tag{D-8}$$

The linearized version of the first exponential term in Equation D-5c is:

$$\exp\left(\frac{-\alpha_c F(V+\gamma C_o^{*\prime})}{RT}\right)\left\{1-\frac{\alpha_c \gamma F}{RT}\Delta_o'\right\} \tag{D-9}$$

where the ' denotes differentiation with respect to ς. The second exponential term is handled in a similar manner. The equations for the exponential and preexponential terms are substituted into Equation D-5c, and higher order terms of the form $\Delta_i \cdot \Delta_j$ are eliminated. This leads to the final linearized form suitable for use with the BAND subroutine.

D.3. Computer Programs

For Subroutines BAND and MATINV see Section C.5

```
C Simulate homogeneous kinetics on disk electrode
C Dissociation-Dimerization homogeneous kinetics
C Y=2O
C 2(O + ne = R)

      Real*8 zetam,h,etat,crat,bb,elecn,acon,Cob,currs,omg
      Real*8 zeta,tol,del,deld
      Real*8 gamma,thop,Rs,sno,so,sr
      Real*8 diffu,conv,reac,etac,etaa,ohmic
      Real*8 kb,kf,Keq,curr,curr0,nu,Dco,Sc,F,R,Temp,alpha,alphc
      Real*8 C(3,1003),Cn(3,1003)
      Real*8 A(3,3),B(3,3),D(3,7),X(3,3),Y(3,3),G(3)
      Real*8 gro1,gro2,gro3,gro4
      Real*8 dsqrt,dexp,dfloat,dabs,dlog
      Real*8 star,end,step
      Real*8 term(2),zoc,zrc,zoa,zra
      Integer NJ,itnum,itmax
      Integer istar,iend,istep,int
      Common /BLK1/ A,B,C,D
      Common /BLK2/ G,X,Y,N,NJ
      Data R,F /8.314,96500.0/
      Data acon /0.51023/

C Variables:
C alpha, anodic transfer coefficient
C alphc, cathodic transfer coefficient
C C(1,j), concentration of O
C C(2,j), concentration of R
C C(3,j), concentration of Y
C Cob, bulk concentration of O (mole/cm**3)
C crat, Cob/Crb
C curr, current (A/cm**2)
C curr0, exchange current density (A/cm**2)
C currs, dimensionless current
C Dco, diffusion coefficient (cm**2/sec)
C elecn, number of electrons in overall reaction
C etaa, activation overpotential (volts)
C etac, concentration overpotential (volts)
C etat, applied potential between working and reference electrode (volts)
C F, Faraday (coulombs/equiv)
C itmax, maximum number of iterations allowed
C itnum, current iteration count
C kb, rate constant for dimerization reaction (cm**3/mole-sec)
C Keq, equilibrium constant for dissociation-dimerization reac. (mole/cm**3)
C kf, rate constant for dissociation reaction (1/sec)
C NJ, mesh points
C nu, kinematic viscosity (cm**2/sec)
C ohmic, ohmic overpotential (volts)
C R, universal gas constant (J/mole-K)
```

```
C Rs, solution resistance between working and reference electrode
C Sc, Schmidt number
C sno, stoichiometric number
C so, stoichiometric coefficient of species 0
C sr, stoichiometric coefficient of species R
C Temp, temperature (K)
C zeta, dimensionless distance from interface
C zetam, maximum value of zeta
C zoa, anodic reaction order for O
C zoc, cathodic reaction order for O
C zra, anodic reaction order for R
C zrc, cathodic reaction order for R


C Open files
      Open (Unit=7,File='homodisk2.out',Status='New')
      Open (Unit=8,File='conc2.pro',Status='New')
      Open (Unit=9,File='iV.gph',Status='New')
      Open (Unit=10,File='input3.par',Status='Old')
C Number of equations
      N=3

C Tolerance for convergence
      tol=1.0e-7

C Maximum number of iterations
      itmax = 25

C Read parameters
      Read (10,5) kf,Keq,curr0,omg,elecn
5     Format (f16.7)
      Read (10,10) crat,alpha,Temp,Cob,sno,zoc,zoa,zrc,zra
10    Format (f16.7)
      Read (10,11) star,end,step
11    Format (f16.7)
      Read (10,12) Rs
12    Format (f16.7)
      Read (10,15) NJ
15    Format (i3)

      alphc= (elecn/sno)-alpha
      Dco=1.e-5
      nu=0.01
      Sc=nu/Dco
      kb=kf/Keq
      gamma = elecn*F*Dco*Cob*dsqrt(omg/nu)*Rs
      so = zoc - zoa
      sr = zra - zrc

C Set up space mesh
      zetam=5.0/(Sc**0.33)
      h= zetam/(NJ-2)
```

```
C Write info to file
      Write (7,20)
      Write (8,20)
      Write (9,20)
20    Format (' **Results For Dissociation-Dimerization Kinetics',/)
      Write (7,25) NJ,zetam,h
      Write (8,25) NJ,zetam,h
      Write (9,25) NJ,zetam,h
25    Format (' **Mesh points =',i3,5x,'zeta max =',1pe10.2,5x
     1,'Step size = ',e10.2)

      Write (7,28) Temp,Rs
      Write (8,28) Temp,Rs
      Write (9,28) Temp,Rs
28    Format (' **Temperature =',f7.1,' K',
     1/,' **Rs =',f7.1,' ohm-cm**2')

      Write (7,30) Sc,omg
      Write (8,30) Sc,omg
      Write (9,30) Sc,omg
30    Format (' **Schmidt No. = ',f10.1,5x
     1,'Rot. Speed = ',f8.1,' rad/sec')

      Write (7,35) curr0,sno,alpha,elecn,alphc
      Write (8,35) curr0,sno,alpha,elecn,alphc
      Write (9,35) curr0,sno,alpha,elecn,alphc
35    Format (' **Ex. curr. =',1pe10.2,' A/cm**2',
     15x,'Stoichiometric No. =',0pf5.1,/,1x,'**alpha anod. = ',
     2f6.2,5x,' No. of elec. =',f5.1,5x,'alpha cath = ',f6.2)

      Write (7,38) zoc,zoa,zrc,zra
      Write (8,38) zoc,zoa,zrc,zra
      Write (9,38) zoc,zoa,zrc,zra
38    Format (' **zoc=',f5.1,5x,'zoa=',f5.1,
     1/,' **zrc=',f5.1,5x,'zra=',f5.1)

      Write (7,40) kf,kb,Keq
      Write (8,40) kf,kb,Keq
      Write (9,40) kf,kb,Keq
40    Format (' **kf = ',1pe10.2,5x,'kb = ',e10.2,5x
     1,'Keq = ',e10.2)

      Write (7,45) crat,Cob
      Write (8,45) crat,Cob
      Write (9,45) crat,Cob
45    Format (' **Cob/Crb = ',1pe10.2,5x,'Cob = ',e10.2, ' mole/cm**3',/)

      gro1=1.0/Sc
      gro2=kb*Cob/omg
      gro3=kb*Keq/omg
      gro4=curr0*dsqrt(nu)/(elecn*F*Dco*dsqrt(omg)*Cob)
C Write header
      Write (7,300)
```

```
300     Format (' Overpotential',5x,'Dim. Current',7x,'Current')
        Write (7,301)
301     Format (6x,'(mV)',27x,'(mA/cm**2)')
        do 91 ind1=1,3
                do 90 ind2=1,NJ
                        Cn(ind1,ind2)=1.0
90              Continue
91      Continue

        istar = int(star)
        iend = int(end)
        istep = int(step)
C Solve for concentration profile and current at each value of overpotential
        do 500 ijk = istar,iend,istep

C Set potential difference between working and reference electrode
        etat = dfloat(ijk)/1000.0
C First iteration
        itnum=0
C Initial Guess
        Cn(1,2)=0.1
        Cn(2,2)=1.0

C Come here if solution has not converged
75      Continue
C Derivative at interface
        thop = (Cn(1,3)-Cn(1,1))/(2.*h)
        bb =dexp(F*(etat+gamma*thop)/(R*Temp))
C Zero Concentration array
        do 50 ind=1,203
                C(1,ind)=0.0
                C(2,ind)=0.0
                C(3,ind)=0.0
50      Continue

C Set up for first mesh point (j=1)
C Zero arrays
        do 150 ind1=1,3
                do 100 ind2=1,3
                        B(ind1,ind2)=0.0
                        D(ind1,ind2)=0.0
                        X(ind1,ind2)=0.0
100             Continue
                G(ind1)=0.0
150     Continue

C Flux relation between O and R at interface
        B(1,1)=-crat
        B(1,2)=-1.0
        X(1,1)=crat
        X(1,2)=1.0

C Heterogeneous kinetics, including iR losses
```

```
      term(1)=-zoc/sno*(Cn(1,2)**(zoc/sno-1.))*
     1(Cn(2,2)**(zrc/sno))*(bb**(-alphc))
      term(2)=zoa/sno*(Cn(1,2)**(zoa/sno-1.))*
     1(Cn(2,2)**(zra/sno))*(bb**alpha)
      D(2,1)=2.*h*gro4*(term(1)+term(2))

      term(1)=-zrc/sno*(Cn(1,2)**(zoc/sno))*
     1(Cn(2,2)**(zrc/sno-1.))*(bb**(-alphc))
      term(2)=zra/sno*(Cn(1,2)**(zoa/sno))*
     1(Cn(2,2)**(zra/sno-1.))*(bb**alpha)
      D(2,2)=2.*h*gro4*(term(1)+term(2))

      term(1)=gro4*(bb**(-alphc))*alphc*F*gamma/(R*Temp)*
     1(Cn(1,2)**(zoc/sno))*(Cn(2,2)**(zrc/sno))
      term(2)=gro4*(bb**alpha)*alpha*F*gamma/(R*Temp)*
     1(Cn(1,2)**(zoa/sno))*(Cn(2,2)**(zra/sno))
      X(2,1) = 1.+term(1)+term(2)

      B(2,1) = -X(2,1)

      term(1)=gro4*(bb**(-alphc))*(Cn(1,2)**(zoc/sno))*
     1(Cn(2,2)**(zrc/sno))*(1.-zoc/sno-zrc/sno+alphc*
     2F*gamma*thop/(R*Temp))
      term(2)=-gro4*(bb**alpha)*(Cn(1,2)**(zoa/sno))*
     1(Cn(2,2)**(zra/sno))*(1.-zoa/sno-zra/sno-
     2alpha*F*gamma*thop/(R*Temp))
      G(2)=2.*h*(term(1)+term(2))

C No faradaic reaction of Y
      X(3,3)=1.0
      B(3,3)=-1.0
C Now call BAND
      Call BAND(1)

C For interior points
      do 200 j=2,NJ-1
            do 165 ind1=1,3
                  do 160 ind2=1,3
                        A(ind1,ind2)=0.0
                        B(ind1,ind2)=0.0
                        D(ind1,ind2)=0.0
160.                Continue
                    G(ind1)=0.0
165         Continue
            zeta = dfloat(j-2)*h
            term(1)= acon*zeta*zeta*h/2.0
            A(1,1) = gro1-term(1)
            B(1,1) = -2.0*(gro1 + 2.*gro2
     1*Cn(1,j)*h*h)
            B(1,3) = 2.*gro2*h*h
            D(1,1) = gro1 + term(1)
            G(1) =-2.*gro2*Cn(1,j)*Cn(1,j)*h*h
```

```
                A(2,2) = gro1 - term(1)
                B(2,2) = -2.0*gro1
                D(2,2) = gro1 + term(1)

                A(3,3) = gro1 - term(1)
                B(3,1) = 2.*gro3*Cn(1,j)*h*h
                B(3,3) = -1.0*(gro3*h*h + 2.0*gro1)
                D(3,3) = gro1 + term(1)
                G(3) = gro3*Cn(1,j)*Cn(1,j)*h*h

                Call BAND(j)
200     Continue

C Last mesh point
        do 220 ind1=1,3
                do 215 ind2=1,3
                        Y(ind1,ind2)=0.0
                        A(ind1,ind2)=0.0
                        B(ind1,ind2)=0.0
215             Continue
                G(ind1)=0.0
220     Continue

        B(1,1)=1.0
        B(2,2)=1.0
        B(3,3)=1.0
        G(1)=1.0
        G(2)=1.0
        G(3)=1.0

        Call BAND(NJ)

C Check for convergence
        do 295 ind1=1,3
                do 275 j=1,NJ
                If(dabs((C(ind1,j)-Cn(ind1,j))/C(ind1,j)) .gt. tol) Then
C Increment the iteration number by 1
                        itnum=itnum+1

C Check to see if itmax has been exceeded
                        If(itnum .gt. itmax) Then
                                Write (6,260) etat,itmax
260                             Format (' at eta = ',
   1f8.2,' max iteration count',i2,' exceeded')
                                Stop
                        Endif

C Save the concentrations
                        do 265 m1=1,3
                                do 264 m2=1,NJ
                                        Cn(m1,m2)=C(m1,m2)
264                             Continue
265                     Continue
```

```
C Go back and solve the equations again
                        goto 75
                Endif
275             Continue
295     Continue

C Come here if the solution has converged

C Calculate current
        currs=-(C(1,3)-C(1,1))/(2.0*h)
        curr=currs*curr0/gro4

C Calculate overpotentials
        ohmic = curr*Rs
        etac = R*Temp/(elecn*F)*(dlog(C(1,2))-dlog(C(2,2)))
        etaa = etat - etac -ohmic

C Write out results for this overpotential
        Write (6,440) etat*1000.0,curr*1000.0,itnum
440     Format (f8.2,f16.7,i2)
        Write (7,450) etat*1000.0,currs,curr*1000.0
450     Format (f8.2,6x,2f16.7)
        Write(9,452) etat*1000.0,curr*1000.0
452.    Format (f8.2,f16.7)

C Write out concentration profile in boundary layer
C At every 10th value of overpotential
        If (float(ijk)/10.0 .eq. float(int(ijk/10)) ) Then
        Write (8,451) etat*1000.0,currs,curr*1000.0
451     Format (/,' eta =',f8.2,' mV',/
   1,' Dimensionless Current =',f16.7,/
   2,' Current =',f16.7,' mA/cm**2',/)
        Write (8,579) etac*1000.0,etaa*1000.0,ohmic*1000.0
579     Format (' etac =',f8.2,' mV',/
   1,' etaa =',f8.2,' mV',/
   2,' ohmic =',f8.2,' mV',/)
        If (dabs(etat) .gt. 1.e-5) Then
                del = (C(1,2)-1.0)/currs*dsqrt(nu/omg)
                deld=1.61*(Dco**0.333)*(nu**(1./6.))/dsqrt(omg)
                Write(8,581) del*1.e4,deld*1.e4
581             Format (' delta =',f9.3,' microns';/
   1,' delta (diffusion) =',f9.3,' microns',/)
        Endif

C Header
        Write (8,562)
562     Format (4x,'zeta',5x,'Co',7x,'Cr',8x,'Cy',7x,'Diffusion',3x
   1,'Convection',2x,'Homo. Reaction')

        do 458 j=1,NJ
                zeta =(j-2)*h
                diffu =gro1*(C(1,j+1)-2.*C(1,j)+C(1,j-1))/(h*h)
                conv =acon*zeta*zeta*(C(1,j+1)-C(1,j-1))/(2.*h)
```

```
                reac = 2.*(kb*Cob/omg)*(C(3,j)-C(1,j)*C(1,j))
                If (j .eq. 1) Then
                Write(8,455) -h,C(1,1),C(2,1),C(3,1)
455             Format (4f9.4)
                Else If ((j .eq. 2) .or. (j .eq. 3)) Then
                        Write (8,453) zeta,C(1,j),C(2,j),C(3,j)
   1,diffu,conv,reac
                Else
                        If ((dabs(1.-C(1,j)) .lt. 1.e-5) .and.
   1(dabs(1.-C(2,j)) .lt. 1.e-5) .and.
   1(dabs(1.-C(3,j)) .lt. 1.e-5)) Then
                                Write (8,453) zeta,
   1C(1,j),C(2,j),C(3,j),diffu,conv,reac
453                     Format (4f9.4,3x,f9.4,3x,f9.4,3x,f9.4)
                                goto 465
                        Endif
                        If (float(j)/10.0 .eq. float(int(j/10)) ) Then
                        Write (8,453) zeta,C(1,j),C(2,j),C(3,j)
   1,diffu,conv,reac
                        Endif
                Endif
458     Continue
        Endif
465     Continue

500     Continue

        Stop
        End
```

D.4.
Sample Output

**Results For Dissociation-Dimerization Kinetics

**Mesh points = 502 zeta max = 5.12e-01 Step size = 1.02e-03
**Temperature = 313.0 K
Rs = 1.7 ohm-cm2
**Schmidt No. = 1000.0 Rot. Speed = 100.0 rad/sec
Ex. curr. = 7.50e-04 A/cm2 Stoichiometric No. = 1.0
**alpha anod. = 1.50 No. of elec. = 2.0 alpha cath = 0.50
**zoc= 1.0 zoa= -1.0
**zrc= 0. zra= 1.0
**kf = 3.50e-03 kb = 4.04e+08 Keq = 8.66e-12
Cob/Crb = 5.35e-05 Cob = 5.35e-08 mole/cm3

Overpotential (mV)	Dim. Current	Current (mA/cm**2)
-50.00	-19.8371383	-0.2048284
-45.00	-19.0976147	-0.1971924
-40.00	-18.2115955	-0.1880438
-35.00	-17.1472240	-0.1770537
-30.00	-15.8653215	-0.1638174
-25.00	-14.3177132	-0.1478375
-20.00	-12.4452360	-0.1285033
-15.00	-10.1754144	-0.1050662
-10.00	-7.4198134	-0.0766133
-5.00	-4.0711138	-0.0420363
0.	0.0000000	0.0000000
5.00	4.9479984	0.0510906
10.00	10.9555190	0.1131212
15.00	18.2360028	0.1882958

eta = -50.00 mV
Dimensionless Current = -19.8371383
Current = -0.2048284 mA/cm**2

etac = -20.29 mV
etaa = -29.36 mV
ohmic = -0.35 mV

delta = 3.922 microns
delta (diffusion) = 16.162 microns

zeta	Co	Cr	Cy	Diffusion	Convection	Homo. Reaction
-0.0010	0.2016	1.0002	0.9998			
0.	0.2221	1.0002	0.9998	-0.4110	0.	0.4110
0.0010	0.2422	1.0002	0.9998	-0.4070	0.0000	0.4070
0.0082	0.3711	1.0002	0.9998	-0.3734	0.0006	0.3728
0.0184	0.5226	1.0002	0.9998	-0.3165	0.0023	0.3143
0.0287	0.6409	1.0001	0.9998	-0.2590	0.0042	0.2548
0.0389	0.7320	1.0001	0.9998	-0.2066	0.0060	0.2006

0.0491	0.8015	1.0001	0.9998	-0.1618	0.0072	0.1546
0.0594	0.8539	1.0001	0.9998	-0.1250	0.0080	0.1170
0.0696	0.8932	1.0001	0.9999	-0.0955	0.0082	0.0874
0.0798	0.9225	1.0001	0.9999	-0.0724	0.0080	0.0644
0.0900	0.9441	1.0001	0.9999	-0.0544	0.0075	0.0470
0.1003	0.9599	1.0001	0.9999	-0.0407	0.0068	0.0339
0.1105	0.9715	1.0001	0.9999	-0.0302	0.0060	0.0242
0.1207	0.9799	1.0001	0.9999	-0.0223	0.0052	0.0172
0.1310	0.9860	1.0000	0.9999	-0.0164	0.0044	0.0120
0.1412	0.9903	1.0000	0.9999	-0.0119	0.0036	0.0083
0.1514	0.9933	1.0000	1.0000	-0.0086	0.0029	0.0057
0.1617	0.9955	1.0000	1.0000	-0.0062	0.0023	0.0039
0.1719	0.9970	1.0000	1.0000	-0.0044	0.0018	0.0026
0.1821	0.9980	1.0000	1.0000	-0.0031	0.0014	0.0017
0.1924	0.9987	1.0000	1.0000	-0.0022	0.0010	0.0011
0.2026	0.9992	1.0000	1.0000	-0.0015	0.0008	0.0007
0.2128	0.9995	1.0000	1.0000	-0.0010	0.0006	0.0005
0.2231	0.9997	1.0000	1.0000	-0.0007	0.0004	0.0003
0.2333	0.9998	1.0000	1.0000	-0.0004	0.0003	0.0002
0.2435	0.9999	1.0000	1.0000	-0.0003	0.0002	0.0001
0.2538	0.9999	1.0000	1.0000	-0.0002	0.0001	0.0001
0.2640	1.0000	1.0000	1.0000	-0.0001	0.0001	0.0000
0.2742	1.0000	1.0000	1.0000	-0.0001	0.0001	0.0000
0.2845	1.0000	1.0000	1.0000	-0.0000	0.0000	0.0000
0.2896	1.0000	1.0000	1.0000	-0.0000	0.0000	0.0000

eta = -40.00 mV
Dimensionless Current = -18.2115955
Current = -0.1880438 mA/cm**2

etac = -16.35 mV
etaa = -23.33 mV
ohmic = -0.32 mV

delta = 3.858 microns
delta (diffusion) = 16.162 microns

zeta	Co	Cr	Cy	Diffusion	Convection	Homo. Reaction
-0.0010	0.2786	1.0002	0.9998			
0.	0.2974	1.0002	0.9998	-0.3941	0.	0.3941
0.0010	0.3158	1.0002	0.9998	-0.3892	0.0000	0.3892
0.0082	0.4337	1.0001	0.9998	-0.3515	0.0005	0.3510
0.0184	0.5714	1.0001	0.9998	-0.2932	0.0021	0.2912
0.0287	0.6784	1.0001	0.9998	-0.2372	0.0038	0.2334
0.0389	0.7604	1.0001	0.9998	-0.1877	0.0054	0.1823
0.0491	0.8227	1.0001	0.9998	-0.1462	0.0065	0.1397
0.0594	0.8697	1.0001	0.9999	-0.1124	0.0071	0.1053
0.0696	0.9048	1.0001	0.9999	-0.0857	0.0073	0.0784
0.0798	0.9309	1.0001	0.9999	-0.0648	0.0071	0.0577
0.0900	0.9502	1.0001	0.9999	-0.0486	0.0067	0.0420
0.1003	0.9643	1.0001	0.9999	-0.0363	0.0060	0.0303
0.1105	0.9746	1.0001	0.9999	-0.0270	0.0053	0.0216
0.1207	0.9821	1.0000	0.9999	-0.0199	0.0046	0.0153

0.1310	0.9875	1.0000	0.9999	-0.0146	0.0039	0.0107
0.1412	0.9914	1.0000	0.9999	-0.0106	0.0032	0.0074
0.1514	0.9941	1.0000	1.0000	-0.0077	0.0026	0.0051
0.1617	0.9960	1.0000	1.0000	-0.0055	0.0021	0.0035
0.1719	0.9973	1.0000	1.0000	-0.0039	0.0016	0.0023
0.1821	0.9982	1.0000	1.0000	-0.0028	0.0012	0.0015
0.1924	0.9988	1.0000	1.0000	-0.0019	0.0009	0.0010
0.2026	0.9993	1.0000	1.0000	-0.0013	0.0007	0.0006
0.2128	0.9995	1.0000	1.0000	-0.0009	0.0005	0.0004
0.2231	0.9997	1.0000	1.0000	-0.0006	0.0004	0.0003
0.2333	0.9998	1.0000	1.0000	-0.0004	0.0002	0.0002
0.2435	0.9999	1.0000	1.0000	-0.0003	0.0002	0.0001
0.2538	0.9999	1.0000	1.0000	-0.0002	0.0001	0.0001
0.2640	1.0000	1.0000	1.0000	-0.0001	0.0001	0.0000
0.2742	1.0000	1.0000	1.0000	-0.0001	0.0000	0.0000
0.2845	1.0000	1.0000	1.0000	-0.0000	0.0000	0.0000
0.2875	1.0000	1.0000	1.0000	-0.0000	0.0000	0.0000

Appendix E

Heat Transfer Analysis

E.1. Estimation of the Physical Properties of Air

The viscosity of air as a function of temperature was determined from:

$$\mu = 2.6693\times10^{-5}\frac{\sqrt{MT}}{\sigma^2\Omega_\mu} \tag{E-1}$$

With σ=3.711 Å and Ω_μ=1, Equation E-1 predicted the viscosity of air within 7.5% over the temperature range of 0 to 80 °C. The value of μ was used to predict the value of the thermal conductivity k from the Eucken formula for polyatomic gases:

$$k = \left(C_p + \frac{5R}{4M}\right)\mu \tag{E-2}$$

where C_p=3.5R/M for a diatomic, ideal gas. Combination of Equations E-1 and E-2 allows the value of Pr to be calculated:

$$Pr = \frac{C_p}{C_p+1.25R} \tag{E-3}$$

For the estimation of the density (ρ) and volume coefficient of expansion (β), air was assumed to behave as a mixture of ideal gases. This is a good approximation at atmospheric pressures and in the temperature range consisidered here (20 to 80 °C). Thus:

$$\rho = \frac{PM}{RT} \tag{E-4}$$

and

$$\beta = \frac{1}{T} \tag{E-5}$$

E.2. Computer Programs

```
C Determine the temperature given the heat input
      Real*8 par(4),x(1),fnorm,wk(22)
      Real*8 htlnc,htlrd,htlfc
      Real*8 Tf,Cp,mu,k,MW,R,sigma,rho,beta,Pr,Gr,hnc,g
      Real*8 dsqrt,Re,hfc
      Integer nsig,n,itmax,ier
      Data R,MW,sigma /8.314,29.0,3.711/
      Data g /980.0/
      External fcn


C Read heat flux, air temperature, length
      Read (5,10) par(1),par(2),par(3),par(4)
10    Format (4f16.7)

      n=1
      nsig=7
      itmax=100

C Initial guess
      x(1)=par(2)+50.0

      Call ZSCNT (fcn,nsig,n,itmax,par,x,fnorm,wk,ier)

C Film temperature
      Tf=(x(1)+par(2))/2.
C Heat capacity (joule/g-K)
      Cp=3.5*R/MW
C Viscosity (g/cm-sec)
      mu=2.669e-5*dsqrt(MW*Tf)/(sigma*sigma)
C Thermal conductivity (W/cm-K)
      k=(Cp+ (5.*R)/(4.*MW))*mu
C Density
      rho= (1.*MW)/(82.06*Tf)
C Expansion factor
      beta=1./Tf
C.Prandtl number
      Pr=Cp/(Cp+1.25*R/MW)
C Grashof number
      Gr= rho*rho*beta*g*(par(3)**3)*(x(1)-par(2))/(mu*mu)
C Reynolds number
      Re=par(4)*par(3)*rho/mu
C Heat transfer coefficient for natural convection
      hnc=(k/par(3))*0.54*((Gr*Pr)**(1./4.))
C Heat transfer coefficient for forced convection
      hfc=(k/par(3))*0.664*dsqrt(Re)*(Pr**(1./3.))
C Heat loss due to natural convection
      htlnc= hnc*(x(1)-par(2))
C Heat loss due to forced convection
      htlfc= hfc*(x(1)-par(2))
```

```
C Heat loss to to radiation
      htlrd= 5.672e-12*( (x(1)**4) - (par(2)**4) )

      Write (6,20) x(1),par(2),(x(1)-par(2)),Tf
20    Format (' Cell Temperature=',f9.2,' K',/
     1,' Air Temperature=',f9.2,' K',/
     2,' DeltaT=',f9.2,' C',/,' Film Temp.=',f9.2,' K')

      Write (6,22) Gr,Pr,Gr*Pr,Re
22    Format (' Gr=',1pe10.2,3x,'Pr=',e10.2,3x
     1,'Gr*Pr=',e10.2,/,' Re=',e10.2)

      Write (6,25) hnc*1761.1,hfc*1761.1
25    Format (' hnc=',f9.3,' BTU/hr-F-ft**2',/
     1,' hfc=',f9.3,' BTU/hr-F-ft**2')

      Write (6,30) htlfc*1000.0,htlnc*1000.0,htlrd*1000.0
30    Format(' Heat loss due to for. conv.=',f8.2,' mW/cm**2',/
     1,' Heat loss due to nat. conv.=',f8.2,' mW/cm**2',/
     1,' Heat loss due to radiation=',f8.2,' mW/cm**2')

      Stop
      End
```

```
      Subroutine fcn (x,f,n,par)
      Real*8 x(1),f(1),par(4)
      Real*8 Tf,Cp,mu,k,MW,R,sigma,rho,beta,Pr,Gr,hnc,g
      Real*8 dsqrt,Re,hfc
      Integer n
      Data R,MW,sigma /8.314,29.0,3.711/
      Data g /980.0/

C Film temperature
      Tf=(x(1)+par(2))/2.
C Heat capacity (joule/g-K)
      Cp=3.5*R/MW
C Viscosity (g/cm-sec)
      mu=2.669e-5*dsqrt(MW*Tf)/(sigma*sigma)
C Thermal conductivity (W/cm-K)
      k=(Cp+ (5.*R)/(4.*MW))*mu
C Density
      rho= (1.*MW)/(82.06*Tf)
C Expansion factor
      beta=1./Tf
C Prandtl number
      Pr=Cp/(Cp+1.25*R/MW)
C Grashof number
      Gr= rho*rho*beta*g*(par(3)**3)*(x(1)-par(2))/(mu*mu)
C Reynolds number
      Re=par(4)*par(3)*rho/mu
C Heat transfer coefficient for natural convection
      hnc=(k/par(3))*0.54*((Gr*Pr)**(1./4.))
C Heat transfer coefficient for forced convection
      hfc=(k/par(3))*0.664*dsqrt(Re)*(Pr**(1./3.))

      f(1)=par(1)-hnc*(x(1)-par(2))-5.672e-12*
     1( (x(1)**4) - (par(2)**4) ) -hfc*(x(1)-par(2))


      Return
      End
```

E.3.
Sample Output

For a heat input of 70 mW/cm**2, cell length 3 cm and 1 m/sec wind velocity:

```
Cell Temperature=  313.12 K
Air Temperature=  293.00 K
DeltaT=   20.12 C
Film Temp.=  303.06 K
Gr=  7.24E+04  Pr=  7.37E-01  Gr*Pr=  5.33E+04
Re=  1.93E+03
hnc=   1.192 BTU/hr-F-ft**2
hfc=   3.822 BTU/hr-F-ft**2
Heat loss due to for. conv.=  43.67 mW/cm**2
Heat loss due to nat. conv.=  13.62 mW/cm**2
Heat loss due to radiation=  12.72 mW/cm**2
```

This report was done with support from the Department of Energy. Any conclusions or opinions expressed in this report represent solely those of the author(s) and not necessarily those of The Regents of the University of California, the Lawrence Berkeley Laboratory or the Department of Energy.

Reference to a company or product name does not imply approval or recommendation of the product by the University of California or the U.S. Department of Energy to the exclusion of others that may be suitable.

LAWRENCE BERKELEY LABORATORY
TECHNICAL INFORMATION DEPARTMENT
UNIVERSITY OF CALIFORNIA
BERKELEY, CALIFORNIA 94720